UNIVERSITY OF
LIVERPOOL

Femtosecond serial crystallography of two classes of copper nitrite reductase

Thesis submitted in accordance with the requirements of the University of Liverpool for the degree of Doctor of Philosophy

by
Thomas Philip Halsted

June 2018

Acknowledgments

The work described in this thesis was jointly funded by the University of Liverpool, RIKEN and the Science and Technology Funding Council (STFC).

Firstly, I would like to thank my supervisors at the University of Liverpool and the RIKEN SPring-8 Centre, Professor S. Samar Hasnain and Dr Masaki Yamamoto. I am thankful for their guidance, patients and support throughout the four years of my PhD program.

Dr Svetlana Antonyuk was a constant source of help and advice and responsible for my understanding of crystallography theory.

My understanding of synchrotron radiation and X-ray free electron masers is due to Dr Mark Roper and I thank him for his advice and encouragement.

All my scientific endeavour when studying at SPring-8 was thanks to Dr Hideo Ago who organised my beamtime and was constant source of guidance.

Professor Robert Eady was a great source of discussion and helped me to understand the finer points of denitrification and the relationship between the crystal structures and other biochemical data.

Dr Keitero Yamashita, who helped me out in more ways than I can count with processing serial crystallography data, was of constant help during my stay in Japan.

I would also specifically like to thank Dr Matthew Blakeley, Dr Gareth Wright, Dr Nicolas Burdet and Chai Gopalasingam for scientific and friendly advice and discussion of the course of my PhD.

I must acknowledge all the hard work and effort put in by the staff at the RIKEN SPring-8 Centre for the operation of the synchrotron and XFEL without which none of this work would be possible and who organised and looked after me during my stay.

Thanks are due the lab members of both the Molecular Biophysics Group at the University of Liverpool and the SR Life Sciences Instrumentation Group at the RIKEN SPring-8 Centre for interesting discussions, ideas and good times I've had during my studies.

Finally, I would like to personally thank my family for their encouragement and support and especially to Charlotte Mekis for her editorial skills and for putting up with me during this whole experience.

Abstract

Copper-containing nitrite reductases (CuNiR) catalyse the reduction of nitrite to the gaseous product nitric oxide. The enzyme forms part of the denitrification pathway which, in some bacteria, forms part of their respiratory network where nitrogen reduction is coupled to the synthesis of adenosine triphosphate. Denitrifying bacteria, through the production of nitrous oxide, have a large greenhouse gas impact and are also opportunist pathogens often found infecting immunocompromised patients.

The structure and biochemical properties of CuNiRs have been extensively studied revealing a common functional core of one type 1 copper (T1Cu) site and one type 2 copper (T2Cu) site, linked by a cysteine-histidine bridge. The T1Cu is reduced by a partner redox protein and that electron is transferred to the T2Cu to reduce nitrite along with two protons. The order of this reaction is unknown, however with T2Cu reduction possible before or after nitrite binding.

The structural study of this reaction is complicated by radiation damage effecting the copper sites when probed by synchrotron X-ray crystallography (SRX). The copper sites are highly prone to reduction by photoelectrons generated by the radiolysis of solvent inside the crystal. As the probe alters the redox states of the copper sites during data collection, the redox state of multiple species in the crystal change over the course of data collection, preventing them from being refined individually and obscuring the active site intermediates that may establish the enzyme mechanism order.

To overcome the radiation damage, data collection was carried out at the SPring-8 angstrom compact free electron laser (SACLA), an X-ray free electron laser (XFEL), which produces femtosecond scale X-ray pulses that allow the diffraction to be captured before the onset of any radiation damage. The size of the pulse width also precludes any molecular rotation or vibration producing a 'time-frozen' structure. XFEL collection operates on the principle of 'diffraction before destruction' where the high intensity of the X-ray pulse destroys the crystal material and so new crystalline material must be inserted into the beam after each shot.

Using this approach, the oxidised structure of two CuNiRs were collected from *Achromobacter xylosoxidans* (*Ax*NiR) and *Achromobacter cycloclastes* (*Ac*NiR) along with the reduced and nitrite-bound structures of *Ac*NiR. This XFEL data along with other structural data revealed a basis for the oxidase activity in *Ax*NiR and the pH dependence of *Ac*NiR suggesting an ordered mechanism. This thesis reveals the specific changes that SRX can cause to radiation sensitive metalloproteins and the importance of overcoming it.

Contents

List of Figures

List of Tables

List of Schemes

Glossary of abbreviations

*Ac*NiR	*Achromobacter cycloclastes* copper nitrite reductase
*Af*NiR	*Alcaligenes faecalis* copper nitrite reductase
AMO	Ammonia monooxygenase
AOA	Ammonia-oxidizing archaea
AOB	Ammonia-oxidizing bacteria
ATP	Adenosine triphosphate
*Ax*NiR	*Achromobacter xylosoxidans* copper nitrite reductase
BW	Bandwidth
CC	Correlation coefficient
ccNiR	Cytochrome *c* nitrite reductase
cNOR	Cytochrome *c*-oxidising nitric oxide reductase
CuNiR	Copper nitrite reductase
Cu_A	Binuclear copper A coordination centre
Cu_Z	Tetranuclear copper Z coordination centre
CV	Column volume
DAPHNIS	Diverse application platform for hard X-ray diffraction in SACLA
DEAE	Diethylethanolamine
DMSO	Dimethyl sulfoxide
E. coli	*Escherichia coli*
Euk-NR	Eukaryotic assimilatory nitrate reductase
EuXFEL	European X-ray free-electron laser
FID	Free interface diffusion
GDVN	Gas dynamic virtual nozzle
*Gt*NiR	*Geobacillus thermodenitrificans* copper nitrite reductase
HAO	Hydroxylamine oxidoreductase
HCO	Haem-copper oxidase
*Hd*NiR	*Hyphomicrobium denitrificans* copper nitrite reductase
ID	Insertion devices
IPTG	Isopropyl β-D-1-thiogalactopyranoside
Kan	Kanamycin
LB	Lysogeny broth
LCLS	Linac Coherent Light Source
LN_2	Liquid nitrogen
LPC	Lipidic cubic phases
MSOX	Multiple structures serially obtained from one crystal
MWCO	Molecular weight cut-off

MX	Macromolecular crystallography
NiR	Nitrite reductase
NOB	Nitrite-oxidizing bacteria
NOR	Nitric oxide reductase
NR	Nitrate reductase
Nap	Periplasmic dissimilatory nitrate reductase
Nar	Membrane-bound respiratory nitrate reductase
Nas	Cytoplasmic assimilatory nitrate reductase
NADH	Nicotinamide adenine dinucleotide
NADPH	Nicotinamide adenine dinucleotide phosphate
MP(CCD)	Multiport charged-coupled device
NX	Neutron crystallography
NXR	Nitrite oxidoreductase
N_2OR	Nitrous oxide reductase
SDS-PAGE	Sodium dodecyl sulphate - Polyacrylamide gel electrophoresis
PAL-XFEL	Pohang Accelerator Laboratory's hard X-ray free electron laser
PCET	Proton-coupled electron transfer
PDB	Protein Data Bank
PEG	Polyethylene glycol
PHM	Peptidylglycine α-hydroxylating monooxygenase
*Ps*NiR	*Pseudomonas chlororaphis* copper nitrite reductase
qNOR	Quinol-oxidising nitric oxide reductase
RF	Radio frequency
*Rp*NiR	*Ralstonia pickettii* copper nitrite reductase
*Rs*NiR	*Rhodopseudomonas sphaeroides* copper nitrite reductase
RT	Room temperature
SACLA	SPring-8 Angstrom Compact Free-electron Laser
SASE	Self-amplified spontaneous emission
SEC	Size exclusion chromatography
SFX	Serial femtosecond crystallography
SF-ROX	Serial femtosecond rotational crystallography
SR(X)	Synchrotron radiation (crystallography)
SSX	Serial synchrotron crystallography
SO	Sulphite oxidase
SOD	Superoxide dismutase
SPring-8	Super Photon Ring – 8 GeV
SwissFEL	X-ray free-electron laser at the Paul Scherrer Institute
T1Cu	Type 1 copper coordination centre
T2Cu	Type 2 copper coordination centre
XAFS	X-ray absorption spectroscopy
(X)FEL	(X-ray) Free electron laser

Chapter 1 – Denitrification and copper nitrite reductase

1.1. The nitrogen cycle

1.1.1. Terrestrial nitrogen cycle

The ability of an organism to grow and thrive is dependent on the availability of nutrients in its surrounding environment. Nitrogen is a requisite element for all forms of life as a building block of nucleic and amino acids to make DNA and proteins, for chlorin production in plants and as part of the energy transfer molecule adenosine triphosphate (ATP). Dinitrogen (N_2) is abundant in the terrestrial atmosphere, accounting for 78% by volume, making it readily accessible to most organisms. However, the ability to utilise N_2 is limited by chemistry, dominated by the N_2 triple bond[1]. The dissociation energy of the N≡N bond is equal to 945.41 kJ mol^{-1}, making it unreactive and inaccessible to most living organisms. The energy barrier in converting atmospheric nitrogen to organic nitrogen leads to a scarcity of useable nitrogen in most ecological niches and therefore it is often the limiting factor in biological biomass synthesis. Microbes play a key role in facilitating the supply of fixed nitrogen to all organisms through a series of enzymatic reaction steps. N_2 is converted to a fixed form, ammonia (NH_3), which is utilised by living organisms to form the biopolymers that make up all living

organisms (Figure 1.1)[2]. After organism death, these biopolymers undergo decay whereby the nitrogen is returned to the environment, converted by microbes to nitrates (NO_3^-) and nitrites (NO_2^-), and the energy stored is released for use by the decomposers. These three processes, nitrogen fixation, nitrification and denitrification, and the interconversion reactions of nitrogen between the inorganic and organic forms are collectively known as the nitrogen cycle.

Biological nitrogen fixation is carried out by diazotrophs, organisms able to thrive without an external source of fixed nitrogen[3]. Diazotrophs exist as free-living and symbiotic bacteria, both of which contain the nitrogenase enzyme which catalyses the nitrogen fixation reaction (Figure 1.2). Atmospheric N_2 is converted to NH_3 by coupling the hydrolysis of 16 ATP molecules and is accompanied by the formation of one hydrogen (H_2) molecule.

$$N_2 + 8H^+ + 8e^- \rightarrow 2NH_3 + H_2$$

Mo-nitrogenase consists of two proteins, the Fe protein and the FeMo protein[4]. The Fe protein is a homodimer containing an [Fe_4S_4] cluster and acts to transfer electrons from partner electron transfer proteins to the FeMo protein. Electron transfer is facilitated by ATP hydrolysis inducing a conformational change in the complex, reducing the distance between the Fe and FeMo cores[5]. The FeMo protein is heterotetramer, containing two [Fe_4S_4] clusters and two FeMoco cofactors forming the reaction centres[6]. After

intermolecular electron transfer from the Fe protein to the FeMo $[Fe_4S_4]$ cluster, intramolecular electron transfer occurs from the $[Fe_4S_4]$ cluster to the FeMoco cofactor, reducing bound N_2 to NH_3. Closely related nitrogenase systems based on V or only Fe have also been identified[7].

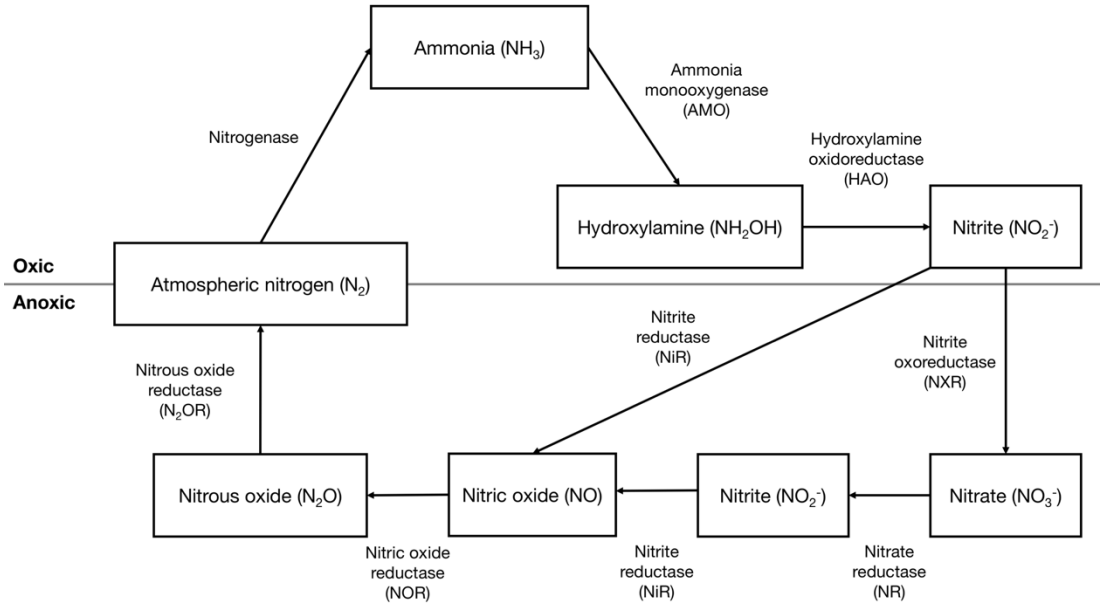

Figure 1.1. A schematic of the terrestrial nitrogen cycle. Atmospheric dinitrogen is fixed into ammonia and converted through several intermediates in both oxic and anoxic environments before being returned to the atmosphere. Aerobic, anaerobic and O_2 evolving photosynthetic diazotrophs have evolved to prevent nitrogenase inactivation by O_2. The bacterial enzyme associated with each step is listed beside the arrow indicating the reaction order.

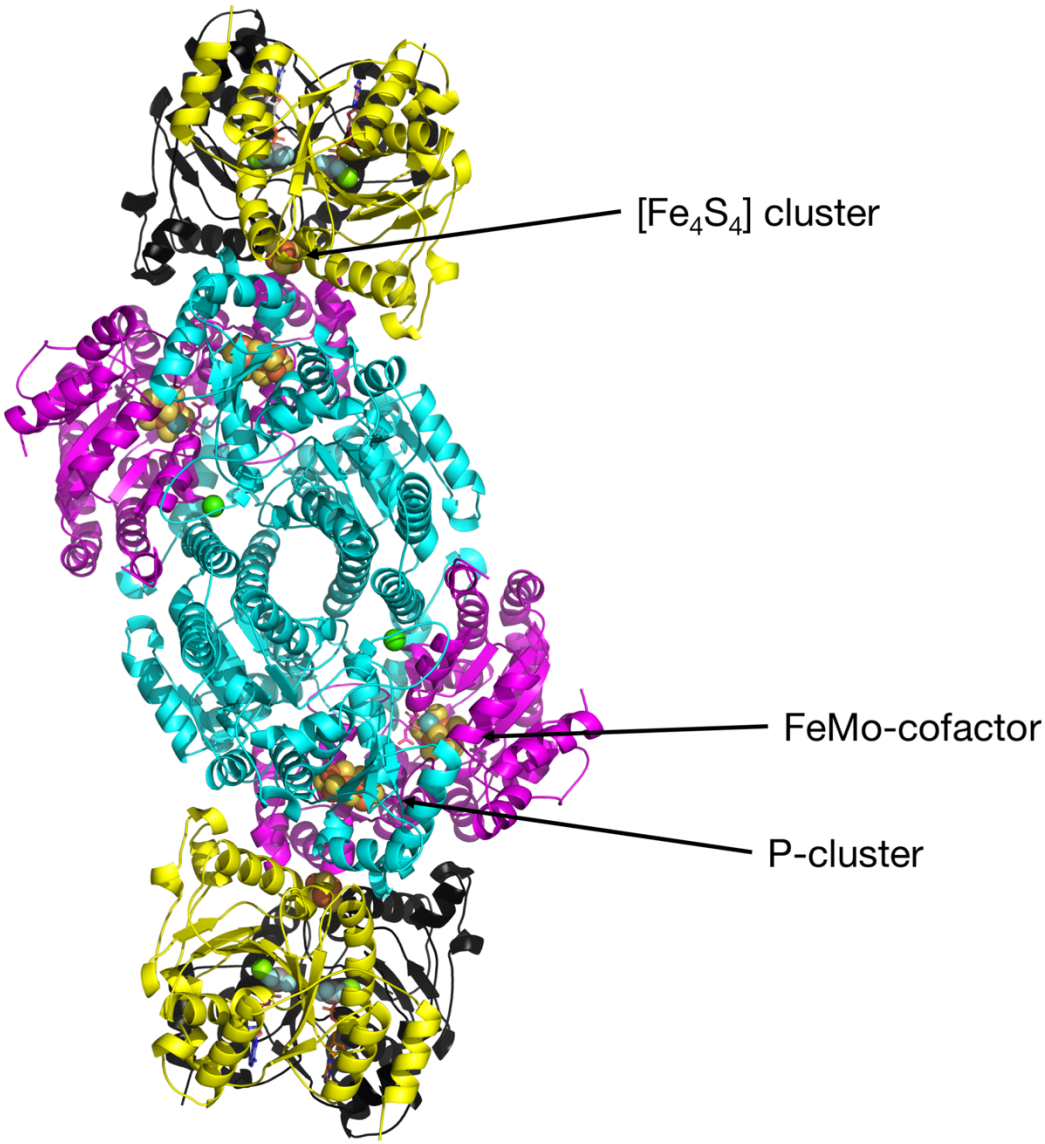

Figure 1.2. The structure of the nitrogenase complex from *Azotobacter vinelandii* at 3.0 Å in complex with a nucleoside triphosphate analogue. The FeMo α-subunits are shown in magenta and the β-subunits in cyan. The two subunits of each Fe-protein are shown in yellow and black respectively. Bound co-factors and ligands are coloured according to element (PDB: 1N2C).

Fixed nitrogen in the form of NH_3 or ammonium (NH_4^+) is subsequently oxidised by ammonia-oxidizing bacteria (AOB)[8] and ammonia-oxidizing archaea (AOA)[9] into NO_2^- which itself is oxidised by nitrite-oxidizing bacteria (NOB) into NO_3^-. These microorganisms are chemolithoautotrophs utilising carbon dioxide (CO_2) for biomass production and energy from the redox reaction. The first nitrification reaction:

$$2NH_4^+ + 3O_2 \rightarrow 2NO_2^- + 2H_2O + 4H^+$$

leads to the formation of NO_2^- and is broken down into two steps. This is catalysed first by ammonia monooxygenase (AMO), oxidising NH_4^+ to hydroxylamine (NH_2OH), and then by hydroxylamine oxidoreductase (HAO) oxidising NH_2OH to NO_2^-. This second step has recently come under scrutiny, however, with recent field work suggesting that nitric oxide (NO) is the product of the HAO reaction[10]. The second nitrification reaction:

$$2NO_2^- + O_2 \rightarrow 2NO_3^-$$

is catalysed by nitrite oxidoreductase (NXR), oxidising NO_2^- to NO_3^-. Ammonia-oxidizing and nitrite-oxidizing organisms tend to exist in equilibrium which prevents NO_2^- accumulation. During the oxidation of NH_2OH the electrons produced are passed into an electron transport chain to generate a proton gradient and produce ATP via ATP synthase. The completion of the nitrogen cycle following the conversion of NH_3 to NO_3^- is

the reduction of NO_3^- back to atmospheric N_2 known as denitrification. This will be covered after the following section that discusses the human impact on the nitrogen cycle.

1.1.2. Human impact on the nitrogen cycle

The activity of humans has a major impact on the environmental distribution of nitrogen, primarily as the result of changes in the energy and agricultural requirements of humans. The scarcity of fixed nitrogen sources was a limiting factor on food production and consequently human population[11]. The development of the Haber-Bosch process allowed large quantities of NH_3 to be generated from H_2 and atmospheric N_2. Since the development of the Haber process in the early 20th century, the removal of the fixed nitrogen limit has seen a population boom that has coincided with a huge increase in food production, with one hectare of arable land now estimated to support 4.3 people in 2008, as opposed to 1.9 people in 1908[12]. Agriculture productivity improvement is estimated to be 30 to 50% of crop yield[13]. The industrial revolution, based on the burning of fossil fuels, has also been consequential in increasing the amount of fixed nitrogen in the atmosphere[2]. Nitrous oxide (N_2O) has a major global warming potential, three hundred times more potent than CO_2. It is currently the fourth most abundant greenhouse gas in the atmosphere, with an absolute increase of 54 ppb, from 270 ppb in 1750 to 324 ppb in 2011[14]. The increase in biologically available nitrogen in the environment has led to serious imbalance in a number of terrestrial and marine ecosystems[15,16]. Over and improper use of N-fertiliser has led to increased levels of NO_3^- in wastewater, which can lead to algae bloom and eutrophication of fresh and salt water sources[17]. Excess nutrients in the water lead to a rapid increase in plant and algal growth that quickly outcompetes other species by blocking sunlight to the deeper water and using

up limited resources. Once the plants and algae reach maximum density, the decrease in other organisms causes them to die due to a lack of other required nutrients. Decomposition then proceeds, causing the body of water to be starved of oxygen, creating a hypoxic region free of aerobic life.

Understanding the human impact on the nitrogen cycle and its interconnections with the ecosystem at large is the first step in curtailing anthropogenic effects[18]. The series of steps that follow the conversion of NO_3^- back to atmospheric N_2 as already discussed are collectively known as denitrification. If the denitrification pathway can be understood in detail, then the effects of human intervention may be mitigated.

1.1.3. Denitrification

The denitrification pathway consists of a series of enzymes to convert NO_3^- in the terrestrial environment to atmospheric N_2, thus completing the cycle started by nitrogen fixing microorganisms and preventing a build-up of fixed nitrogen in soil[19]. Various components of the cycle are found in bacteria, archaea and fungi with each species utilising the fixed nitrogen in its own ecological niche, in both terrestrial and marine environments. In bacteria, the synthesis of ATP is coupled to a series of reactions, leading to energy production in anaerobic environments, but other uses include assimilatory and dissimilatory ammonification (Figure 1.3)[20]. The reduction pathway consists the reaction series:

$$NO_3^- \rightarrow NO_2^- \rightarrow NO \rightarrow N_2O \rightarrow N_2$$

The whole process can be expressed as redox reaction:

$$2NO_3^- + 10e^- + 12H^+ \rightarrow N_2 + 6H_2O$$

Each step in the reaction is catalysed by an enzyme class that will be discussed in detail.

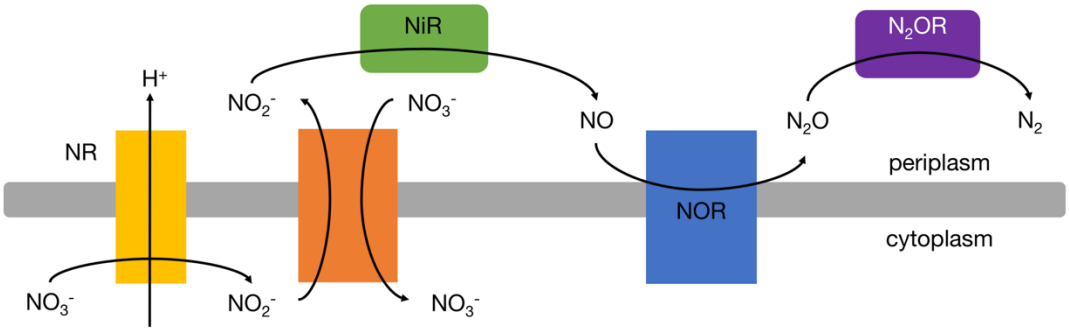

Figure 1.3. A diagram of the bacterial denitrification pathway. In the absence of oxygen, bacteria containing all the necessary dentification enzymes can utilise nitrogen oxides as electron acceptors. The electron transport chain is used to drive a proton pump, forming an electrochemical gradient used to drive ATP synthase.

1.1.4. Denitrifying bacteria

Denitrifying bacteria are classified by the ability to metabolise nitrogen oxides to form N_2O or atmospheric N_2 gas[19]. Denitrifying bacteria exist as both facultative aerobic heterotrophs, which utilise fixed nitrogen as a terminal electron acceptor when oxygen is unavailable, and as facultative autotrophs, which utilise inorganic sulphur compounds[19]. Enzymes involved in denitrification are found in a wide variety of bacteria; this diversity has allowed for the evolution of many specific denitrifying bacteria able to tolerate extreme thermophilic and halophilic conditions[19]. Certain genera of denitrifying bacteria are observed infecting immunocompromised patients in nosocomial conditions[21]. The *Achromobacter* genus is environmentally pervasive and is considered an opportunist pathogen in patients susceptible to infection[21]. They are classified as lactose-nonfermenting, gram-negative bacilli that are highly motile via multiple, long flagella. The classification of these bacteria has switched a number of times, first being classified as members of the *Achromobacter* genus and then moved to the *Alcaligenes* genus, before recently being reclassified back to the *Achromobacter* genus[22,23]. While most members of this genus are not pathogenic, a number are repeatably found infecting patients with suppressed immune systems and underlying conditions that rely on repeated hospitalisation, specifically cystic fibrosis, haematological, solid organ malignancies and renal failure[24,25]. Of all the *Achromobacter* bacteria, *Achromobacter xylosoxidans* is the most commonly observed opportunist[21]. The pathogenicity of this particular species is derived from a number of genomic features including a series of antibiotic efflux

pumps and modifying genes[26]. Because of their ubiquity, including as a part of usual gut flora, any subsequent infection is difficult to treat because of their innate antibiotic resistance. Their ability to utilise fixed nitrogen as a terminal electron acceptor is also important in the scheme of resistance to host immune defence, specifically the reduction of NO, produced by macrophages to destroy invading cells[27]. Peroxynitrite ($ONOO^-$), formed via combination of NO and superoxide (O_2^-), is routinely utilised by macrophages to overwhelm invading cells and destroy their reproductive machinery before their pathogenesis becomes problematic. *Achromobacter* bacteria have however been recognised to contain superoxide dismutase (SOD) that converts O_2^- into O_2 or H_2O_2, reducing the formation of the two radical species and limiting the host immune response[28]. It is important to note the dual importance of these bacteria from both an environmental and a public health viewpoint with the steady rise in global population age and with it, an increase in nosocomial conditions[29].

1.2. The denitrification pathway

1.2.1. Nitrate reductase (NR)

Nitrate reductase (NR) catalyses the reduction of NO_3^- to NO_2^- according to reaction:

$$NO_3^- + 2e^- + 2H^+ \rightarrow NO_2^- + H_2O$$

There are four main classes of NRs; three bacterial enzymes, consisting of the cytoplasmic assimilatory (Nas), periplasmic dissimilatory (Nap) and membrane-bound respiratory (Nar) NRs, plus the eukaryotic assimilatory NRs (Euk-NR)[30–33]. The bacterial NRs belong to the dimethyl sulfoxide (DMSO) reductase family, while the eukaryotic NRs belong to the sulphite oxidase (SO) family. The Nars group consists of membrane-anchored heterotrimeric enzymes. The active site consists of a molybdenum (Mo) atom coordinated by two pterin groups via the four sulphur atoms. The monomeric Naps share the coordinated Mo atom, but here it is coordinate by the pterin sulphur atoms plus a cysteine ligand and a hydroxo/oxo group. An $[Fe_4S_4]$ cluster is coordinated near the N-terminus as part of the intramolecular electron transfer network. The Nas active site is Mo coordinated by pterin cofactor with a guanine dinucleotide (Mo-*bis*MGD). The protein structure varies between different organisms and are the least well characterised NR group. The Euk-NRs are found in a wide range of algae, fungi and plants and function as homodimer with activity dependent on the Moco core[34]. Euk-NRs can be nicotinamide adenine dinucleotide (NADH) or nicotinamide adenine

dinucleotide phosphate (NADPH) dependent or independent and are classified as such.

1.2.2. Nitrite reductase (NiR)

The first committed step in denitrification is the reduction of NO_2^- to form gaseous nitric oxide, which is carried out by the enzyme nitrite reductase (NiR) in reaction:

$$NO_2^- + e^- + 2H^+ \rightarrow NO + H_2O$$

Two distinct classes of periplasmic NiR exist in denitrifying bacteria reducing NO_2^- using either an iron- or copper-based active centre. The iron-based class contains several enzymes. Cytochrome *cd₁* NiR couples the oxidation of cytochrome c_{551} to the reduction of NO_2^- to NO. It's comprised of two chains both containing a haem type *c* and *d* group forming the active tetrahaem protein[35]. Cytochrome *c* nitrite reductase (ccNiR) is a pentahaem protein that catalyses the second step of the conversion of NO_2^- to NH_3[36]. Like cytochrome cd_1, ccNiR is a homodimer with a total of ten type *c* haem's in the active form with quinone carriers serving as electron donors. Copper nitrite reductases (CuNiR) are homotrimer proteins that contain one T1 (T1Cu) and one T2 (T2Cu) copper-binding site per catalytic unit[37,38]. Electron transfer from the T1Cu to T2Cu site occurs via a Cys-His bridge, reducing of the T2Cu and subsequently the NO_2^- ligand. Azurin acts as the electron carrier for blue NiR and pseudoazurin for green NiR with intermolecular electron transfer occurring from the azurin to the T1Cu centre. Low molecular weight *c*-type cytochromes also function as electron donors to these enzymes.

1.2.3. Nitric oxide reductase (NOR)

The third step of denitrification is catalysed by membrane-bound nitric oxide reductase (NOR) in the reaction:

$$2NO + 2e^- + 2H^+ \rightarrow N_2O + H_2O$$

The NO produced by NiR is cytotoxic and must be removed immediately by NOR. Some pathogenic bacterial express NORs to defend against NO produced by host immune system macrophages[39]. N_2O production by NORs is also important to study from an environmental perspective. N_2O is 310 times more powerful than CO_2 as a greenhouse gas and can catalytically break down the ozone layer[40]. As microorganisms produce a large percentage of the terrestrial N_2O emissions, an understanding of their enzymatic mechanisms is necessary for the prediction of future N_2O emissions and the discovery of possible inhibitors[41]. The NORs are members of the haem-copper oxidase (HCO) super-family. This super-family can be further divided into the quinol-oxidising NORs (qNOR) and cytochrome *c*-oxidising NORs (cNOR). Crystal structures have been determined for both types of NOR[42,43]. cNOR is a heterodimer with one smaller subunit (NorC) containing a haem *c* group which acts as the external electron acceptor and the larger subunit (NorB) containing the catalytic centre. A haem *b* group mediates electron transfer from the haem *c* group, the catalytic centre, which consists of another haem *b* group (haem b_3) and one non-haem iron (Fe_B). The active site structure is

conserved in qNOR, but the rest of the structure shows marked differences, especially in the lack of the haem *c* group.

1.2.4. Nitrous oxide reductase (N_2OR)

The copper-containing enzyme nitrous oxide reductase (N_2OR) catalyses the reduction of N_2O to N_2 in the final step of microbial denitrification:

$$N_2O + 2e^- + 2H^+ \rightarrow N_2 + H_2O$$

N_2OR is a homodimeric metalloprotein, located in the periplasm and containing two copper centres, Cu_A and Cu_Z, in each monomer (Figure 1.4)[44]. Each monomer consists of two domains, one cuperodoxin domain and one β-propeller domain. The dimer packs with a 'head-to-tail' motif that places the Cu_A site of one monomer in proximity of the Cu_Z site of the other, creating the active site of the enzyme at the dimer interface[45]. The Cu_A centre is coordinated in the cuperodoxin domain of one monomer and consists of two Cu atoms bridged by two cysteine residues. The catalytic Cu_Z centre is in the β-propeller domain and is a unique cluster that consists of four Cu atoms bridged by inorganic sulphide and coordinated by seven histidine residues adopting a distorted tetrahedral geometry. N_2O binds side-on to the Cu_Z centre and following electron transfer from the Cu_A site is converted to N_2. The catalytic cycle of this enzyme has yet to be determined as no intermediate states have been captured structurally. With the production of N_2 the denitrification pathway comes full circle, with the fixed nitrogen returned to the atmosphere.

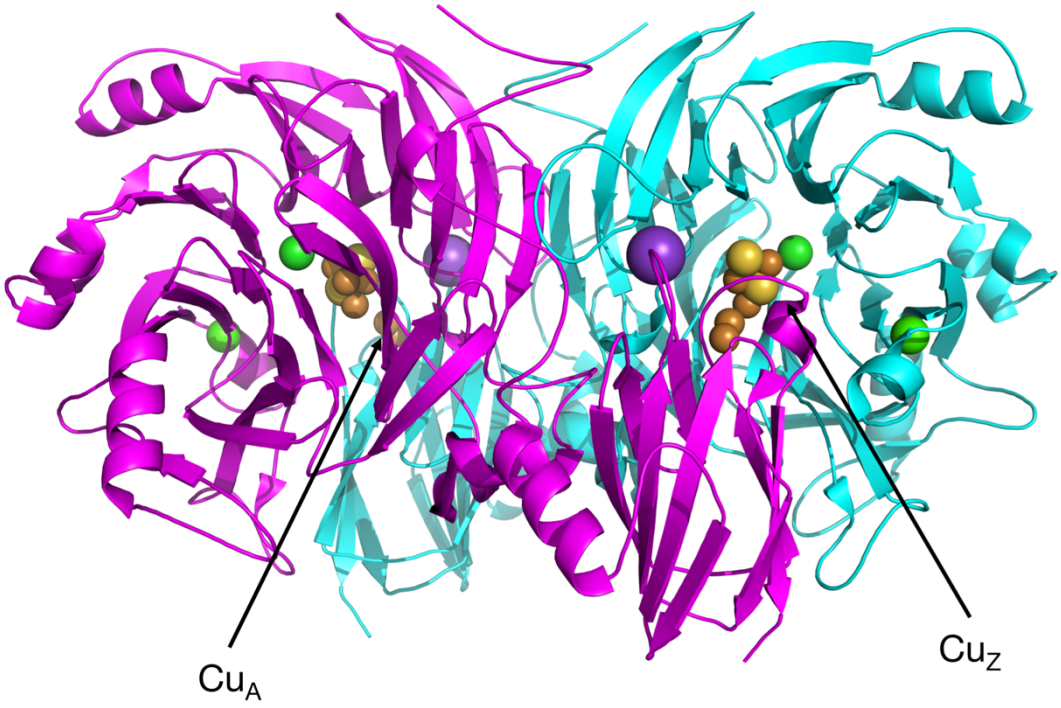

Figure 1.4. Structure of N_2OR from *Pseudomonas stutzeri* at 1.7 Å. The enzyme is a homodimer with one binuclear copper (Cu_A) and one tetranuclear copper (Cu_Z) site per subunit. The homodimer packs such that the Cu_A in one monomer can interact with the Cu_Z in the adjacent monomer (PDB: 3SBQ).

1.3. Copper nitrite reductase (CuNiR)

1.3.1. Global structure

CuNiRs have been extensively studied for many years with various structural, biochemical and spectroscopic methods[19]. CuNiR is encoded by the *nirK* gene first identified in *Pseudomonas sp.* strain G-179[46] and *Alcaligenes faecalis* S-6[47] in 1993. Until recently all CuNiRs were thought to be homotrimeric with a molecular weight of ~37 kDa per monomer with each monomer composed of two domains (Figure 1.5). The monomers take the form of two Greek key β-barrel structures with cuperodoxin-like homology, along with two short and one long α-helical regions. Differences in the T1Cu site geometry caused CuNiRs to previously be classified blue or green[48]. In blue CuNiR, the T1Cu methionine ligand maintains an axial position, relative to the His-His-Cys plane whereas by contrast, in green CuNiR, the ligand is perturbed from the tetrahedral shape leading to distortion, via the Cys-His bridge, of the T2Cu site[49]. The differences in the copper ligand geometry causes a shift in the absorption spectral bands of the oxidised enzyme from 450 nm to 600 nm, changing the colour of the protein from green to blue.

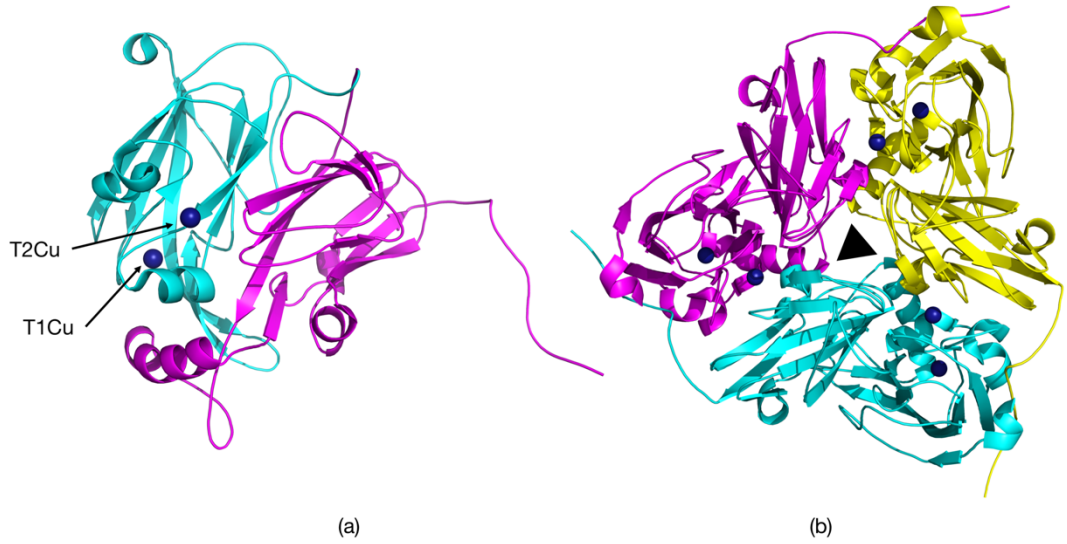

Figure 1.5. The structure homotrimeric CuNiR from *Achromobacter xylosoxidans* (*Ax*NiR). (a) The domain structure of the *Ax*NiR monomer. The two cuperodoxin domains are shown in magenta and cyan. The two copper sites are shown in dark blue and labelled respectively. (b) The *Ax*NiR trimer has three identical subunits forming the functional enzyme. The T1Cu site is buried below the protein surface while the T2Cu is ligated between the boundary of two of the monomers forming three active sites per trimer. The three-fold rotational symmetry is designated by the black triangle (PDB: 1OE1).

1.3.2. Copper centres

The two copper sites in the two-domain monomer form the main catalytic unit of CuNiR. The T1Cu is buried ~7 Å below the protein surface in a distorted tetrahedral geometry. It is ligated by two histidine residues, one cysteine and one methionine, and acts to accept electrons from partner redox proteins azurin and pseudoazurin[50]. Electron transfer from the T1Cu to T2Cu site occurs via a Cys-His bridge spanning 11 covalent bonds and ~12.6 Å (Figure 1.6). The T2Cu site sits at the interface between two of the monomers where the Cu is ligated by three histidine residues as well as a water molecule in the resting state[51]. Upon reduction of the T2Cu the water ligand is lost, leaving the T2Cu ligated by just the three histidine resides[52]. The local environment of the T2Cu site contains several conserved residues that contribute to the enzymatic reaction. Conserved aspartic acid (Asp_{CAT}) and histidine (His_{CAT}) residues that are necessary for enzymatic activity sit adjacent to the T2Cu ligated water molecule (Figure 1.7)[53]. The water molecule is hydrogen bonded to the Asp_{CAT} which in turn is hydrogen bonded to His_{CAT} via a linking water molecule visible in both oxidised and reduced structures. Both these residues are predicted to play a role in proton donation with one proton donated from each amino acid.

In AcNiR Asp_{CAT} has been observed in a dual conformation termed 'proximal' and 'gatekeeper' positioned near to and away from the T2Cu respectively[54]. Structural studies carried out using X-ray crystallography have revealed both ligand and product binding to CuNiR. The observed mode of ligand binding has varied between different CuNiR species with both

symmetric and asymmetric NO_2^- binding observed. In CuNiR from *Achromobacter cycloclastes* (*Ac*NiR), NO_2^- binds in a side-on bidentate manner with the two oxygen atoms equidistance from the T2Cu termed 'side-on'[55]. An isoleucine residue (Ile_{CAT}) positioned above the T2Cu is predicted to play a role in positioning the NO_2^- molecule and therefore may play a role in the reaction order based on the nature of the ligand binding mode[56]. In the CuNiR from *Geobacillus thermodenitrificans* (*Gt*NiR), the mutation of this residue to valine causes the NO_2^- to shift to a monodentate binding mode, binding to the T2Cu via a single O atom[57]. NO_2^- accesses the T2Cu site via a channel formed between the monomer-monomer interface consisting of a 12 Å hydrophobic cleft that helps to mediate the control of substrate availability. The residue Ile_{CAT} extends into the cleft and partially blocks direct solvent access to the active site[51]. Two polar residues, Glu133 and His313, mark the entrance to the cleft and hydrogen bond with surrounding water molecules creating a well-ordered system (Figure 1.8). A water molecule also resides in the cleft itself, hydrogen bonded to the carbonyl oxygen of Ala131. This selective nature is necessary to maintain normal catalytic efficiency by excluding excess substrate and water from the T2Cu site. Therefore, mutations in residues situated in the channel can influence the enzyme action. *Ax*NiR-F306C substitution changes the rate-limiting step and displays a major decrease in catalytic efficiency[58]. The large hydrophobic nature of Phe306 acts to restrict solvent access to the T2Cu site to the single ligated water molecule. When this residue is mutated, secondary water molecules can access the substrate entry channel. However, some CuNiR structures do have two water molecules

ligated to the T2Cu in resting state, especially at non-cryogenic temperatures [59]. Too reduced NO_2^-, the T2Cu H_2O ligand must first displace the H_2O by disrupting the coordinate bond. With two H_2O ligands the energy barrier the NO_2^- must overcome to exchange with the water molecules is increased, leading to a less energetically favourable reaction.

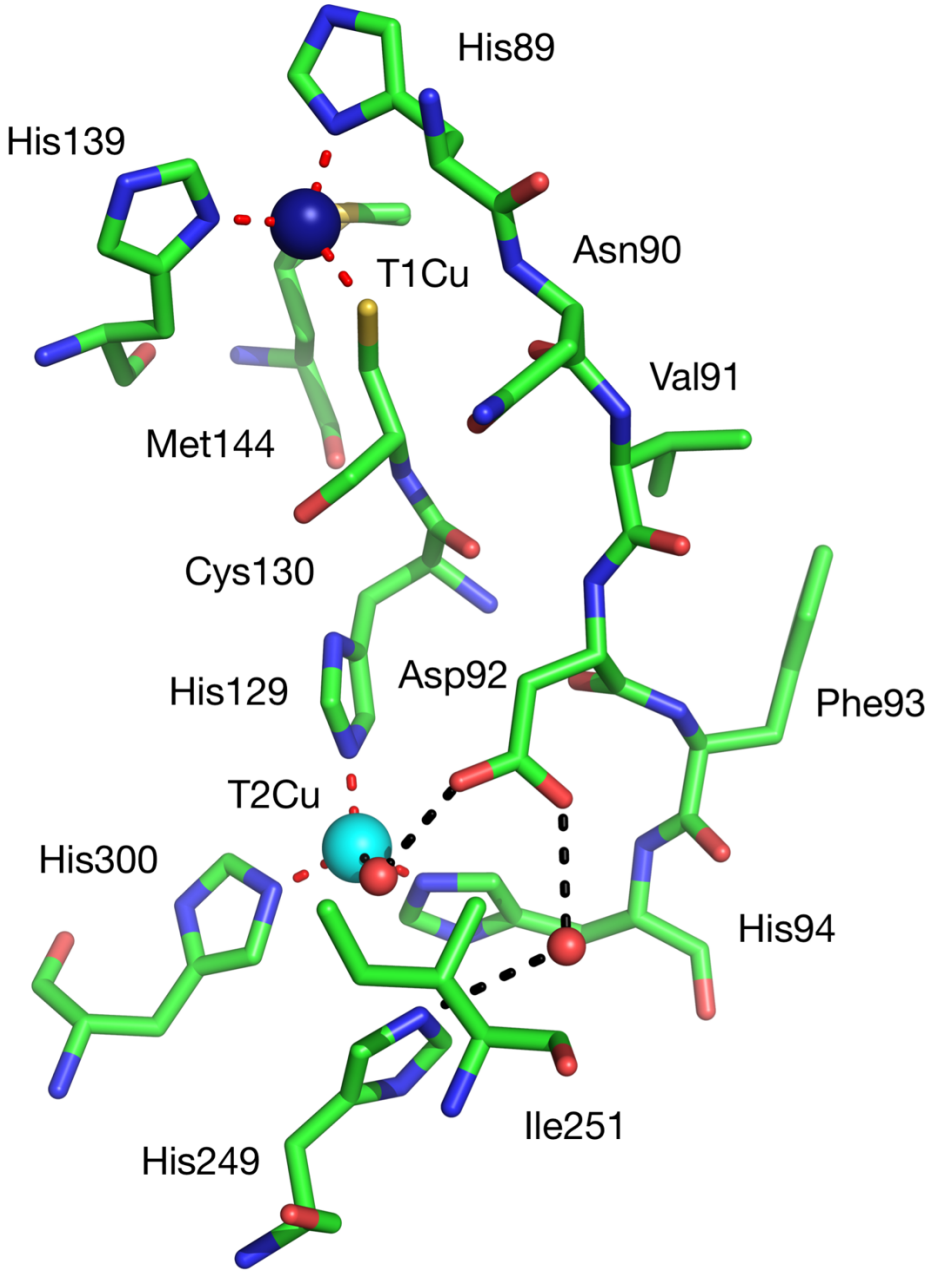

Figure 1.6. The copper sites of *Ax*NiR. The two copper sites are linked by a Cys-His bridge that facilitates electron transfer between them. The T1Cu site, shown in dark blue, is ligated by two histidine, one cystine and one methionine residues, while the T2Cu site, shown in cyan, is ligated by three histidine residues. The T2Cu is ligated by a water in the resting state which is hydrogen bonded to Asp_{CAT}, which itself is hydrogen bonded to His_{CAT} via a linking water molecule. The atoms are coloured by element (PDB: 1OE1).

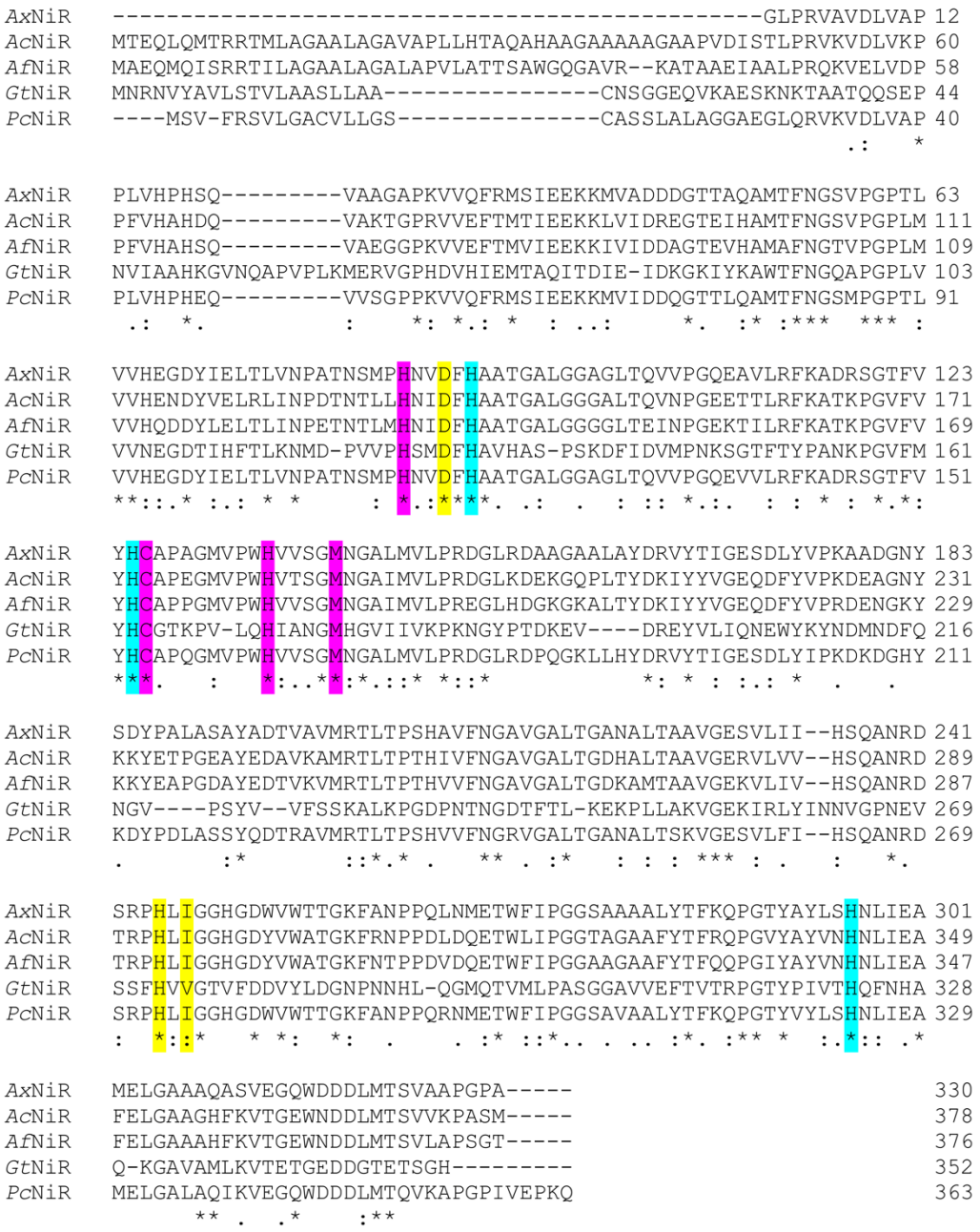

Figure 1.7. A multiple sequence alignment of five CuNiRs. Residues such as those forming the copper binding sites and catalytic residues are conserved across species. The T1Cu binding site residues are shown in magenta, the T2Cu binding site residues in cyan and the catalytic residues in yellow. Alignment performed using *Clustal Omega*[60] (1.2.4).

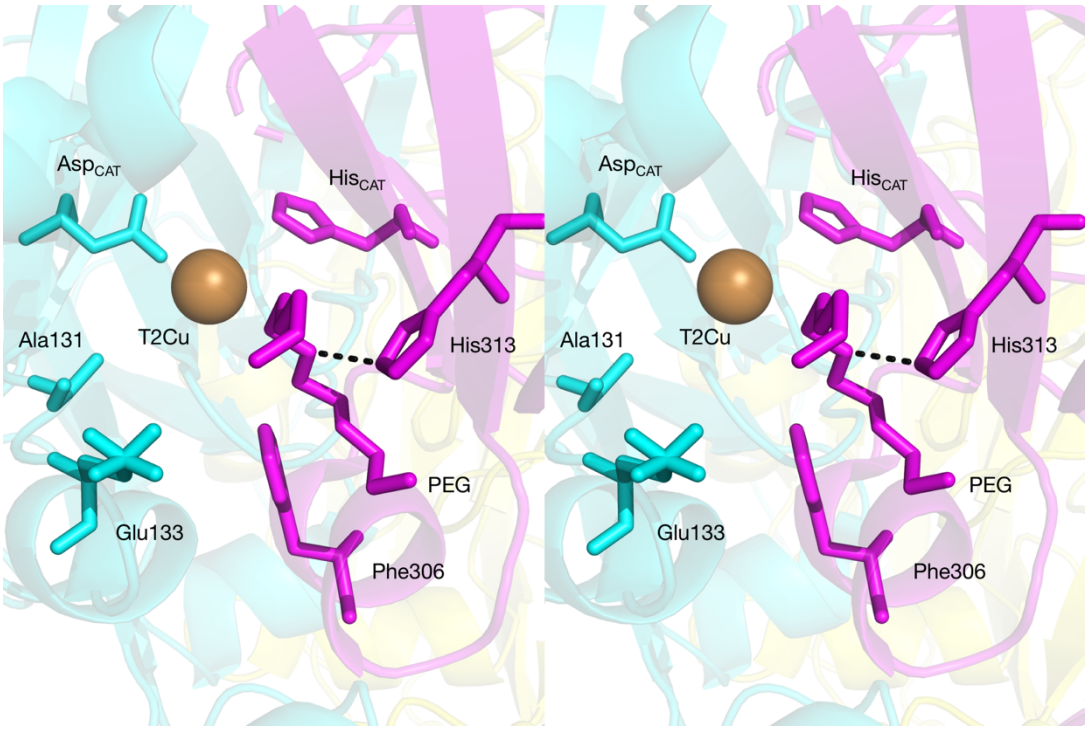

Figure 1.8. A cross-eyed stereo picture of the substrate entry channel of *Ax*NiR. His313 and Phe306 mark the entrance to the substrate channel. In this crystal form of *Ax*NiR (H3), crystallised with polyethylene glycol (PEG), PEG can be seen hydrogen bonding to His313. This prevents NO_2^- being soaked into these wild type crystals. Mutation of the His313 residue to cysteine allows substrate soaking to take place. Different colours represent different protein chains (PDB: 1OE1).

1.3.3. Enzyme mechanism

The mechanism for NO_2^- reduction starts with the resting state enzyme defined by the oxidised T2Cu site with a bound fourth water ligand. A hydrophobic channel, ~6 Å from the protein surface, made up of residues from the monomer-monomer interface, acts as the point of substrate entry. NO_2^- binds to the T2Cu ion supplanting the bound water molecule (Figure 1.9). NO_2^- binding causes an increase in the redox potential of the T2Cu site that allows the otherwise unfavourable electron transfer from the T1Cu to the T2Cu site[52]. Upon reduction of the T2Cu site, proton transfer takes place from the Asp_{CAT} residue to the NO_2^- to form the Cu(I)-NOOH intermediate. The His_{CAT} residue then donates a second proton causing the cleavage of the NO-N bond releasing the NO product, leaving water to ligate to the oxidised copper site[54]. Studies of CuNiR mechanisms had yielded conflicting evidence on whether electron transfer occurs before or after NO_2^- binding. In the proposed random-sequential mechanism, NO_2^- binds to both oxidised and reduced T2Cu[61] (Scheme 1.1). This proposal was based on kinetic data whereby the steady-state kinetics observed for CuNiR showed the electron transfer rate was dependent on NO_2^- concentration and pH. Alternatively, an ordered-sequential mechanism proposed NO_2^- binding only to the oxidised T2Cu. In the absence of NO_2^-, the difference in the redox potentials between the T1Cu and T2Cu sites is insignificant at physiological pH implying equal electron distribution between the two copper centres[52]. Premature reduction of the T2Cu site resulting in the loss of the water ligand can leave CuNiR in a dead-end state, unable to bind NO_2^-. Specific photoreduction of the T1Cu site does

not trigger electron transfer between the T1Cu and T2Cu, demonstrating an ordered-sequential mechanism. Electron transfer is therefore only allowed when NO_2^- binds the T2Cu site, causing its redox potential to increase. This alters the equilibrium of the redox potential now making it favourable for electron transfer to take place[62]. Photo-excitation studies of *Ax*NiR in deuterated water revealed that electron transfer was coupled to proton transfer. The reduction of NO_2^- by *Ax*NiR requires consumption of two protons, provided by Asp_{CAT} and His_{CAT}. The observed rate of proton up-take from the surrounding solvent matches the rate of electron transfer. pH-lowering assays established protonation as the trigger for electron transfer. Proton-coupled electron transfer (PCET) occurs in the absence of NO_2^- in the native enzyme. However, in *Ax*NiR-N90S, which displays a severely reduced proton transfer rate, PCET is not observed in the absence of NO_2^-. When NO_2^- does bind the active site of N90S mutants, the proton channel is partially restored via the movement of a loop connecting the T1Cu ligands, Cys130 and His139[63]. Now, however, a reaction scheme has been proposed whereby two electron transfer routes operate in parallel with different NO_2^- binding sequences, the choice of pathway being determined by NO_2^- concentration and varying pH[64].

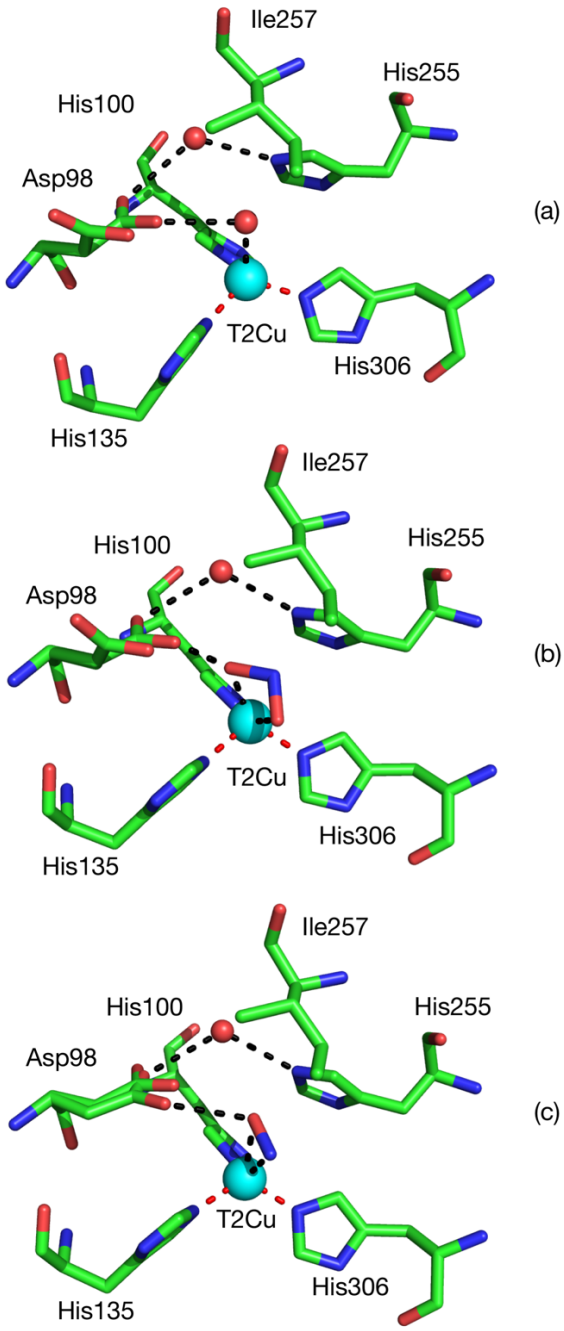

Figure 1.9. The resting state, ligand and product bound T2Cu site. (a) Resting state T2Cu site from *Ac*NiR (PDB: 2BW4). T2Cu is ligated by a single water molecule. (b) NO_2^- bound T2Cu site (PDB: 2BWI). The NO_2^- is bound in a side-on manner with near equidistant O and N-T2Cu bond lengths. (c) The NO bound T2Cu site (PDB: 2BW5). The NO has equidistant O-T2Cu and N-T2Cu bond lengths.

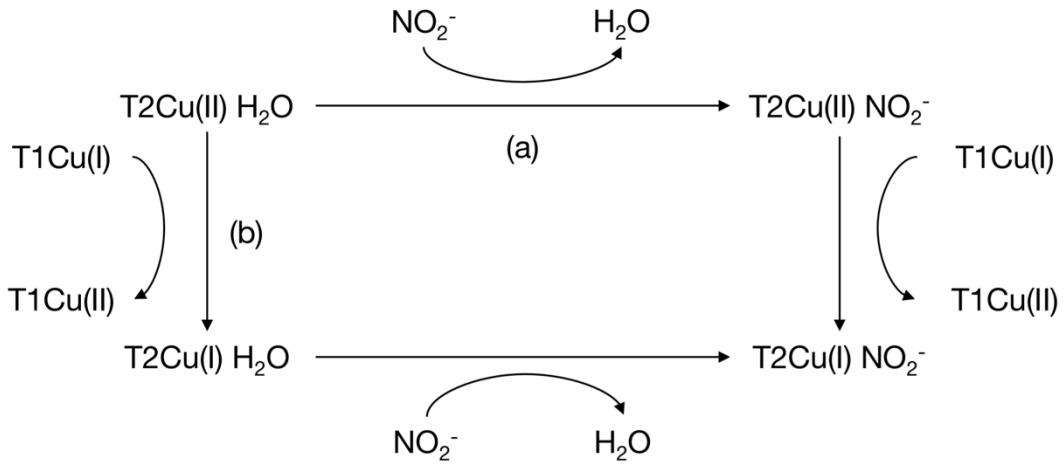

Scheme 1.1. The random sequential mechanism of CuNiR. There are two reaction pathways to end up with NO_2^- bound to reduced T2Cu. Either (a) NO_2^- binds, supplanting the ligated water ligand followed by electron transfer from T1Cu to T2Cu or (b) electron transfer occurs first, followed by NO_2^- binding. Which branch predominates is dependent on pH and NO_2^- concentration. In the ordered mechanism, only branch (a) can occur.

1.3.4. Intramolecular electron and proton transfer

Proton and electron transfer to the catalytic site is crucial for the reduction of NO_2^-. Two protons and one electron are required in total and must be directed to the substrate bound T2Cu to prevent inappropriate metal reduction. In a protein structure crystallised at low pH, proton transfer occurred from the enzyme surface to the T2Cu centre via a well-ordered, hydrogen-bonded water network[51]. This 'primary' channel extends along the monomer-monomer interface, connecting the conserved Asp_{CAT} residue at the T2Cu site to the protein surface via the His_{CAT} residue. Later crystal structures showed a second proton channel, connecting Asp_{CAT} to the surface via residues Ala131, Asn90, and Asn107 plus several water molecules. This channel was discovered in protein crystallised at high pH and hence termed the 'high-pH' channel[54]. Both channels are conserved among different two domain CuNiRs and mutagenesis studies of the residues that make up the channel have shown that the primary channel is not the main channel as originally thought. The *Ax*NiR-H254F mutant disrupts the primary proton channel due to the loss of two hydrogen bonds His_{CAT} is involved in. The mutation has little to no effect on the catalytic rate however, indicating that proton transfer can still occur via an alternate route. In comparison, *Ax*NiR-N90S mutants, in the high-pH channel, show a ~70% decrease in specific activity compared to the wild type while still retaining an equivalent K_m for the substrate[65]. Intramolecular electron transfer was identified as occurring via the Cys-His bridge since mutation of the T1Cu cysteine ligand in *Ax*NiR led to vacant T1Cu site and a complete loss of activity[66].

1.3.5. Intermolecular electron transfer

The transfer of electrons from the T1Cu site to the T2Cu is finely tuned and controlled, and so the transfer of electrons from redox partner protein to the T1Cu site must be similarly controlled. Azurin and pseudoazurin are known to bind to a hydrophobic patch on the enzyme surface and transfer electrons from the azurin T1Cu site to the CuNiR T1Cu site. Mutation of the *Ax*NiR-W138 residue located on the hydrophobic patch causes a severe decrease in catalytic activity when azurin is used as the electron donor, suggesting it has a role to play in complex formation[67]. The self-interaction of CuNiR via the so-called head-to-head mechanism correlates with the packing crystal of azurin II. Superposition of azurin II and *Ax*NiR-M114L mutant show near identical overlap and direct access to His139 residue through the hydrophobic patch, which is believed to be the direct link to the T1Cu centre[68]. The decrease in catalytic activity when Trp138 and Met87, a docking residue, are mutated suggest this model is correct[67]. The transient nature of electron transfer complexes has made structural studies of the complex difficult. However, recently an electron transfer complex crystal structure has been published formed between *Ax*NiR and a partner Cyt_{c551} protein revealing docking via the predicted hydrophobic patch[69]. A CuNiR crystal complex with azurin or pseudoazurin has yet to be determined.

1.3.6. Three-domain CuNiRs

The standard homotrimeric CuNiR is structurally defined by a trimeric two cuperodoxin-like domain monomer core. Recently several new, modified CuNiRs have been identified via a wide genomic analysis where the two-domain monomer presents with a third additional domain fused at the N- or C-terminus, either a third cuperodoxin-like[70] or cytochrome-like[71] domain (Figure 1.10). The first of these to be characterised was the CuNiR from *Hyphomicrobium denitrificans* (*Hd*NiR)[72]. The sequenced genome was used to predict a second T1Cu-containing domain, fused to the N-terminus. *Hd*NiR maintains the conserved two domains Cu core and it is not presently established whether this extra domain plays a catalytic role. The extra T1Cu site has a different geometry to the two domain T1Cu, giving the protein a blue-green colour. The crystal structure of *Hd*NiR revealed a trimer self-interaction with the extra T1Cu domains interacting to form a hexameric structure[73]. This extra fused domain is partly analogous to a CuNiR azurin complex, but the structure of the protein revealed a 14 Å distance between the two internal T1Cu sites, limiting the possibility for internal electron transfer. More recently the structure of NiR from *Ralstonia pickettii* (*Rp*NiR) was reported, revealing a C-terminal fused haem-*c* domain[74]. Again, the catalytic nature of this domain has yet to be determined although in this case the haem and T1Cu sites are internally positioned much closer than in *Hd*NiR, raising the possibility of internal haem T1Cu electron transfer. The structure of *Rp*NiR revealed a unique Tyr residue located in the substrate entry channel, generating a steric hindrance to any substrate/ligand from binding to the

catalytic site. Here the T2Cu water ligand is stabilised by a two extra hydrogen bonds reducing the ability of NO_2^- to displace it in the oxidised form.

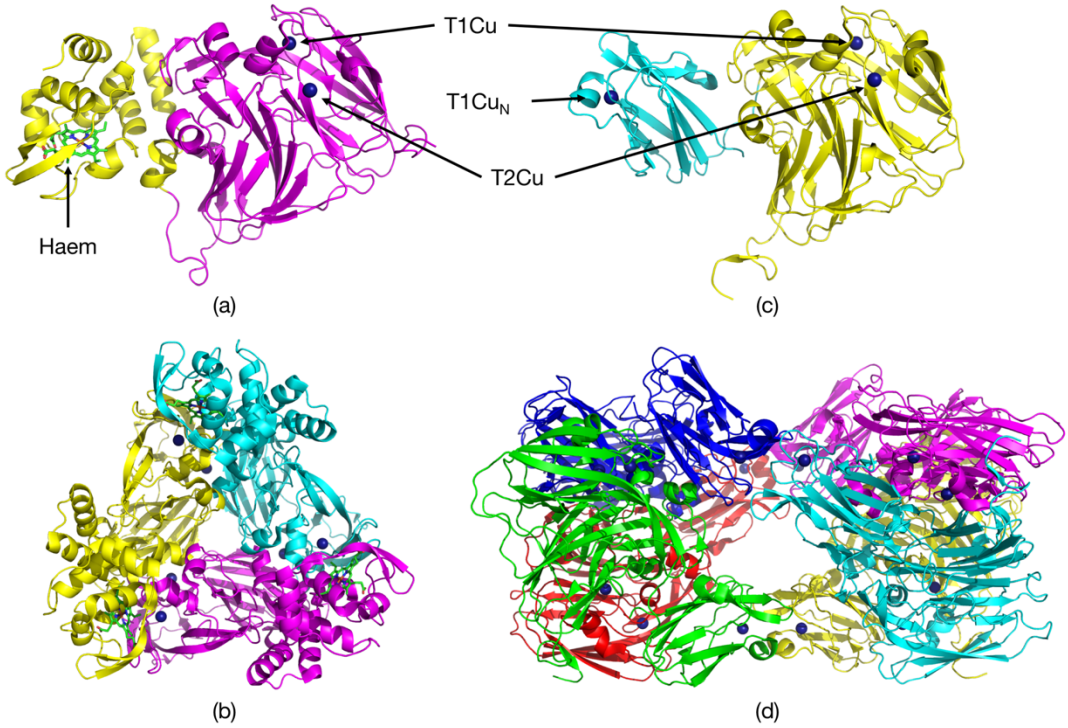

Figure 1.10. The monomeric and oligomeric structures of 3-domain CuNiRs. (a) Monomer of *Rp*NiR (PDB: 3ZIY). The two cuperodoxin domains are shown in magenta with the C-terminal cytochrome domain shown in yellow with the haem group highlighted. (b) The *Rp*NiR homotrimer showing the 3-fold rotational axis. (c) Monomer of *Hd*NiR (PDB: 2DV6). The two cuperodoxin domains are shown in yellow with the N-terminal cuperodoxin domain shown in cyan with the extra T1Cu$_N$ is highlighted. (d) The *Hd*NiR homohexamer shown side-on.

1.3.7. Superoxide dismutase (SOD) activity

In addition to their nitrite reductase function, CuNiRs are also known to have superoxide dismutase activity[52,75]. Studies of native CuNiR from *Rhodopseudomonas sphaeroides f. sp. denitrificans* (*Rs*NiR) and *Ax*NiR found they have ~33% and ~56% the SOD activity of bovine Cu,Zn SOD although no NiR activity is measurable in Cu,Zn SOD from those organisms. SODs relieve cytotoxic oxidative stress by alternatively oxidising or reducing O_2^- into less harmful species water (H_2O) or hydrogen peroxide (H_2O_2):

$$Cu^{2+} + O_2^- \rightarrow Cu^+ + O_2$$

$$Cu^+ + O_2^- + 2H^+ \rightarrow Cu^{2+} + H_2O_2$$

The reduced T2Cu site of CuNiR shares structural similarity to the active site of Cu,Zn SOD, and O_2 bound to the T2Cu has been observed previously in structural studies of CuNiR[76] (Figure 1.11). Here O_2 takes up the same position as NO does when bound after reduction. This structure is unique as oxygen binding has not been observed in any other CuNiR through structural studies. *Gt*NiR has a unique valine residue located over the top of the T2Cu site in place of the isoleucine residue (Ile_{CAT}) present in other CuNiRs. This generates a much larger substrate binding pocket which might allow for dioxygen binding and stabilisation. Unlike the nitrite reductase mechanism however, the dismutation mechanism of CuNiR has not been fully characterised because of the rapid nature of dismutation reactions. Many denitrifying bacteria also produce a Cu,Zn SOD including *A. xylosoxidans*

(E3HM88)[77], *H. denitrificans* (D8JSQ1)[78] and *Alcaligenes faecalis* (A0A0A2NGZ8)[79].

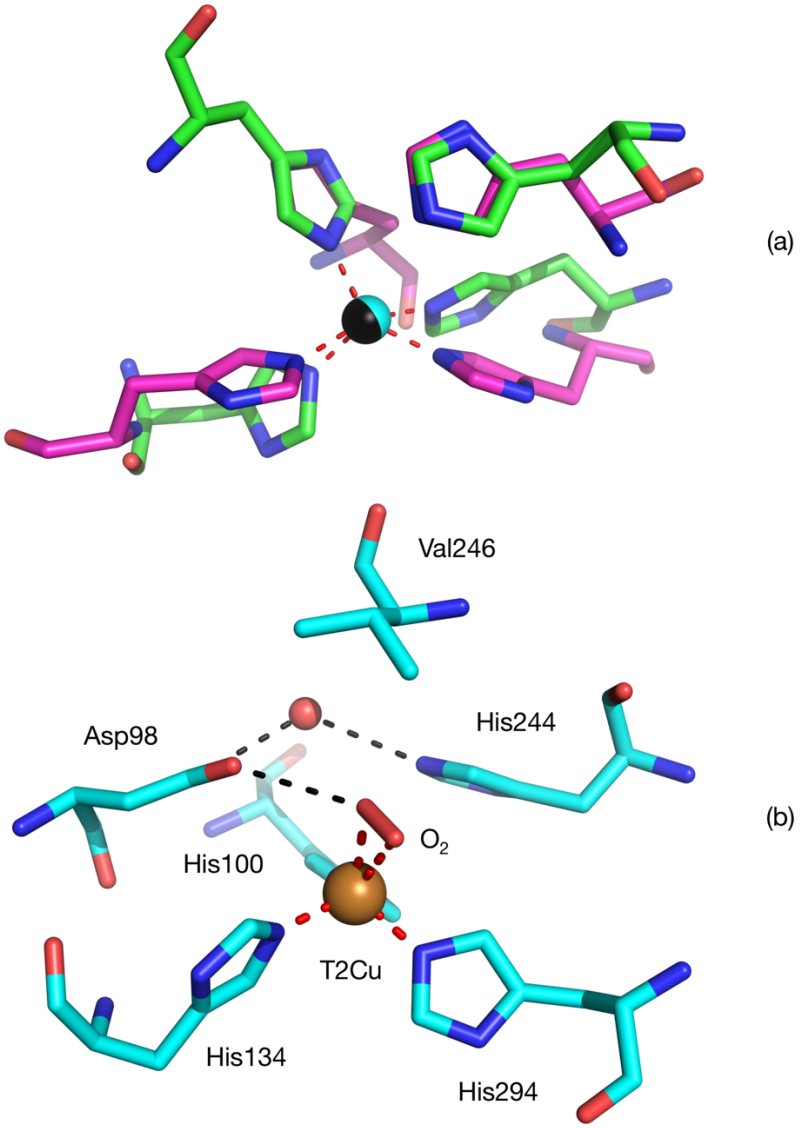

Figure 1.11. Copper-site comparison of dioxygen-binding enzymes. (a) Superposition of the reduced bovine Cu,Zn SOD Cu site (PDB: 1Q0E) and the *Ax*NiR T2Cu site (PDB: 1OE1). bSOD is shown in magenta and *Ax*NiR is shown in green with the copper atoms shown in cyan and black respectively. bSOD coordinate bonds shown in blue and *Ax*NiR coordinate bonds are shown in red. Both active copper sites have tri-histidine ligation. The AxNiR His_{CAT} residues occupies a similar position to the bSOD bridging imidazole residues. (b) The active site of CuNiR from *Gt*NiR with bound dioxygen (PDB: 3WNJ). The oxygen is bound in a side-on manner.

Chapter 2 - Synchrotron radiation and X-ray free electron lasers for structure determination

2.1. Synchrotron radiation (SR)

2.1.1. X-ray tubes

Material science involves the imaging of materials on a macro and micro scale and the study of their atomic, electronic and magnetic structure. Sources of electromagnetic radiation can be used to probe the electronic structure of biological molecules and determine their three-dimensional structure. A covalent bond is ~0.1 nm, so to resolve atomic positions the probe wavelength must be equal or less than 0.1 nm. On the electromagnetic spectrum, this wavelength falls in to the X-ray class consisting of 0.01 to 10 nm photons. X-rays can be generated by an X-ray tube using electron impact with a target. An electron is released by a hot cathode and accelerated by a high voltage to a target anode[80]. When the electron collides with the anode it decelerates, and the kinetic energy is converted into X-ray radiation[80]. Two types of X-ray radiation are produced by the collision; Bremsstrahlung or braking radiation and characteristic radiation[80]. Bremsstrahlung X-ray emission covers a continuous spectrum while characteristic X-ray emission produces X-rays at a few discrete frequencies[80]. The discrete frequency is

characteristic to the anode material and is caused by the colliding electron knocking an orbital electron out of an inner electron shell of the anode material[80]. Electrons from higher energy levels then drop down to fill the vacated lower levels and in doing so emit X-ray photons at an energy equal to the difference in energy between the levels[80]. The total X-ray spectrum therefore consists of a broad, continuous spectrum of X-ray wavelengths with discrete spikes relating the characteristic K and/or L lines, depending on which orbital the dropping electron is filling[80]. The X-rays must be directed at the sample to be probed; however, the X-rays are emitted in a cone over 2π steradians and so only a small proportion of the X-rays produced can be used to probe the target[80]. X-ray sources such as X-ray tubes therefore have low brilliance where brilliance is defined as photons/s/mm^2/mrad^2/0.1%BW where the number of photons per second is divided by its divergence, cross-sectional area and the percentage of photons falling within a bandwidth 0.1% of the central wavelength[81]. Because the emission is divergent, and the characteristic radiation has the highest intensity, most X-ray tubes are limited to producing the characteristic radiation of the anode material for useful experimentation. This process of X-ray production is inefficient, with $<1\%$ of the accelerated electron energy being emitted as X-rays and the rest lost as heat[80]. As the flux produced by the X-ray tube is limited by the acceleration energy, reducing the average energy density on the anode allows the production of higher flux[82]. Rotating the anode allows the electron energy to be averaged out of the circumference of the anode as opposed to a single spot which would eventually melt it[82].

2.1.2. Synchrotron light source

The limitations in brilliance and spectrum of X-ray tubes for biological structural characterisation were overcome with the discovery of synchrotron radiation and the construction of synchrotron light sources. Synchrotron radiation is produced when the path of an accelerated electron is curved by a magnetic field[83]. Electrons travelling at non-relativistic speeds emit synchrotron radiation in a dipolar pattern with a total radiated power proportional to the square of the acceleration[83]. If the electron is accelerated up towards the speed of light, it becomes relativistic and the emission pattern is Lorentz shifted forwards[83]. The X-rays are emitted as a narrow cone, with the wavelength being further contracted by the relativistic speed relative to the rest frame of the electron[83]. The contracted wavelength and forward-pointing cone of radiation means these accelerators produce highly brilliant X-rays beams[83]. Accelerator facilities called synchrotron light sources are used to accelerate electrons up to relativistic speeds[84]. Electrons produced by an electron gun are accelerated in a linear accelerator (linac) which are injected into a booster synchrotron, used to further accelerate the electrons[84]. The electrons travel around a fixed path and are kept in place by a magnetic field which curves the electrons around the ring[84]. The magnetic field strength is synchronised to the kinetic energy of the electrons to keep the electrons orbiting the ring in the same path[84]. Once at the required kinetic energy the electrons are injected into the storage ring which contains insertion devices (ID) to generate synchrotron radiation[84]. Although the whole light source facility is known as a synchrotron, the whole machine consists of these three

different accelerators; the linac, the booster and the storage ring (Figure 2.1)[84]. In the storage ring, the electrons orbit is maintained by arrangements of dipole magnets[84]. Between the dipole magnets in straight sections, quadrupole and sextupole focusing magnets are used to contain the shape and structure of the electron beam[84]. The electrons orbit the storage ring in bunches which lose energy when they emit synchrotron radiation and so must be reenergised through radio frequency (RF) field cavities located in the straight sections[84]. As the electrons are curved around the light source, synchrotron radiation is emitted which is much more brilliant than that from an X-ray tube, but still divergent[84].

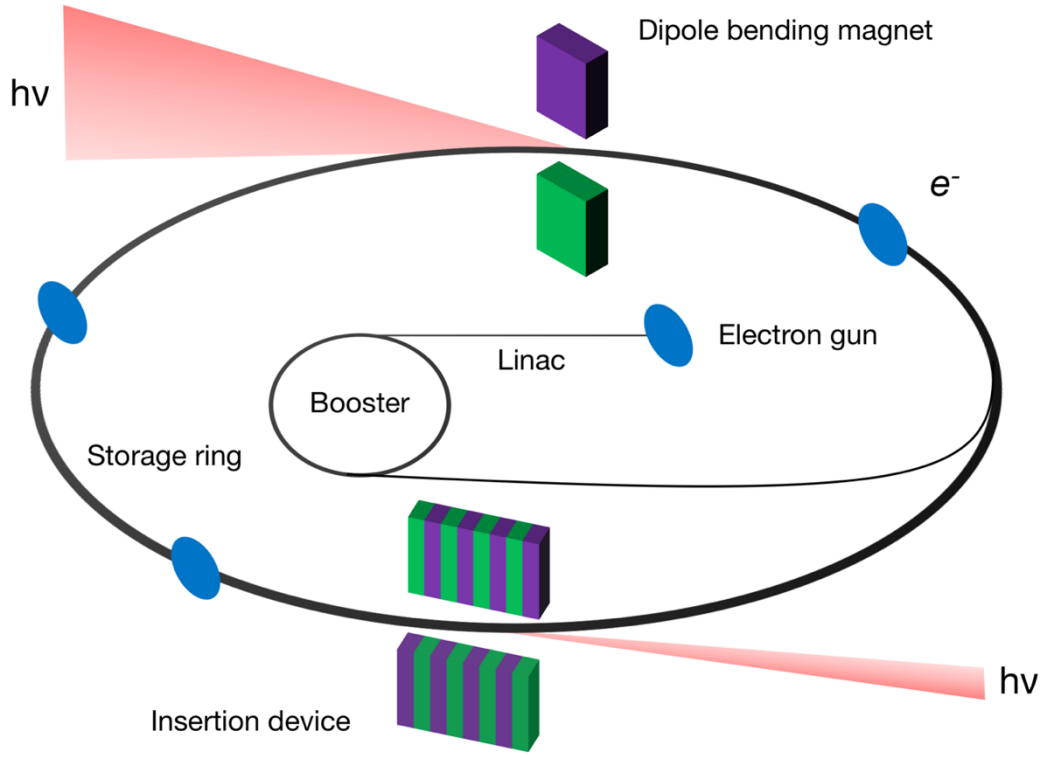

Figure 2.1. A diagram of a synchrotron light source. Electrons generated by an electron gun are accelerated in a linac and injected into a booster synchrotron where they are further accelerated in a closed path. Upon reaching the required energy, they are injected into the storage ring to circulate at that energy. The electron bunches pass though bending magnets or IDs where the electron energy is radiated as photons. IDs are periodic magnetic structures which generate much more brilliant light than simple bending magnets.

2.1.3. Insertion devices (ID)

The brilliance of the synchrotron radiation emitted by a light source can be improved with the addition of IDs to the straight sections of the storage ring[84]. There are three types of IDs; wavelength shifters, multi-pole wigglers and undulators (Figure 2.2). All three operate by inducing a large deflection in the electron path using powerful magnets, causing the emission of synchrotron radiation[84]. A wavelength shifter is a basic ID which deflects the electron beam laterally once and then returns it to the normal orbit[84]. This type of ID produces a similar type of emission to a normal dipole magnet except that the radiation is shifted to a shorter wavelength[84]. A multipole wiggler is a periodic array of magnets that cause the electron beam to undergo a transverse oscillation with the resulting changes in velocity causing the emission of synchrotron radiation[84]. The oscillations of the electrons do not overlap and hence the emission is incoherent, so a wiggler can be considered as a series of wavelength shifters connected together[84]. Undulators are mechanically similar to wigglers but produce much more brilliant synchrotron radiation[84]. Here the oscillations of the electrons overlap causing them to constructively interfere, producing a narrow bandwidth centred around its wavelength fundamental and odd harmonics[84]. The emission wavelength is effectively the Lorentz contracted period of the undulator from the electron frame, which is then Lorentz shifted to a shorter wavelength by the observer in the rest frame[84]. A longer undulator with more periods has a higher brilliance, as the bandwidth is inversely proportional to the number of periods, while the intensity scale by N^2 where N is the number of periods[84].

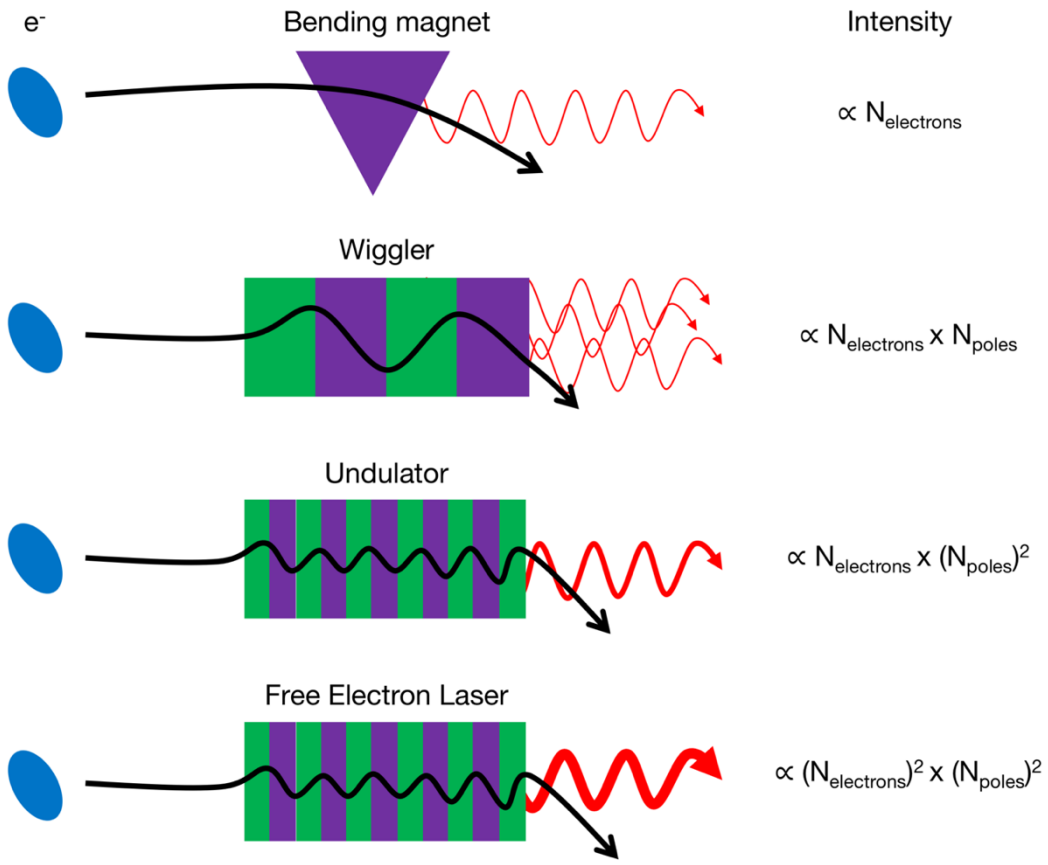

Figure 2.2. The generation of synchrotron radiation. Synchrotron radiation can be generated by bending magnets, wigglers, undulators and free electron lasers. The structure of the magnetic arrangements can increase the intensity of the radiation. Upon radial acceleration, relativistic electrons produce a forward pointing cone of synchrotron radiation.

2.1.4. Synchrotron facilities

Macromolecular crystallography (MX) has become one of the most important uses for synchrotrons facilities providing biological structural data for structure-based drug design and enzyme mechanism study. This is particularly important for membrane proteins that transmit signals across cell membranes and play a large role in human health and disease[85]. The first decade of the 21st century produced a major structural genomics effort to take advantage of new genomic sequencing technologies[86]. High-throughput crystallisation resulting in improved screening and automated data collection at most synchrotron facilities generated a wealth of structural data. The Protein Data Bank (PDB) currently contains ~140,000 structures of biological macromolecules and complexes[87]. Biological structural determination is dominated by X-ray crystallography, accounting for 90%, with the other 10% made up with structures determined by nuclear magnetic resonance, 3D cryo-electron microscopy and others[87]. This increased rate of throughput, fuelled by the availability of genomic data, required the construction of specialist MX beamlines at synchrotrons around the world. The majority of the work discussed in the thesis was carried out at the Super Photon Ring – 8 GeV (SPring-8) synchrotron located in Hyogo prefecture, Japan and will be used as an example to discuss specialist MX beamlines.

SPring-8 is a third-generation synchrotron facility consisting of a 1 GeV linac, an 8 GeV synchrotron and an 8 GeV storage ring, currently the highest energy in the world[88]. Third generation synchrotron facilities were designed and built to produce the most brilliant X-rays from insertion devices. SPring-8

currently has 56 operating beamlines, operating in the hard X-ray (300 keV) to soft X-ray (300 eV) range. Of these 56, six are dedicated MX beamlines; BL26B1/2, BL32XU, BL38B1, BL41XU and BL44XU. A 7th, BL12B2 is a multi-function beamline designed for a range of experiments including MX. Each beamline is designed and constructed to meet a specific experimental need. BL26B1/2[89] and BL38B1[90] are utilised as general, high-throughput beamlines, designed for testing crystal diffraction and high throughput data collection. BL32XU[91] is specifically designed to deal with small protein crystals, on the order of microns. As already discussed, membrane proteins usually prove the most biologically important targets, but also most difficult crystallography targets. The optimal data collection strategy involves matching the size of the X-ray beam to the size of the crystal, primarily to reduce background scattering and increase the signal-to-noise ratio. Small membrane protein crystals therefore require a small X-ray beam, and so BL32XU was designed to produce a micro-focused beam, specifically a 1 x 1 μm^2 beam size with photon flux density of 6 x 10^{10} photons/sec/μm^2 at the sample position. An alternative design approach is utilised at BL41XU[92] which currently produces the highest flux of any beamline in the world at 1 Å ($2.2 \times 10^{12} \sim 1.1 \times 10^{13}$ photons/s). The increased flux in a spot size 80 (H) x 22 (V) μm^2 helps boost the diffraction signal from weakly diffracting crystals at the expense of simultaneously amplifying the background as well. BL44XU[93] is designed specifically for the collecting the structures of large biological macromolecular assemblies such as protein complexes and virus particles. These beamlines are prolific in producing highly cited research papers such as the crystal structure

of the CRISPR-Cas9 complex[94]. Despite this, the use of synchrotron radiation is limiting for MX samples as will be discussed later, and a new type of light source, the X-ray free electron laser, has recently been developed to improve on the current restrictions.

2.2. X-ray Free electron lasers

2.2.1 Free electron laser structure

An X-ray free electron laser (XFEL) is an X-ray source based on a linear accelerator in which relativistic electrons are forced to radiate coherently in extremely short pulses, producing X-ray pulses with a brilliance typically nine orders of magnitude higher than that from synchrotron light sources[95]. The main components of an XFEL are a linac which accelerates short bunches of electrons to multi-GeV energy followed by a series of long undulator modules[95]. The undulator modules are periodic magnetic structures that cause the electrons to oscillate sinusoidally and transversely to the beam direction (Figure 2.3)[95]. In the first undulator modules the electron bunches radiate spontaneously at a fundamental wavelength determined by the undulator period and the strength of the oscillation[95]. The periodic nature of the undulator results in interference of the radiation emitted at each period in the magnetic structure and this causes the spontaneous radiation to be emitted in a narrow range of wavelengths centred about the fundamental and odd harmonics[95]. This is the standard undulator radiation exploited on modern synchrotron radiation sources to produce intense, highly collimated, and narrow-bandwidth X-ray beams[95]. While the spectral properties of the undulator radiation are well defined, the temporal properties of the X-ray pulse are determined by the length of the electron bunch passing through the undulator, which is typically only picosecond duration in a storage ring-based synchrotron radiation source[95]. Also, the length of the bunch means the electrons along the bunch cannot radiate coherently, and so the total light

output is linearly proportional to the number of electrons in the bunch, which is limited by the electron beam dynamics of the storage ring[95]. All these factors limit the X-ray intensity that can be generated at a synchrotron light source[95]. However, unlike lasers that produce visible light, no material exists that can reflect hard X-rays, meaning the X-ray laser cannot use a resonance cavity to produce an in-phase photon source[95]. Therefore, the photons must be emitted in phase after a single pass through the XFEL undulator with sufficient intensity[95].

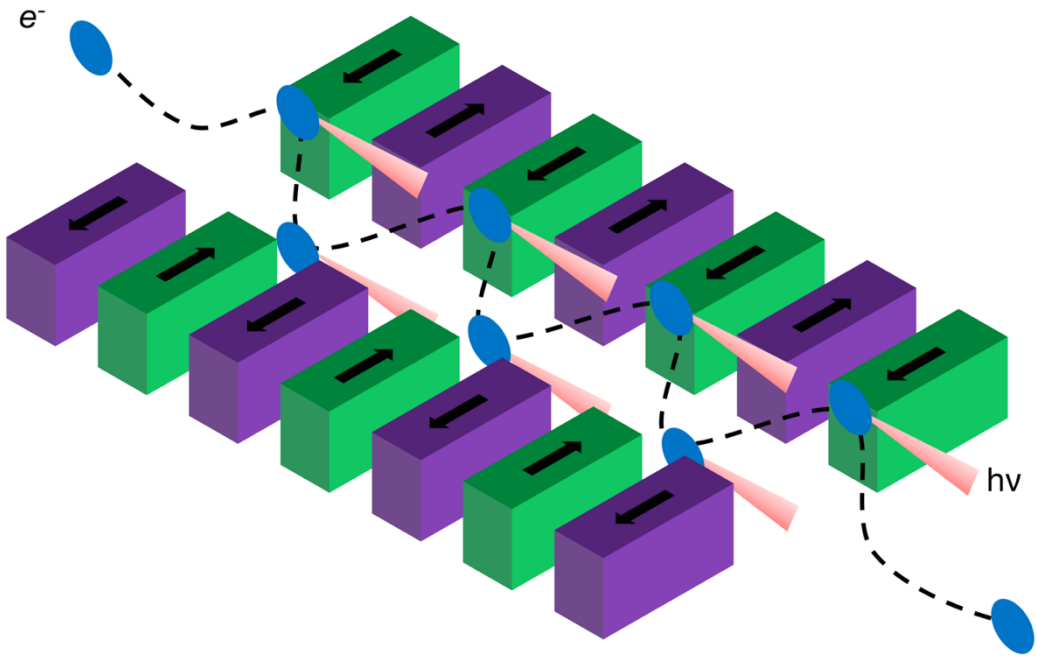

Figure 2.3. **A diagram of an undulator.** The periodic arrangement of magnets causes the electron to oscillate transversely to the magnetic arrangement. The changing velocity causes the emission of synchrotron radiation in a narrow, forward cone that is Lorentz shifted to a shorter wavelength. The X-rays emitted at each peak constructively interfere to increase to intensity by N^2.

2.2.2. Self-amplified spontaneous emission (SASE)

An XFEL is designed to go beyond the limits of the spontaneous undulator radiation from synchrotron radiation sources to give shorter and more intense pulses by forcing the electrons to radiate coherently[96]. The first step is to use a linac rather than a storage ring as this allows the electron bunches to be made much shorter because there is no need to recirculate them[96]. A linac can be made to compress the electron bunches down to lengths ~50 fs or shorter, depending on the charge they contain[96]. This will give short pulses of radiation but bunches this short will not inherently give coherent emission at X-ray wavelengths and it is necessary to modulate the charge profile within the electron bunch at the required radiation wavelength[96]. In the simplest type of XFEL this is achieved by a process known as Self-Amplified Spontaneous Emission (SASE)[96]. The spontaneous radiation emitted in the first undulator modules propagates with the electron bunches, which interacts with the electron bunches in the following modules in such a way as to modulate the charge profile of the bunches at the wavelength of the radiation field[96]. This process, known as micro-bunching, compresses the electrons closer together so that they radiate coherently with each other, and the intensity of the emitted light rises exponentially until saturation occurs[96]. The saturation output is actually proportional to $N^{(4/3)}$, where N is the number of electrons radiating[96]. Although this is below the N^2 relation for perfect coherent emission, the brilliance gain of the XFEL over a storage ring undulator is many orders of magnitude through a combination of the short pulse and the coherent emission, which increases the number of photons

emitted per electron and reduces the phase-space of the source[96]. Although the SASE process is simple to implement it does have a significant disadvantage in that, because the amplification process starts from a distribution of random frequencies within the spontaneous bandwidth, the precise wavelength of the radiation output is not absolutely defined[96]. Indeed, in general the output consists of many longitudinal modes that vary in wavelength and relative intensity on a shot-by-shot basis[96]. The modes exist within a total pulse length that is determined by the electron bunch length[96]. The SASE pulse is thus a set of random radiation spikes that are spectrally within an envelope that is similar to the spontaneous emission envelope and temporally within the envelope determined by the overall bunch length[96]. Thus, although the SASE mode of operation can give X-ray pulses that are very short, <10 fs, the pulses tend to fluctuate in overall intensity and have poor wavelength stability and temporal coherence, though transverse coherence is normally very high[96]. However, there is much active research being undertaken into developing techniques to improve the temporal properties of the SASE output[96]. For example, a technique known as self-seeding is now well established to improve the temporal coherence and wavelength stability by filtering the SASE radiation to a narrow frequency band at an intermediate point in the amplification process[97,98]. However, the intensity fluctuations remain.

2.2.3. XFEL facilities

There are currently five XFEL facilities either currently operating or undergoing commissioning; LCLS (Linac Coherent Light Source) in the USA[99], SACLA (SPring-8 Angstrom Compact Free-electron Laser) in Japan[100], the EuXFEL (European X-ray free-electron laser) in Germany[101], PAL-XFEL (Pohang Accelerator Laboratory's hard X-ray free electron laser) in South Korea[102] and SwissFEL (X-ray free electron laser at the Paul Scherrer Institute) in Switzerland[103]. A technical comparison is provided in Table 2.1. LCLS is the first XFEL to demonstrate the effectiveness of the self-seeding method by using self-seeding X-rays from the first half of the undulator modules to seed to the second half[98]. A chicane is used to bend the electron beam around a diamond monochromator which generates a temporally coherent seed for the photons produced in the second set of modules, producing a near bandwidth-limited pulse. EuXFEL has been constructed to produce a repetition rate of 27,000 Hz compared to 120 Hz for LCLS achieved through the use of superconducting RF cavities.

Table 2.1. A comparison of the five currently operating X-ray free electron lasers.

	LCLS	SACLA	EuXFEL	PAL-XFEL	SwissFEL
Location	USA	Japan	Germany	South Korea	Switzerland
Commissioning	2009	2011	2016	2016	2016
Repetition rate (Hz)	120	60	27,000	60	100
Minimum wavelength (nm)	0.15	0.08	0.05	0.06	0.1
Maximum electron energy (GeV)	14.3	8.5	17.5	10.0	5.8
Peak brilliance (photons/s/mm/mrad/0.1% BW)	2×10^{33} (2.75×10^{34} with seeding)	1×10^{33}	5×10^{33}	1.3×10^{33}	1×10^{33}
Facility length (km)	3.0	0.75	3.4	0.74	1.1
Number of undulators	1	3	3	2	1
Number of experimental stations	7	4	6	3	3

2.3. Metalloprotein radiation damage

2.3.1. Radiation damage in MX

The interaction of the ionizing X-ray beam with the biological crystal is a limiting factor for X-ray crystallography. During the development of the field, room temperature (RT) data collection was the norm, and during data collection the diffractive power of the crystal was observed to fade with increasing X-ray exposure[104]. This problem was originally overcome by collecting partially complete datasets from a number of crystals and combining them, a solution crystallography is starting to return to in the present[105]. The advent of cryocrystallography where protein crystals are flash frozen in liquid nitrogen (LN_2) and maintained at 100 K during data collection allowed full datasets to be collected from one single crystal, at much higher resolution, reducing the amount of protein required to collect a dataset[106]. Compared to RT, cryogenic temperature data collection allows for 70 times more absorbed dose before the diffraction quality began to reduce[107]. However, with the advent of higher energy synchrotrons and, subsequently, higher flux density beamlines, radiation damage has also been observed at cryo temptures[108]. Given all the effort required to overcome the crystallography bottleneck, growing the crystal, it is necessary to limit the effects of radiation damage to ensure that an atomic model can be determined.

2.3.2. Elastic scattering, inelastic scattering and the photoelectric effect

When the X-ray beam interacts with protein crystal, it interacts in three district ways; elastic (Thompson) scattering[109], inelastic (Compton) scattering[110] and the photoelectric effect (Figure 2.4)[111]. In a perfect situation 100% of the X-ray beam would be scattered elastically by the crystal and phase shifted to produce a constructive diffraction pattern. The X-ray energies used for X-ray crystallography are around 12.4 keV (1 Å), corresponding to atomic bond lengths[112]. At 12.4 keV for a 50 µm thick crystal, ~1% of the photons will interact with the crystal, with the rest being deposited in to the beamstop[112]. Of the ~1% of the interacting beam, ~0.1% is scattered elastically, contributing to the diffraction pattern and not depositing any energy into the crystal[112]. The rest of the beam, however, does deposit energy in the crystal through Compton scattering and photoelectron production[112]. Compton scattering involves an X-ray photon interacting with an atomic electron and either causing it to become excited and move up an energy level, or if it has a high enough energy, ejecting it completely from its orbit, resulting in the X-ray being transmitted at a longer wavelength[112]. This only accounts for ~10% of non-elastic interactions however, with the predominant form occurring via the photoelectric effect[112]. Here, the atom absorbs the X-ray photon and an atomic electron is ejected from its orbital[112]. Photoelectrons have been observed moving through the crystal ~4 µm from the point of ejection[112]. As photoelectrons travels through the crystal they interact with atoms in their path until the photoelectron loses all its energy[112]. Each interaction can theoretically create up to ~500 further ionizations events and

is the reason that causes photoelectrons to be the major destructive component of X-ray absorption, with one photon able to set off a chain reaction of ionization events[113]. Here we can separate the primary damage event, the X-ray absorption, and the secondary damage event, the subsequent ionizations events caused by the emitted photoelectron. As protein crystals contain 30 - 80% solvent, photoelectrons split water into a proton and a hydroxyl radical (·OH) which contribute to secondary radiation damage[112].

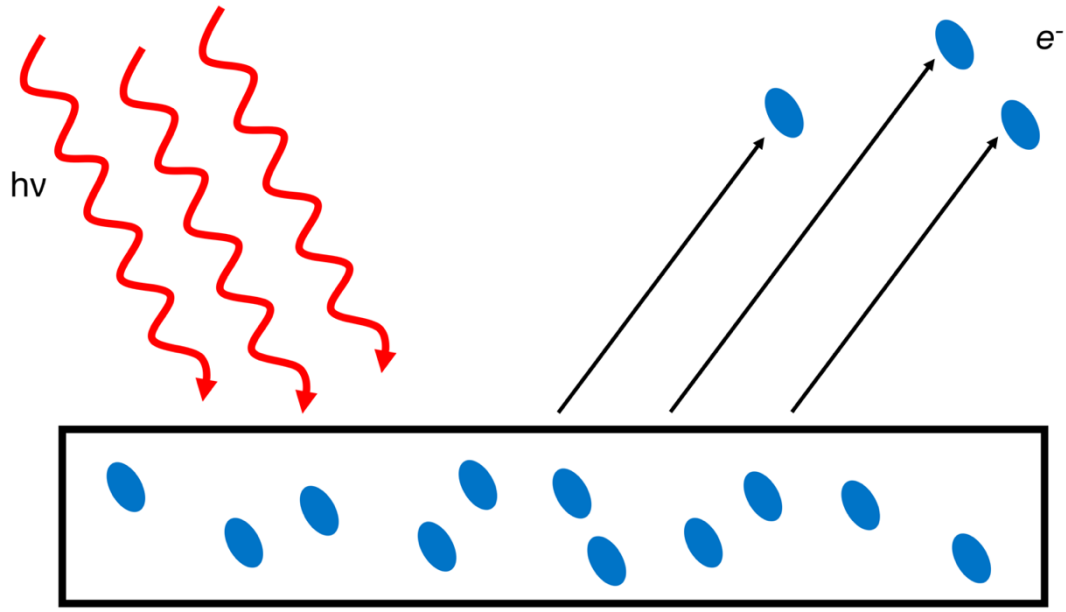

Figure 2.4. The photoelectric effect. Incoming photons strike a material and cause the emission of electrons from the material. The incoming photons must have energy above a threshold level to cause the electrons to be ejected. Photoelectrons generated in a protein crystal can set off a cascade of ionisation events and damage the local and subsequently global structure.

2.3.3. The effects of radiation damage

The physical and chemical effects of radiation damage are divided into two parts; global and specific effects. The most notable effect of global damage as already mentioned is a reduction in the diffractive power of the crystal with increasing absorbed dose. This leads to an overall decrease in the resolution limit over the course of data collection[114]. After data processing, the other effects of global damage are evident in the cell dimensions and merging statistics. The volume of the unit cell, the Wilson B-factor, R_{merge} and the crystal mosaicity all generally increase with dose, while $I/\sigma(I)$ decreases[115–117]. Monitoring these changes during data collection is important so the experimenter knows when the crystal should be discarded. The loss of diffracting power relates to a general degradation in the crystalline order of the crystal (Figure 2.5). The effects of global damage were originally thought to be a consequence of the X-ray beam heating up the crystal and that cooling the crystal using liquid helium instead of LN_2 would reduce radiation damage further. The effectiveness of this method, while positive, was small and not enough to explain the effects of global damage[118]. More recently it has been suggested that radiation induced hydrogen abstraction is the cause of the increase in crystalline disorder[119]. Hydrogen gas produced throughout the crystal can diffuse inside the crystal, but at cryogenic temperatures diffusion is slow and most of the gas converges at the grain boundaries, deforming the lattice and increasing the unit cell size[120]. Along with the degradation of the crystal lattice, diffusing photo and Auger electrons can attack particularity sensitive parts of proteins. These include the reduction of disulphide

bridges[121], glutamic and aspartic acid residues decarboxylation[122] and the reduction of metal ligands[123]. Specific radiation damage occurring in and around the active site of an enzyme complicates the interpretation of the true electron density map, especially if the damage is not recognised by the experimenter for what it is. The active sites of enzymes are often under the most steric and chemical stress and so may be more susceptible to attack from energised electrons[117,124]. Novel protein structure with no suitable homologue may require experimental phasing to solve the phase problem. Radiation damage can be deleterious to phasing techniques where differences in the intensity of Bijvoet reflection pairs must be measured accurately to work out the difference of the effect of anomalous scattering. Radiation damage can prevent the Bijvoet ratio from being measured correctly and prevent correct structure determination. Conversely, radiation damage can also be used to solve the phase problem by inducing measurable structure changes with a long X-ray exposure[125].

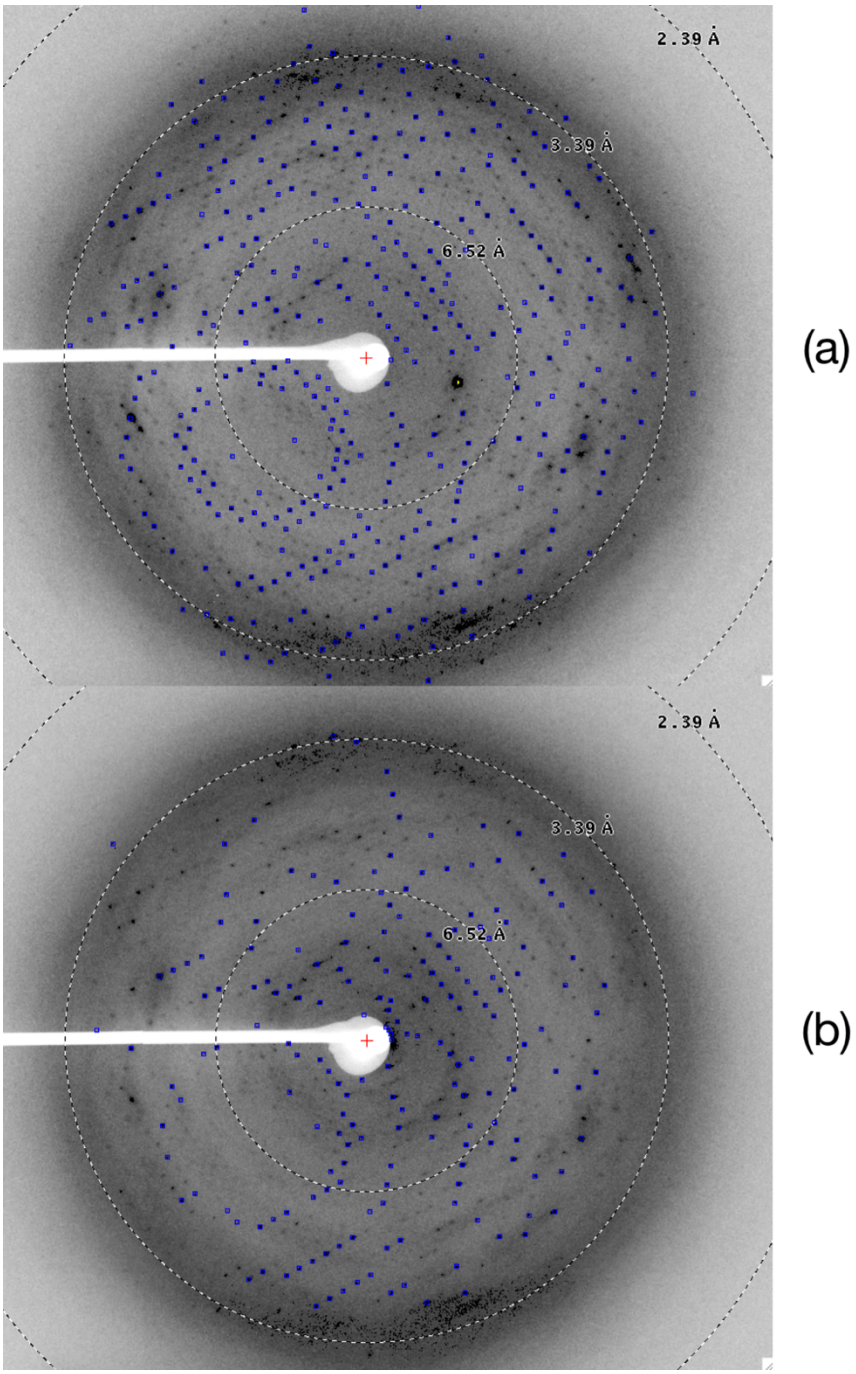

Figure 2.5. A comparison of diffraction patterns after XFEL exposure. A single crystal of *Ax*NiR collected at SACLA BL3 with a 1 mm Al attenuated beam. The crystal was exposed with the highly attenuated beam twice in the same spot. The spot count, based on a threshold of $I/\sigma = 5$, was for (a) 395 and (b) 222. A reduced reflection count is indicative of global radiation damage.

2.3.4. The mitigation of radiation damage

The most important step of mitigating radiation damage is to recognise its impact in the first place. The effects of global damage are clearly visible in the loss of diffraction power with absorbed dose and can be monitored simply by a measure of the number of Bragg reflections during data collection[126]. Specific radiation damage on the other hand can normally only be interpreted from the electron density map. However, on-line monitoring has now become common place at modern synchrotron facilities where UV–visible absorption, and in some cases X-ray absorption spectroscopy (XAFS), can be carried simultaneously with data collection to monitor the redox states of metal sites within the crystal[127]. As the effects of specific radiation damage usually occur at a much lower dose than global damage, it is important to know at what dose the change has occurred and prevent the joint refinement of two distinct redox states[128]. Once the level of radiation damage can be measured, the most common and most important response is to reduce X-ray dose. With a large protein crystal ($>100\ \mu$m), it may be advantageous to subdivide the crystal and collect part of the data from individual segments such that merging them would provide a complete data set. This spreads the absorbed dose over a larger crystal volume, maximising the experimentally useful diffraction from the whole crystal. While the interaction of the X-ray with the crystal and subsequent absorption (primary event) cannot be prevented, the diffusion of the subsequent energized electrons can be reduced by reducing the overall energy of the system. Maintaining the temperature of the crystal at 100 K during data collection using LN_2 prevents the diffusion of radical products

produced by the radiolysis of solvent in the crystal. Even at 100 K quantum mechanical effects are still able to operate and electrons and holes are able to tunnel along the protein backbone[129]. Cryocrystallography is the current dominant method for all structural biology, but with 4th generation synchrotrons starting to be brought online offering even higher flux densities the limits are beginning to be tested[130]. Single photon counting detectors are now common on modern synchrotron beamline which operate with a fast readout time, 3 ms compared to >100 ms for a charge-coupled device (CCD) detector. Because of the fast readout there is no requirement to open and close the X-ray shutter, waiting for the goniometer movement. With shutterless data collection, detectors are beginning to match the intensities coming out of the samples, reducing the amount of dose that must be deposited as more of the diffraction is captured.

While little can currently be done about primary damage or quantum tunnelling, all crystallographers are able to utilise a good data collection strategy to get the best experimental data from their crystals. Firstly, this involves using the lowest photon irradiance required to collect a complete dataset, at the expense of resolution. This last point is important in the case of radiation sensitive proteins or if there is a need to experimentally phase the structure. Many synchrotrons now offer automated data collection strategy software designed to aid crystallographers to extract the best quality data from their crystals. Taking into account crystal size to match the beam, crystal symmetry to collect the smallest amount of rotational data and predicted merging statistics to collect to the predicted highest resolution, a strategy can

be suggested to aid decision making with radiation damage in mind[131]. Dose can also be spread out by using helical data collection strategies on long, rod shaped crystals, merging partial datasets from a number of crystals or, more recently, merging many thousands of single images from many tiny crystals to complete a dataset. This last option is part of recent development of data collection at XFEL facilities where the crystalline material is destroyed from a single shot of X-ray laser pulse lasting <10 fs and must be replenished in a serial manner to complete a dataset.

2.4. Serial Crystallography using SR and XFEL

2.4.1 Diffraction before destruction

XFELs produce X-ray pulses on a femtosecond timescale with a peak intensity a billion times higher than any synchrotron source. An X-ray tube has a brilliance of $\sim 10^{7}$, a synchrotron light source $\sim 10^{22}$, compared to an XFEL $\sim 10^{33}$. In synchrotron crystallography photons are scattered and absorbed by the protein crystal, contributing to radiation damage while data collection is occurring. The timescale of synchrotron data collection is in the order of a few 10s of seconds for modern beamline setup. Despite this relatively rapid data collection, crystals can undergo significant radiation induced changes during this period, and X-ray radiolysis has been used to exploit the capturing of a redox reaction in a biological system[132]. This means that the collected diffraction pattern is not a true representation of the protein structure. This requires that great care is taken when modelling electron density maps not to attribute biological significance to artefacts generated by radiation damage. The opposite it also true, where biologically significant structural information is lost from the crystal during data collection. XFELs have the ability to overcome this problem of data collection timescale because of the unique pulse structure they produce. XFEL facilities generate pulses on the timescale of femtoseconds, much shorter than the timescale for radiation damage to occur[133]. This allows the X-ray pulses to outrun the effects of radiation damage, undergoing elastic scattering in the crystal and being collected on the detector before deposited photons have the chance to affect the biological crystal[134]. This timescale is even shorter than the motions of

molecular vibrations (10^{-10} s) and rotations (10^{-13} s) and produces time-frozen structures prior to the onset of any molecular motion or reaction induced by X-rays[135]. Because radiation damage can now be outrun the crystal can be exposed to a much greater dose, and much more weakly diffracting crystals can be used for data collection. This also removes the need to cryocool them as the temperature of the crystal is irrelevant at a timescale shorter than molecular movement for preventing radiation damage. This huge increase in photon intensity, however, is accompanied by the complete ionization and destruction of any material placed in the beam path, meaning only one single, undamaged image can be obtained per crystal. These images are snapshots, with no oscillation and must be processed in a different manner to conventional synchrotron datasets. To collect a full dataset, a constant supply of homogenous crystalline material must be fed into the XFEL beam in a serial manner.

2.4.2. Serial femtosecond crystallography (SFX)

One of the most successful systems taking advantage of the high repetition rate of the XFEL at LCLS and SACLA has been an injection system that is designed to extrude a volume of protein microcrystals combined with a carrier matrix into the beam path[136]. This process has subsequently been designated serial femtosecond crystallography (SFX) (Figure 2.6). The use of microcrystals for X-ray diffraction experiments has presented a new hope for crystallographers working to increase the size of their membrane protein or protein complex crystals, required for MX experiments. The success of an SFX experiment is dependent on the ability to grow a large volume of well-diffracting, homogenous, micro- or nano-crystals along with a compatible carrier matrix[137]. As the crystals are injected, the diffraction images are collected from the crystals with random orientations. The first iteration of injector was a liquid jet, which was convenient to use from a data collection standpoint but wasteful in terms of sample as the flow rate is very high, as well as having a propensity for ice crystal formation. To reduce the sample consumption and ice formation, gas dynamic virtual nozzles (GDVN) were developed consisting of two capillaries, one inside the other[138]. The sample flow down the inside tube is focused by a flow of helium gas along the outside capillary. This reduces the risk of crystals clogging the nozzle and reduces the background scattering by reducing the diameter of the stream. However, despite the improvement over liquid jets, GDVN's still run with a high flow rate (10–30 ml min^{-1}), still wasteful of sample, particularly given how difficult some membrane proteins can be to purify. The limited repetition rate at

SACLA (60 Hz) relative to LCLS (120 Hz) means half as many crystals have no opportunity to interact with an XFEL pulse. To further reduce the crystal flow rate, the viscosity of the sample delivery matrix can be increased with a flow rate closer to (0.1–3 ml min^{-1})[139,140]. This can be either a grease[140] or cellulose[141] matrix for soluble proteins or lipidic cubic phases (LCP)[142,143] for membrane proteins. As the microcrystals pass in front of the FEL pulse, a series of randomly oriented, crystal snapshots are collected before the crystal is destroyed. The quality of the diffraction images is variable because of variations in crystal quality and size, and the location of the FEL pulse hitting the crystal with diffraction occurring through different amounts of crystal volume. Unlike storage rings, the shot to shot variation is significant. New iterative processing methods are required to reduce the error captured during data collection.

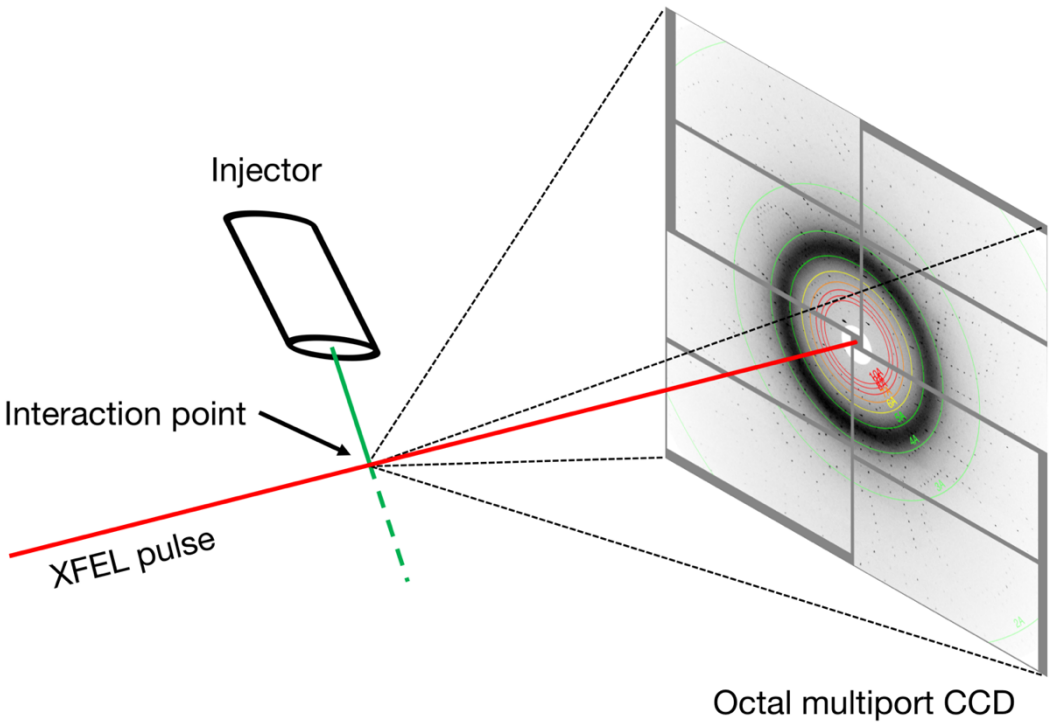

Figure 2.6. A diagram of an SFX experiment. An injector system constantly introduces randomly oriented nanocrystals into the path of the XFEL pulses. The hit rate is dependent on the speed of the XFEL repetition rate, the density of the microcrystals and the flow rate of the injector. Crystals hit by the beam produce a diffraction pattern and then are destroyed by the pulse[47].

2.4.3. Serial femtosecond rotational crystallography (SF-ROX)

Using microcrystals to produce an electron density map has inherent limitations for collecting high resolution X-ray diffraction data. The low hit rate combined with the small size of the crystal means large numbers of repeat experiments are required to produce good quality data, as many independent partial observations must be averaged from many different crystals. An alternate approach is to use a large crystal with a goniometer similar to SR crystallography known as serial femtosecond rotation crystallography (SF-ROX). Because the size of the crystal volume interacting with the X-ray beam scales linearly with the complete diffraction intensity, larger crystals are desirable for the collection of high resolution data[144]. However, large crystals have a number of potential problems, where the ever-increasing size the crystal produces more opportunities for regional crystal variation such as un-oriented crystallites. The ability to collect the high-resolution data is necessary for mechanistic understanding of enzyme reactions. Using a single large crystal with a FEL allows for the use of the usual synchrotron goniometer setup, and the diffraction data can be processed in the same manner as at a synchrotron beamline as the rotation sequence of the images is known (Figure 2.7). Large crystals (~1 x 1 x 0.05 mm) are picked with traditional cryoloops and mounted on the beamline either at cryo or room temperature using the humid air and glue method[126,145]. The crystal is centred manually but because of the crystal size and the need to maximise image numbers from each crystal, the crystal is defined by centring each corner and relaying the coordinates to a data collection strategy

program. To achieve the desired ‘diffraction before destruction’ effect, the crystal must be translated between each shot to expose fresh, undamaged crystal which was determined in cytochrome *c* oxidase to be 50 µm for a beam size of 1.8 (H) x 1.2 (V) μm^2, i.e. ~25 times the size of the X-ray pulse. The crystal must also be rotated between each exposure to process the data in a similar manner to conventional SR data collection. By rotating the crystal, conventional MX programs could treat the snapshots (still images) as oscillation images with an oscillation range equal to the between rotation step, even though a selection of the spot intensity would be missing. Tests using lysozyme crystals determined one-third of the crystal’s mosaicity to be an appropriate rotation step between shots.

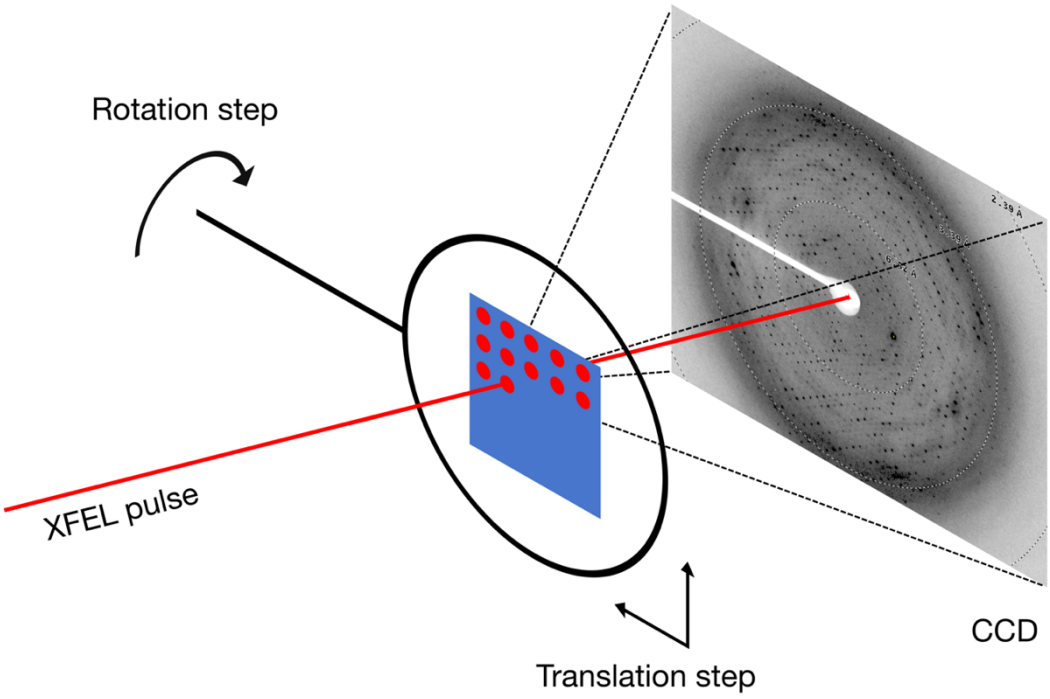

Figure 2.7. A diagram of an SF-ROX experiment. Large, loop mounted crystals are positioned on the goniometer and translated horizontally and vertically in the XFEL beam. Multiple snapshots are collected from the crystal with characteristic holes left, drilled by the XFEL pulse. The crystal is translated 50 μm in between each shot to prevent the shots overlapping in radiation damaged zones. A rotation step is also introduced between snapshots to cover the reciprocal space of the crystal lattice[37].

2.4.4. Serial synchrotron crystallography (SSX)

With the advent of microfocus beamlines data can be collected from much smaller crystals at synchrotron sources. To overcome the limits of radiation damage, high-dose but small wedge datasets are collected from a number of microcrystals and scaled to produce the full dataset[146]. With the advent of serial crystallography at XFELs and the subsequent development of brand new data collection systems, strategies and software, much of that work has recently found its way back to the synchrotron[105,139,147]. While the effects of radiation damage cannot be overcome in the same manner as with an XFEL, the use of serial crystallography is appealing as it allows the absorbed dose to be shared over an enormous number of nanoscale crystals limited only by the intensity of the synchrotron X-ray source and the sample volume. This means the signal can be captured from each nanocrystal with the minimum dose and, while not outrunning the photoelectric effect, may allow secondary radiation damage to be overcome[148]. The advent of fourth generation synchrotron facilities, such as MAX IV, Lund, Sweden which uses a multi-bend achromat lattice to achieve sub-nanometre radian electron beam emittance, will hopefully allow for full advantage to be taken of these techniques[130]. Sample delivery occurs either using an injector system or a fixed target system. Injector systems, developed from SFX experimental setups, operate in much the same manner. The benefits of reduced sample consumption and use of micro- or nanocrystals still exist, as well as the benefit of time-resolved data collection, albeit at a reduced timescale of milliseconds, compared to femtoseconds[55]. Fixed target data collection

methods have been developed more aggressively for the synchrotrons than for XFELs as data collection occurs over a longer time period, allowing for a more controlled strategy to reduce sample consumption. Fixed-target systems based on crystals held in silicon nitride chips[149], grids[150] or loops[126] developed for XFELs, that all led to significant reductions in sample consumption, have been replicated at synchrotrons (Figure 2.8). Recently, a new sample delivery system was demonstrated using a polyimide tape drive pass crystal suspension through the X-ray beam[151]. Using the tape to transfer the crystal solution allows for inhibitor mixing prior to crystal deposition on the tape, and for time-resolved experiments to be carried out by varying the mixing and tape speed.

While the photoelectrons generated by primary radiation damage are a hindrance to 'damage-free' data collection, they can in some cases be harnessed for driving the chemical reactions in the crystals during data collection. In enzymes such as CuNiRs, where the enzyme mechanism is reliant on an input of electrons, these solvated electrons are generated in the crystal and used to drive the nitrite reduction mechanism[152]. This property was first exploited in cytochrome P450cam, where irradiation of the adduct bound crystallised enzyme caused the breakdown of the adduct and the formation of an intermediate and associated structural changes, which in turn were observed in-situ[153]. The resolution of the crystal must be high enough to observe all the partial occupancy intermediates of the enzyme during data collection. The crystal also needs to be robust enough to survive multiple datasets collected from the same region in quick succession. The recent

development of rapid, shutterless X-ray detectors, such as the Pilatus 6M-F (Dectris) detector, has facilitated the fast and sequential data collection required for this technique[154,155]. This technique has recently been applied to *Ac*NiR where a series of 45 consecutive datasets were collected from a single crystal soaked in NO_2^- [132]. Known as multiple structures serially obtained from one crystal (MSOX), this allowed a molecular movie to be generated showing the complete reduction reaction. The generated photoelectrons reduce the T1Cu which transfer along the Cys-His bridge to the T2Cu converting NO_2^- to side-on NO which then dissociates allowing water to rebind the T2Cu. The use of single large crystals for time-resolved data collection has a number of advantages in that it avoids the problem of crystal heterogeneity experienced in serial crystallography and uses a large diffraction volume to obtain high resolution[139]. MSOX has subsequently been used with *Ac*NiR to access temperature dependent protein conformations during irradiation through varying the temperature at which data collection occured[156].

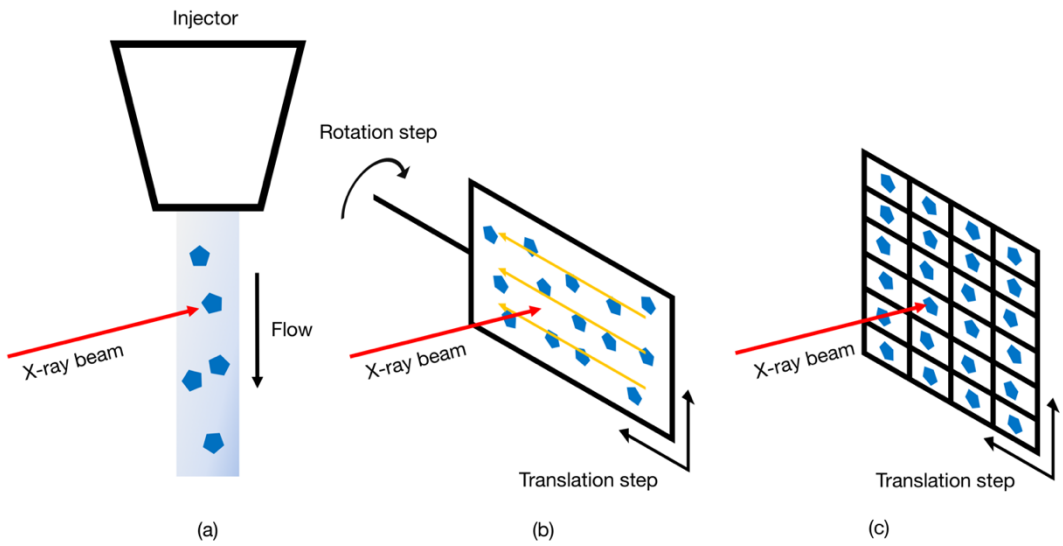

Figure 2.8. Three examples of SSX experimental setups. Three crystal sample delivery methods for synchrotron radiation crystallography. (a) An injector system based on the system developer for XFEL sources. (b) Randomly orientated microcrystal slurry frozen in a cryo holder loop which is scanned by the X-ray beam. (c) Microcrystals are held in silicon nitride chip. The beam can be directed at specific points giving a high hit rate.

2.4.5. Processing serial data

Serial data collection refers to a situation where one, or a small number of images, are collected from a single crystal. During a classical MX experiment at a synchrotron or an in-house set up, the crystal is rotated in the X-ray beam during illumination to move reflections through the Bragg condition. In XFEL experiments, the pulse is so short that no rotation occurs and only a snapshot, i.e. a still image, is collected. As crystalline material is delivered into the beam path, the detector is constantly read out, regardless of any interaction between the beam and crystal. This creates two classes of frames; one with diffraction data, hits, and one without, misses. The first processing step requires accurate detection of images with true Bragg spots. The detector readout is processed and images with a set number of spots, usually 10-30, are sorted, while blank images are discarded. Processing snapshot data starts with the recognition of two problems caused by the instant destruction of the crystal from the femtoseconds pulse. Each image contains the diffraction from one, now destroyed, crystal, which had an unknown orientation and unit-cell parameters when it interacted with the XFEL pulse[157]. The collection of femtosecond data is currently limited by the lack of photon-counting detectors which are unable to readout in time with a current limit of ~ 10^7 photons/s/pixel[42].

To start data processing, this data must be gleaned from the snapshot image, which covers a very small region of the reciprocal space compared to MX oscillation experiment. This also presents the problem of partiality. In an oscillation experiment, as the crystal is rotated during illumination, the

reciprocal lattice point moves through the Bragg condition and the diffracted intensity is recorded[159]. This is represented as a Gaussian distribution, with the intensity highest in the middle and decreasing at both tails. The entirety of that curve is integrated to give the full reflection intensity. Because XFEL images are recorded as snapshots, the reflection does not pass fully through the Bragg condition, and as such only a section of the curve is measured, producing a partial intensity. This partiality can be corrected if the experimental geometry can be calculated correctly. For purposes of clarity, multiplicity in this thesis will refer to several partial intensity measurements and not to fully integrated intensities that will be referred to as redundancy.

Processing serial data requires a more automated approach than at synchrotron beamlines because of the high rate of data collection; at SACLA approximately 1.6 terabytes of data are collected in an hour[160]. Currently, three software suites exist for processing XFEL crystallography data; *CrystFEL*, *ccbtx.xfel* and *nXDS*[161–163]. These three software suites contain inbuilt spot finding algorithms, but at SACLA, *Cheetah* is used to process images in real time in a parallel manner using a high-performance cluster to allow data processing during collection[164]. The data processing pipeline at SACLA utilises *CrystFEL* for data processing[165]. As each image is a snapshot, a large number are required to complete the dataset. Each image is indexed individually, and the unit cell is derived from a distribution of the cell lengths and angles. *CrystFEL* does not have an inbuilt indexing and integration program but acts as framework to link with multiple programs such as *MOSFLM*, *DirAx* and *XDS* to solve the problem of indexing still images[166–168]. The space group of a

crystal is only a hypothesis until the structure is solved. In an MX experiment with a novel crystal the data is merged in the lowest symmetry, and higher symmetries are explored later. Determination of a crystal space group using serial crystallography requires the opposite approach. In special cases where the crystal symmetry classes have less rotational symmetry than their lattices, each image must be allocated the indexing assignment; otherwise, after merging, the data will indicate an artificial twinning signal[169]. Therefore, datasets are merged in the highest possible symmetry to begin with, before identifying and resolving the ambiguity. This is implemented in *CrystFEL* as *Ambigator* which uses a clustering algorithm to calculate a correlation coefficient between each and every other image, and then the mean coefficient between each indexing assignment is compared[170]. Refinement of detector geometry is specifically important for XFEL data collection because of the multi-panel design implemented[171,172]. Data collection with multi-port detectors, where the detector surface is made up of a number of small panels, benefits from geometry optimisation of each panel individually relative to the crystals and beam position. Refinement of the beam energy per image is also important due to the shot-to-shot variation in a SASE X-ray beam. Partial diffraction intensities are then merged in a Monte Carlo-like fashion to produce the output *hkl* file[173,174]. Data processing results benefit from post refinement of image B-factors and better estimation of the partialities of the reflections. There are two main programs available for dealing with partial reflections; *Partialator* (*CrystFEL*) and *Prime* (*ccbtx.xfel*)[170,175]. After post-

refinement, the data are exported into MTZ format and can be treated like crystallographic data obtained at a synchrotron.

The quality of the data produced from a serial experiment can be judged by splitting the data into two half-datasets and merging them independently. This has been implemented to produced two figures of merit, R_{split} and CC*, which will be used to assess serial crystallography data quality in this thesis. R_{split} is defined as

$$R_{split} = 2^{-1/2} \frac{\sum |I_{even} - I_{odd}|}{\frac{1}{2}\sum (I_{even} + I_{odd})}$$

where the agreement between the two intensity lists is compared[161]. CC* is a defined as

$$CC^* = \sqrt{\frac{2CC_{1/2}}{1 + CC_{1/2}}}$$

where $CC_{1/2}$ is a Pearson correlation coefficient between two half datasets and CC* estimates the value of the true CC value, based on a finite sample size[176,177]. Resolution cut-offs will be based on R_{split} and the $CC_{1/2}$ derivative of CC*.

2.5. Research aims

CuNiRs represent important research targets because of their role in denitrification and pathogenesis. Denitrification is part of the nitrogen cycle, and as such is of central importance in agrochemical balance especially relating to anthropogenic effects. Several denitrifiers have emerged as opportunistic pathogens, as denitrifying conditions prevail in patients, particularly those suffering from cystic fibrosis or requiring catheter assistance. The two copper sites at the heart of the enzyme form a PCET core that is utilised in the nitrite reduction mechanism, but structural, kinetic and theoretical methods have provided conflicting evidence on the order of the reaction[61,62,64,178]. One explanation for this is that during structural studies, CuNiR crystals are damaged by the incident X-rays which induce new photochemistry in the enzyme. One of the copper sites, T1Cu, is prone to specific radiation damage, becoming reduced at a very low X-ray dose, almost immediately during modern synchrotron data collection[127]. The mode of substrate and product binding has also to be resolved with two distinct orientations visible in high-resolution structures[156,179]. High resolution, damage-free structural determination of the ligand binding modes, electron and proton transfer pathways and the active site water network is necessary to explain the mechanism. The motive for this PhD was to investigate whether radiation damage is obscuring any mechanistic structural data in CuNiR. In this work two CuNiRs, *Ax*NiR and *Ac*NiR were expressed, purified and crystallised for serial crystallography data collection at the SACLA XFEL facility in Japan. *Ac*NiR was also selected for expression in heavy water for

production of crystal suitable for neutron crystallography (NX) with the goal of identifying the protonation states of resting state, catalytic residues. Crystal structures of both enzymes were determined using femtosecond crystallography and these are presented here along with accompanying work.

Chapter 3 - Methods and materials

3.1. Production of recombinant *Ax*NiR

3.1.1. Cloning and preparation of expression hosts

A DNA fragment encoding the ORF of wild-type *nirK* gene of *A. xylosoxidans* without its periplasmic signal peptide, was cloned into a pET-28a(+) vector (Merck KGaA, Darmstadt, Germany). The gene was amplified by PCR using the oligonucleotide primers:

*Ax*NiR_fw (5^0-CCCGTCTCCCATGCAGGACGCCGACAAGC-3^0)

*Ax*NiR_rv (5^0-GGAAGCTTTCAGCGCGGAATCGGC-3^0)

(restriction sites underlined) and cloned between the *HindIII* and *NcoI* restriction sites of the vector, to give a recombinant vector, pET-28a(+)-*nirK* for overexpression. pET-28a(+)-*nirK* plasmid was transformed into competent *Escherichia coli* (*E. coli)* cells (BL21 DE3) using heat shock transformation. The transformant was cultured on Lysogeny broth (LB) agar, 50 µg/mL kanamycin (Kan) to isolate individual colonies.

3.1.2. Overexpression

A starter culture of 100 mL LB, 50 µg/mL Kan, was inoculated with a single transformant colony and incubated for 4 hours with 180 RPM shaking at 37°C. 10 ml of starter culture was transferred to 6 x 5 L baffled flasks containing 1 L LB supplemented with 50 µg/ml Kan. Culture flasks were incubated in New Brunswick Scientific™ Innova® 44 incubators at 37°C with 110 RPM shaking until the optical density had reached OD_{600}~0.5 AU (NanoDrop 1000). Protein overexpression was induced with 0.5 mM isopropyl β-D-1-thiogalactopyranoside (IPTG) and 1 mM $CuSO_4$. The temperature was lowered to 25°C and cell incubated overnight. Cell pellet were collected by centrifugation at 6000 RPM (Hitachi, R9A rotor) for 15 minutes. 41 g of cell pellet was collected from 6 L of LB broth and was stored at -70 °C.

3.1.3. Purification of cell lysate

Five grams of cell pellet was resuspended in 50ml lysis buffer (20 mM Tris-HCl, pH 7.0, 0.1 mg/ml Lysozyme, 1 mg/ml Roche Protease Inhibitor Cocktail Set III and 0.1 mg/ml DNase) and stirred on ice for 30 minutes. Cells were disrupted by sonication (Branson™ Sonifer® SFX 550). The lysate was sonicated for 10, 30 s periods with 30 s pause in between. Cell debris was removed by centrifugation at 20,000 RPM (Hitachi, R20A2 rotor) for 30 minutes. Cell lysate was collected in 50 kDa molecular weight cut-off (MWCO) dialysis tubing (Thermo Fisher Scientific™ SnakeSkin®) and dialyzed against 2 L dialysis buffer (20 mM Tris-HCl, pH 7.0, 1 mM $CuSO_4$) to restore the copper content of the T2Cu site to the Cu(II) oxidisation state. This was repeated twice for 2 hours each, followed by 12 hours of dialysis against just 20 mM Tris-HCl, pH 7.0.

3.1.4. Weak-cation exchange chromatography

The cell lysate collected from the dialysis tube after 12 hours had a blue colour. A small amount of precipitate formed during dialysis was removed by centrifugation at 20,000 RPM (Hitachi, R20A2 rotor) for 30 minutes. The lysate was applied to 10 cm of carboxymethyl cellulose resin (Whatman, CM52) set in a gravity chromatography column (ID 2.5 cm), with column volume (CV) 50 ml. The resin was pre-washed with 1 CV of 1 M Tris-HCl, pH 7.0, followed by 4 CV H_2O, followed by 1 CV of 20 mM Tris-HCl, pH 7.0. A blue fraction band was observed binding at the top of the column after protein loading. The lysate flow-through and all subsequent fractions were collected. The column was then washed with 1 CV 20 mM Tris-HCl, pH 7.0 followed by a step NaCl gradient (1 CV 20 mM Tris-HCl, pH 7.0 + 0, 50, 100, 150, 300, 1000 and 1500 mM NaCl). The blue protein eluted in the 100 mM NaCl fraction. This was observed by eye and confirmed with sodium dodecyl sulphate polyacrylamide gel electrophoresis (SDS-PAGE) (Figure 3.1).

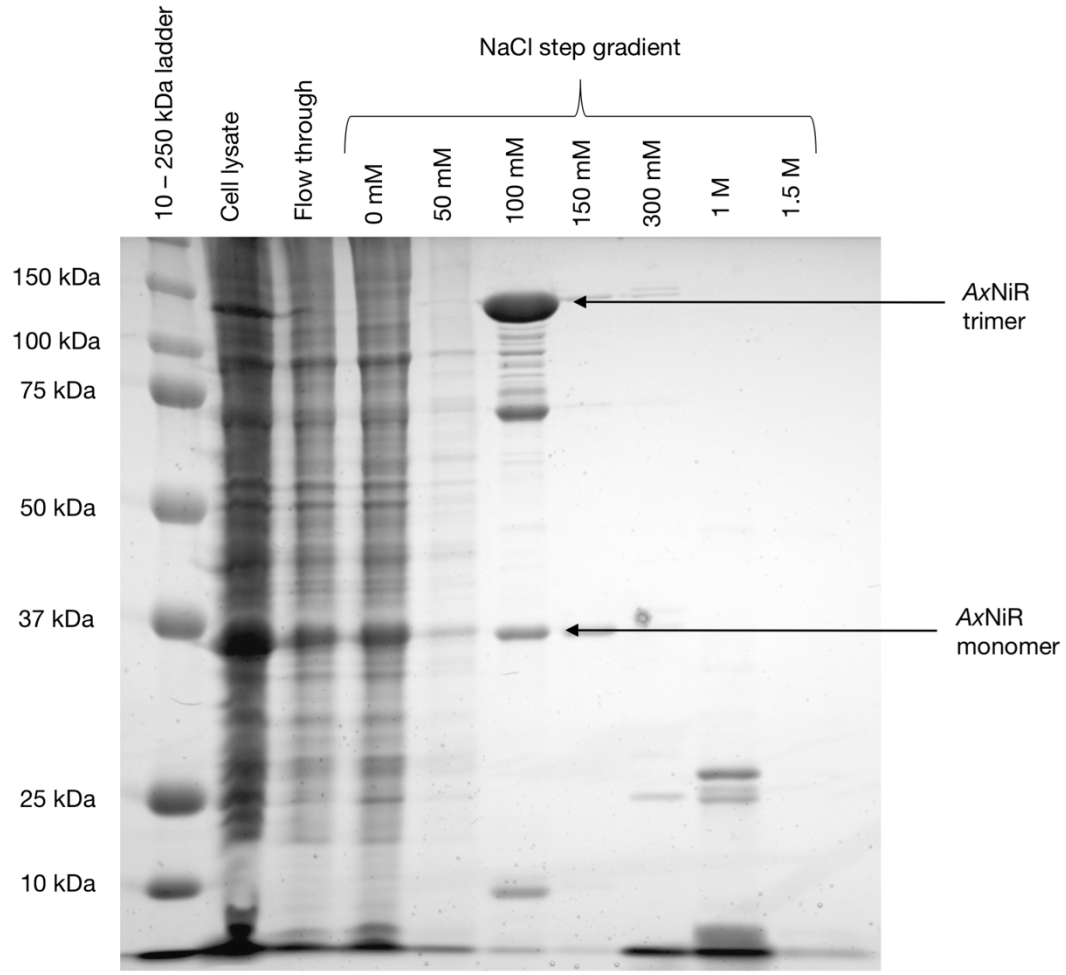

Figure 3.1. An SDS-PAGE gel showing the purification of *Ax*NiR using carboxymethyl cellulose. The 100 mM NaCl fraction from the carboxymethyl cellulose column contained the eluted *Ax*NiR. Both the monomeric and oligomeric forms are visible on the gel despite this being an SDS gel. This is often observed with trimeric CuNiRs due to the trimer formation around the catalytic T2Cu site forming a strong affinity.

3.1.5. Size exclusion chromatography

The blue 100 mM NaCl carboxymethyl cellulose fraction was concentrated to 1 ml using a Millipore™, Amicon® 50 kDa MWCO centrifugal filter. This fraction was applied to a GE HiLoad® 16/600 Superdex® 200 pg size exclusion chromatography (SEC) column attached to an GE™ AKTA® Explorer 900. The mobile phase was 10 mM Tris-HCl, pH 7.0, 200 mM NaCl. The pump was set to 1 ml/min and the UV–visible absorbance was observed at 280, 260 and 600 nm. The blue *Ax*NiR fraction eluted in a single peak at 74.7 ml (Figure 3.2). Protein concentration was determined by spectrophotometric absorbance (NanoDrop 1000) at 280 nm using a molar attenuation coefficient of 43,890 M^{-1} cm^{-1}. 5 g of cell pellet per purification run produced on average 15 mg of *Ax*NiR.

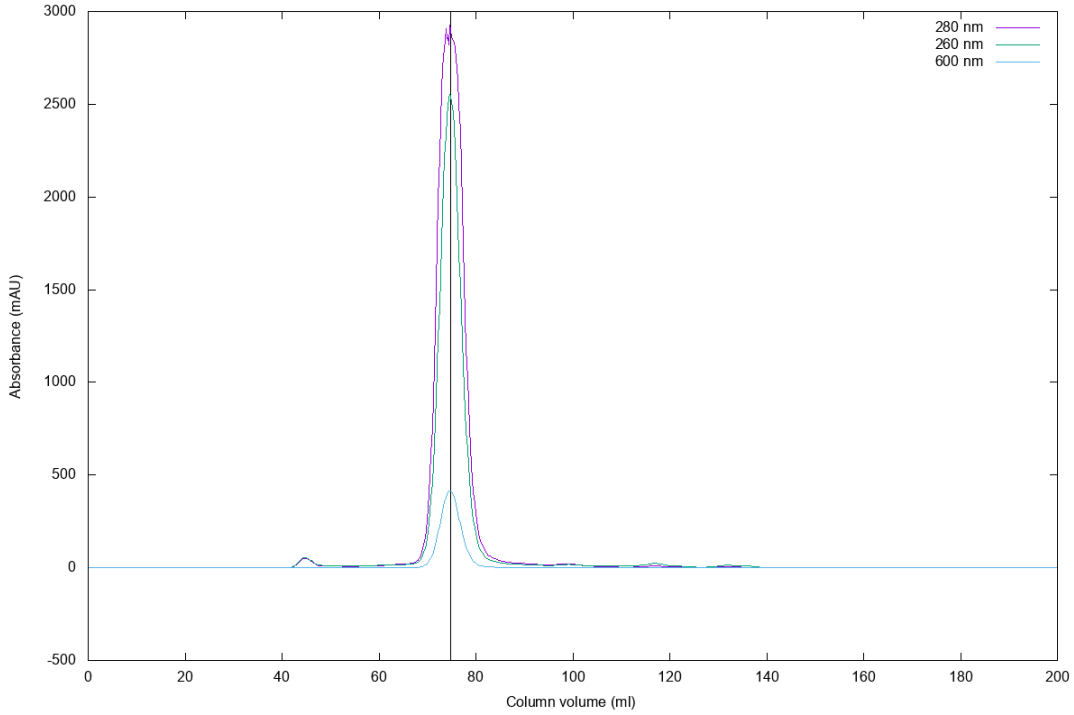

Figure 3.2. A size exclusion elution profile of *Ax*NiR. The column was a GE Healthcare HiLoad™ 16/600 Superdex™ 200 pg running at 1 ml/min with 10 mM Tris-HCl, pH 7.0, 200 mM NaCl buffer. Chromatogram trace shows UV–visible absorbance at 280 nm (purple), 260 nm (blue) and 600 nm (green). The blue *Ax*NiR fraction eluted in a single peak centred at 74.7 ml indicated by the black vertical line.

3.2. Production of recombinant *Ac*NiR

3.2.1. Overexpression

A pET-26b(+) plasmid (Merck KGaA, Darmstadt, Germany) containing the *nirK* gene from *Achromobacter cycloclastes* with codon optimization for expression in *E. coli* was acquired from GenScript. pET-26a(+)-*nirK* plasmid was transformed into competent *E. coli* cells (BL21 DE3) using heat shock transformation. The transformant was cultured on LB agar, 30 µg/mL Kan to isolate individual colonies. A starter culture of 50 mL LB Broth, 30 µg/mL Kan, was inoculated with a single transformant colony and incubated for 12 hours with 220 RPM shaking at 37°C. 6 ml of starter culture was transferred to 6 x 2 L baffled flasks containing 500 mL LB supplemented with 30 µg/ml Kan. Culture flasks were incubated in New Brunswick Scientific™ Innova® 44 incubators at 37°C, 180 RPM until the optical density had reached OD_{600}~0.5 AU. Protein overexpression was induced with 2 mM IPTG and 1 mM $CuSO_4$. The temperature was lowered to 18°C and cells were incubated overnight. Cell pellet were collected by centrifugation at 4000 RPM (Sorvall RC-5B) for 10 minutes. 18 g of cell pellet was collected from 3 L of LB broth and was stored at -70 °C.

3.2.2. Purification of cell lysate

Five grams of cell pellet was resuspended in 50ml lysis buffer (20 mM Tris-HCl, pH 7.5, 0.1 mg/ml Lysozyme, 1 mg/ml Roche Protease Inhibitor Cocktail Set III and 0.1 mg/ml DNase) and stirred on ice for 30 minutes. Cells were disrupted by sonication (MSE Soniprep 150 Plus). The lysate was sonicated for 10, 30 s periods with 30 s pause in between. Cell debris was removed by centrifugation at 18,000 RPM (Sorvall RC-5B) for 20 minutes. Cell lysate was loaded in 10 kDa MWCO dialysis tubing (Thermo Fisher Scientific™ SnakeSkin®) and dialyzed against 2 L, 20 mM Tris-HCl, pH 7.5, 2 mM $CuSO_4$ to restore the copper content of the T2Cu site of the Cu(II) oxidisation state for 4 hours at 4°C. This was followed by two dialysis steps against two lots of water for 2 hours.

3.2.3. Weak-anion exchange chromatography

The cell lysate collected from the dialysis tube after 12 hours now with a green colour. A small amount of precipitate formed during dialysis was removed by centrifugation at 20,000 RPM 18,000 RPM (Sorvall RC-5B) for 20 minutes. The lysate was applied to 10 cm of diethylaminoethyl (DEAE) cellulose resin (Sigma-Aldrich) set in a gravity chromatography column (ID 2.5 cm), with CV 50 ml. The resin was pre-washed with 4 CV MQ H_2O, followed by 1 CV of 20 mM Tris-HCl, pH 7.5. A green fraction band was observed binding at the top of the column after lysate flow-through. The lysate flow-through and all subsequent fractions were collected. The column was washed with 5 CV of 20 mM Tris-HCl, pH 7.5 followed by 5 CV of 100 mM Tris-HCl, pH 7.5. The protein was eluted by a step NaCl gradient (1 CV 20 mM Tris-HCl, pH 7.5 + 50, 100, 150, 200 and 250, 300 mM NaCl). The green protein eluted in the 150 mM NaCl fraction. This was observed by eye and confirmed with SDS-PAGE (Figure 3.3).

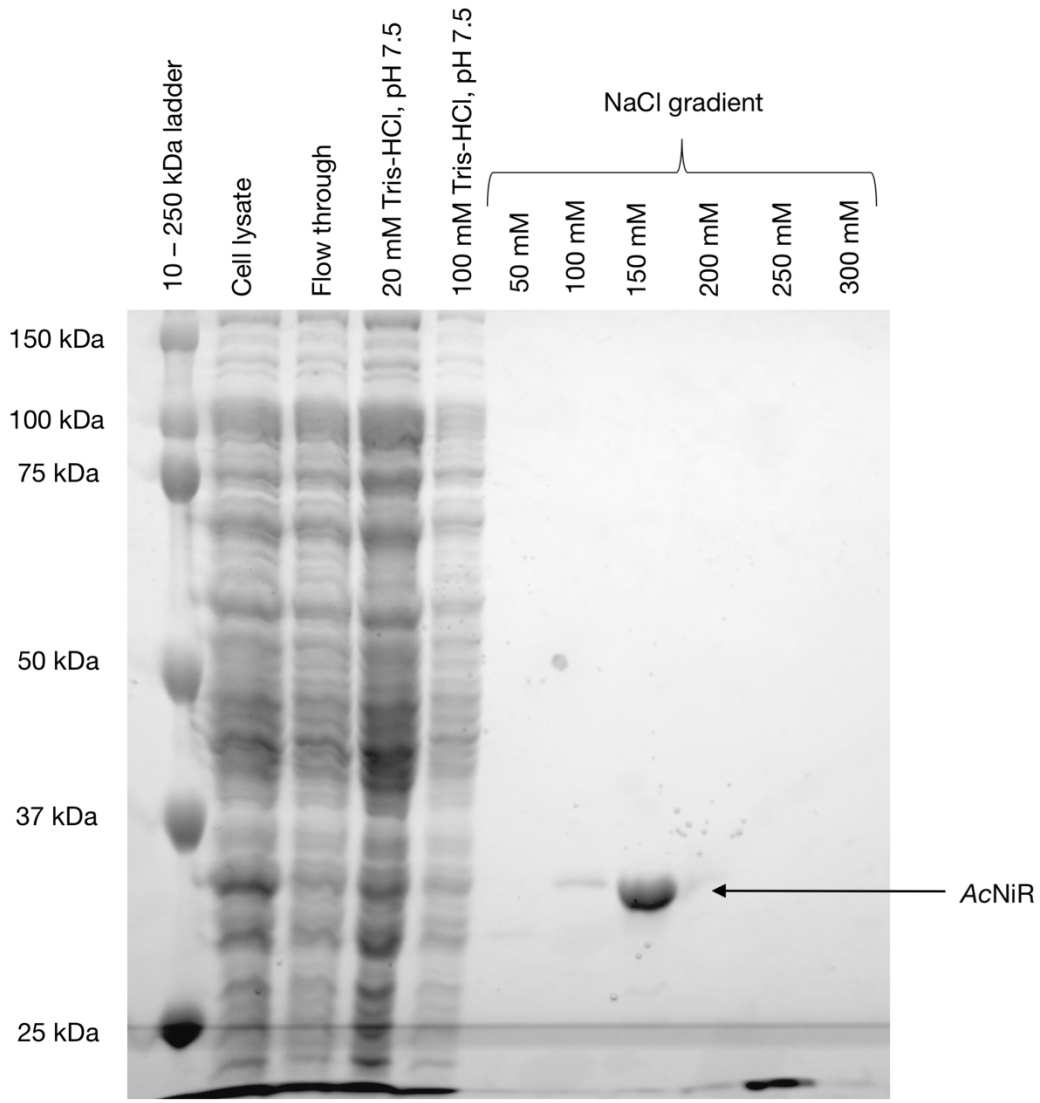

Figure 3.3. An SDS-PAGE gel showing the purification of *Ac*NiR using DEAE-cellulose. The 150 mM NaCl fraction from the DEAE cellulose column contained the eluted *Ac*NiR.

3.2.4. Ammonium sulphate precipitation

The green 150 mM NaCl DEAE-cellulose fraction was concentrated to 1 ml using a Millipore™, Amicon® 50 kDa MWCO centrifugal filter at 50 g and transferred into 50 mM HEPES-OH, pH 6.5. 100 mM citrate buffer, pH 4.7 was added to fraction to precipitate proteins unstable at low pH. 4 M ammonium sulphate was then added to precipitate all protein and the precipitant was collected using centrifugation, 13,200 RPM for 10 minutes. The precipitate was dissolved in 10 mM HEPES-OH, pH 6.5 followed by another round of centrifugation and the supernatant was collected. 100 mM citrate buffer, pH 4.7 was added again and tube was incubated at 15 °C for 1 hour. 0.1 M ammonium sulphate was then added and mixed thoroughly followed by centrifugation and this step was repeated until any green precipitate started to form. Finally, all protein was fully precipitated with 4 M ammonium sulphate and dissolved in dissolved in 10 mM HEPES-OH, pH 6.5. Protein concentration was determined by spectrophotometric absorbance (NanoDrop 1000) at 280 nm using a molar attenuation coefficient of 41,370 M^{-1} cm^{-1}. 5 g of cell pellet per purification run produced on average 129 mg of *Ac*NiR.

3.3. Production of perdeuterated recombinant *Ac*NiR

3.3.1. Purification of cell lysate

To produce perdeuterated *Ac*NiR, the pET-26a(+)-*nirK* plasmid acquired from GenScript was sent to the Deuteration Laboratory[180] at the Institut Laue-Langevin. The Deuteration Laboratory provided frozen cell pellet containing *Ac*NiR overexpressed in *E. coli* cells grown in D_2O. 5 g of cell pellet was resuspended in 50ml lysis buffer (20 mM Tris-HCl, pH 7.5, 150 mM NaCl, 0.1 mg/ml Lysozyme, 1 µg/ml Roche Protease Inhibitor Cocktail Set III and 0.1 mg/ml DNase) and stirred on ice for 30 minutes. Cells were disrupted by sonication (MSE Soniprep 150 Plus). The lysate was sonicated for 10, 30 s periods with 60 s pause in between. Cell debris was removed by centrifugation at 19,000 RPM (Sorvall RC-5B) for 15 minutes. Cell lysate was collected in 50 kDa MWCO dialysis tubing (Thermo Fisher Scientific™ SnakeSkin®) and dialyzed against 2.5 L, 20 mM Tris-HCl, pH 7.5, 1 mM $CuSO_4$ to restore the copper content of the T2Cu site of the Cu(II) oxidisation state for 2 hours at 4°C. 2 µl of H_2O_2 was added to the protein solution to a total concentration of 0.1 mM in order to maintain the Cu(II) oxidation state. Further dialysis against just 20 mM Tris-HCl, pH 7.5 was carried out for another 2 hours.

3.3.2. Mixed-mode ion exchange chromatography

A small amount of precipitate formed during dialysis was removed by centrifugation at 20,000 RPM 18,000 RPM (Sorvall RC-5B) for 20 minutes. The lysate was applied to 10 cm of hydroxyapatite column resin (Sigma-Aldrich) set in a gravity chromatography column (ID 2.5 cm), with CV 50 ml. The resin was pre-washed with 4 CV MQ H_2O, followed by 1 CV of 100 mM Tris-HCl, pH 7.5. After loading the protein lysate, the column was washed with 30 ml of 10 mM Tris-HCl, pH 7.5 and 20ml of 5 mM potassium phosphate buffer, pH 7.5. A green fraction was eluted using a potassium phosphate, pH 7.5 step gradient using one CV of 10 mM, 20 mM, 30 mM, 50 mM, 100 mM and 150 mM buffer. The green protein eluted in the wash, 10 mM and 20 mM fraction. This was observed by eye in the 10 mM fraction and confirmed with SDS-PAGE (Figure 3.4).

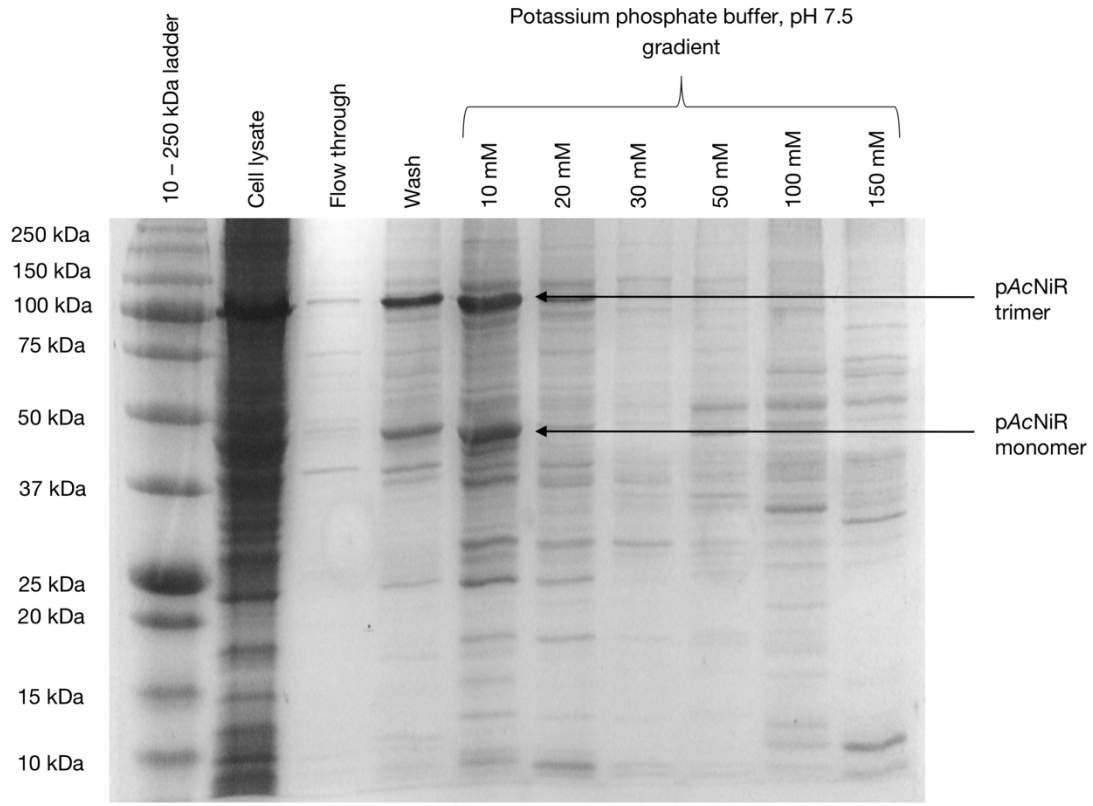

Figure 3.4. An SDS-PAGE gel showing the purification of perdeuterated *Ac*NiR using hydroxyapatite. The column wash and the 10 mM potassium phosphate buffer, pH 7.5 fraction from the hydroxyapatite column contained the eluted *Ac*NiR. Both the monomeric and oligomeric forms are visible on the gel despite this being an SDS gel. This is often observed with trimeric CuNiRs due to the trimer formation around the catalytic T2Cu site forming a strong affinity.

3.3.3. Weak-cation exchange chromatography

The 10 mM fraction from the hydroxyapatite column was concentrated with a Millipore™, Amicon® 50 kDa MWCO centrifugal filter from 50 ml to 10 ml. A 5 ml GE Healthcare HiTrap™ DEAE Sepharose Fast Flow IEX Column was equilibrated with 20 mM Tris-HCl, pH 7.5 and attached to an GE™ AKTA® Explorer 900. The pump was set to 1 ml/min and the UV absorbance was observed at 280 and 260. The perdeuterated *Ac*NiR was eluted with a continuous NaCl gradient from 50 mM to 250 mM plus 20 mM Tris-HCl, pH 7.5. 7, 20 ml fractions were collected from 100 ml to 240 ml (Figure 3.5). This was observed by eye in the 10 mM fraction and confirmed with SDS-PAGE (Figure 3.6).

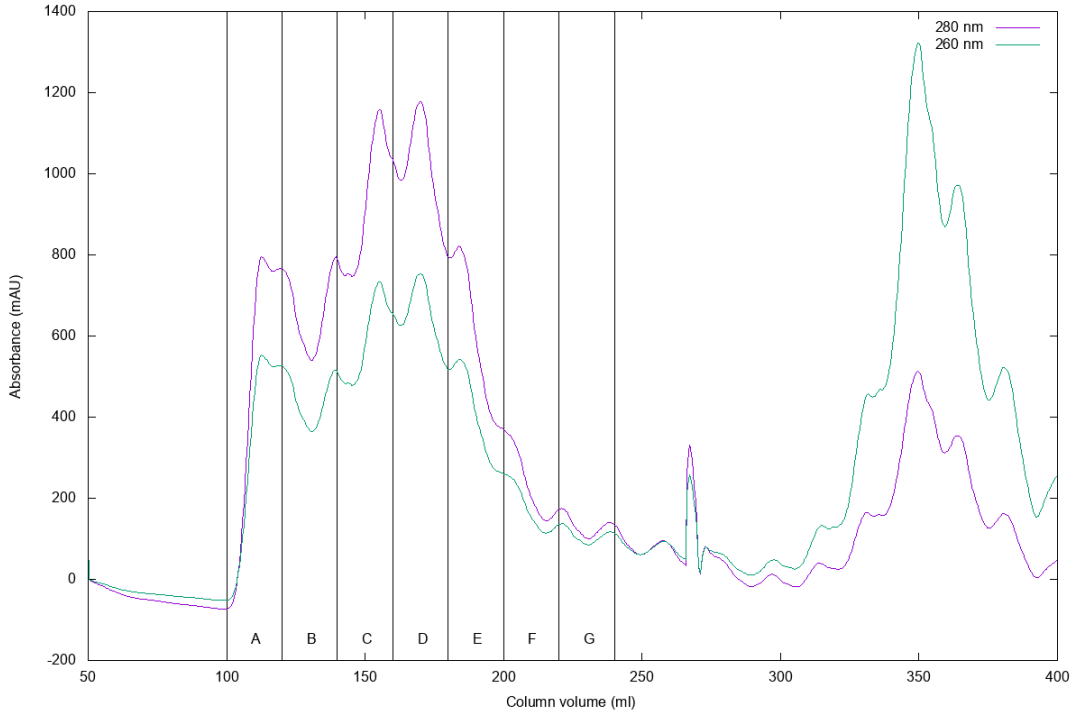

Figure 3.5. A weak-cation exchange elution profile of perdeuterated *Ac*NiR using DEAE-Sepharose. The column was a 5 ml GE Healthcare HiTrap™ DEAE Sepharose Fast Flow IEX Column running at 1 ml/min with 20 mM Tris-HCl, pH 7.5 with a continuous NaCl gradient of 50 mM to 250 mM. Chromatogram trace shows UV absorbance at 280 nm (purple) and 260 nm (green). The green *Ax*NiR fraction eluted across three fractions; A, B and C.

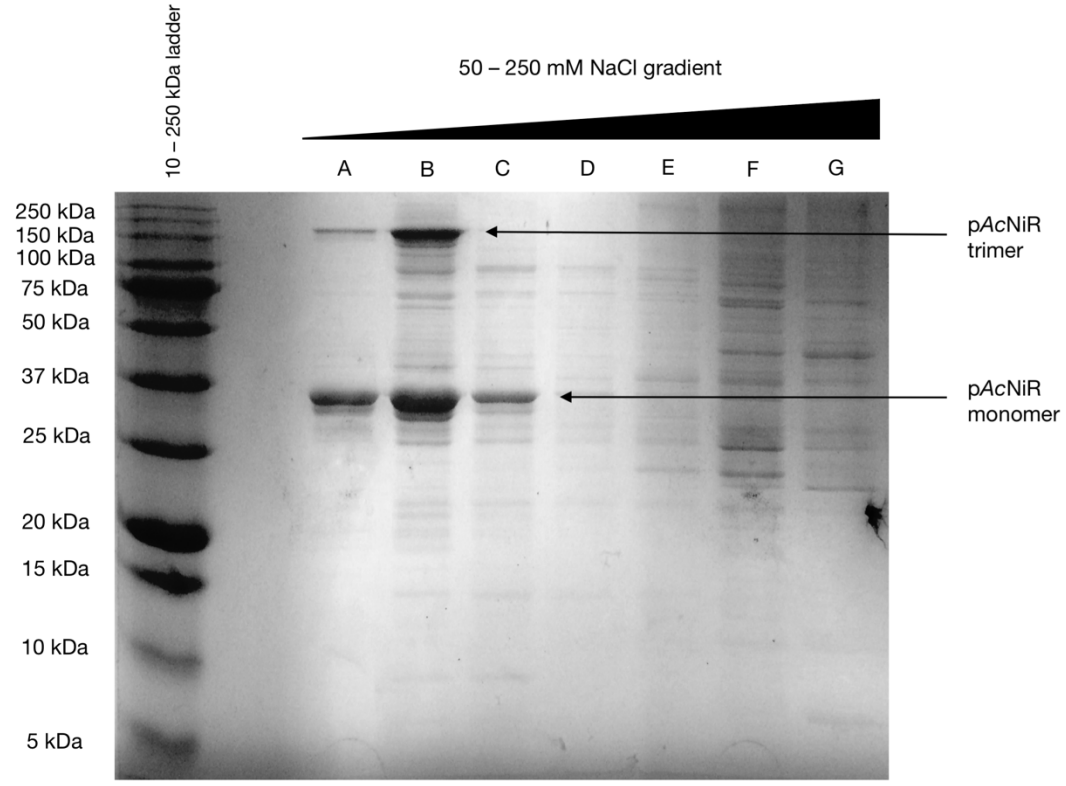

Figure 3.6. An SDS-PAGE gel showing the purification of perdeuterated *Ac*NiR using DEAE-Sepharose. Fractions A, B and C contained all the eluted perdeuterated *Ac*NiR. Both the monomeric and oligomeric forms are visible on the gel despite this being an SDS gel. This is often observed with trimeric CuNiRs due to the trimer formation around the catalytic T2Cu site forming a strong affinity.

3.3.4. Size exclusion chromatography

Fraction B from the hydroxyapatite column was concentrated with a Millipore™, Amicon® 50 kDa MWCO centrifugal filter from 50 ml to 1 ml. This fraction was applied to a GE HiLoad® 16/600 Superdex® 200 pg SEC column attached to an GE™ AKTA® Explorer 900. The mobile phase was 20 mM Tris-HCl, pH 7.5, 150 mM NaCl. The pump was set to 1 ml/min and the UV absorbance was observed at 280 and 260 nm. The green perdeuterated *Ac*NiR fraction eluted in a peak at 72.4 ml (Figure 3.7). The peak had a shoulder and this fraction was collected separately from the main peak with a total volume of 10 ml.

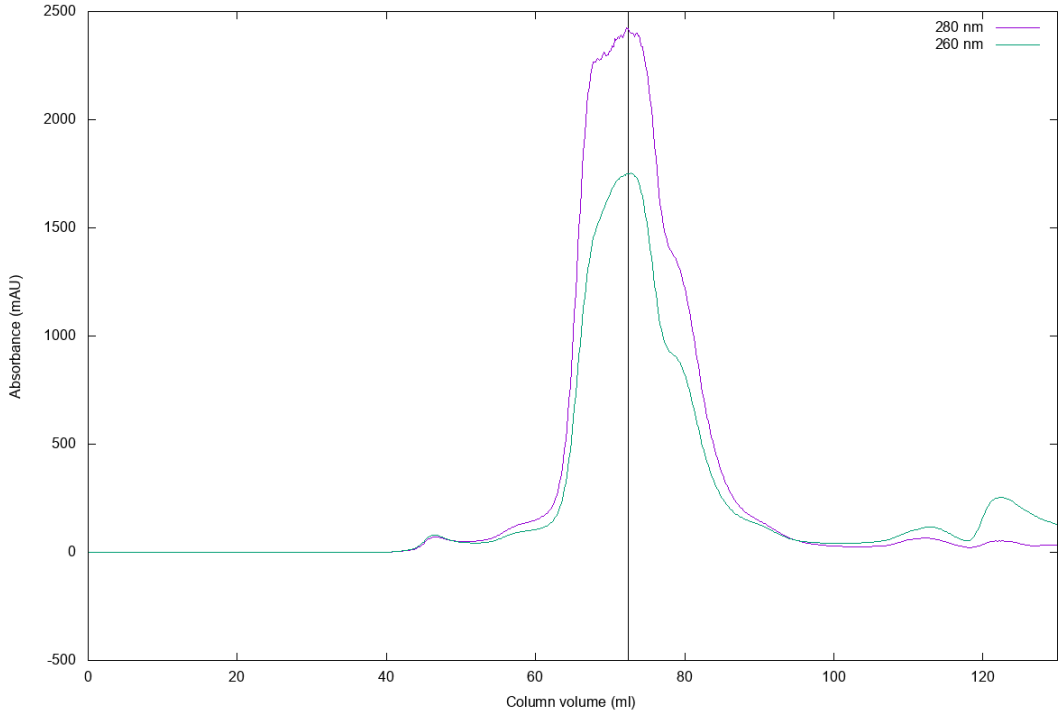

Figure 3.7. A size exclusion elution profile of perdeuterated *Ac*NiR. The column was a GE Healthcare HiLoad™ 16/600 Superdex™ 200 pg running at 1 ml/min with 20 mM Tris-HCl, pH 7.0, 150 mM NaCl buffer. Chromatogram trace shows UV absorbance at 280 nm (purple) and 260 nm (green). The green perdeuterated *Ac*NiR fraction eluted in a peak centred at 74.7 ml indicated by the black vertical line.

3.3.5. Ammonium sulphate precipitation

The SEC fraction was concentrated to 1 ml using a Millipore™, Amicon® 50 kDa MWCO centrifugal filter at 50 g for over three 10-minute runs and transferred into 50 mM MES-OH, pH 6.5. 100 mM Na-acetate, pH 5.0 was added to precipitate proteins unstable at low pH. 4 M ammonium sulphate was then added to precipitate all protein and the precipitant was collected using centrifugation, 13,200 RPM for 10 minutes. The precipitate was dissolved in 50 mM MES-OH, pH 6.5 made up in D_2O followed by another round of centrifugation and the supernatant was collected. Protein concentration was determined by spectrophotometric absorbance (NanoDrop 1000) at 280 nm using a molar attenuation coefficient of 41,370 M^{-1} cm^{-1}. 5 g of cell pellet per purification run produced on average 10 mg of perdeuterated *Ac*NiR.

3.4. Analytical Techniques

3.4.1. Polyacrylamide gel electrophoresis

Sample was diluted into SDS loading buffer (0.2 M Tris-HCl pH 6.8, 10 mM 2-mercaptoethanol, 10% w/v SDS, 0.05% w/v bromophenol blue, 20% v/v glycerol) at a sample to buffer ratio of 5:1. The diluted sample was then loaded onto a 12% polyacrylamide gel and run for 60 min with the application of 210 V. Precision Plus Protein™ Dual Colour Standards (Bio-Rad) and Precision Plus Protein™ All Blue Standards (Bio-Rad) were used as marker ladders (10 – 250 kDa). Protein was visualised using Coomassie Brilliant Blue (Bio-Rad).

Chapter 4 - *Ax*NiR serial femtosecond crystallography

4.1. Theory of X-ray crystallography

4.1.1. Diffraction theory

The interaction of X-rays with protein crystals allows for the determination of the protein atomic structure. Collecting data from a single, cryocooled crystal at a synchrotron facility is currently the most common approach known as MX or synchrotron radiation crystallography (SRX) . X-rays have a wavelength between 0.01 to 10 nm which covers the average atomic bond length of ~1.2 Å allowing for an effective resolution of the structure[181]. A crystallised protein is placed in the path of an X-ray beam which scatters the beam and the scattered photons are collected on a detector forming a diffraction pattern. The detector records the positions and intensity of each reflection relating to a specific plane of the crystal lattice. The crystal is subsequently rotated in the beam which brings new lattice planes within the crystal to scatter the incident X-rays. Following full data collection, the data are merged and, when combined with the phase, an electron density map of the protein atomic structure can be calculated. This pipeline for the determination of a proteins three-dimensional structure is reliant on the crystal elastically scattering the incident photons, called diffraction. The

incident beam produced by modern synchrotron facility is of a single wavelength, monochromatic, which with a periodic object will scatter the incident photons in distinct directions. After the photons are scattered, the wavelength is consistent with that of the incident beam, but the phase and amplitude of the scattered wave is dependent on the inherent periodicity of the object being probed. As the photons position and amplitude are recorded, the information relating to the X-ray phase is lost[182]. The phase and amplitude data are connected to the periodicity of the scattering object by the Fourier transform. As the phase cannot be measured directly, the information must be inferred from other sources such as homology models (Molecular Replacement) or from crystal inelastic scattering (Experimental Phasing).

The angle (θ) at which a periodic object will scatter the incident X-rays if defined by distance between the lattice points in the crystal (d_{hkl})[183].

$$n\lambda = 2d_{hkl}sin\theta$$

When scattering from the crystal satisfies the Bragg condition, discrete diffraction reflections are observed from an object (Figure 4.1). The construction of an Ewald sphere is useful when looking to demonstrate the satisfaction of Braggs law (Figure 4.2)[184]. When the Ewald sphere is superimposed upon the reciprocal lattice of an object, the reciprocal lattice points that intersect the Ewald sphere satisfy the Bragg condition. As the crystal is rotated in the incident beam, new lattice points move to intersect the Ewald sphere allowing the complete measurement of all diffraction

conditions. As the X-rays scatter off atomic electron clouds in the crystal, the distribution of those electrons can be calculated anywhere in unit cell (x,y,z). The density of electrons (ρ) is given by a Fourier series.

$$\rho(x,y,z) = \frac{1}{V}\sum_{h}\sum_{k}\sum_{l} F(hkl)\exp\left(-2\pi i(hx+ky+lz)\right)$$

The structure factors (F) reflect the material scattering of the object allowing the interpretation of diffraction pattern. It describes the amplitude and phase of a wave diffracted from crystal lattice planes characterised by Miller indices (hkl), reciprocal lattice basis vectors representing 3D crystallographic lattice planes. Here, the coordinates of the j^{th} atom are represented by x_j, y_j and z_j and the scattering factor of the j^{th} atom is described by f_j.

$$F(hkl) = \sum_{j=1}^{N} f_j \exp\left(2\pi i(hx_j + ky_j + lz_j)\right)$$

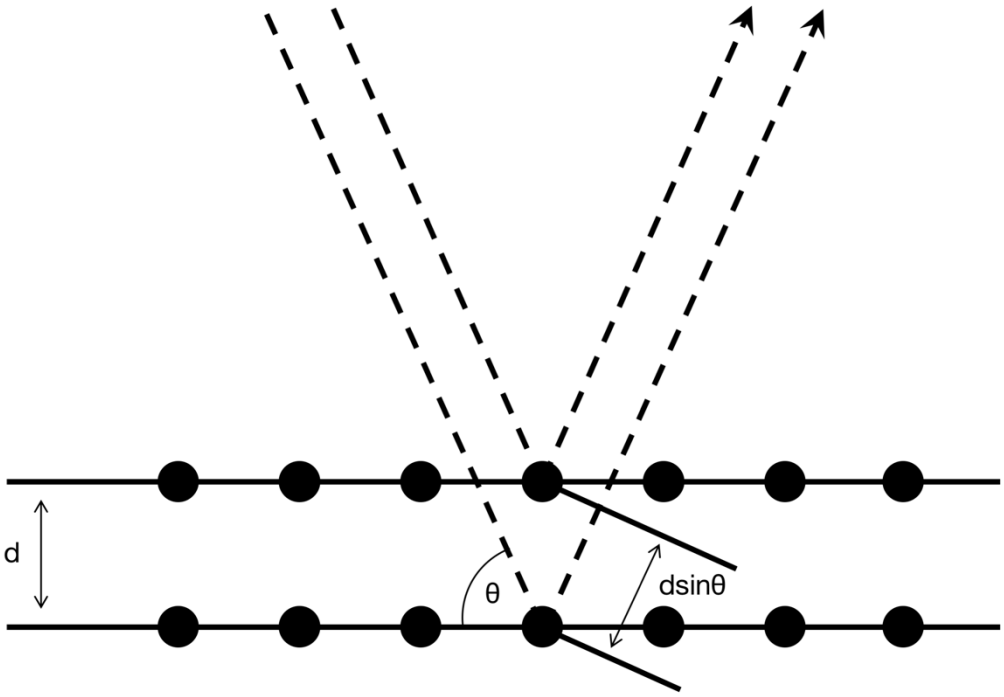

Figure 4.1. A diagram showing the conditions for Bragg diffraction. Two photon beams are scattered by two lattice planes. The second beam travels 2dsinθ further than the first beam. If the two beams have equal wavelengths and phases, they will constructively interfere once scattered by an ordered lattice.

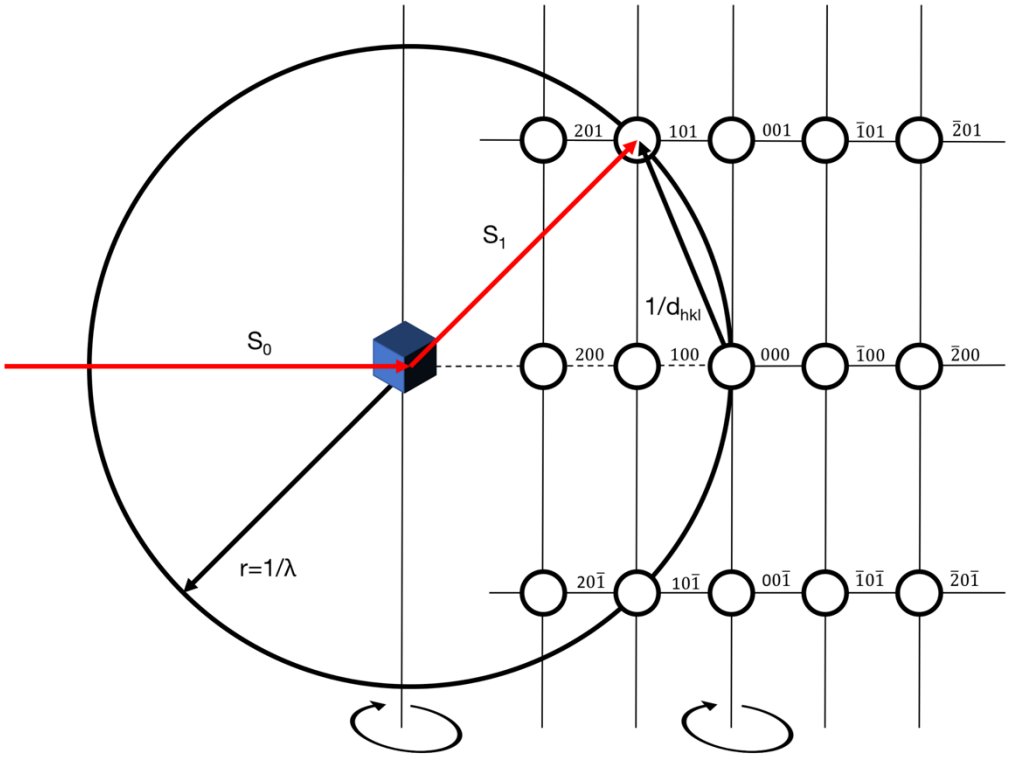

Figure 4.2. The Ewald construction. When a crystal lattice point fulfils Braggs law, it intercepts the Ewald sphere. As the crystal is rotated in the X-ray beam (S_0), different lattice points will intercept the Ewald sphere allowing the full dataset to be collected.

The structure factors can be simplified to a relationship between the measured amplitude (F_{hkl}) and the phase data (α_{hkl}) that must be calculated indirectly.

$$F(hkl) = F_{hkl}\exp(i\alpha_{hkl})$$

To calculate the structure factors of a protein crystal, it is necessary to analyse the symmetry operators present. Interpterion of the structure must satisfy the crystal symmetry and incorrect symmetry assignment can hinder structural determination. The symmetry of a crystal should be a major contributing factor to the strategy employed to collect the diffraction data from the crystal. The total symmetry of a crystal is defined by its space group. These symmetry elements include translation, rotation (two-, three-, four- and six-fold operation) and combination operations (screw-axes and glide planes). There are 230 total unique space groups formed by the various combinations of these symmetry elements[185]. In three-dimensional space, there are 14 Bravais lattices which are generated by translation elements obtained by combining one of the seven lattice systems with one of the centring classes. Because proteins are chiral molecules, certain types of symmetry are forbidden in protein crystals. Inversion, rotoreflection, glide planes and mirror planes would all bring about change in chirality in the crystal which is not possible in a chiral system. This leaves a total of 65 chiral space groups to choose from when determining the space group of a protein molecule[186]. To do so requires an analysis of the Miller indices of each reflection to determine the systematic

absences. This requires two basic assumptions are made. First that the structure factors at reciprocal space vectors are complex conjugates.

$$F(hkl) = F^*(\bar{h}\bar{k}\bar{l})$$

This means that the corresponding diffraction intensities are equal in value, known as Friedel's law and the crystal diffraction is centrosymmetric regardless of the crystal itself. Friedel's law only holds if all atoms scatter with no phase delay. If they do, they scatter anomalously and gain an imaginary component to the phase, f", which breaks Friedel's law (Figure 4.3).

$$I(hkl) = I(\bar{h}\bar{k}\bar{l})$$

Secondly, that the point symmetry of the crystal is maintained in the diffraction pattern meaning the point group of the diffraction pattern is the centrosymmetric parent of the point group of the crystal. Translational symmetry elements while not affecting the symmetry of the diffraction pattern, do cause the absence of diffraction intensities at specific sets of reciprocal lattice points, known as systematic absences. If these can be identified and their pattern recognised, then the point group and subsequently space group can be identified. However, of the 32 crystallographic point groups, 10 are described as polar, meaning they have more than a single point that is unmoved by all the symmetry operations. To identify the correct indexing solution, a guess has to be made to select the

origin. If this guess fails, the data can be reindexed to allow structural determination to proceed.

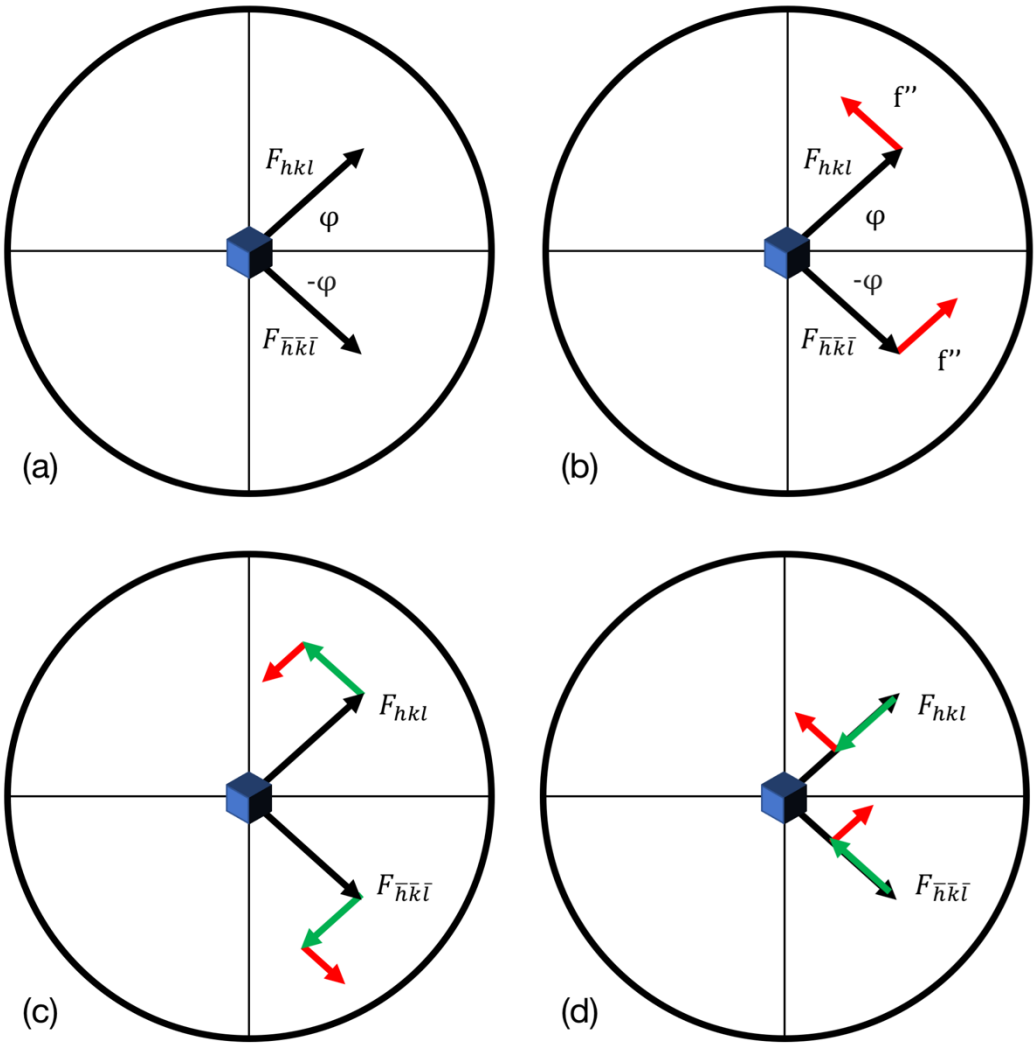

Figure 4.3. A diagram showing anomalous scattering breaking Friedel's law. (a) All atoms scatter equally, i.e. in the absence of anomalous scattering, so Friedel's law is true. (b) The amplitudes remain equal, but the phase data are no longer consistent. (c) If atoms scatter anomalously both the amplitude and phase data is no longer consistent. If the non-anomalous scattering atom is out of phase by $\pi/2$ compared to the anomalous scattering atom, the signal, ΔF, is large compared to (d) where the non-anomalous scattering atom is in phase with the anomalous scattering atom.

4.1.2. Twinning theory

Twinning is an anomaly in crystal growth where two or more crystal domains in the same crystal grow together and overlap according to a particular symmetry operation[187]. When collecting diffraction data from a twinned crystal, each reflection is a combination of the diffraction from different domains. Depending on the prevalence of one domain over the other, the problem can be solved mathematically but twinning still presents one of the most difficult problems to overcome in structure determination. In a perfect twin the twin fraction is equal to ½ meaning each domain contributes equally to each refection. Inaccurate higher symmetry appears in the intensity statistics which can be detected by the L test where pairs of local reflections are compared[188]. Because the domains contribute equally, structural determination becomes highly improbable. Usually molecular replacement can be carried out, but when trying to refine the data there is little improvement in R_{work} and the structure cannot be resolved[189].

4.2. *Ax*NiR SFX

4.2.1. Microcrystallisation

SFX experiments requires the growth of a large volume of well-ordered microcrystals of homogeneous size distribution that tolerate an injector-based approach[137]. *Ax*NiR microcrystals was produced using the free interface diffusion (FID) method by mixing a 1:1 ratio of 50 mg/ml *Ax*NiR in 10 mM Tris-HCl, pH 7.2 with a precipitant solution composed of 35% (w/v) PEG 550 MME, 20 mM $ZnSO_4$, 50 mM MES-OH, pH 6.5. 100 μl of precipitant solution was layered on top of 100 μl of protein solution in an Eppendorf tube. Microcrystals were produced by incubation for 30 mins at 4°C after which the Eppendorf contained two distinct layers of crystals. Firstly, a sedimented layer at the bottom of the Eppendorf containing crystals ~15 μm in size followed by a crystal suspension of ~60 μm sized crystals (Figure 4.4).

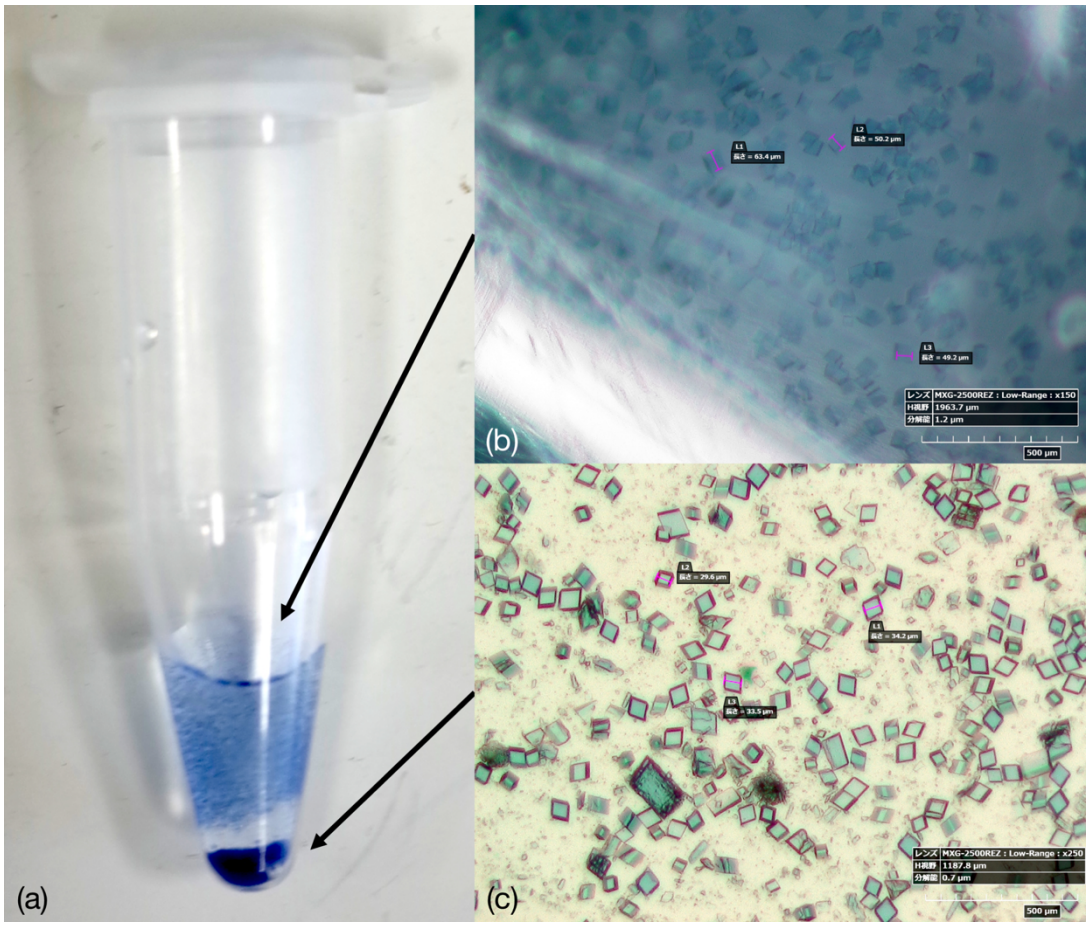

Figure 4.4. The microcrystallisation of *Ax*NiR. (a) Two microcrystal species were present 30 minutes after layering protein and precipitant; a top layer (b) containing crystals ~60 μm in size and a sedimented layer (c) ~15 μm in size. Crystals in the sedimented were selected for SFX data collection trials.

Using the FID method to crystallise *Ax*NiR microcrystals was rapid at producing crystals but they needed to be removed from the supersaturate zone before they grew too large for the injector system. Optimal crystal size for SFX data collection at SACLA was suggested to be between 10 - 30 μm with a crystal density of 10^7 – 10^8 crystals/ml[140]. A smaller crystal size is recommended to reduce the sample flow rate as a smaller nozzle can be used for injection. The smaller crystals sedimented at the correct density for SFX using the Diverse application platform for hard X-ray diffraction in SACLA (DAPHNIS)[190]. Low speed centrifugation was used to collect the crystals once they reached a size of ~20 μm across, removing them from the protein-precipitant interface and preventing further crystal growth.

To successfully inject the crystals into the XFEL beam, a suitable crystal-carrying matrix was required. For membrane proteins, the lipid cubic phase they are crystallised in can be used as the injector carrier[143] but for soluble proteins, a carrier must be introduced. A grease-matrix carrier has been shown to maintain soluble protein stability under ambient condtitions[140]. To test the stability of the microcrystals in the grease matrix, a 10 μl of crystal suspension was mixed with the grease matrix on a flat surface using a spatula. The mixture was then placed on a cover slide with a slip and observed under the microscope. The crystals were visually unaffected by the grease after 0, 1 and 6-hour intervals.

To test the crystal diffraction, 10 μl of crystal suspension was mixed with the grease matrix. The mixture was loaded into the wide end of a quartz capillary tube and squeezed into the narrow section using more grease. This

was left for 4 hours to check for visual crystal degradation. The capillary was then placed on the goniometer of a Rigaku FR-E+ Superbright microfocus rotating anode generator with a Rigaku R-AXIS V image plate detector. The capillary was exposed for 3 minutes. The crystals were weakly diffracting with the highest resolution being 2.8 Å after exposure. The same protocol was then used to test the microcrystals in grease matrix at BL32XU where they diffracted to 1.8 Å at RT without grease and RT with grease (Figure 4.5). As the microcrystals showed no decrease in diffraction power, they were considered ready for SFX data collection at SACLA.

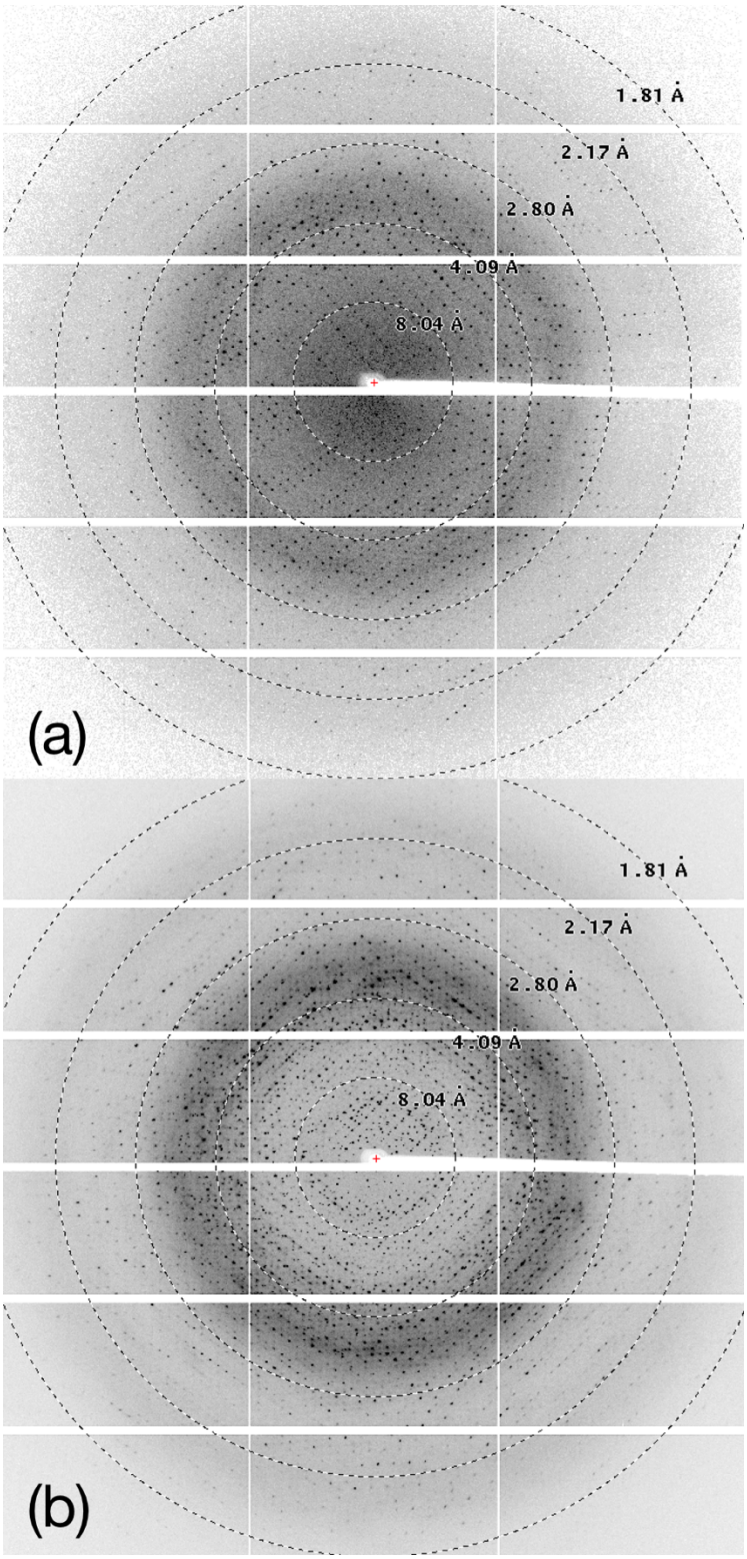

Figure 4.5. *Ax*NiR microcrystal test diffraction. (a) Single image collected without using grease matrix. Maximum resolution spots were visible at 1.8 Å. (b) After the addition of grease, no decrease in diffraction power or spot count was observed. Single shot diffraction images collected at BL32XU at RT.

4.2.2. SFX data collection

SFX data collection was carried out at SACLA BL3 EH4[191]. 60 µl of *Ax*NiR microcrystals suspension grown in 35% (w/v) PEG 550 MME, 20 mM $ZnSO_4$, 50 mM MES-OH, pH 6.5 were passed through a 20 μm micro-filter. The suspension was mixed with 40 µl grease-based matrix on a flat surface with a spatula[140]. The mixture was packed in an injector syringe with internal nozzle aperture diameter of 110 μm and external nozzle aperture diameter of 210 μm. The injector was installed in the helium ambiance, diffraction chamber enclosure, DAPHNIS[190]. The grease extruded with a pump set at 0.1 MPa pressure and was focused with a helium jet to produce a flow rate of 0.5 µl/min. The sample chamber was maintained at a temperature of 293 K with a relative humidity of 85%. SACLA X-ray wavelength was set at 7 keV with a pulse energy of ~456 μJ/pulse. The X-ray beam was focused to 1.5 × 1.5 µm^2 by Kirkpatrick-Baez mirrors on the midpoint of the extruded grease[192]. The XFEL pulses were of <10 fs duration and consisted of 7 × 10^{10} photons/pulse. The beam was attenuated with 10 mm Al. The repetition rate was 30 Hz and the diffraction data were collected with multiport CCD detector (MPCCD) with a camera length of 50 mm[172]. Diffraction resolution was limited to 2 Å due to the crystal to detector distance imposed by the DAPHNIS chamber (Figure 4.6). The experiment lasted 180 minutes and 312,972 snapshot images were collected in total.

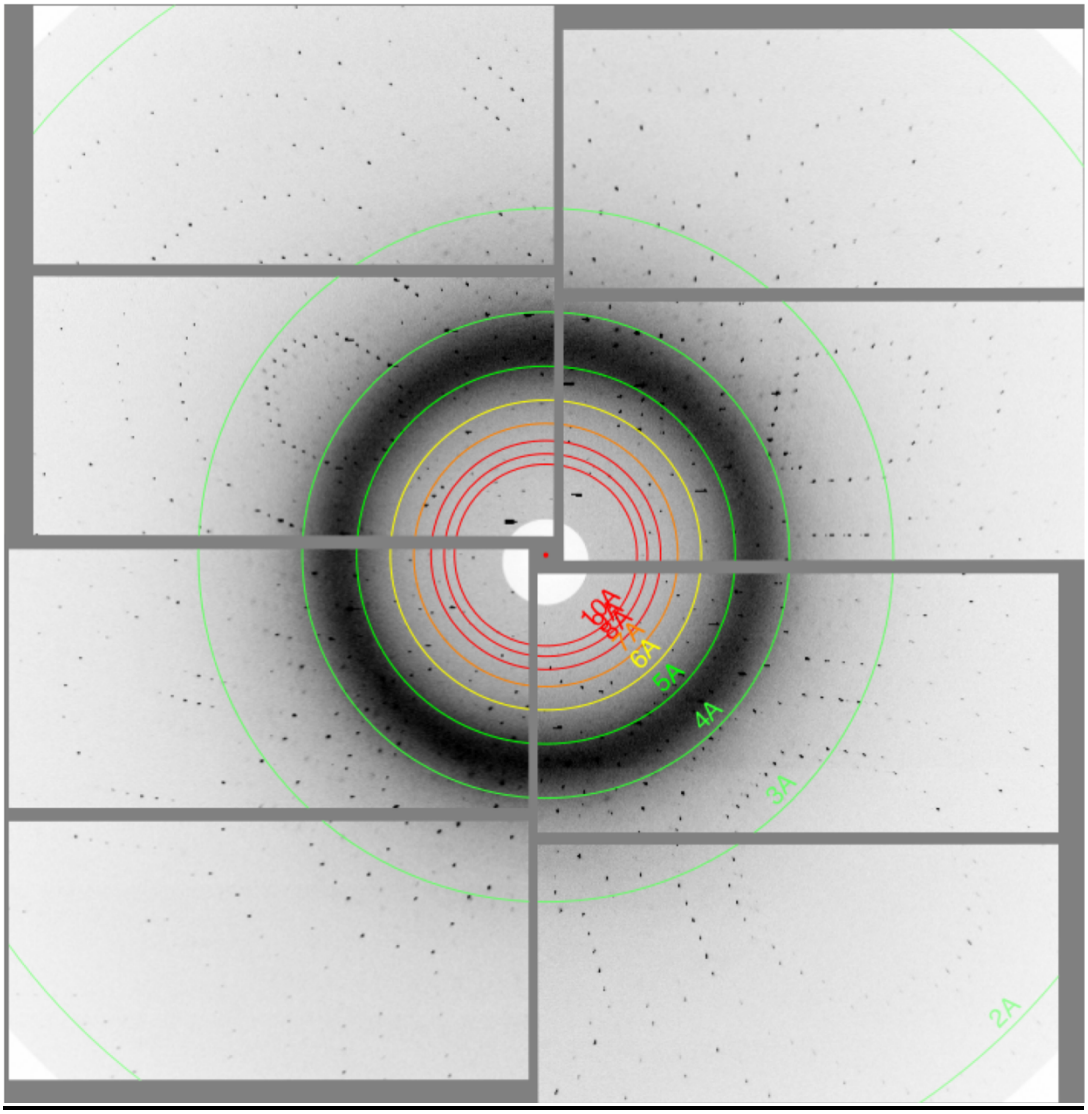

Figure 4.6. A snapshot diffraction image collected from an *Ax*NiR microcrystal. The eight distinct panels of the MPCCD are clearly visible. Diffraction spots can be seen at the edge of the detector at 2 Å. The image was collected at SACLA BL3 EH4.

4.2.3. SFX data processing

Cheetah[164] was used to check for hits in real time with images containing <15 Bragg reflections rejected. This produced a total of 102,968 diffraction images equating to hit rate of 32.9%. This real time image processing was achieved with the online stage of the SACLA data processing pipeline[160,165]. The diffraction images were processed using *CrystFEL*[161]. Spot-finding was carried out using the inbuilt algorithm *zaef*. *CrystFEL* called on *DirAx*[167] for indexing the snapshot images in space group H3 (Figure 4.7). Of the 102,968 image hits, 61,163 were able to be indexed corresponding to a 59.4% indexing rate. The inner, middle and outer integration radii were set to of 3, 4 and 7 pixels respectively. H3 is known to have a twin operator *h,k,-l* and this was used to resolve the indexing ambiguity using *ambigator*[170] (Figure 4.8). Partial reflections were then merged from the successfully indexed crystals using the Monte Carlo method with frame scaling[174]. Data were cut-off at 2.1 Å based on a $CC_{1/2}$ value of ~0.3 and a R_{split} value of 81.2 % in the outer shell (Figure 4.9).

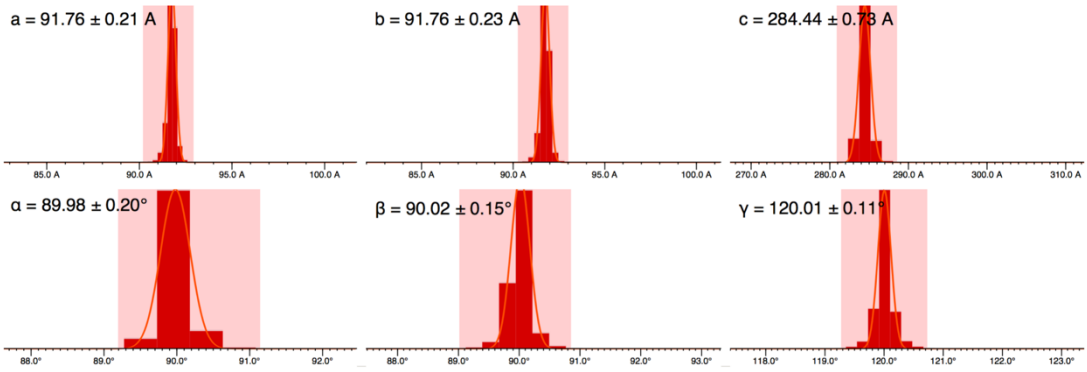

Figure 4.7. The distribution of unit cell parameters from *Ax*NiR microcrystals. The unit cell lengths and angles from individually indexed snapshots from *indexamajig* displayed as a distribution. Red colouring represents these parameters that fall into a H centred space group. The average unit cell parameters are shown as a normal distribution.

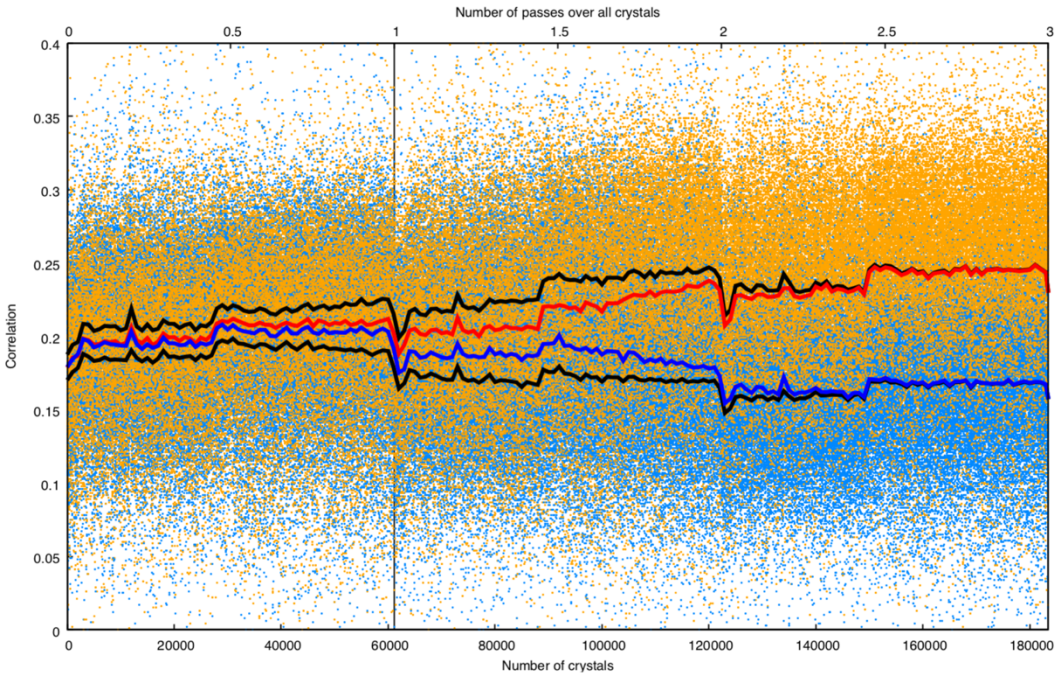

Figure 4.8. Resolving the indexing ambiguity in *Ax*NiR microcrystals. The program *ambigator*[169,170] calculates correlation coefficients between the current crystal intensity and all other crystal intensities in a turn-by-turn manner, shown by blue and orange dots. The mean of the correlation coefficient is taken over all crystals which have the same indexing assignment (*f*, blue) as the current pattern while a second mean is taken over all crystals which have indexing assignments opposite to the current crystal (*g*, orange). The indexing assignment is then changed for each crystal if $g > f$. Three iterations of *ambigator* were run with operator *h,k,-l*. The two mixed indexing solutions were separated into two clusters shown by the red and blue lines showing the smoothed moving average values of *f* and *g*, respectively. The upper and lower black lines show the smoothed moving average values of whichever of *f* or *g* is greater or lower, respectively, for the current crystal which should converge on the average values of *f* and *g*.

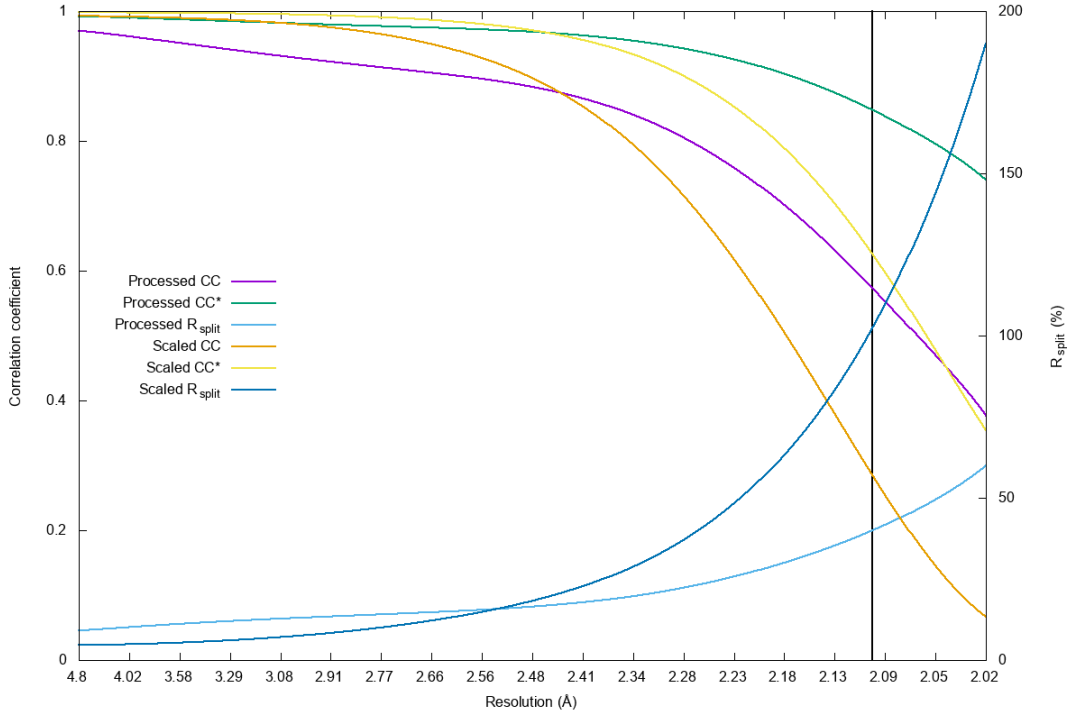

Figure 4.9. SFX data processing of *Ax*NiR. Graph shows the values for CC, CC* and R_{split} for *Ax*NiR SFX data collection. The 2.1 Å cut-off is shown with a vertical black line. A comparison is made between the merged individual intensities with and without frame scaling.

4.2.4. SFX structural determination

Intensities from *CrystFEL* were converted to amplitudes using *CTRUNCATE*[193]. The phase problem was solved using *MOLREP*[194] with the *Ax*NiR monomer used as the starting model (PDB: 1OE1)[51]. Two copies of the *Ax*NiR monomer were located in the asymmetric unit (Figure 4.10, 4.11). Refinement was performed by *REFMAC5*[195] in the *CCP4*[193] suite with riding H atoms and isotropic B factors. The *Coot*[196] graphics interface was used for manual model rebuilding and water addition in between each cycle of refinement. The data-processing and refinement statistics for the SFX structure are given in Table 4.1 After the first round of refinement, R_{work} did not drop significantly as would be expected for this good a starting model. The electron density around the main chain and copper sites looked reasonable but no density was visible for any solvent molecules (Figure 4.12). After three rounds of refinement, the data were checked for intensity anomalies. After performing the L-test[188], it was determined that the data had close to a 0.4 twinning fraction (Figure 4.13). Refinement was re-run using twin refinement with R_{work} reaching a minimum of 35%. *REFMAC5* determined the twin fraction to be 0.3 but no improvement in the R_{work} could be achieved. The fast rate of crystal growth led to widespread crystal twinning and prevented structural determination. In light of this, it was determined that SFX was not a viable structural determination method for *Ax*NiR crystals and that other femtosecond crystallographic data collection techniques would be more appropriate.

Table 4.1. Data processing and refinement statistics for *Ax*NiR collected by SFX.

	SFX
Data collection	
Space group	H3
Unit cell dimensions	
a=b, c (Å)	91.80, 284.10
α=β, γ (°)	90, 120
Resolution (Å)	22.95 – 2.10 (2.12 – 2.10)[a]
R_{split} (%)	6.3 (81.2)[a]
$<I/\sigma(I)>$	11.0 (1.38)[a]
$CC_{1/2}$	0.996 (0.342)[a]
Completeness (%)	100.0 (100.0)[a]
Multiplicity	629.0 (169.6)[a]
Wilson B-factor ($Å^2$)	45.8
Refinement	
No. of unique reflections	52146 (2648)[a]
R_{work}/R_{free} (%)	35.3/36.5
R.m.s deviations	
Bond length (Å)	0.091
Bond angles (°)	1.396

a. The highest resolution shell is shown in parenthesis.

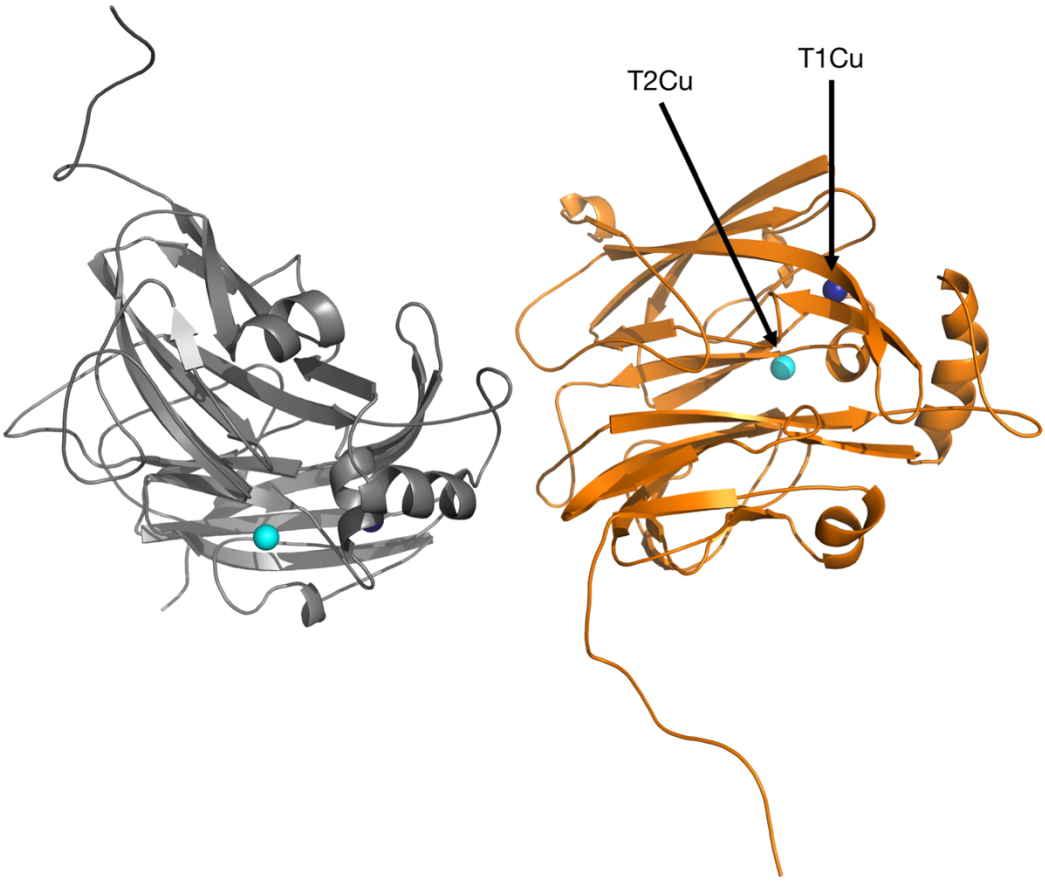

Figure 4.10. Molecular replacement solution of SFX *Ax*NiR. Two copies of the *Ax*NiR monomer were present in the asymmetric unit. The T1Cu and T2Cu coppers are shown in dark blue and cyan respectively.

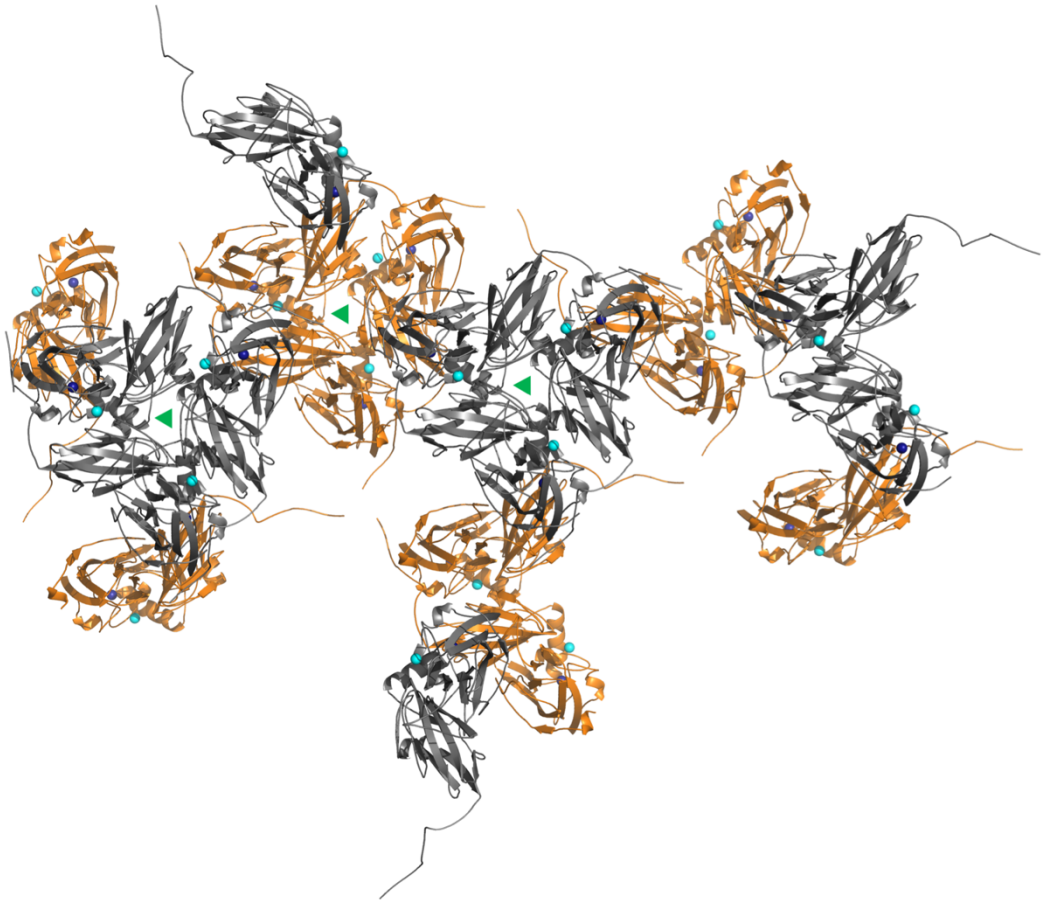

Figure 4.11. Crystal packing in H3 *Ax*NiR microcrystals. The functional trimer is formed three times with all symmetry mates within a cut-off of 12 Å. The 3-fold symmetry is shown with green triangles. The formation of the biological assembly suggested that this is the correct molecular replacement solution.

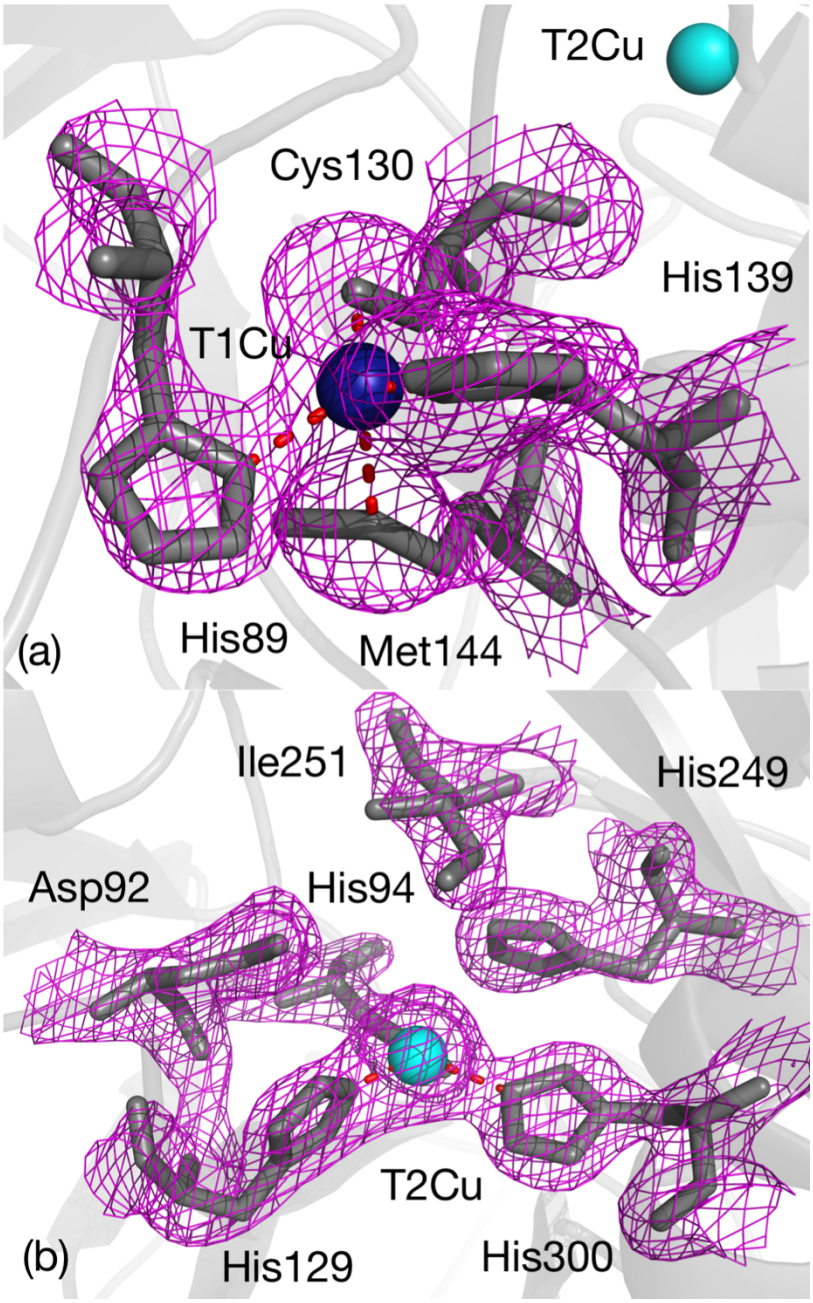

Figure 4.12. The copper sites of *Ax*NiR determined by SFX. (a) The T1Cu site showing His_2-Cys-Met ligation. (b) The T2Cu with His_3 ligation. No water molecules are present ligated to the T2Cu or bound between Asp_{CAT} and His_{CAT}. The map showed a lack of viable solvent electron density due to the input model biased refinement against twinned intensity data. $2F_o$-F_c electron density is contoured at 1σ level and shown as magenta mesh. T2Cu as a cyan sphere and metal coordinating bonds are shown as red dotted lines.

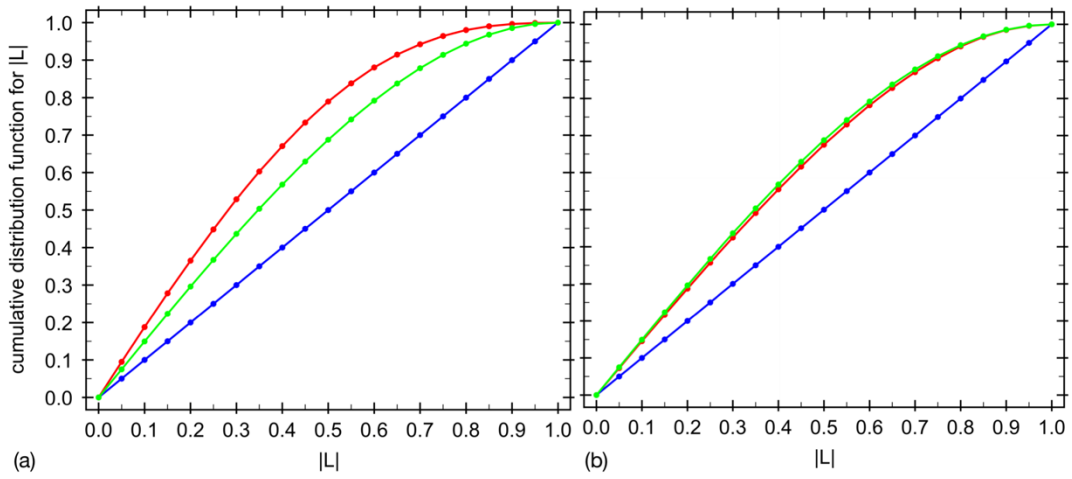

Figure 4.13. L-test results from *Ax*NiR SFX data collection. Intensity statistics show for SFX data (a) before and (b) after running the stream though *ambigator* with operator *h,k,-l*. Cumulative distribution function for |L| observed shown in red, expected (untwinned) in blue and expected (twinned) in green. The L test revealed the crystals were highly twinned even after the resolution of the indexing ambiguity.

4.3. SF-ROX data collection

4.3.1. Batch crystallisation

After the failure to determine the radiation damage-free structure using SFX, the SF-ROX data collection method was attempted to overcome the problems with crystal twinning. SF-ROX data collection required that *Ax*NiR crystallisation be optimised to produce numerous, large, homogenous *Ax*NiR crystals. To increase the overall size of the crystals, a fine screen was carried out over the crystallisation conditions already recorded; 5 – 40 % (w/v) PEG 550 MME, 5 – 50 mM $ZnSO_4$, 10 – 200 mM MES-OH, pH 6.5. An increase in MES concentration caused crystals to grow longer and more like 2D plates then 3D cubes (Figure 4.14). Decreasing the concentration of PEG and $ZnSO_4$ slowed down crystallisation time but lead to the formation of large 2D plates such as Figure 4.14d which were optimal for SF-ROX. However, a number of problems complicated the consistent production of these homogenous crystals.

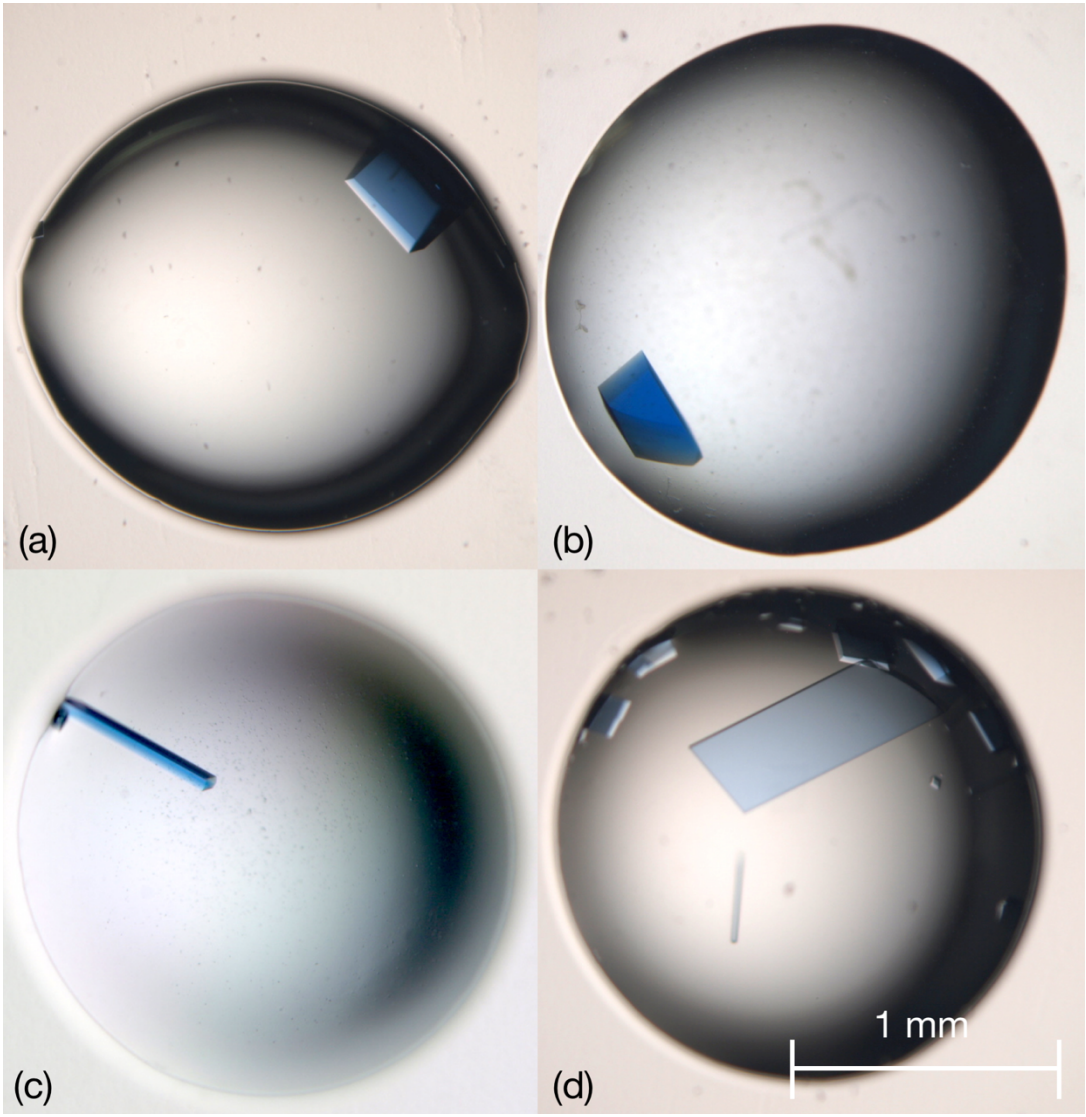

Figure 4.14. Batch crystallisation of *Ax*NiR for SF-ROX experiments. Conditions were; (a) 30% (w/v) PEG 550 MME, 20 mM $ZnSO_4$, 40 mM MES-OH, pH 6.5; (b) 15% (w/v) PEG 550 MME, 30 mM $ZnSO_4$, 60 mM MES-OH, pH 6.5; (c) 15% (w/v) PEG 550 MME, 20 mM $ZnSO_4$, 50 mM MES-OH, pH 6.5; (d) 10% (w/v) PEG 550 MME, 10 mM $ZnSO_4$, 100 mM MES-OH, pH 6.5. Higher MES concentration along with lower PEG and $ZnSO_4$ concentrations lead to the growth of large (~1 mm) 2D crystal plates (d).

Like the *Ax*NiR microcrystals, the batch crystals had a propensity to grow as perfect or near-perfect twins in space group H3, a trigonal space group with twin operator *h, k, -l*. Crystals set according to published methodology grew regularly with near perfect twinning fractions, a trait not previously observed[62]. Twinning on this scale severely hampered attempts to optimise crystal growth for SF-ROX experiments. To determine the cause the crystal growth rate was slowed, allowing only one nucleation point to form, allowing the crystal should grow with a single ordered lattice. To slow down the rate of crystal growth, crystal trays were set with a lower protein concentration (10 → 8 mg/ml) and at a lower temperature (25 °C → 4 °C). Datasets from each crystal were collected to 2.4 Å using an in-house source and were processed using *XDS*[168]. *phenix.xtriage* was used to quickly assess the collected intensities and determine the level of twinning[197]. The result, given as a Mahalanobis distance from expected untwined intensity values, suggests twinning above a threshold of 3.5 in the program[198]. In total 80% of the datasets collected from crystals set in the H3 conditions were twinned with Z-scores all above 15, suggesting perfect twins. Of those over 65% were from crystals set at room temperature and 10 mg/ml protein concentration. Growing at 4 °C reduced the percentage of crystals twinned to 4% while reducing the protein concentration to 8 mg/ml lead to a twinning rate of 11%. Together, these measures allowed the growth of H3 *Ax*NiR crystals that showed no sign of twinning. It was found that if one crystal in one plate well was twinned then generally all other crystals in the plate were twinned.

Therefore, checking a single crystal from a plate could be used to predict the condition of the others.

Over the course of scaling up the production of *Ax*NiR crystals for SF-ROX, a second problem with the crystallisation conditions was discovered. As crystals were screened for signs of twinning in the tray, two separate species of the H3 crystal form were identified. The first was the same as from the microcrystals with a unit cell *c* length of ~ 288 Å. In this form, two copies of *Ax*NiR monomer were present in the asymmetric unit. The second had a unit cell *c* length of ~ 144 Å, exactly half the first species with only a single *Ax*NiR monomer in the asymmetric unit although with different unit cell packing (Figure 4.15). The presence of both these forms in the same drop presented a problem for serial crystallography where snapshots from multiple images must be merged to form the complete dataset. The probability of crystals to grow with two c unit cell lengths appeared to be dependent on PEG concentration with high PEG concentration (>25 %) produced the *c* ~ 288 Å variant and low PEG concentration (<15 %) produced the *c* ~ 144 Å variant. The *c* ~ 144 Å variant tended to diffract to slightly higher resolution and so this along with the efforts to remove twinning resulted in an optimum crystallisation condition of 10 % (w/v) PEG 550 MME, 10 mM $ZnSO_4$, 100 mM MES-OH, pH 6.5 (Figure 4.16) (Table 4.2).

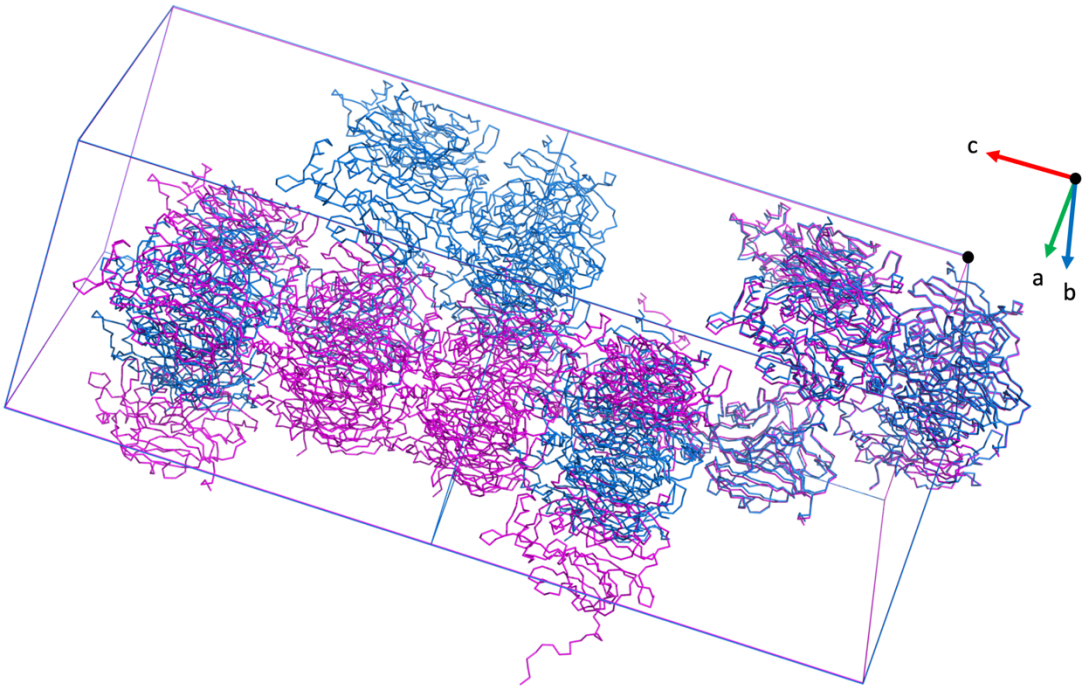

Figure 4.15. Crystal packing in H3 crystals. The unit cell packing of crystals with *c* cell lengths of ~ 288 Å and ~ 144 Å are compared. The contents of the *c* ~ 288 Å unit cell were generated (magenta) and aligned with two copies of the *c* ~144 Å unit cell (blue) in the *c* direction. The monomers matrices at the origin are aligned in the right of the picture but the other contents of the unit cell do not overlap showing differing unit cell packing. The biological trimer assembly is formed from the crystal packing in both unit cells. The origin and cell axes are indicated by the black dot.

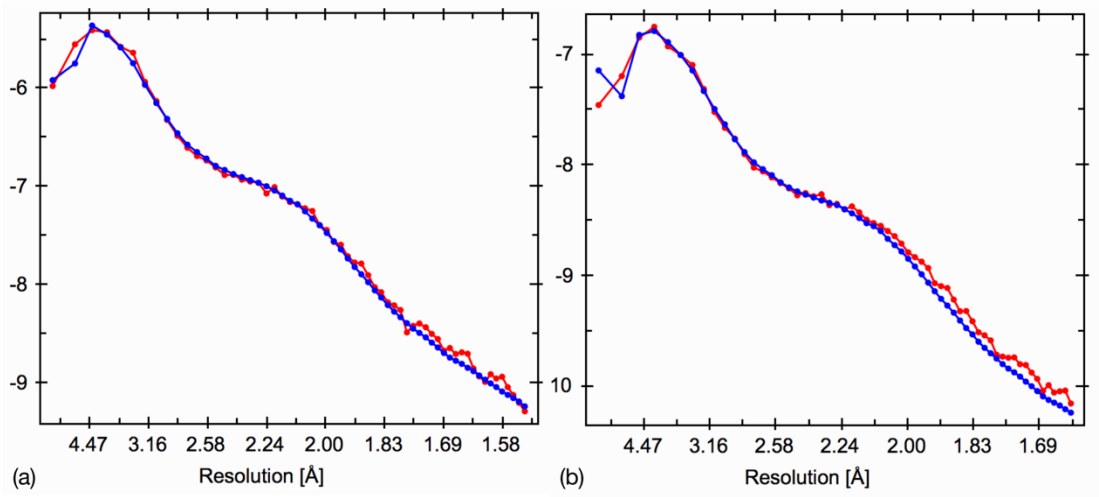

Figure 4.16. Wilson plots for the *Ax*NiR processed in space group H3. (a) Data merged in H3 with c~288 and (b) c~144. Spot intensity tails off as resolution increases with a linear relationship at higher resolution. The peak at 4 Å relates to the distribution of interatomic spacings in polypeptides with an increased number of such spacings.

Table 4.2. Data processing and refinement statistics for two *Ax*NiR crystal species.

Data collection		
Wavelength (Å)	0.98	0.98
Space group	H3	H3
Unit cell dimensions		
a=b, c (Å)	89.53, 288.22	89.96, 144.12
α=β, γ (°)	90, 120	90, 120
Resolution (Å)	46.3 – 1.63 (1.66 – 1.63)[a]	45.0 – 1.54 (1.57 – 1.54)[a]
$R_{p.i.m.}$ (%)	7.0 (34.3)[a]	5.8 (40.9)[a]
$<I/\sigma(I)>$	5.8 (1.7)[a]	7.6 (1.6)[a]
$CC_{1/2}$	0.987 (0.752)[a]	0.998 (0.706)[a]
Completeness (%)	98.4 (98.4)[a]	99.2 (96.5)[a]
Redundancy	2.9 (2.4)[a]	2.8 (2.2)[a]
Wilson B-factor ($Å^2$)	16.4	16.7
No. of molecules in ASU	2	1
Refinement		
No. of unique reflections	105832 (5240)[a]	63897 (3112)[a]
R_{work}/R_{free} (%)	15.7/17.3	18.7/21.4
R.m.s deviations		
Bond length (Å)	0.013	0.014
Bond angles (°)	1.609	1.745

a. The highest resolution shell is shown in parenthesis.

*Ax*NiR crystals for SF-ROX were grown using the hanging drop vapour diffusion method. The as-isolated enzyme was transferred to 10 mM Tris-HCl, pH 7.1 and concentrated to 10 mg/ml. Crystals were grown in 24 well Hampton crystallisation trays at 4°C with 150 trays set in total to produce the large number of crystals required for data collection. Trays were set with a 400 µl well volume containing 10% (w/v) PEG 550 MME, 10 mM ZnSO4, 100 mM MES buffer, pH 6.5. 2 µl of crystallisation mixture was mixed with 2 µl protein solution on a cover slide. Crystals reached their maximum size after one week and were stored ready for data collection. The crystals were soaked in 35% (w/v) PEG 550 MME, 10 mM $ZnSO_4$, 100 mM MES buffer, pH 6.5 for 60 s before freezing by plunging into liquid nitrogen. The crystals had average dimensions of size 1 x 0.8 x 0.05 mm with a 2D plate morphology with crystals smaller than this or of incorrect morphology rejected. Crystals that had lost their bright blue colour were also rejected. Crystals were stored in canes in liquid nitrogen and then transferred to Uni-Pucks ready for data collection. In total, 111 crystals of appropriate size, morphology and oxidation state were grown, frozen and stored for the SF-ROX experiment.

4.3.2. Initial SF-ROX test data collection

To test the efficacy of the large *Ax*NiR crystals, a series of 32 images were collected at SACLA BL3 EH4 from a single *Ax*NiR crystal (Figure 4.17a). This also provided an opportunity to see the physical effect of the XFEL pulse on the crystal and to plan for the data collection strategy. The X-ray energy was set to 10 keV and the pulses were of <10 fs duration. With the beam focused on the crystal, the high energy X-ray pulses drilled holes through the protein crystal and subsequently cracked the entire crystal and so positioning the crystal downstream of the beam focal point was recommended for complete data set collection. Two datasets were collected from the same crystal, going over the same exposure points to assess the propagation of radiation damage in the *Ax*NiR crystals after XFEL exposure based on the protocol described here[126]. A point in the crystal was exposed to the unattenuated XFEL beam. For both cytochrome *c* oxidase[126] and photosystem II[199] crystals from which SF-ROX data collection had already been tested, no perceptible radiation damage could be detected 11 µm beyond the original unattenuated hit. To avoid the spread of radiation damage in the crystal, the final agreed upon translation distance was 50 µm between snapshots. Consistent with this advice, 32 images were collected for the first test dataset with a 50 µm translation and 0.1° rotation of crystal between the images. The 32 images had an average number of 425 reflections per image. The beam was then highly attenuated with 1 mm Al and a second dataset was collected over the same spots to observe the effects of the XFEL pulse. The average number of reflections per image dropped to 98. Because the diffraction

images are collected with a known rotational step in between, the images could be processed using standard MX data processing software, in this case *XDS*[168]. This allows for a consistent sampling of the diffraction data, increasing data quality[126]. *XDS* recorded a data completeness of 18% for the first 32 images. A significant diffraction signal (>1σ) was present at 2.7 Å (Figure 4.17b). Processing of the second dataset reduced the limit to 3.6 Å (Figure 4.17c).

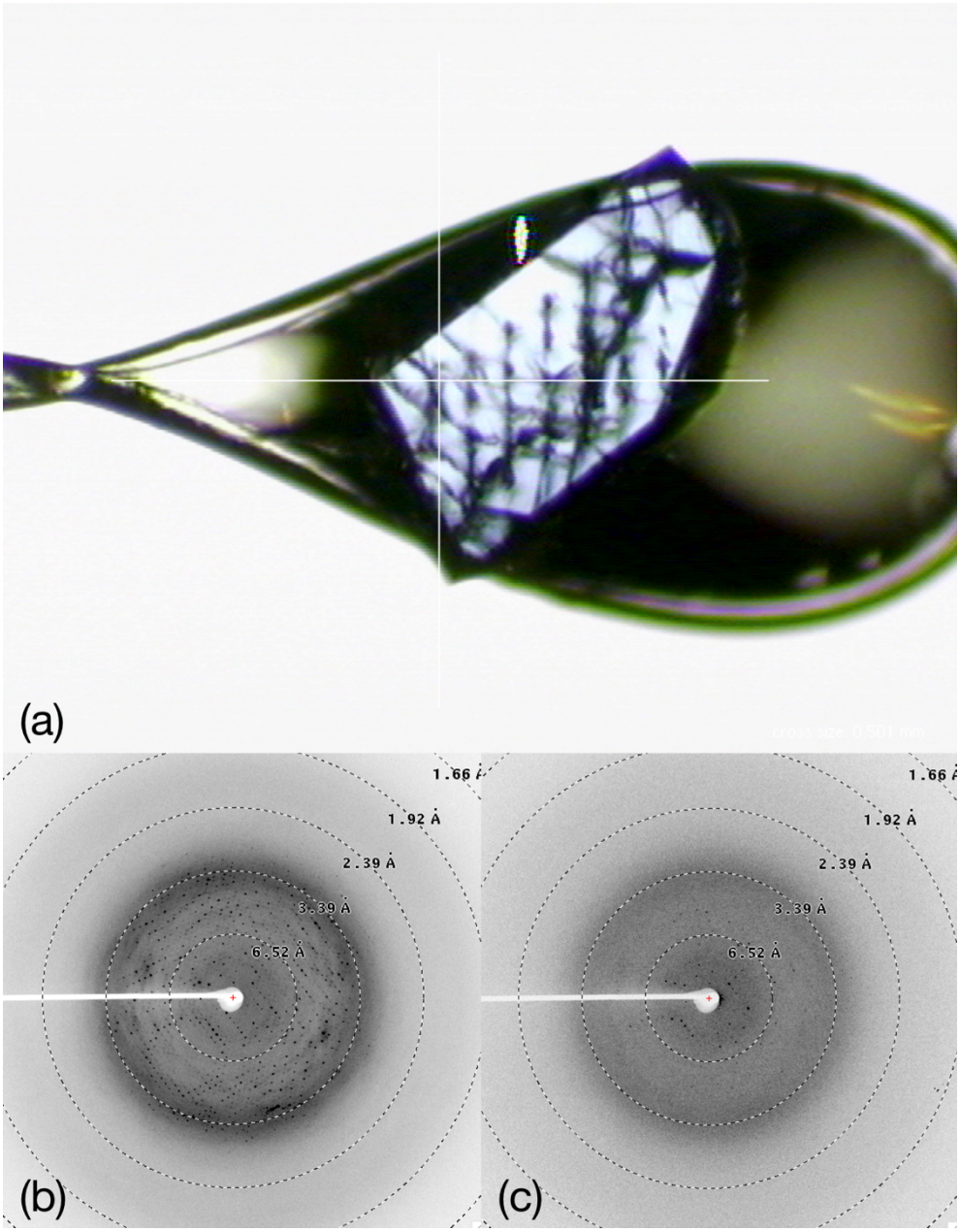

Figure 4.17. SF-ROX test *Ax*NiR crystal. (a) A large crystal of *Ax*NiR (0.8 x 0.4 x 0.05 mm) in a cryoloops after data collection at SACLA BL3 EH4. The crystal contains a series of holes, drilled by the XFEL, 50 µm apart. After full data collection, the crystal was full of major cracks. A diffraction pattern from the crystal (b) after full intensity XFEL exposure with diffraction spots observed at a maximum of 2.7 Å and (c) a second exposure with a maximum resolution of 3.6 Å.

4.3.3. SRX data collection and processing

A comparison dataset was collected from one of the *Ax*NiR batch grown crystals to determine the effects of radiation damage on the enzyme. Atomic resolution structures of *AxNiR* exist but it was necessary to have a comparison collected from the same protein stock, the same crystal batch and at the same X-ray wavelength[51]. Data collection took place at SPring-8 BL41XU, chosen because of its high X-ray flux and tuneable beam energy[92]. Data collection at SACLA would be at 10 keV so the beam energy of BL41XU was set to the same. A single frozen crystal was mounted on the goniometer and centred. 360 images were collected from the crystal using PILATUS 6M detector in shutterless mode which took a total of 72 s for the full data set. The beam size was set to 44.0 (H) x 12.0 (W) µm with photon flux 1.5 x 10^{13} photons/s and beam attenuation of Al 460 µm.

The images were processed using *XDS*[168] in space group H3. Data reduction and scaling was carried out in the *CCP4* suite[193] using *AIMLESS*[200]. 5% of reflections were selected to be used for R_{free} and not used for refinement. The resolution limit was cut-off at 1.6 Å based on $CC_{1/2}$~0.5. The phases were determined using molecular replacement with *MOLREP*[194] using the *Ax*NiR monomer (PDB: 1OE1) as the model[51]. Refinement was performed using *REFMAC5*[195] with riding hydrogen atoms and isotropic B-factors. *Coot*[196] graphic interface was used for manual model rebuilding and water addition in between each cycle of refinement. The quality of the final model was checked using *MolProbity*[201]. All data processing and refinement statistics for SRX structures are shown in Table 4.3.

4.3.4. Full SF-ROX data collection

Full SF-ROX data collection was carried out at the SACLA XFEL's BL3 EH4[191]. Crystals were maintained at 100 K before and during data collection and loaded sequentially onto the goniometer using the SPACE sample changer[202]. As observed in the test, focusing the XFEL pulses onto the crystal caused significant damage to the protein crystal before data collection could be completed, wasting crystal stock and beamtime. After one exposure at the focus position, with a beam size of 2.0 (H) x 1.3 (W) µm, most crystals cracked after a few shots with some being ejected from the loop entirely. The beam focus was then moved 15 mm downstream of the focal point to produce a flux of 3 x 10^{10} photons and beam size of 3.0 (H) x 1.9 (W) µm. With the beam defocused on the crystal, the crystals no longer cracked during data collection with only evidence of exposure, a lattice of small 'drilled' holes with 50 µm spacing (Figure 4.18).

Because of the crystal morphology, they mounted consistently in large cryoloops, flat to the plane of the loop. This enabled the rotation range to be matched from crystal to crystal resulting in the high completeness of dataset (Table 4.3). The first crystal was mounted and orientated so the flat plane of the crystal was square on to the online camera. This orientation was then defined as 0° ϕ. The four corners of the crystal were then centred individually to maximise the number of images that could be collected from each crystal. After the corners were defined, the starting ϕ was selected and the number of images that could be collected from the crystal was calculated. This was then written out as several data collection strategies running from the top to the

bottom of the crystal with 50 μm in between before translating 50 μm horizontally and beginning the next data collection run. If 50 images could be collected from the first crystal, then the crystal would have rotated 5° by the end of data collection. Therefore, the start ϕ for the next crystal, orientated in the same manner, was set to 5° with the face on position set at 0°. This was then repeated until the total rotation reached +60° at which point the start ϕ was changed to -60° and the rotation moved back towards 0°. This allowed for the crystal diffraction to be sampled consistently. After the crystal rotated more than ±60° a very small number of images could be collected from each crystal due to the morphology (thin face exposed to beam) of the crystal.

For data collection, the photon energy was set to 10 keV with an X-ray pulse length of less than 10 fs. The camera length was set to 120 mm, the minimum distance the geometry of the diffractometer would allow, but the crystals still diffracted to the edge of the detector (Figure 4.19). The crystals were rotated 0.1° between each snapshot equalling approximately one-third of the *Ax*NiR crystal's mosaicity determined from the synchrotron dataset collected previously. In total, 4403 single shot images were collected from 64 crystals over the course of 10 hours. A RAYONIX MX225-HS CCD detector was used with 2x2 binning mode corresponding to the pixel size of 78.2 µm. Of the 4403 images, 3656 with sufficient diffraction spots (>15) were selected for data processing. Analysis of the diffraction intensities was carried out online using *DISTL*[203].

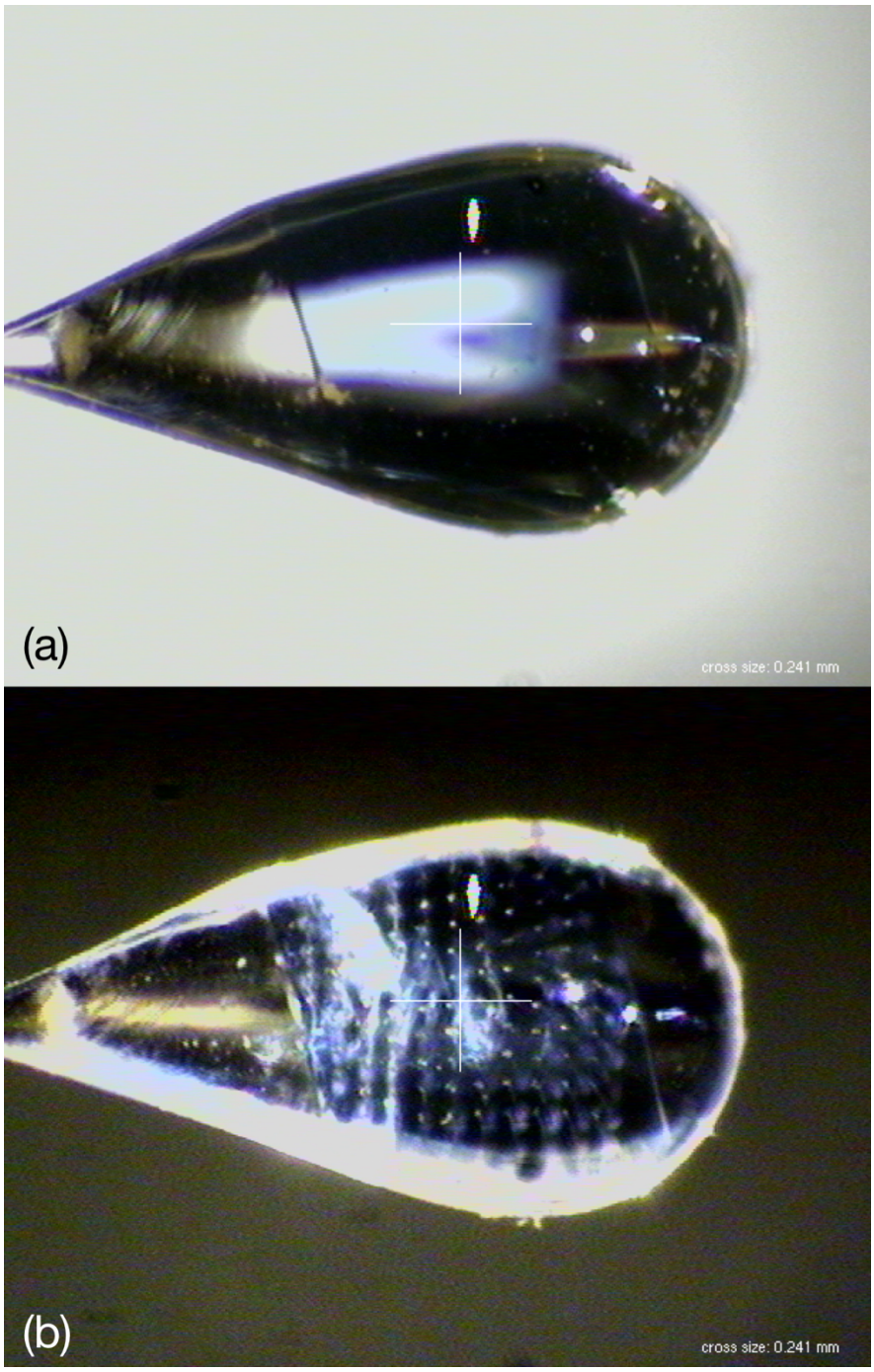

Figure 4.18. *Ax*NiR SF-ROX XFEL exposure. The *Ax*NiR crystal is shown (a) before and (b) after exposure to the XFEL pulses. The crystal size is 1 x 0.7 x 0.08 mm with the blue colour revealing the oxidation state of the copper site. Holes drilled by the XFEL are visible corresponding to the top left to bottom right data-collection strategy. Each hole is 50 µm apart, with a 0.1° rotation between each snapshot.

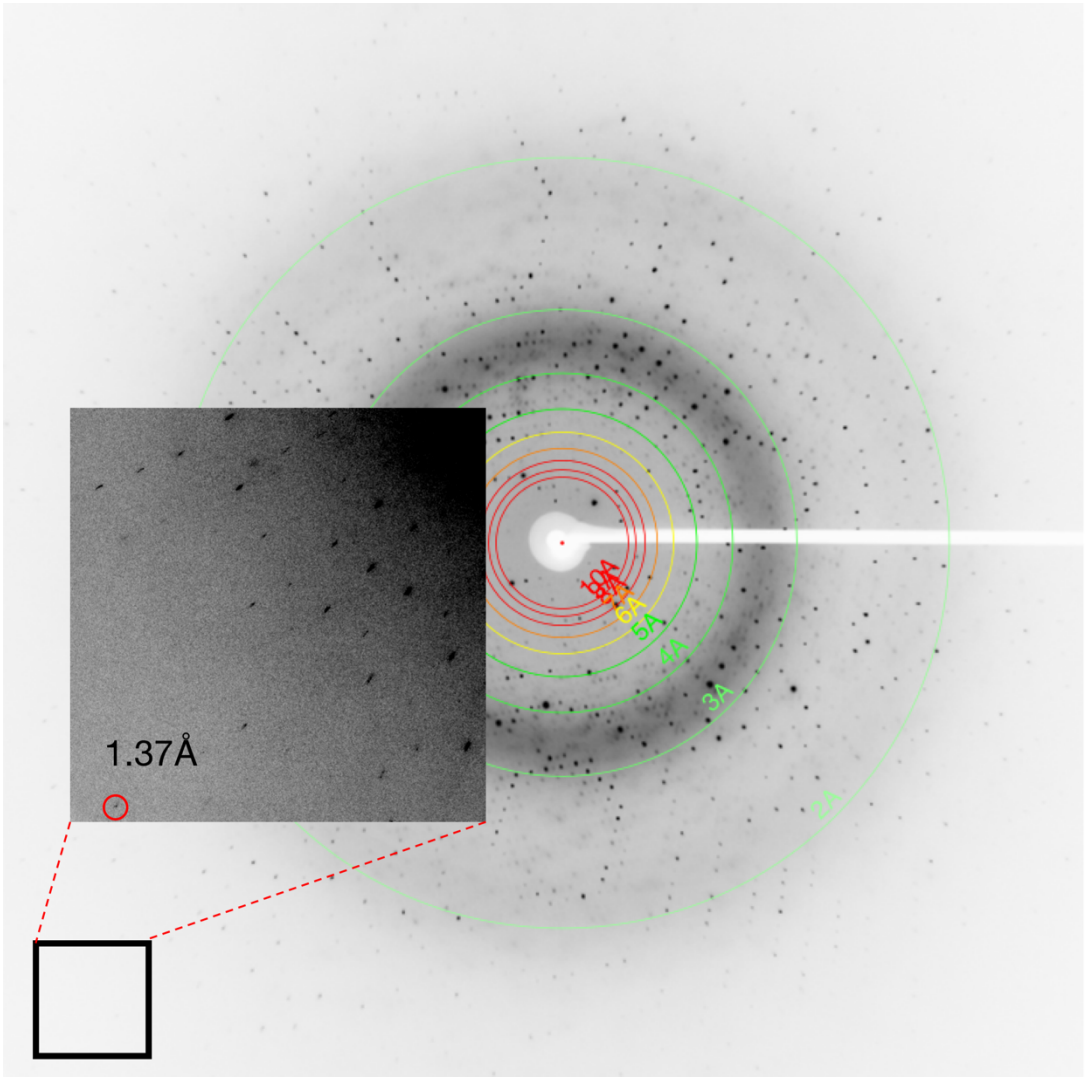

Figure 4.19. A snapshot diffraction image from an *Ax*NiR crystal. Zoomed in section shows diffraction spots at the edge of the detector at 1.37 Å. Collected on a RAYONIX MX225-HS CCD detector with 2x2 binning mode.

4.3.5. SF-ROX data processing

The diffraction images were processed using the *CrystFEL* suite[161]. *Indexamajig* was used for batch indexing and integration. Various trials were scripted and run in parallel on the SACLA HPC cluster to determine the best method and program choice for spot-finding and indexing.

```
test_merge_04/   --indexing=mosflm-nolatt-nocell --int-radius=3,5,7
test_merge_05/   --int-radius=6,7,8
test_merge_06/   beamstop shadow masked
test_merge_07/   --indexing=dirax
test_merge_08/   --indexing=asdf
test_merge_09/   --indexing=mosflm-nolatt-nocell --int-radius=5,7,8
```

test_merge_09 produced the best results using the inbuilt spot finding algorithm *zaef* and indexing carried out using *MOSFLM*[166] in space group H3 with a 95.8% indexing rate (Figure 4.20). The inner, middle and outer integration radii were set to of 5, 7 and 8 pixels respectively. *Ambigator*[170] was used to resolve the indexing ambiguity and Bragg intensities were merged using the Monte Carlo method with frame scaling (Figure 4.21, 4.22, 4.23). The resolution limit was set to 1.6 Å based on $CC_{1/2}$~0.5 in the outer shell. The structure was built and refined with the same method as the SRX structure and the refined SRX structure was used as the starting model for this refinement. The quality of the final model was checked using *MolProbity*[201]. Data processing and refinement statistics are shown in Table 4.3.

Table 4.3. Data processing and refinement statistics for *Ax*NiR collected by SRX and SF-ROX.

	SF-ROX	SRX^{RS}
Data collection		
Space group	H3	H3
Unit cell dimensions		
a=b, c (Å)	89.97, 143.56	90.35, 143.58
α=β, γ (°)	90, 120	90, 120
Resolution (Å)	19.84 – 1.60 (1.63 – 1.60)[a]	47.86 – 1.60 (1.63 – 1.60)[a]
R_{split} (%)	18.6 (77.2)[a]	
$R_{p.i.m.}$ (%)		7.5 (29.6)[a]
$<I/\sigma(I)>$	4.7 (2.0)[a]	5.1 (1.2)[a]
$CC_{1/2}$	0.975 (0.502)[a]	0.981 (0.782)[a]
Completeness (%)	100.0 (100.0)[a]	98.0 (97.8)[a]
Multiplicity	132.3 (47.0)[a]	
Redundancy		3.3 (3.1)[a]
Wilson B-factor ($Å^2$)	26.1	23.6
Refinement		
No. of reflections	57138 (5685)[a]	56521 (2791)[a]
R_{work}/R_{free} (%)	18.5/22.6	19.0/22.3
No. atoms		
Protein	2594	2578
Ligand/ion	42	40
Water	386	378
B-factors ($Å^2$)		
Protein	29.0	27.4
Cu	26.1	25.9
Zn	31.0	28.4
MES	49.2	46.0
PEG	39.1	44.5
Dioxygen	32.1	
Water	40.3	39.0
R.m.s deviations		
Bond length (Å)	0.015	0.018
Bond angles (°)	1.758	1.900
PDB access code	5ONX	5ONY

a. The highest resolution shell is shown in parentheses.

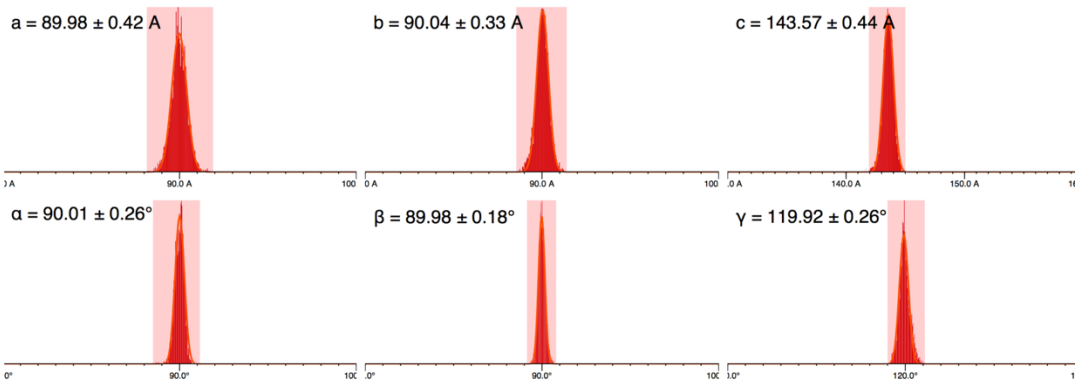

Figure 4.20. The distribution of unit cell parameters from *Ax*NiR crystals. The unit cell lengths and angles from individually indexed snapshots from *indexamajig*. Red colouring represents the parameters that fall into a H centred space group. The unit cell has a c=144 Å length corresponding to a single monomer in the asymmetric unit.

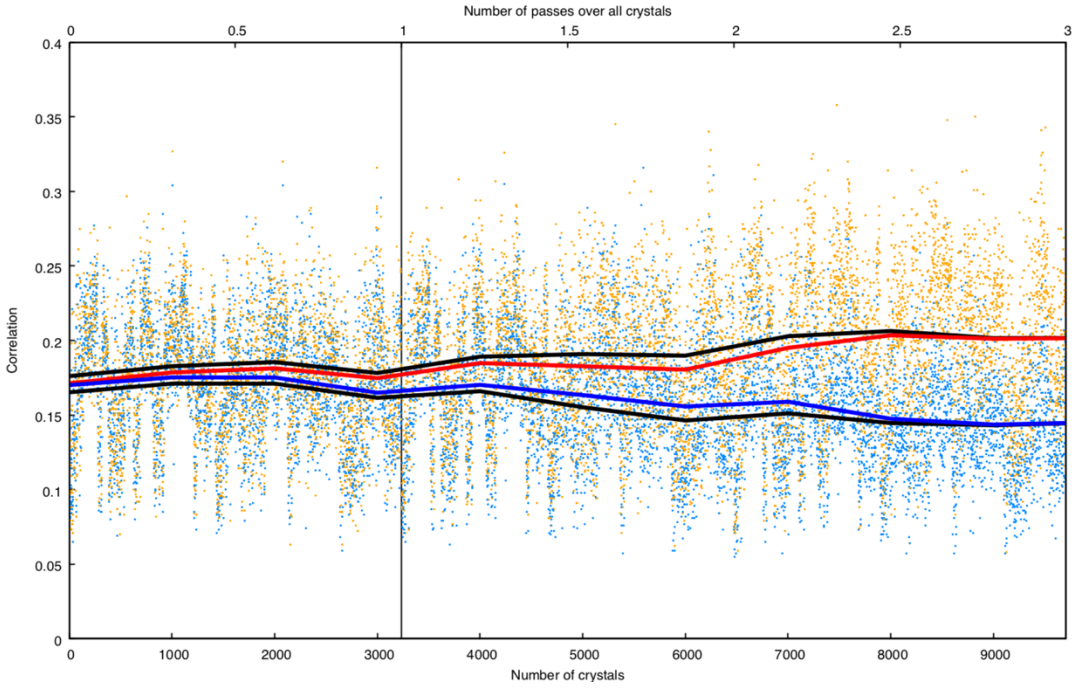

Figure 4.21. Resolving the indexing ambiguity in *Ax*NiR crystals. The program *ambigator*[169,170] calculates correlation coefficients between the current crystal intensity and all other crystal intensities in a turn-by-turn manner, shown by blue and orange dots. The mean of the correlation coefficient is taken over all crystals which have the same indexing assignment (*f*, blue) as the current pattern while a second mean is taken over all crystals which have indexing assignments opposite to the current crystal (*g*, orange). The indexing assignment is then changed for each crystal if $g > f$. Three iterations of *ambigator* were run with operator *h,k,-l*. The two mixed indexing solutions were separated into two clusters shown by the red and blue lines showing the smoothed moving average values of *f* and *g*, respectively. The upper and lower black lines show the smoothed moving average values of whichever of *f* or *g* is greater or lower, respectively, for the current crystal which should converge on the average values of *f* and *g*.

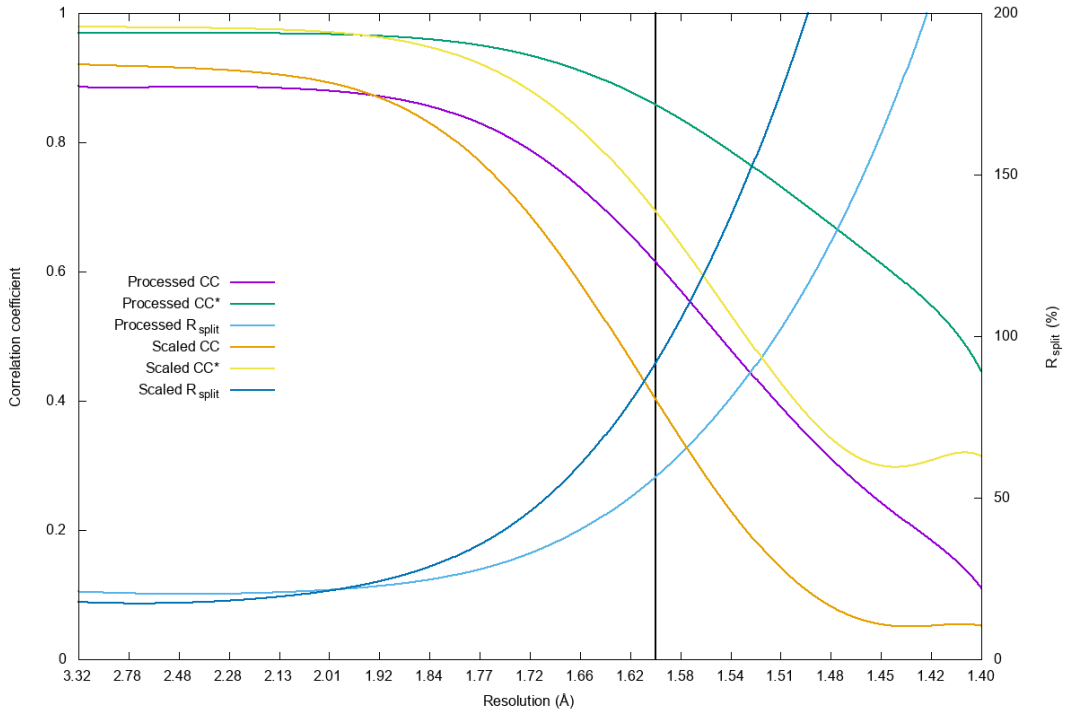

Figure 4.22. SF-ROX data processing of *Ax*NiR. Graph shows the values for CC, CC* and R_{split} for *Ax*NiR SF-ROX data collection. The 1.6 Å cut-off is shown with a vertical black line. A comparison is made between the merged individual intensities with and without frame scaling.

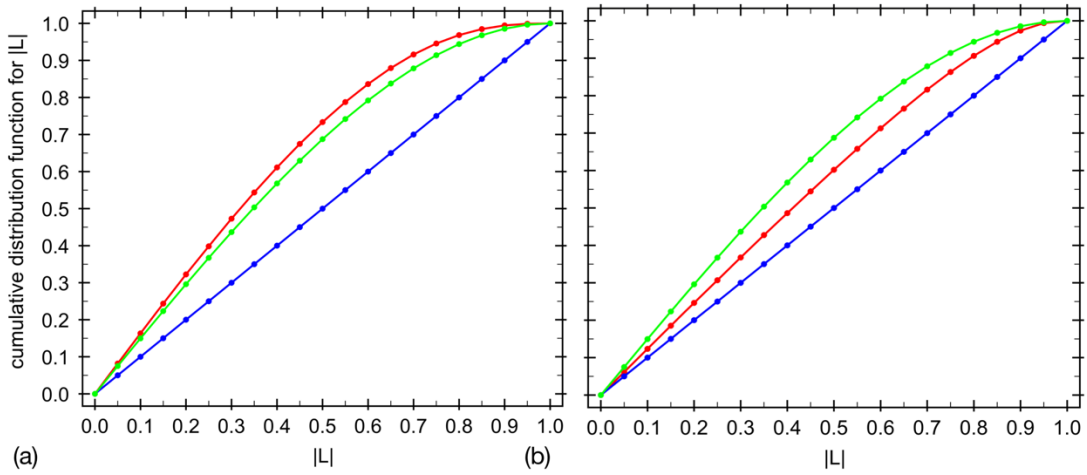

Figure 4.23. L-test results from *Ax*NiR SF-ROX data collection. Intensity statistics show for SFX data (a) before and (b) after running stream though *ambigator* with operator *h,k,-l*. Twinning signal was dispelled after running the program. Cumulative distribution function for |L| observed shown in red, expected (untwinned) in blue and expected (twinned) in green.

4.3.6. Structure of as-isolated *Ax*NiR using SRX

The dataset of *Ax*NiR collected from the same crystal batch as the SF-ROX crystals was processed and refined to 1.6 Å as a comparison (Table 4.3). A single *Ax*NiR monomer was present in the asymmetric unit. The functional trimer was formed by the symmetry operator of the crystal (Figure 4.24). The sequence of *Ax*NiR consists of 336 residues but no electron density was viable for the first or last residues indicating their flexibility leaving a model of 334 residues. His313 is bound to a PEG molecule covering the substrate entry channel preventing NO_2^- soaking. Both the copper sites, T1Cu and T2Cu were fully occupied with copper based on their B-factors relative to the neighbouring atoms in the metal binding pocket (Figure 4.25). A comparison was made to atomic resolution *Ax*NiR structure (PDB: 1OE1) to make sure of no significant differences between this recombinant *Ax*NiR preparation and the native protein used there. The structures were aligned by superposition of the secondary structure elements and protein backbone C_α atoms using the SSM algorithm[204]. No significant changes were observed in the ligand geometry around the T1Cu or T2Cu sites. As well at the three histidine ligands, the T2Cu is ligated by water (W1) molecule in a tetrahedral geometry. The water is hydrogen bonded to Asp92 which is then linked to His249 by second water (W2) as observed in other cryo SRX CuNiR structures (Figure 4.26)[205,206]. The Asp92 is structured in the proximal position with no electron density to suggest a low occupancy gatekeeper secondary conformation. Ile251 is positioned at the top of the T2Cu pocket to produce a hydrophobic, steric restriction to extra solvent accessing the active site.

Figure 4.24. The functional trimer of *Ax*NiR. Two copper sites are present in each of the three monomers (grey, blue and orange). The T1Cu sites are shown in dark blue, buried below the protein surface. The T2Cu sites are shown in cyan, ligated between the monomer-monomer interface (PDB: 5ONY).

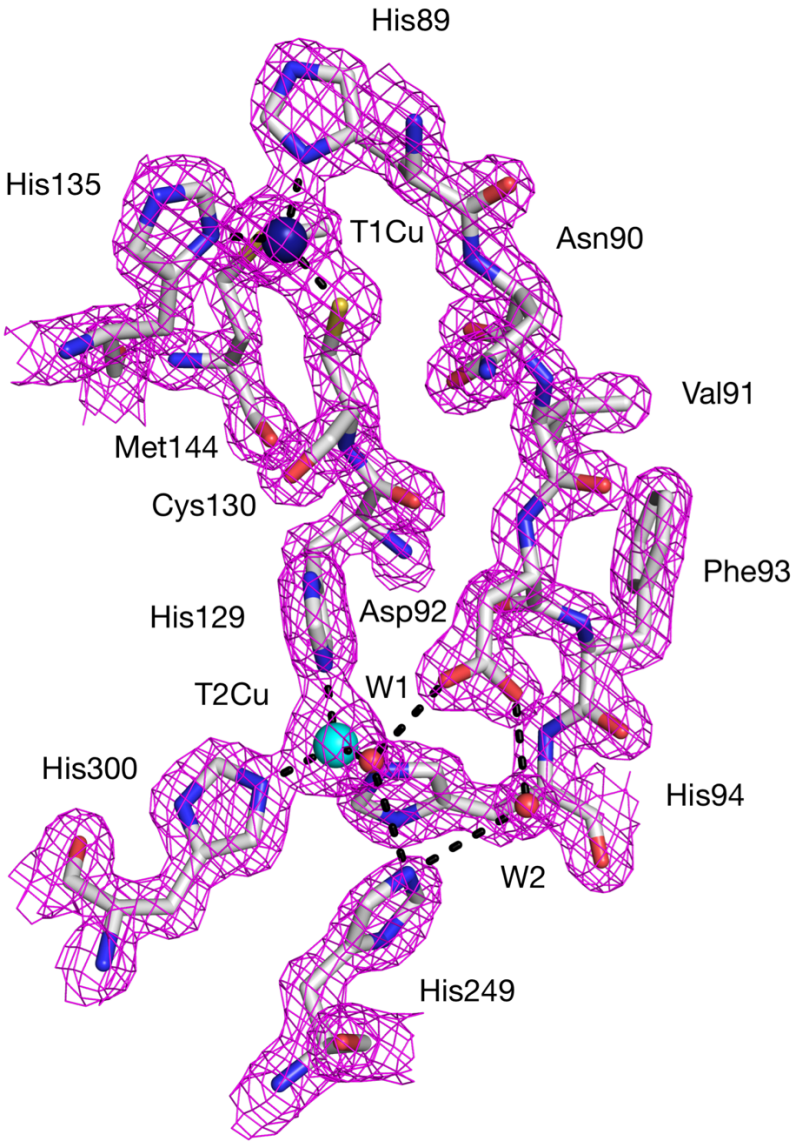

Figure 4.25. The copper sites of *Ax*NiR determined by SRX. The T1 and T2Cu are connected by a Cys-His bridge along which electron transfer takes place. The Cu sites are also connected by the amino acid chain His89, a T1Cu ligand and Asp92, one of the T2Cu catalytic ligands. $2F_o$-F_c electron density is contoured at 2σ level and shown as magenta mesh. Atoms are coloured by element with a different colour scheme used for the different chains; T2Cu as a cyan sphere, water molecules as small red spheres. Metal coordinating bonds are shown as red dotted lines. Selected hydrogen bonds are shown as black dotted lines (PDB: 5ONY).

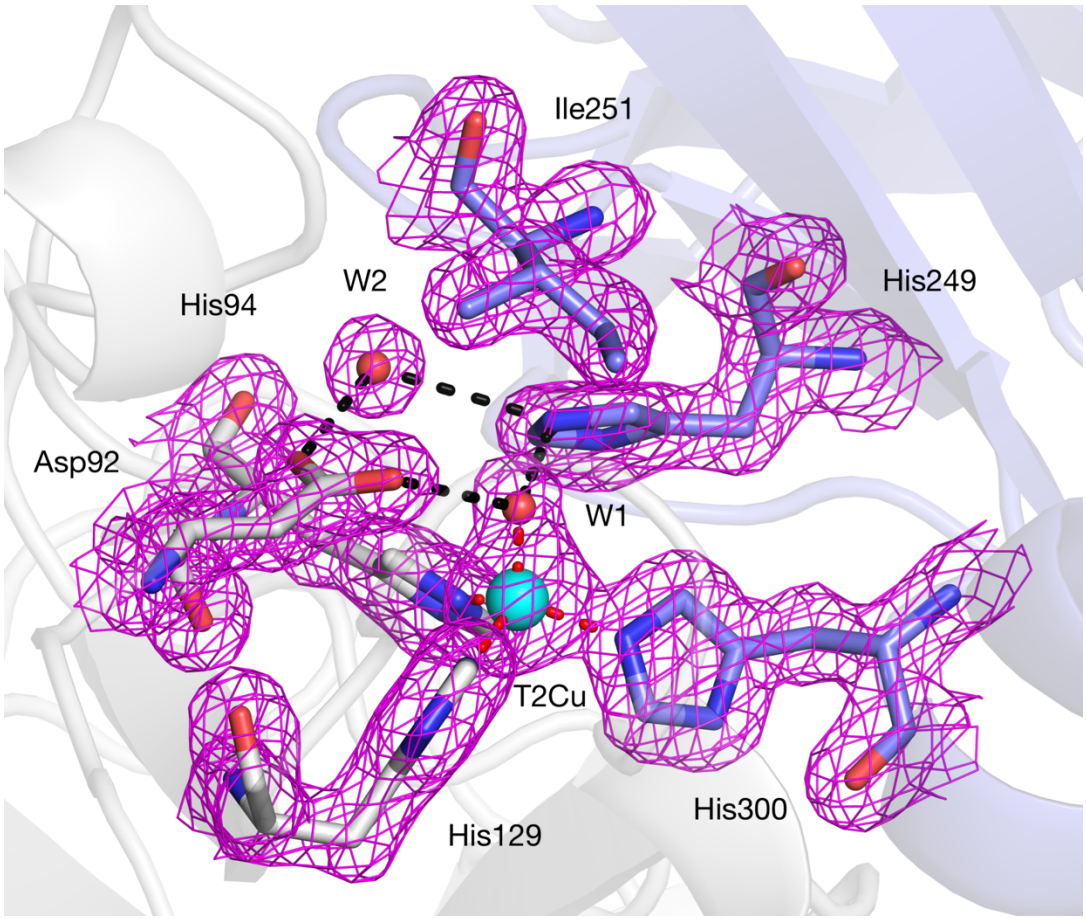

Figure 4.26. The resting state T2Cu site determined using synchrotron radiation. The T2Cu is ligated by three histidine residues and W1. The two catalytic residues, Asp92 and His249, are linked by hydrogen bonding to W1 as well as W2 positioned behind. $2F_o$-F_c electron density is contoured at 2σ level and shown as grey mesh. Atoms are coloured by element with a different colour scheme used for the different chains; T2Cu as a cyan sphere, water molecules as small red spheres. Metal coordinating bonds are shown as red dotted lines. Selected hydrogen bonds are shown as black dotted lines (PDB: 5ONY).

4.3.7. Structure of as-isolated *Ax*NiR using SF-ROX

The synchrotron structure was used as the starting model for SF-ROX refinement. Both the synchrotron and XFEL datasets were determined to the same resolution of 1.6 Å. After assessment and refinement of the rest of structure, the T2Cu ligand was assessed (Table 4.4). A large, elongated patch of positive density was observed atop the T2Cu site. Initially, a single water molecule was assigned, and the structure was refined. However, after refinement, a large proportion of the positive density still remained in-between the two catalytic residues. As two water molecules are sometimes seen binding the T2Cu in room-temperature CuNiR structures, a second water was added manually, and the model was further refined. However, upon reviewing the model, the distance between the two water oxygens was 1.28 Å, much too short for a hydrogen bond between two water molecules. A split occupancy water was then checked but a single split water did not satisfy the density either. In a recent SFX structure of *Af*NiR, a chloride atom was observed binding to the T2Cu in the resting state[179]. In that case the authors had suggested that chloride had originated from the purification or crystallisation protocol where Tris-HCl buffer was used. With this in mind, seeing as Tris-HCl buffer was used in this purification, chloride was modelled and refined. However, chloride also did not satisfy the electron density of SF-ROX of AxNiR which generated a much stronger signal than was observed in the experimental electron density. The ligands and products of *Ax*NiR were then assessed. Endogenous NO_2^- and NO have been previously observed in *Ac*NiR and so had to be considered in this case. The density was too small to

occupy NO_2^- with the density appearing to be consistent with a diatomic molecule. This pointed towards NO being the ligated species but when modelled, the molecule, while satisfying the electron density took up an end-on coordination as opposed to the side-on NO previously observed[207]. In consideration of other possible diatom species, the superoxide dismutase activity of AxNiR was recalled[52]. O_2 was then modelled and refined which satisfied the electron density. The binding was checked by the generation of a 3000 K simulated annealing omit map after full structural refinement which showed the elongated density above the T2Cu (Figure 4.27, 4.28). The distance between the two O atoms was refined using *REFMAC5*[195] restraints. The species refined with an O-O distance of 1.24 Å, compatible with a O_2/O_2^- species. This refinement was compared to a known copper-dependent, dioxygen binding enzyme, peptidylglycine α-hydroxylating monooxygenase (PHM) (Figure 4.29)[208]. Both the SF-ROX refinement and the PHM structure have dioxygen species bound end-on to the copper, as opposed to the side-on binding of NO observed in nitrite reductases[207]. A superposition of the T2Cu site and the Zn site of bovine Cu, Zn-SOD revealed a distinct structural similarity previously observed by Strange *et al.*[52]. The distance between the carboxy oxygen of Asp92 and the dioxygen species, O furthest from the T2Cu had an O-O distance of 2.55 Å. This suggests that Asp92 is protonated on that carboxy group as dioxygen is unable to provide a proton to hydrogen bond.

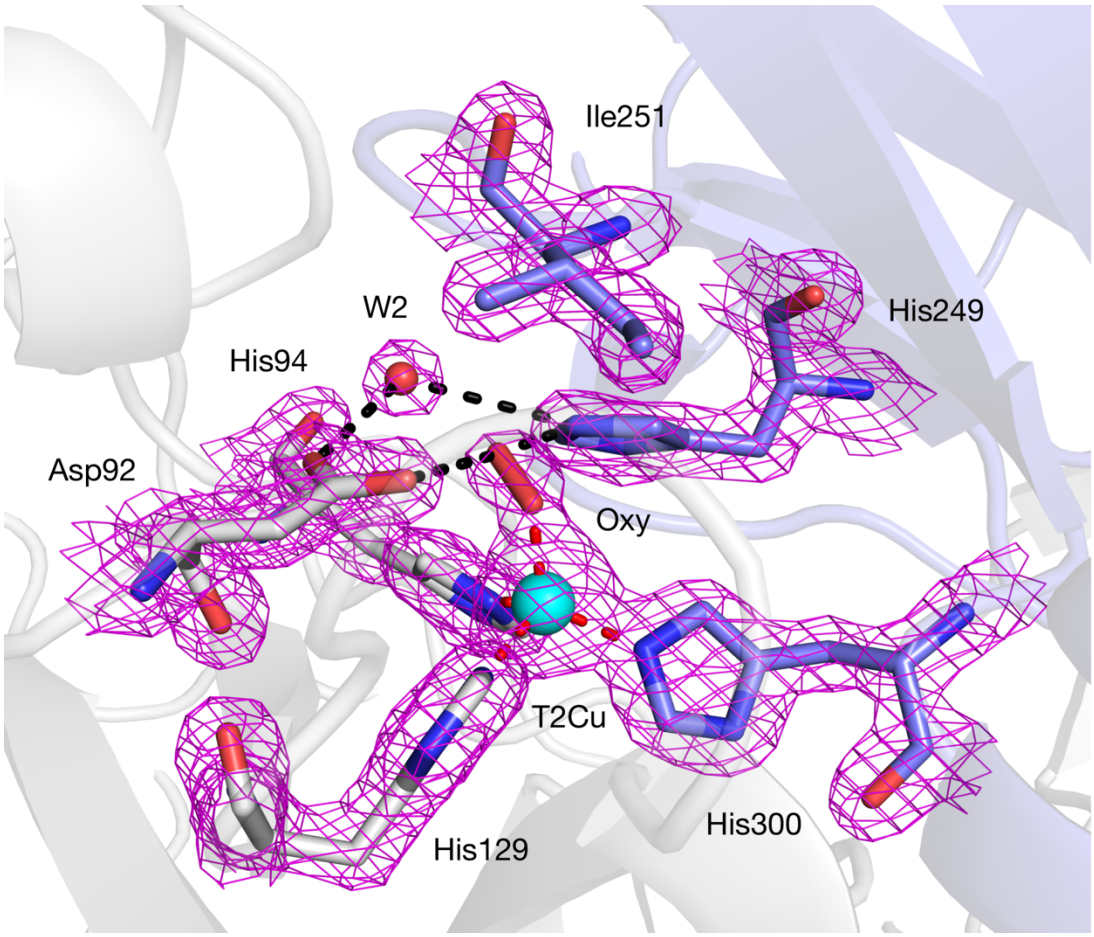

Figure 4.27. The resting state T2Cu site determined using femtosecond crystallography. The T2Cu is ligated by a dioxygen species in an end-on manner. $2F_o$-F_c electron density map contoured at 2σ in magenta mesh. Atoms are coloured by element with a different colour scheme used for the different chains; T2Cu as a cyan sphere, water molecules as small red spheres. Metal coordinating bonds are shown as red dotted lines. Selected hydrogen bonds are shown as black dotted lines (PDB: 5ONX).

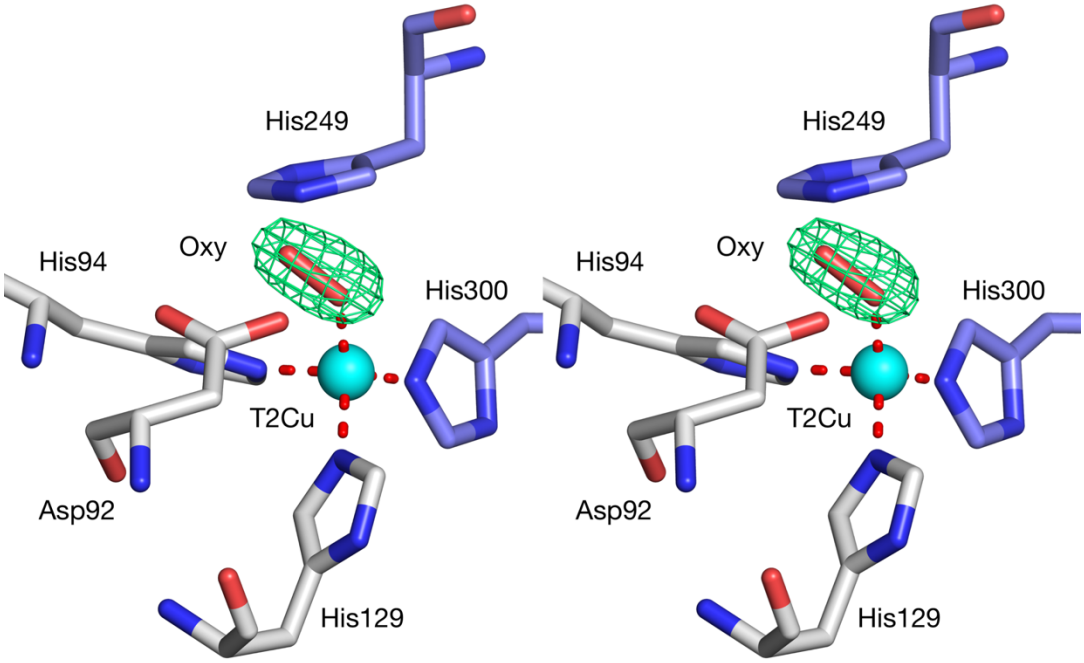

Figure 4.28. A cross-eyed stereo image of the resting state superoxide bound T2Cu site. A 3000 K simulated annealing omit map shows the dioxygen ligand bound to the T2Cu site. F_o-F_c electron density map contoured at 5σ in green mesh around the refined dioxygen ligand. Atoms are coloured by element with a different colour scheme used for the different chains; T2Cu as a cyan sphere, water molecules as small red spheres. Metal coordinating bonds are shown as red dotted lines. Selected hydrogen bonds are shown as black dotted lines (PDB: 5ONY).

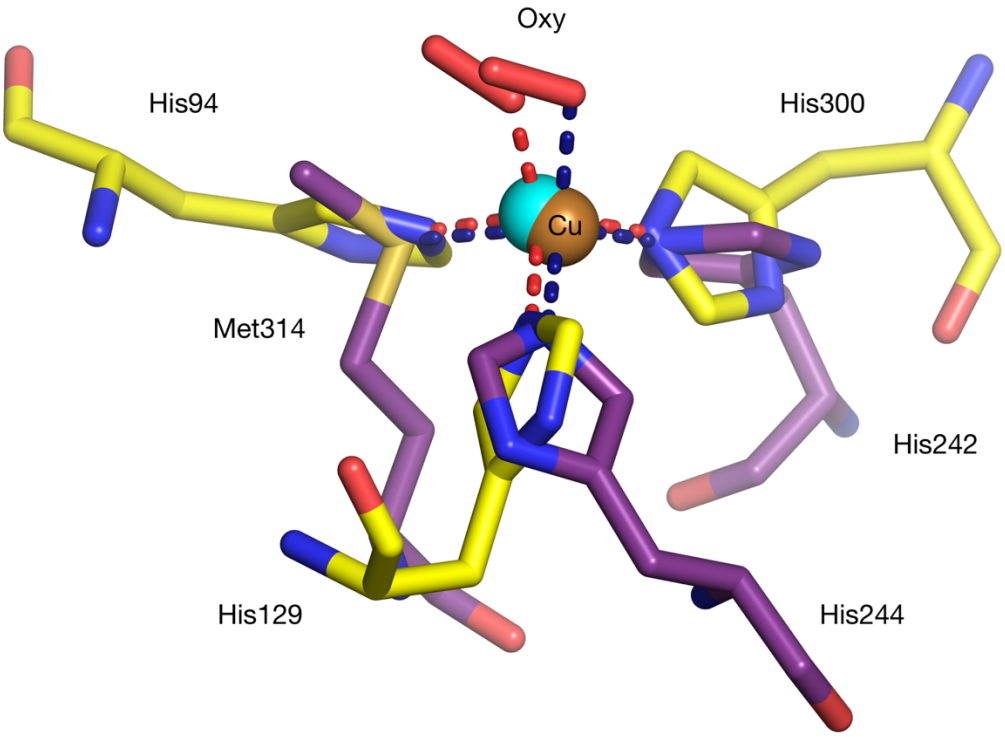

Figure 4.29. Alignment of O_2 bound *Ax*NiR and PHM. Both structures have end-on bound dioxygen shown in red. The tetrahedral ligation of both copper atoms is easily observed. *Ax*NiR is shown in yellow and PHM is shown in purple with the copper atoms shown in cyan/brown respectively. PHM Cu has His_2-Met coordination. *Ax*NiR coordinate bonds are shown in red (PDB: 5ONX) with PHM coordinate bonds shown in blue (PDB: 1SDW)[208].

Table 4.4. Comparison of *Ax*NiR copper-site geometries

	SF-ROX (5ONX)	SRX^{RS} (5ONY)	SRX^{RS} (1OE1)
T1Cu site distances (Å)			
T1Cu – His89 $N^{\delta1}$	1.96	2.11	2.02
T1Cu – Cys130 S^{γ}	2.08	2.11	2.20
T1Cu – His139 $N^{\delta1}$	1.96	2.02	2.03
T1Cu – Met144 S^{δ}	2.72	2.75	2.45/4.26
T1Cu site angles (°)			
His89 $N^{\delta1}$ – Cu – Cys130 S^{γ}	131.7	125.6	121.5
His89 $N^{\delta1}$ – Cu – His139 $N^{\delta1}$	99.9	103.6	100.5
His89 $N^{\delta1}$ – Cu – Met144 S^{δ}	84.3	82.4	88.4/87.5
Cys130 S^{γ} – Cu – His139 $N^{\delta1}$	119.5	122.5	113.9
Cys130 S^{γ} – Cu – Met144 S^{δ}	105.8	106.2	113.5/107.1
His139 $N^{\delta1}$ – Cu – Met144 S^{δ}	109.0	108.4	116.4/124.7
T2Cu site distances (Å)			
T2Cu – His94 $N^{\delta2}$	2.04	2.04	1.96
T2Cu – His129 $N^{\delta2}$	2.02	2.01	2.00
T2Cu – His300 $N^{\delta2}$	2.06	2.09	2.00
T2Cu – Wat1		1.72	1.98
T2Cu – Oxy^{1}	2.65		
T2Cu – Oxy^{2}	1.81		
Asp92 $O^{\delta2}$ – Oxy^{1}	2.55		
His249 $N^{\delta2}$ – Oxy^{1}	2.24		
T1Cu site angles (°)			
His94 $N^{\delta2}$ - T2Cu - His129 $N^{\delta2}$	104.8	108.2	110.9
His94 $N^{\delta2}$ - T2Cu - His300 $N^{\delta2}$	100.0	106.4	103.6
His129 $N^{\delta2}$ - T2Cu - His300 $N^{\delta2}$	112.5	108.6	108.9
T2Cu – His_3 ligand plane (Å)	0.75	0.74	0.72

4.3.8. Comparison of the SRX and SF-ROX structures of *Ax*NiR

The observation of the O_2/O_2^- ligand is novel here due to the binding mode exhibited. CuNiRs have been previously observed binding diatomic molecules, both NO and O_2 but in all case, the binding mode has been side-on with equal bond lengths from both atoms to the copper[76,207]. Here we observe a mononuclear Cu(II)-superoxo complex with asymmetric O-O binding, end-on as opposed to side-on. The oxygen reduction mechanism of CuNiRs has been previously described through its dismutase activity[52] and, more recently, a structure of *Gt*NiR published with a dioxygen molecule ligated T2Cu (Figure 4.30)[76]. The electron density in *Gt*NiR was assigned to dioxygen based on the refined O-O distance and UV–visible spectrum absorbance at 352 nm[209]. Previously, the observation of mononuclear Cu(II)-O_2/O_2^- complexes were thought to be unobservable because of the rapid rate of decomposition. The movement of the dioxygen species from side-on to end-on may have been driven by the change in the Ile_{CAT} residues in *Ax*NiR to Val in *Gt*NiR creating a much larger substrate binding pocket allowing easier access of O_2 to the T2Cu. The binding mode is uniquely similar to dioxygen binding observed in PHM[208]. Both display end-on binding with refined O-O bond distances of 1.23 Å for PHM and 1.24 Å for *Ax*NiR. The *Ax*NiR SF-ROX structure was compared with the structure of *Af*NiR SFX which contains a chloride ion bound to the T2Cu, replacing W1 (Figure 4.31). When comparing the NO_2^--bound structures, the NO_2^- has a top-hat, symmetrical coordination which is connected to the position of NO viewed in *Ac*NiR in the MSOX series as opposed to the coordination of O_2 observed here[132].

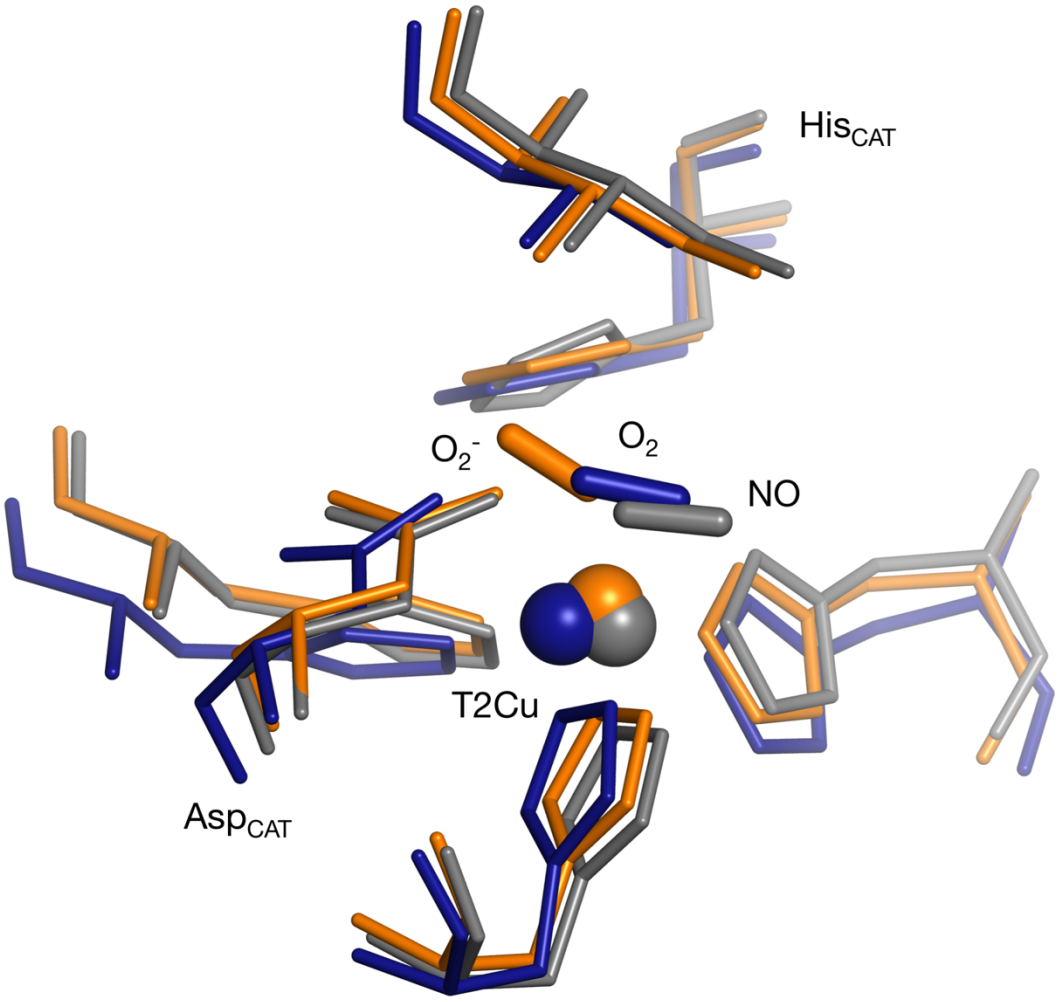

Figure 4.30. A superposition of diatom bound T2Cu. The T2Cu sites of NO-bound *Ac*NiR (grey, PDB: 5I6O)[132], O_2-bound *Gt*NiR (blue, PDB: 3WNJ)[76] and O_2^--bound *Ax*NiR (orange, PDB: 5ONX) CuNiR. Both O_2 binding and NO binding are observed in side-on modes with O_2^- observed in an end-on mode. In *Gt*NiR, the pocket isoleucine residue is replaced with a valine residue, increasing the volume of the active site pocket.

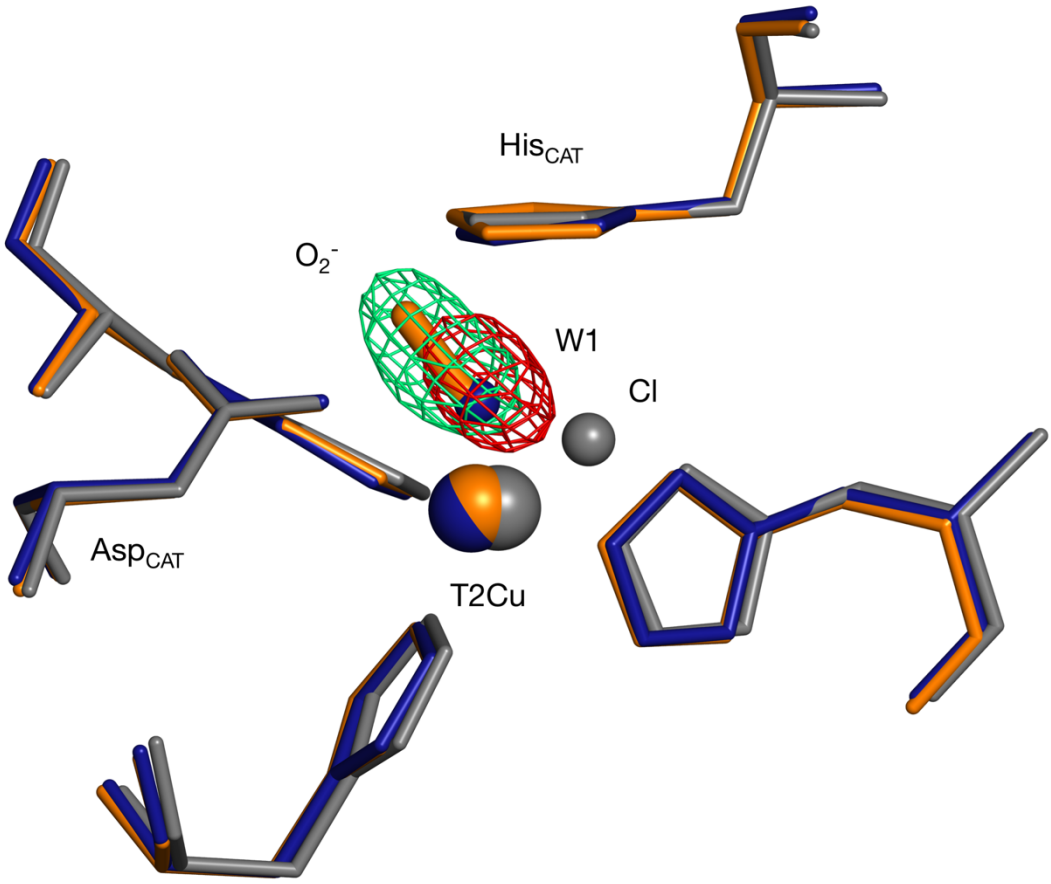

Figure 4.31. A superposition of SRX *Ax*NiR, SF-ROX *Ax*NiR and SFX *Af*NiR resting state T2Cu sites. The O_2^- and W1 are depicted with 3000 K simulated annealing Fo-Fc omit electron density maps, contoured at 6σ in green and red mesh respectively. *Af*NiR determined by SFX is bound by a chloride molecule from the purification and/or crystallisation procedure. The *Ax*NiR SRX structure is shown in blue (PDB: 5ONY), the *Ax*NiR SF-ROX in orange (PDB: 5ONX) and the *Af*NiR SFX in grey (PDB: 4YSC)[179].

4.3.9. *Ax*NiR-superoxide adduct formation

The basis for this work has been to compare the atomic structure of *Ax*NiR collected using femtosecond crystallography and compare it with a structure collected using synchrotron radiation at a synchrotron light source. To make for a complete comparison both datasets were collected from crystals grown in the same batch and from the same recombinant protein stock and so all expression, purification, crystallisation and crystal handling was the same. While the amino acid structure of the protein was the same for both the SF-ROX and SRX structures, the T2Cu ligand was found to be H_2O in the SRX structure as previously observed but a superoxide ligand in the SF-ROX structure. While usually highly reactive as a radical, O_2 has been shown to bind to reduced mononuclear copper centres that result in their oxidation and the stabilisation of the O_2 as O_2^- on the T2Cu forming a copper(II)-superoxo adduct[210].

The <10 fs XFEL pulses used to collect this data occur on a timescale beyond that of any molecular rotation or vibration and therefore can be consisted 'time-frozen' with no photochemistry occurring in the crystal during data collection[135]. The blue *Ax*NiR crystals indicate these crystals are in the Cu(II) oxidised state and so would be unable to bind O_2 from the aerobic conidiations they are produced in. However, during expression and purification CuNiRs are known to bind and remain stable through data collection with ligand and product species such as NO_2^- and NO [54]. Therefore, if a reduced Cu(I) species present in *Ax*NiR was to react with O_2 to form the superoxo adduct it would likely remain stable through crystallisation and data

collection due to an increase in the reduction potential of the T2Cu when NO_2^- is bound preventing the reverse reaction occurring[211]. This structure can represent a trapped intermediate of the oxidase reaction waiting for the delivery of an electron to enable H_2O_2 production. Alternatively, O_2^- can bind to the Cu(II) oxidised T2 (Scheme 4.1).

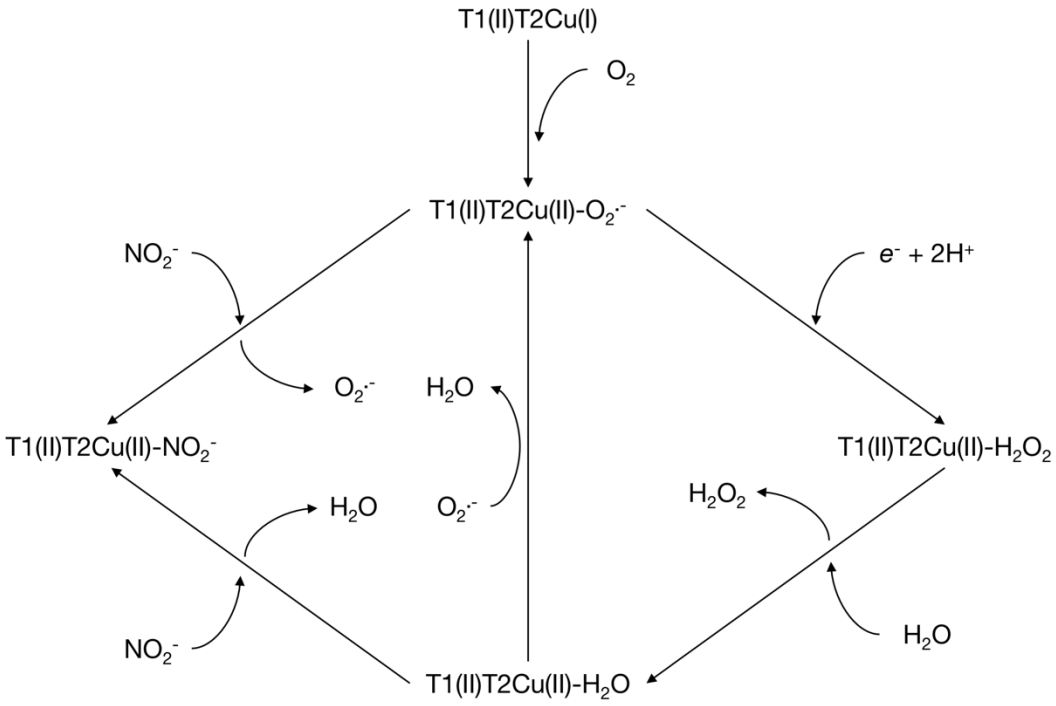

Scheme 4.1. A reaction scheme of O_2 and NO_2^- binding to AxNiR based on structural data. The T2Cu(II)-O_2^- intermediate is stable unless a second electron is delivered to turn the reaction over.

Chapter 5 - *Ac*NiR serial femtosecond crystallography

5.1. Preparation of *Ac*NiR crystals for SF-ROX

5.1.1. Batch crystallisation

The success of *Ax*NiR SF-ROX data collection proved that two-domain CuNiRs crystals were highly amenable to data collection with this method. The method of *Ax*NiR crystallisation however prevented the soaking of NO_2^- ligand into the crystals and so the damaged-free binding mode not able to be observed. Published structures of *Ac*NiR showed that ligand soaking was possible to high resolution with these crystals and so were selected as the next target for data collection[54]. Purified *Ac*NiR was transferred into 10 mM HEPES-OH, pH 6.5 buffer and concentrated to 50 mg/ml for crystallisation. Crystals were grown in anticipation of an SF-ROX experiment and so crystal size was maximised. Large crystals, 0.7 x 0.7 x 0.7 mm in size were grown by hanging drop vapour diffusion at room temperature. 400 μl of crystallisation mixture was added to each well containing 1.2 M ammonium sulphate and 100 mM citrate buffer, pH 5.0. 2 μl of protein solution was mixture with 2 μl of crystallisation mixture and immediately seeded with microcrystals of *Ac*NiR. Crystals grew to the appropriate size after 5 days with a pyramidal morphology (Figure 5.1).

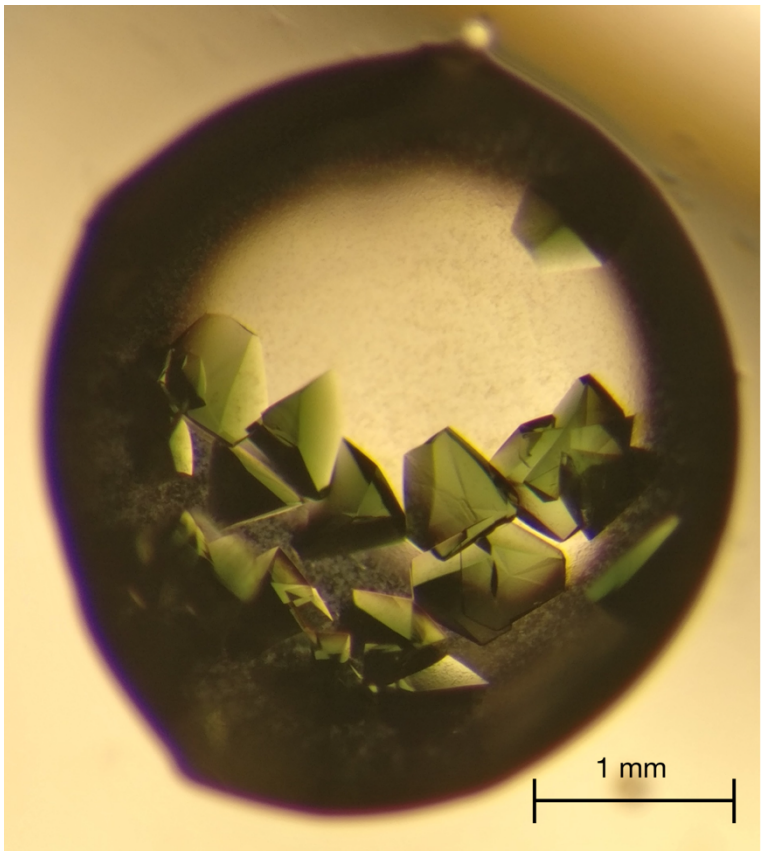

Figure 5.1. Batch crystallisation of *Ac*NiR. Crystals were grown by hanging drop vapour diffusion against 1.2 M ammonium sulphate and 100 mM citrate buffer, pH 5.0 The green colour of the crystals is clearly evident pointing to a fully oxidised T1Cu site.

5.1.2. SRX data collection

To test the diffraction quality of the crystals, a single dataset was collected from one crystal from the same batch as would be used for the SF-ROX data collection. The harvested crystal was soaked in 3.4 M ammonium sulphate and 100 mM citrate buffer, pH 5.0 for 10 s and cryocooled by plunging into LN_2. Data collection was carried out remotely at beamline i04-1 at the Diamond Light Source, Oxford, UK. A full dataset consisting of 3600 images with 0.1° oscillation was collected using a PILATUS 6M-F single photon counting detector in shutterless mode. The X-ray energy was fixed at 13.35 keV with a crystal to detector distance of 172 mm and 10% beam transmission. Diffraction spots were visible at the edge of the detector, the maximum allowed by the geometry of the beamline (Figure 5.2).

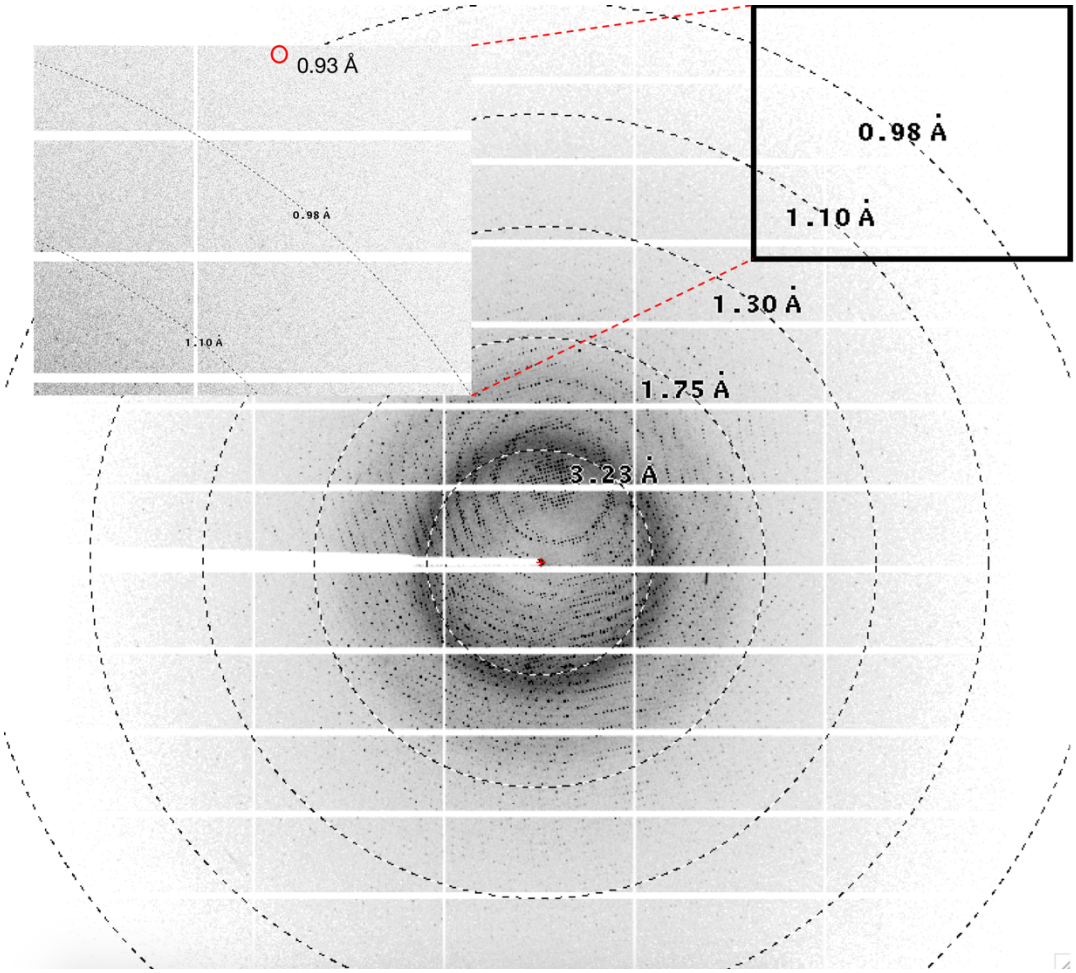

Figure 5.2. A diffraction pattern from *Ac*NiR collected. Diffraction spots are visible at the edge of the detector (0.93 Å) highlighted with a red circle. Data collected on a PILATUS 6M-F detector at Diamond i04-1.

5.1.3. SRX processing and refinement

All 3600 images were processed automatically with the *xia2* pipeline[212] using *DIALS*[213] for indexing and integration and *AIMLESS*[200] for data reduction. However, the data processing statistics did not show a significant diffraction signal out towards the detector edge. The data was then reprocessed manually using *XDS*[168] with the images broken up into 6 groups of 600 images each to check for variation across the datasets. One dataset consisting of image numbers 1201 – 1800 produced by far the best processing statistics as given in Table 5.1 with a maximum resolution of 0.96 Å. The dataset processed in space group $P2_13$ and an *Ac*NiR monomer (PDB: 5AKR)[55] was used as a starting model for refinement. Anisotropic parameters, solvent, ligands and alternate conformations were removed from the model. Initial rigid body refinement was followed by rounds of restrained refinement in *REFMAC5*[195] with isotropic B-factors and riding hydrogens. In between rounds of refinement, *Coot*[196] was used for manual model rebuilding and addition of waters. After each round of isotropic refinement, the resolution limit was raised until the maximum resolution was reached. Anisotropic refinement then started for 10 rounds of refinement after which the R_{factor} in the outer shell reached a minimum of 28%. Based on the diffraction of the crystal and the statistics presented, the resolution of this crystal is better than was able to be collected limited by the diffractometer geometry.

Table 5.1. Data collection and refinement statistics for *Ac*NiR collected using SRX

Data collection	
Space group	$P2_13$
Unit cell dimensions	
a=b=c (Å)	94.99
α=β=γ (°)	90
Resolution (Å)	42.48 – 0.96 (0.98 – 0.96)[a]
$R_{p.i.m.}$ (%)	2.9 (47.9)[a]
$\langle I/\sigma(I) \rangle$	13.8 (1.6)[a]
$CC_{1/2}$	0.999 (0.563)[a]
Completeness (%)	99.4 (96.1)[a]
Redundancy	5.5 (1.9)[a]
Wilson B-factor (Å^2)	5.3
Refinement	
No. of unique reflections	171918 (8172)[a]
R_{work}/R_{free} (%)	10.3/12.2
R.m.s deviations	
Bond length (Å)	0.017
Bond angles (°)	2.023

a. The highest resolution shell is shown in parenthesis.

5.1.4. Structure of as-isolated *Ac*NiR using SRX.

The newly collected structure was compared to the previously published atomic resolution, resting state *Ac*NiR structure (PDB: 2BW4)[54]. The structures were aligned by superposition of the secondary structure elements and protein backbone C_α atoms using the SSM algorithm[204]. No significant changes were present in the geometry of the T1Cu site but the geometry (Figure 5.3) of the T2Cu site was significantly different. In the atomic resolution, resting state *Ac*NiR structure, the T2Cu is ligated by W1, bound apically to the Cu in a true tetrahedral geometry with respect to the three histidine ligands. Two conformations of the Asp98 are present, both proximal and gatekeeper with the proximal predominating. In the new structure, the T2Cu is ligated by two water molecules orientated leaning away (W1) and towards (W3) the catalytic residues (Figure 5.4). The atomic resolution, resting state *Ac*NiR structure is refined from a dataset collected from *A. cycloclastes* purified from the native source while this new structure is from a recombinant enzyme. The appearance of W3 is often associated with RT data collection but is visible here collected at 100 K[59]. The quality of the diffraction and the electron density maps was such that these crystals were considered adequate for SF-ROX data collection.

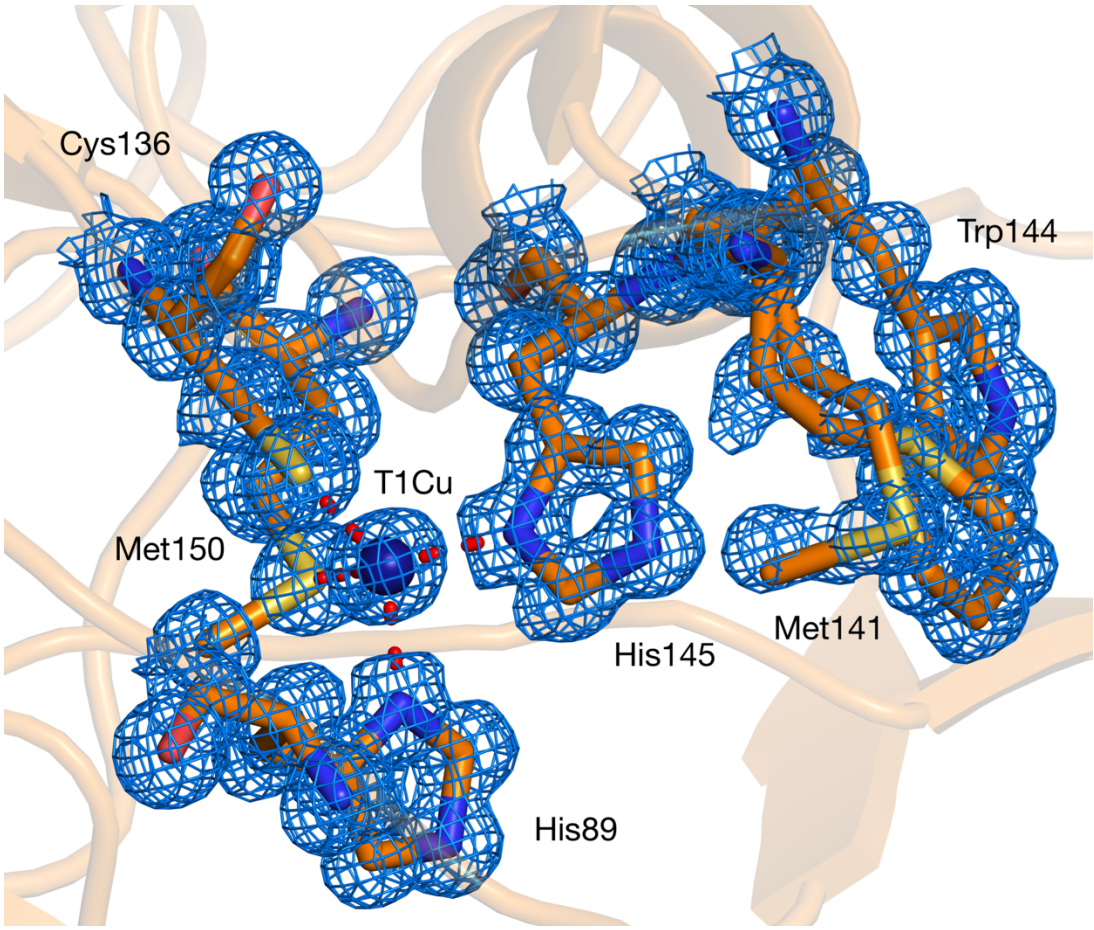

Figure 5.3. The structure of the *Ac*NiR T1Cu site determined by SRX. The T1Cu is ligated with the usual His_2-Cys-Met ligation. Met141 is visible in two conformations orientated away from and pointing towards His145, partially covering the residue. 2Fo-Fc electron density map is contoured at the 1σ level and shown as blue mesh. The T2Cu is shown as a blue sphere. Metal-coordinating bonds are shown as red dotted lines.

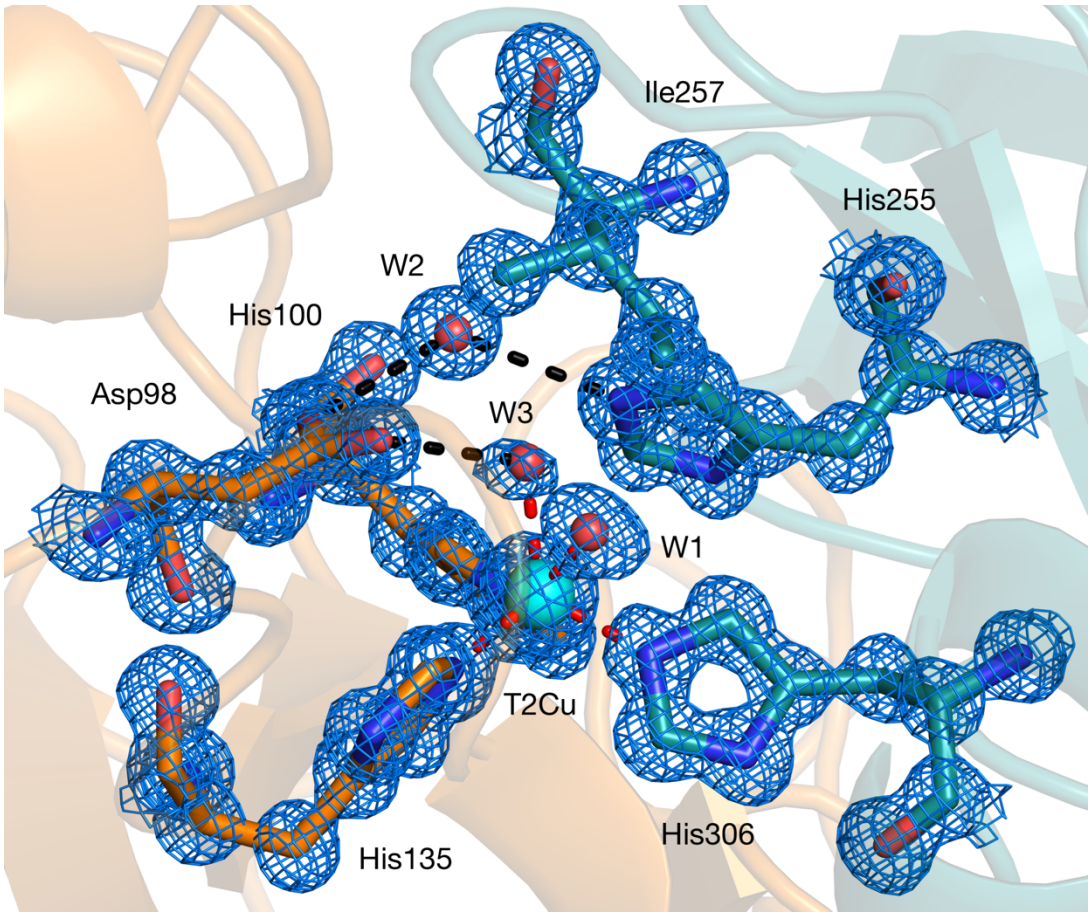

Figure 5.4. The structure of the *Ac*NiR T1Cu site determined by SRX. Two water molecules (W1 and W3) ligate the T2Cu orientated away from and towards the catalytic residues. The W3 is of half occupancy. The linking water (W2) is in its usual position in-between Asp98 and His255. 2Fo-Fc electron density map is contoured at the 1σ level and shown as blue mesh. The T2Cu is shown as a cyan sphere and water molecules as small red spheres. Metal-coordinating bonds are shown as red dotted lines. Selected hydrogen bonds are shown as black dotted lines.

5.2. *Ac*NiR SF-ROX

5.2.1. Crystal treatment

*Ac*NiR crystals from the same batch produced above in Liverpool were stored and taken to SACLA, Japan for SF-ROX data collection. Crystals were transferred to an Eppendorf tube containing 1.8 M ammonium sulphate and 100 mM citrate buffer, pH 5.0. Three hundred and thirty-four crystals were used in total. At the SACLA beamline, crystals were harvested one at a time and soaked in cryoprotectant before freezing by plunging into LN_2. Three different solutions were used for soaking to collect damage-free, time-frozen datasets of *Ac*NiR in three different states; resting (oxidised), reduced and NO_2^--bound. Oxidised crystals were soaked in 3.4 M ammonium sulphate and 100 mM citrate buffer, pH 5.0 for 10 s. Reduced crystals were soaked in 3.4 M Na-malonate, pH 5.0 and 100 mM Na-ascorbate for 30 minutes after which the crystals turned from green to colourless. NO_2^--bound crystals were soaked in 3.4 M Na-malonate, pH 5.0 and 100 mM $NaNO_2$ for 10 s. After freezing, crystals were then loaded into Uni-Pucks for sample exchange using the SPACE sample changer[202].

5.2.2. SF-ROX data collection

SF-ROX data collection was carried out at SACLA Bl2 EH3/EH4. This was one of the first uses of BL2 for user operation. BL3 which was used for *Ax*NiR data collection, is located in line with the accelerator with electrons fed linearly into the undulator. BL2 was brought online using a kicker to push electrons simultaneously pulse-by-pulse into the undulators forming BL3[191] and BL2[214]. The laser pulse energy was expected to be slightly lower than for BL3 with an average of ~437.7 μJ/pulse as opposed to ~456 μJ/pulse. The data collection strategy was the same as utilised for *Ax*NiR. For data collection, the photon energy was set to 10 keV with an X-ray pulse length of less than 10 fs. The camera length was set to 110 mm, the minimum the geometry of the diffractometer would allow but the crystals still diffracted to the edge of the detector (Figure 5.5). After the first crystal exposure, a number of low-resolution reflections were found to be oversaturated, so for subsequent exposures, 0.1 mm Al attenuation was added. The crystals were rotated 0.1° between each snapshot equalling approximately one-third *Ac*NiR the crystal mosaicity determined from the synchrotron dataset collected previously. In total, 3705 single shot still images were collected from 170 crystals over the course of 22 hours. A RAYONIX MX225-HS CCD detector was used with 2x2 binning mode corresponding to the pixel size of 78.2 µm.

5.2.3. SF-ROX data processing

All three datasets were processed using the *CrystFEL* suite[161] in the same manner and so the following processing methodology and figures will discuss the oxidised structure only. No sorting was carried out to separate miss and hit images as a large majority appeared to be hits based on observing the data collection over the course of the experiment. Instead, all images were run through *indexamajig* using *MOSFLM*[166] and *DirAx*[167] for indexing. A bug in the data collection scheduling software was that the first image in each vertical series was a blank image. These invalid images were excluded based on the log file records from which the blank image numbers could be extracted. Hit-finding would not have improved the data quality significantly because >70% of collected images were successfully indexed, but the filtering of bad images, even though they were indexed; for example, low-resolution, multiple lattice, poor prediction accuracy, may help to improve data since few images are merged. However, data quality was already sufficient and so little gain was to be made. Optimization of peak search, indexing, and integration parameters then followed. The inner, middle and outer integration radii were set to of 4, 5 and 7 pixels respectively. As blank images could not be indexed these were not incorporated into the output stream and discarded. All three datasets were indexed into $P2_13$ (Figure 5.6). The indexing ambiguity was resolved using *Ambigator* using operator *-h,l,k* (Figure 5.7). Bragg intensities were merged using the Monte Carlo method with frame scaling (Figure 5.8). Model building was carried out in the *CCP4* suite[193] using *Coot*[196] and PDB: 5AKR[55] as a start model. Refinement was

carried out in *REFMAC5*[195] with riding H atoms and isotropic B-factors. The final quality of the models was assessed using *MolProbity*[201]. Data processing and refinement statistics can be found in Table 5.2.

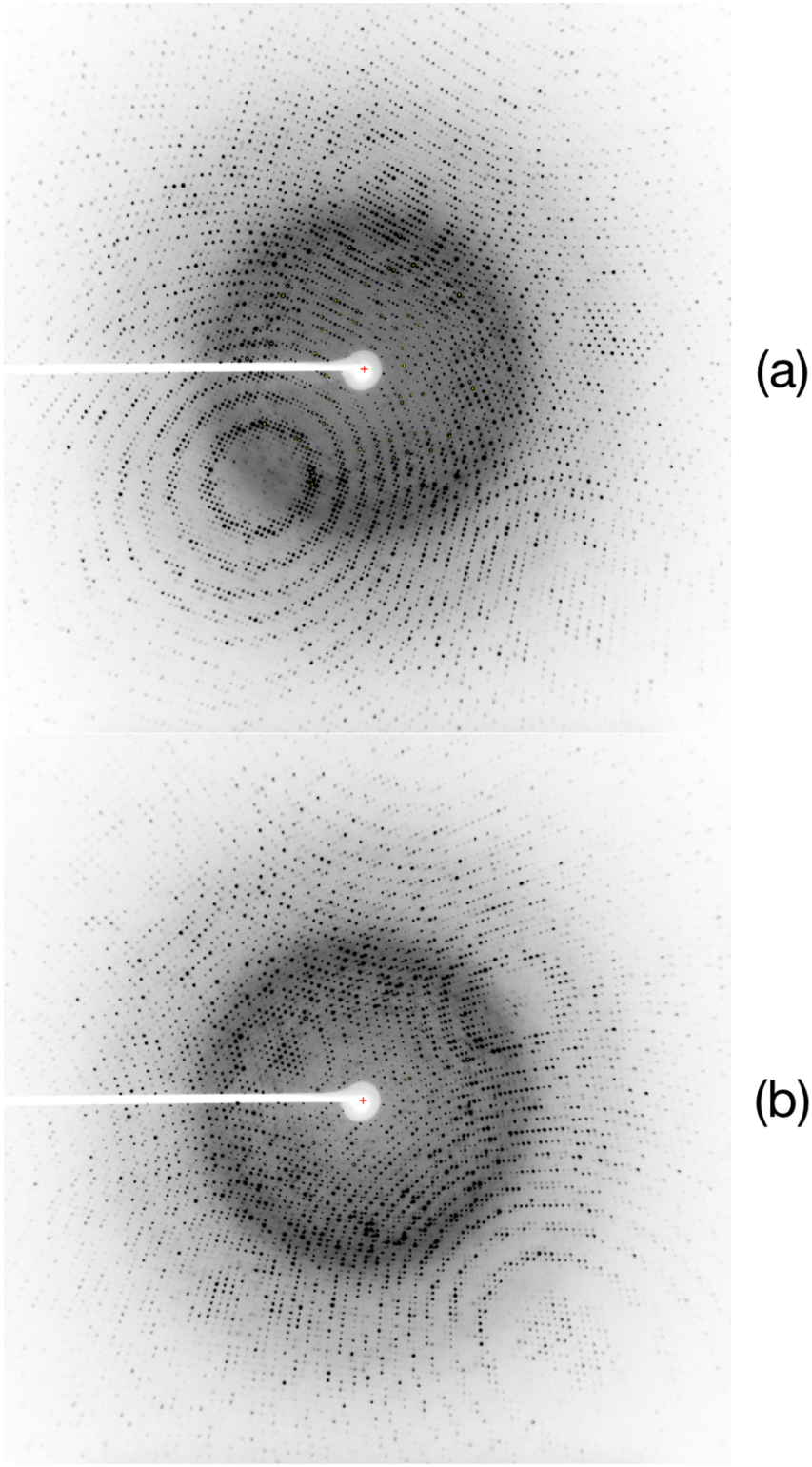

Figure 5.5. A snapshot diffraction image from an oxidised *Ac*NiR crystal. (a) Before and (b) after the addition of 0.1 mm Al attenuation to the beam. The number of oversaturated reflections is reduced. Reflections can be clearly seen at the edge of the detector.

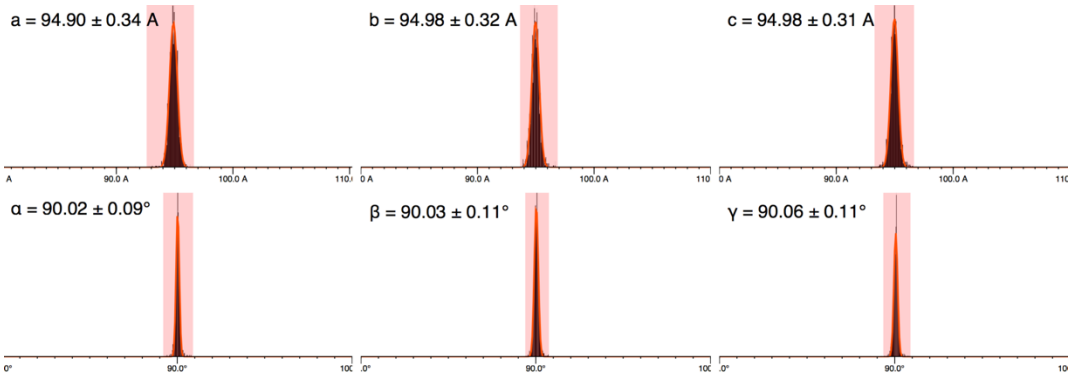

Figure 5.6. The distribution of unit cell parameters from oxidised *Ac*NiR.

The unit cell lengths and angles from individually indexed snapshots from *indexamajig* displayed as a distribution. Black colouring represents these parameters that fall into a P centred space group.

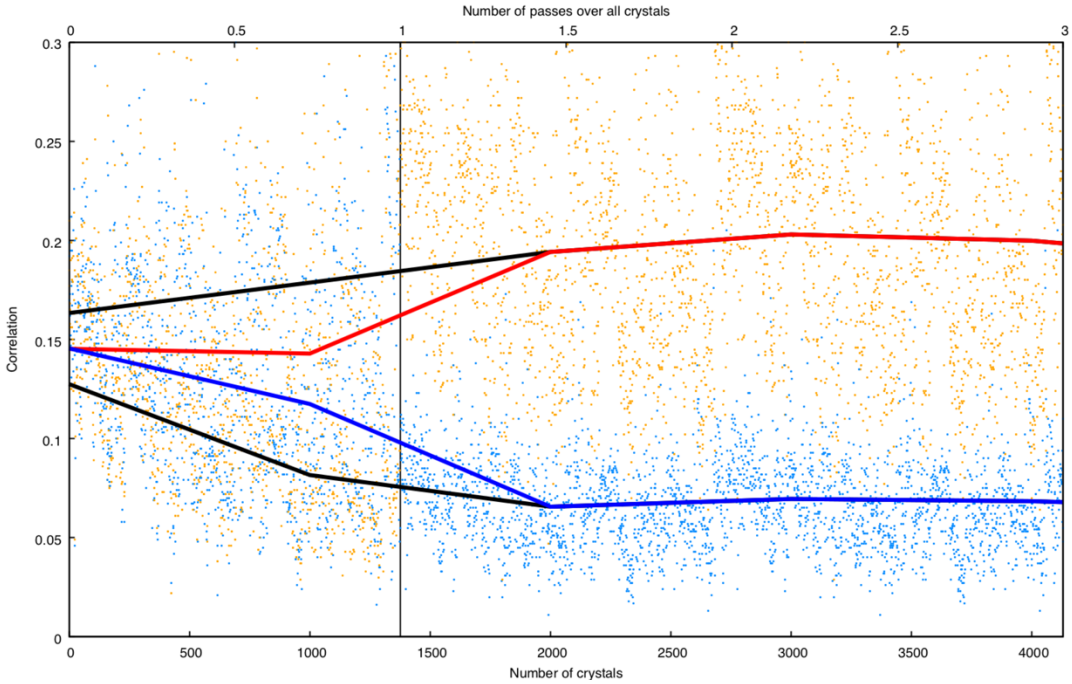

Figure 5.7. Resolving the indexing ambiguity in oxidised *Ac*NiR. The program *ambigator*[169,170] calculates correlation coefficients between the current crystal intensity and all other crystal intensities in a turn-by-turn manner, shown by blue and orange dots. The mean of the correlation coefficient is taken over all crystals which have the same indexing assignment (*f*, blue) as the current pattern while a second mean is taken over all crystals which have indexing assignments opposite to the current crystal (*g*, orange). The indexing assignment is then changed for each crystal if $g > f$. Three iterations of *ambigator* were run with operator *-h,l,k*. The two mixed indexing solutions were separated into two clusters shown by the red and blue lines showing the smoothed moving average values of *f* and *g*, respectively. The upper and lower black lines show the smoothed moving average values of whichever of *f* or *g* is greater or lower, respectively, for the current crystal which should converge on the average values of *f* and *g*.

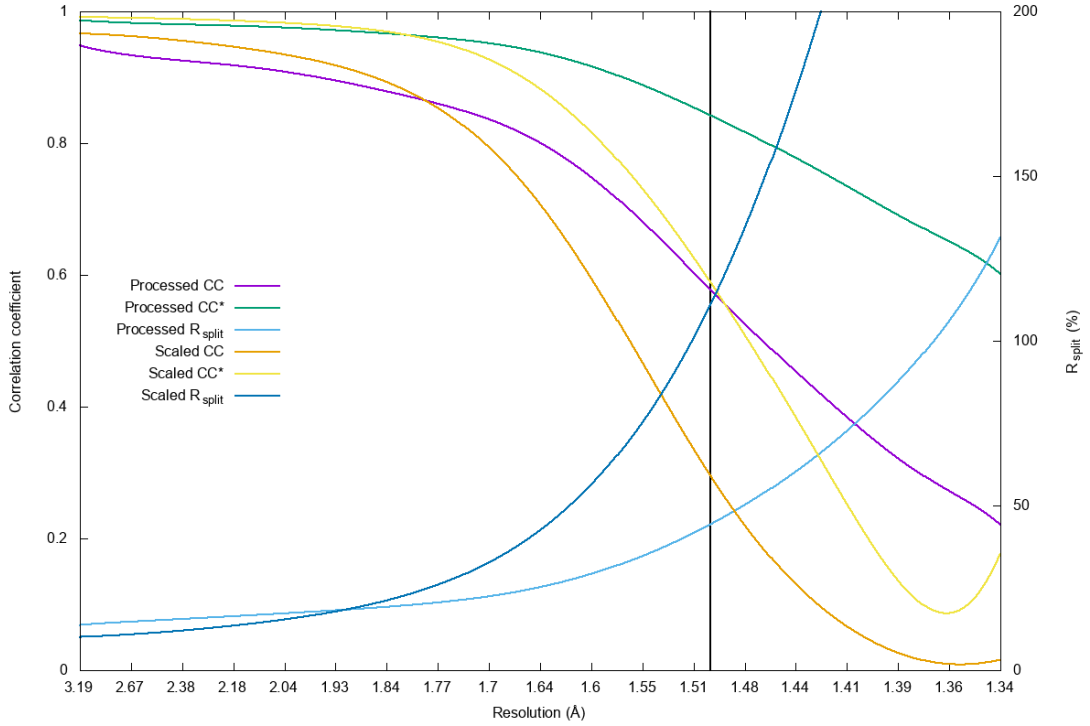

Figure 5.8. SF-ROX data processing of oxidised *Ac*NiR. Data processing of resting state *Ac*NiR collected at SACLA BL2. CC, CC* and R_{split} statistics are shown with and without frame scaling during merging. Scaled data was used for structural determination with a high-resolution cut-off of 1.5 Å.

Table 5.2. Data processing and refinement statistics for *Ac*NiR collected using SF-ROX.

	SF-ROX^{OX}	SF-ROX^{NIT}	SF-ROX^{RED}
No. of crystals	75	62	33
Images collected	1867	1257	581
Images merged	1377	1039	410
Data collection			
Space group	$P2_13$	$P2_13$	$P2_13$
Unit cell dimensions			
a=b=c (Å)	94.95	94.92	94.61
α=β=γ (°)	90	90	90
Resolution (Å)	54.82 – 1.50 (1.54 – 1.50)[a]	54.80 – 1.50 (1.54 – 1.50)[a]	54.62 – 1.60 (1.64 – 1.60)[a]
R_{split} (%)	11.5 (90.4)[a]	10.6 (85.3)[a]	15.8 (70.8)[a]
$<I/\sigma(I)>$	6.3 (2.0)[a]	6.6 (2.3)[a]	5.4 (2.7)[a]
$CC_{1/2}$	0.980 (0.157)[a]	0.984 (0.288)[a]	0.957 (0.384)[a]
Completeness (%)	100.0 (100.0)[a]	100.0 (100.0)[a]	100.0 (100.0)[a]
Multiplicity	220.9 (77.2)[a]	154.7 (50.8)[a]	66.1 (44.3)[a]
Wilson B-factor (Å^2)	23.0	22.6	24.9
Refinement			
No. of unique reflections	45883 (2276)[a]	45846 (2275)[a]	37489 (1858)[a]
R_{work}/R_{free} (%)	14.4/17.7	14.2/17.2	16.5/19.8
No. atoms			
Protein	2608	2595	2580
Ligand/ion	37	22	59
Water	427	425	270
B-factors (Å^2)			
Protein	18.9	18.7	21.9
Cu	17.3	16.3	18.3
SO_4	33.2		
NO_2^-		18.0	
Malonate		32.3	30.1
Water	30.0	30.5	32.7
R.m.s deviations			
Bond length (Å)	0.01	0.01	0.01
Bond angles (°)	1.61	1.57	1.52
PDB access code	6GSQ	6GT0	6GT2

a. The highest resolution shell is shown in parenthesis.

5.2.4. Oxidised structure of *Ac*NiR determined by SF-ROX

The time-frozen, resting state structure of *Ac*NiR was refined to 1.5 Å. A comparison was made with both the native atomic resolution structure previously published (0.90 Å) and the recombinant synchrotron structure discussed above (0.96 Å). When compared to the recombinant structure, the structures are identical with an all-protein atom r.m.s.d. of 0.01 Å compared with 0.29 Å when aligned with the native structure. Both the T1Cu and T2Cu were assigned with full occupancy based on their B-factors relative to the protein backbone and neighbouring residues. The T1Cu was coordinated with the usual His_2-Cys-Met residues (Figure 5.9). In the surrounding residues, Met141 takes up two conformations, one orientated towards, and one away from His145. Adjacent to this residue, a loop consisting of residues 195-202 sits on the surface of the protein. In the SF-ROX structure, there is little electron density for most of these residues except for the Tyr196 side chain and a number of main chain C_α atoms. The T2Cu on the other hand had a number of marked differences. Like the atomic resolution structure (PDB: 2BW4), the T2Cu is ligated by a single water molecule (W1) (Figure 5.10). This is in marked contrast to the recombinant synchrotron structure where the T2Cu was ligated by two water molecules (W1 and W3). However, like the recombinant structure, W1 is highly ordered with a B-factor just slightly higher than that of the T2Cu. It is also orientated, pointing away from the catalytic resides. The distorted tetrahedral geometry relative to the His_3 plane is distinct from the native structure where W1 binds with true tetrahedral geometry including the His_3 plane. The Asp98 residue takes up two

conformations, one, the proximal position but the second is previously unobserved. The new conformation is a distorted proximal position with the $O^{\delta 1}$ atom position fixed and the side-chain rotating around such that the $O^{\delta 2}$ is hydrogen bonding directly to the T2Cu. Both conformations have equal (0.5) occupancy and because of the fixed $O^{\delta 1}$ position both hydrogen bond to W2 linking Asp98 to His255. The distorted proximal position is also able to hydrogen bond to W1 unlike the proximal position which hydrogen bonds to two waters in the solvent entry channel.

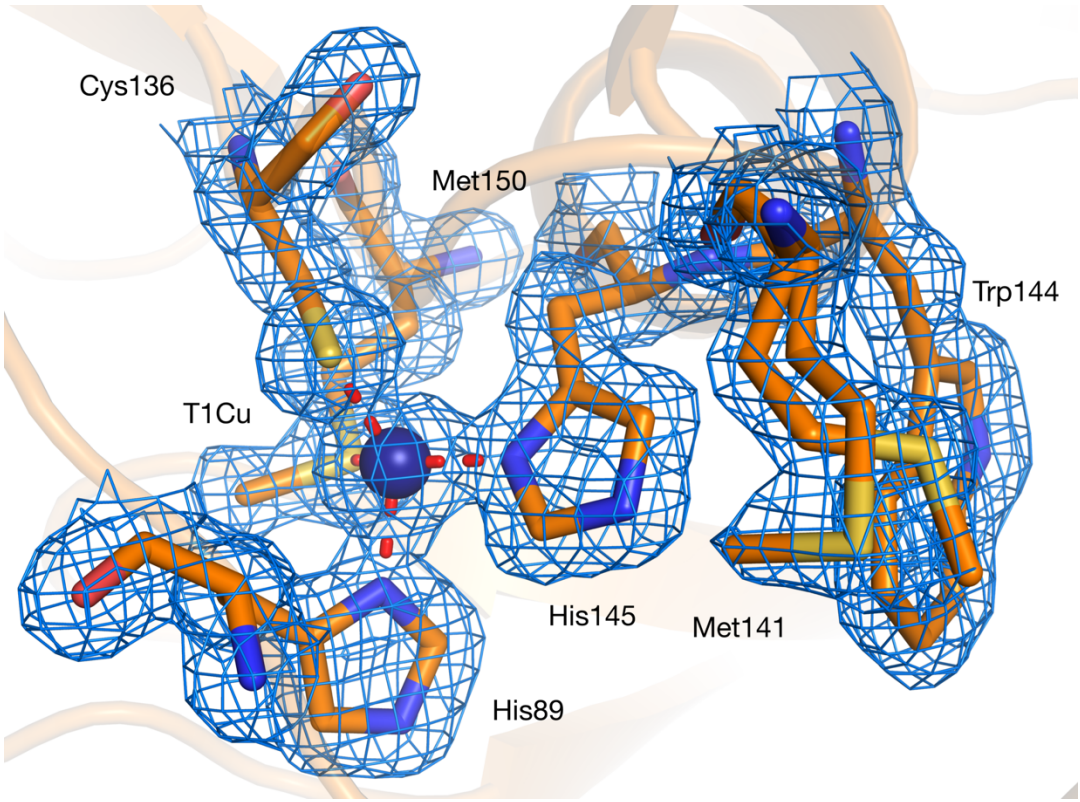

Figure 5.9. The SF-ROX structure of oxidised *Ac*NiR T1Cu. The T1Cu is ligated by the usual four ligands. Met141 is visible in it two conformations. 2Fo-Fc electron density map is contoured at the 1σ level and shown as blue mesh. The T2Cu is shown as a blue sphere. Metal-coordinating bonds are shown as red dotted lines (PDB: 6GSQ).

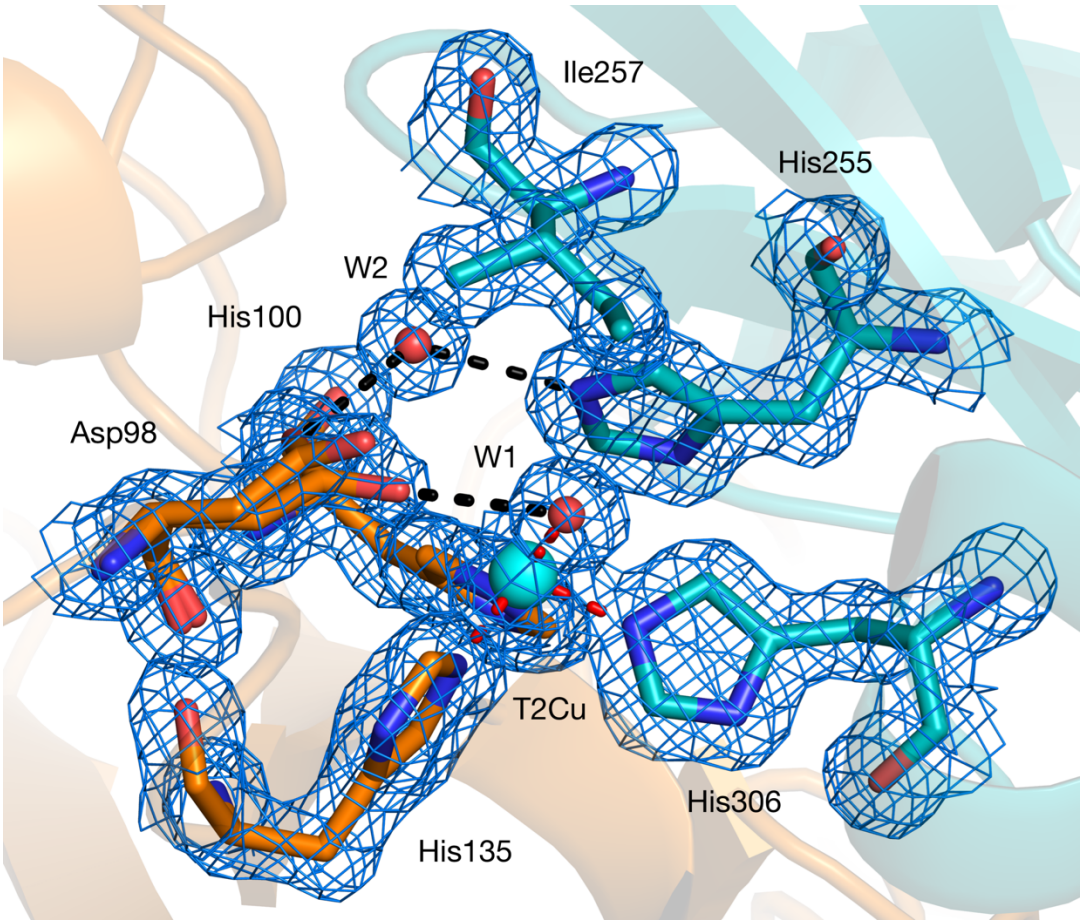

Figure 5.10. The SF-ROX structure of oxidised *Ac*NiR T2Cu. A single water molecule (W1) is ligated to the T2Cu in distorted tetrahedral geometry. The Asp98 is visible in two conformations, the distorted position hydrogen bonding directly to the T2Cu water. 2Fo-Fc electron density map is contoured at the 1 σ level and shown as blue mesh. The T2Cu is shown as a cyan sphere and water molecules as small red spheres. Metal-coordinating bonds are shown as red dotted lines. Selected hydrogen bonds are shown as black dotted lines (PDB: 6GSQ).

5.2.5. Reduced structure of *Ac*NiR determined by SF-ROX

The reduced structure of *Ac*NiR was refined to 1.6 Å. The resolution was lower than that of the resting state structure because of the effects of chemical reduction *via* soaking. To reduce the oxidised *Ac*NiR crystals, they were soaked in 100 mM ascorbate solution until all green crystal colour was lost. This, on average took around 30 minutes by observing the crystal under a microscope during soaking. No cracking or dissolving of the crystals took place. Soaking was stopped once the crystals turned completely colourless indicating their full reduction. Beyond this point, the crystals began to dissolve rapidly thus fishing and freezing the crystals in a rapid manner was vital. Because of the percentage of lost crystal volume, fewer images could be collected per image and fewer crystals could be used overall as ~50% dissolved too rapidly to be frozen. Once the crystals were frozen and maintained at 70 K, no more crystal degradation occurred. Soaking the crystals for such a long time in strong reductant was thought to degrade the crystal but the crystals diffracted just as well as the oxidised crystals. A full dataset was able to be collected from just 33 crystals because of their high symmetry albeit with a lower redundancy. Both T1 and T2 copper sites show marked changes from the oxidised structure. The T1Cu was assigned with a split position, one major (0.7 occupancy) and minor (0.3 occupancy) (Figure 5.11). When the oxidised and reduced structures were aligned, the minor copper position aligned well with the oxidised T1Cu. Therefore, the minor position remains as a small amount of oxidised T1Cu. The major position corresponds to the reduced T1Cu position. The Met141 residue is fully open

in the reduced structure with a water (W238) molecule linking His145 to Met141. Such a change upon reduction has never been observed in any nitrite reductase nor in any cuperodoxin and may arise from the ability to obtain 'true' reduced structure from single <10 fs shot images. The electron density for the surface loop is much more distinct than in the oxidised structure and the surface loop is shifted significantly. The T2Cu site is also rearranged upon reduction. The W1 in the oxidised structure is lost with the copper taken on just the His_3 ligation (Figure 5.12). Asp98 is present only in the proximal conformation with no electron density for the distorted proximal or gatekeeper conformations. The sidechain of Ile275 flipped down to compress the volume of the active site pocket to prevent any further ligand ligating to the reduced T2Cu which is pushed 0.5 Å into the histidine plane. A malonate present in the crystallisation mixture is present in the substrate entry channel causing a rearrangement of the channel water molecules.

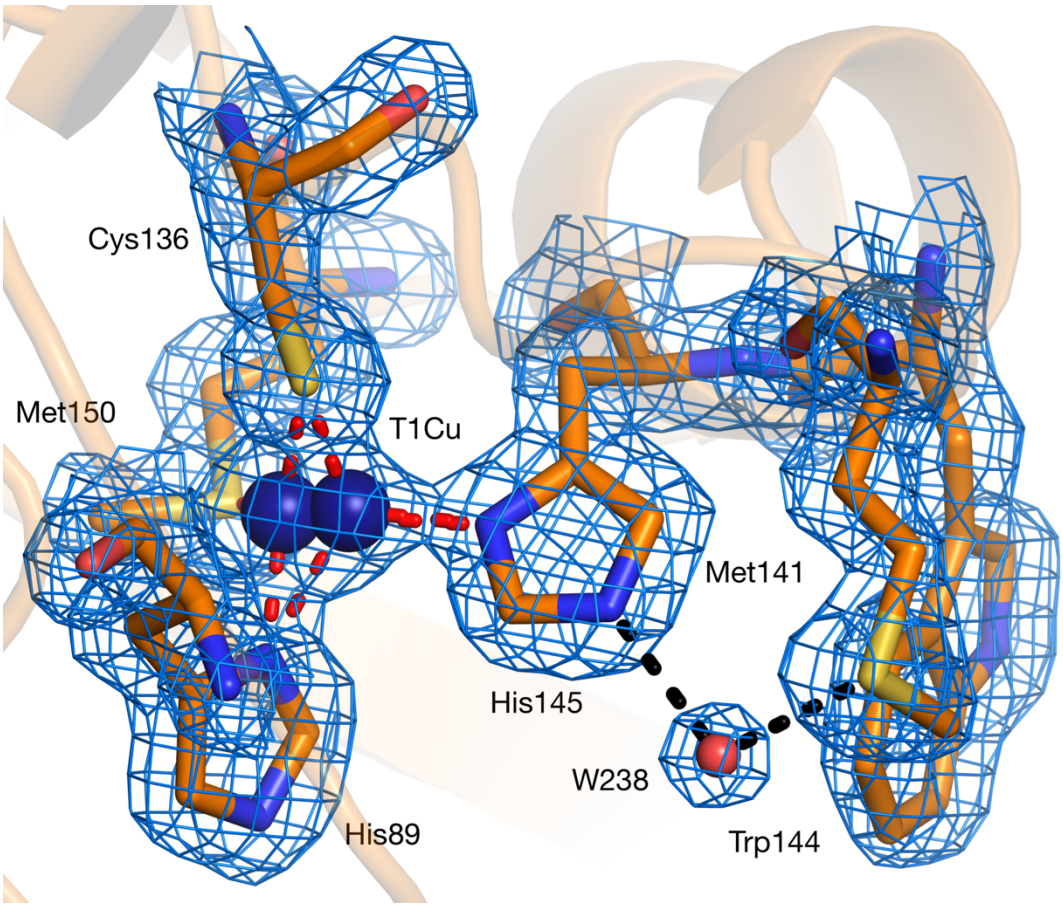

Figure 5.11. The SF-ROX structure of reduced *Ac*NiR T1Cu. The T1Cu is visible in two conformations; one corresponding to the reduced position and one corresponding to a small species of oxidised copper. Met141 is present only in a single conformation. 2Fo-Fc electron density map is contoured at the 1σ level and shown as blue mesh. The T2Cu is shown as a cyan sphere and water molecules as small red spheres. Metal-coordinating bonds are shown as red dotted lines. Selected hydrogen bonds are shown as black dotted lines (PDB: 6GT0).

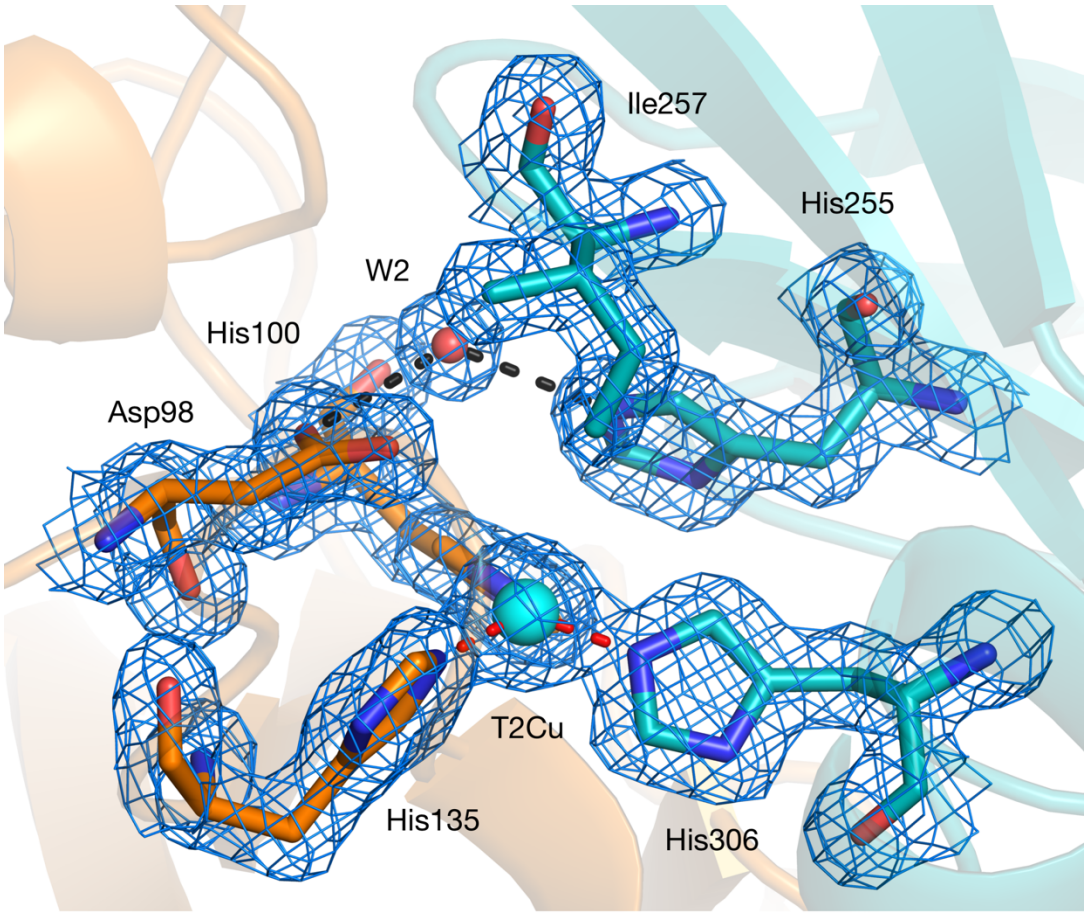

Figure 5.12. The SF-ROX structure of reduced *Ac*NiR T2Cu. The water molecule ligation T2Cu in the oxidised structure is lost. Ile257$_{CAT}$ side-chain flips down to compress the active site volume. 2Fo-Fc electron density map is contoured at the 1σ level and shown as blue mesh. The T2Cu is shown as a cyan sphere and water molecules as small red spheres. Metal-coordinating bonds are shown as red dotted lines. Selected hydrogen bonds are shown as black dotted lines (PDB: 6GT0).

5.2.6. NO_2^--bound structure of *Ac*NiR determined by SF-ROX

The NO_2^--bound structure of *Ac*NiR was refined to 1.5 Å. The switch from ammonium sulphate to Na-malonate as a cryoprotectant had no effect on the crystal diffracting power. There is little structural change in the T1Cu ligand geometry is visible compared to the resting state apart from the movement of Met141 to completely cover His145 (Figure 5.13). Atop the T2Cu, a large patch of positive electron density was visible. A single water did not satisfy the electron density and trying to fit two waters brought them too close together to be present at the same time. NO_2^- was then assigned which fitted well but still do not fully satisfy the electron density with positive patches on either side. It was finally decided that two NO_2^- ligands were present simultaneously (Figure 5.14). One was ligated nearest to the Asp98, bound in a 'top-hat' conformation while the second was furthest from the Asp98, bound in a 'side-on' conformation. Both NO_2^- molecules were assigned 0.5 occupancy based on their B-factors relative to the rest of the structure. Asp98 is present in both the proximal and gatekeeper conformations with 0.5 occupancy each, corresponding to the two NO_2^- conformations. The gatekeeper conformation, pointing away from the T2Cu corresponds to the 'top-hat' mode while the proximal conformation corresponds to the 'side-on' mode. This was based on the possible steric interaction of the proximal conformation with the 'top-hat' mode. A water molecule is present in the crystal structure occupying the proximal position of $Asp98_{CAT}$ when that residue is in the gatekeeper conformation. In the atomic resolution, NO_2^--bound structure of *Ac*NiR (PDB: 2BWI), the NO_2^- occupies a middle position in

between the two conformations visible here. When the reduction of NO_2^- *in crystallo* is initiated with photoelectrons in the X-ray beam, the first structure shows NO_2^- binding in a 'top-hat' and 'side-on' conformation which subsequently stabilises to a 'side-on' conformation after an increase in the absorbed dose[132]. The two NO_2^- ligands bound in that structure bind symmetrically with shared O positions. Here, the NO_2^- molecules are asymmetrical ligated with the O1 atoms, closest to the Asp98 separated by 1.3 Å, while the O2 atoms share the same special position.

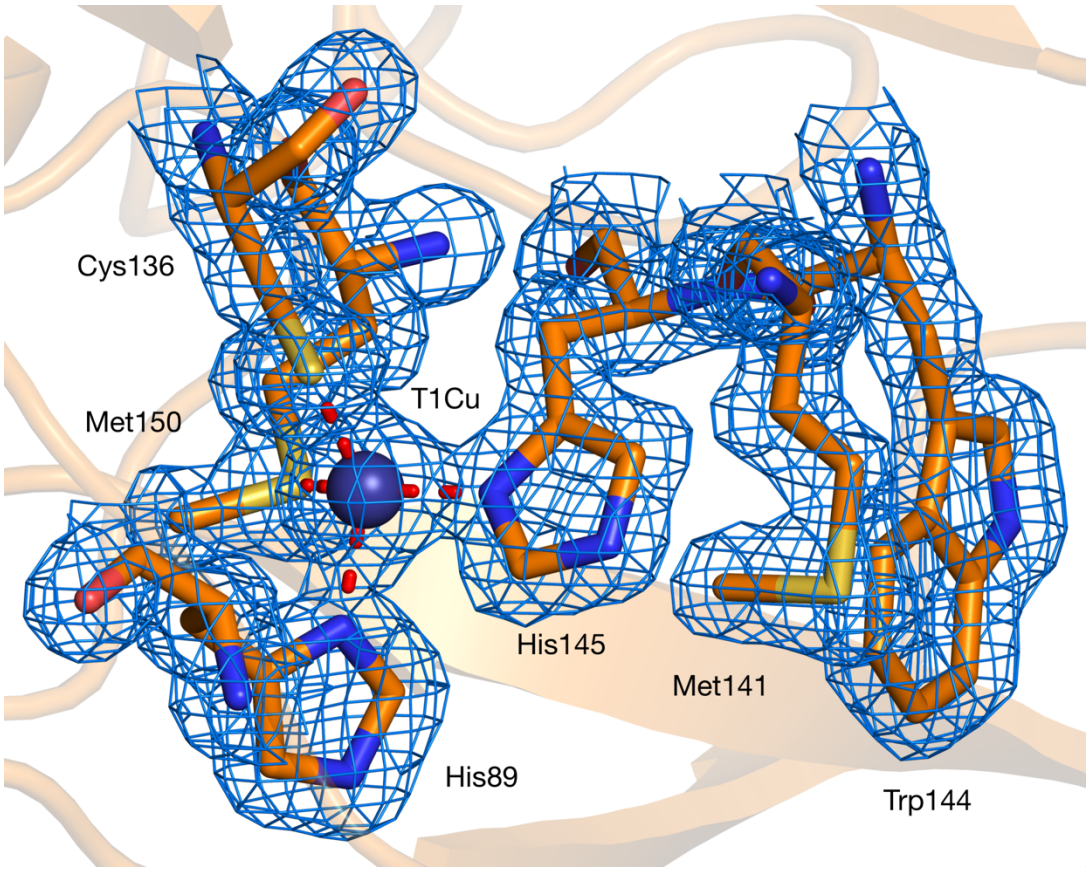

Figure 5.13. SF-ROX structure of NO_2^--bound *Ac*NiR T1Cu. The T1Cu is ligated by the usual four ligands. Met141 is visible in a single conformation coving His145. 2Fo-Fc electron density map is contoured at the 1σ level and shown as blue mesh. The T2Cu is shown as a blue sphere. Metal-coordinating bonds are shown as red dotted lines (PDB: 6GT2).

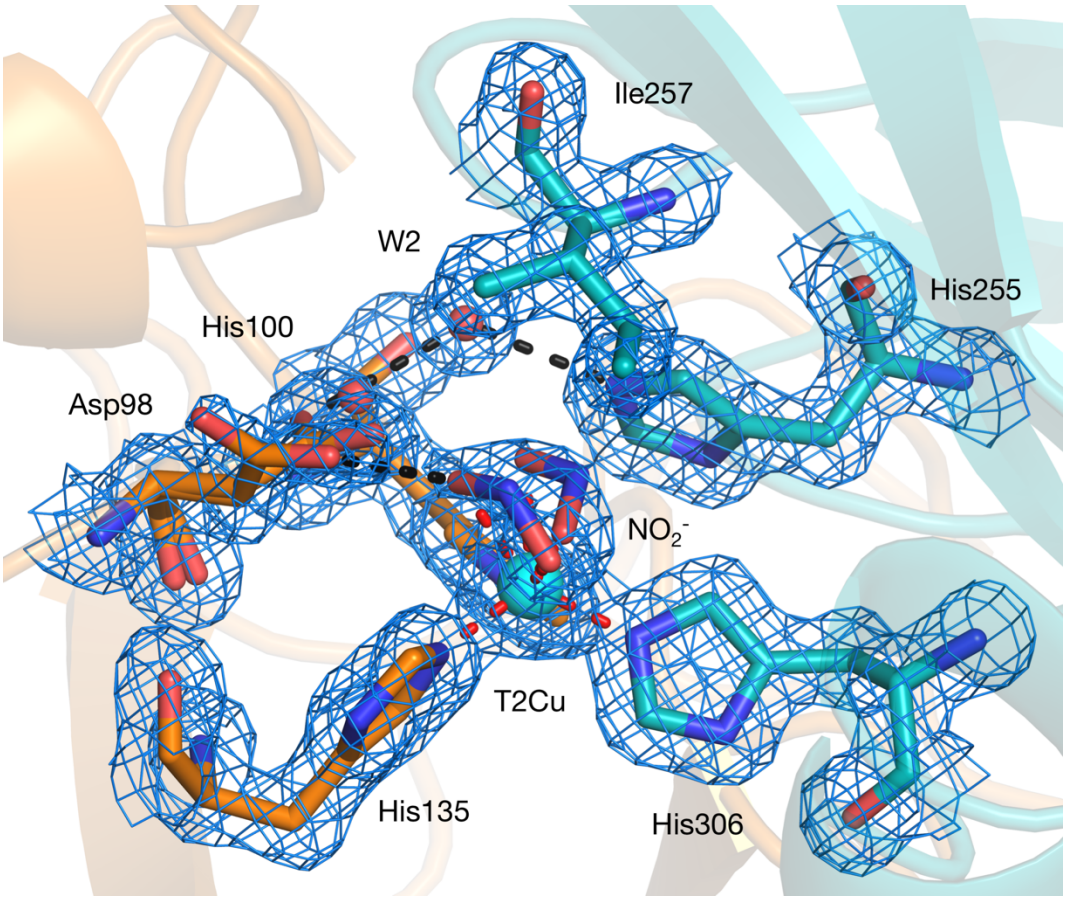

Figure 5.14. SF-ROX structure of NO_2^--bound *Ac*NiR T2Cu. The T2Cu is ligated by two NO_2^- molecules with 0.5 occupancy each. One has a 'top-hat' binding mode and the second has a 'side-on' binding mode. The $Asp98_{CAT}$ is present in two conformations corresponding to the two NO_2^- molecules. 2Fo-Fc electron density map is contoured at the 1σ level and shown as blue mesh. The T2Cu is shown as a cyan sphere and water molecules as small red spheres. Metal-coordinating bonds are shown as red dotted lines. Selected hydrogen bonds are shown as black dotted lines (PDB: 6GT2).

5.3. pH dependence of *Ac*NiR

5.3.1. In-house data collection

The observation of the two NO_2^- species bound to the T2Cu prompted a hypothesis about why the binding mode of NO_2^- changes in the MSOX series with increasing dose[132]. The local T2Cu ligand geometry is well known to change as the pH is altered[215–217]. To investigate if pH was the cause of the differences in NO_2^- binding observed between the SF-ROX structure and the MSOX series, a structural titration experiment was designed and carried out using the in-house source in the Barkla Biophysics Laboratory. Crystals of *Ac*NiR were grown from the same protein batch as for the SF-ROX experiment using the same crystallisation conditions. *Ac*NiR crystallises well between pH 4.5 to 5.0. All data collection so far in the chapter have been at pH 5.0. As the SF-ROX data collection was used to visualise the structure without any radiation damage, the data collection strategy for in-house source had to be changed from usual to limit the dose to as low as possible. The in-house source is a Rigaku FR-E+ SuperBright microfocus rotating anode generator with an EIGER R 4M photon counting detector. The low dose datasets were important to make sure we could distinguish pH dependent changes from irradiation induced changes. 3.4 M Na-malonate solution was prepared at a variety of pHs from 5.0 to 6.5 at 0.5 increments. 1 M $NaNO_2$ was then added to a final concentration of 3.1 M Na-malonate, 100 mM $NaNO_2$. Crystals were soaked for 15 minutes and then frozen directly in the cryo stream on the goniometer. The crystals were exposed for 15 minutes each with 60 images in total equating to 15 s per images with a 1.0° oscillation step per image. The

data were processed as for the SRX structure. The resolution limit limited to 1.5 Å due to the geometric constraints of the diffractometer. Data processing and refinement statistics are given in Table 5.3.

Table 5.3. Data processing and refinement statistics for *Ac*NiR collected with an in-house source.

	pH 5.0	pH 5.5	pH 6.0	pH 6.5
Data collection				
Space group	$P2_13$	$P2_13$	$P2_13$	$P2_13$
Unit cell dimensions				
a=b=c (Å)	95.42	95.47	95.63	95.53
α=β=γ (°)	90	90	90	90
Resolution (Å)	7.90 – 1.50 (1.53 – 1.50)[a]	8.19 – 1.50 (1.53 – 1.50)[a]	8.84 – 1.50 (1.53 – 1.50)[a]	7.90 – 1.50 (1.53 -1.50)[a]
$R_{p.i.m.}$ (%)	3.6 (47.3)[a]	3.6 (50.6)[a]	2.6 (20.1)[a]	2.5 (24.1)[a]
$<I/\sigma(I)>$	14.7 (1.4)[a]	14.1 (1.3)[a]	16.6 (3.1)[a]	17.8 (2.5)[a]
$CC_{1/2}$	0.999 (0.653)[a]	0.999 (0.657)[a]	0.999 (0.917)[a]	0.999 (0.876)[a]
Completeness (%)	99.7 (98.3)[a]	99.7 (96.4)[a]	99.7 (98.5)[a]	99.6 (95.3)[a]
Redundancy	6.2 (3.4)[a]	6.2 (3.4)[a]	6.1 (3.3)[a]	6.1 (3.4)[a]
Wilson B-factor ($Å^2$)	11.3	11.7	9.4	10.7
Refinement				
No. of unique reflections	46390 (2247)[a]	46462 (2204)[a]	46648 (2249)[a]	46466 (2186)[a]
R_{work}/R_{free} (%)	15.1/17.6	15.8/18.2	14.6/17.0	15.1/18.0
No. atoms				
Protein	2630	2653	2642	2673
Ligand/ion	29	22	22	19
Water	474	494	511	496
B-factors ($Å^2$)				
Protein	14.7	14.9	12.9	14.1
Cu	10.9	11.5	9.8	11.4
NO_2^-	12.1	12.9	12.2	13.6
Malonate	24.7	25.9	24.2	27.9
Water	28.1	28.7	26.2	27.0
R.m.s deviations				
Bond length (Å)	0.01	0.01	0.01	0.01
Bond angles (°)	1.66	1.65	1.78	1.75
PDB access code	6GTI	6GTK	6GTL	6GTN

a. The highest resolution shell is shown in parenthesis.

5.3.2. The effects of pH on *Ac*NiR

At the first attempt, crystals were only soaked for 10 s as with the SF-ROX NO_2^--bound structure. At all pH values there was no significant changes observed in any of the structures. The soaking time was then increased to 15 minutes to make sure that the buffer would fully permeate the crystal and change the pH throughout the lattice. The first structure collected at pH 5.0 was the same as the SF-ROX structure, unsurprising as both crystals are at the same pH. Both the 'top-hat' and 'side-on' NO_2^- conformations are visible, bound to the T2Cu in equal occupancy. Both conformations of Asp98 are present with the proximal position in opposition to the 'top-hat' binding mode. The limited electron density observed in the surface loop, residues 195 – 202 is still present. When the pH was increased to 5.5, no conformational changes are visible in the local T2Cu site. No changes occur in the T1Cu geometry, but the position of Met141 now adopts two conformations instead of a single one at pH 5.0 (Figure 5.15). The space generated by this partial movement allows a water molecule to hydrogen bond directly to His145. This bond completes a water network from the T1Cu to the protein surface emerging at the low electron density loop. At pH 6.0, no change is visible in the T2Cu geometry with both NO_2^- conformations present. The conformation of Met141 visible at pH 5.0 is lost with the secondary conformation visible at pH 5.5 taking on full occupancy. This allows the partial water position to also become fully occupied. Adjacent to Met141 is Trp144. At pH 6.0, the side chain of Trp144 rotates 180° around corresponding to a major movement of the surface loop (Figure 5.16). This loop is known to be involved in the

complex of CuNiRs with electron carrier proteins such as azurin or *c*-type cytochromes. The one crystal structure of a CuNiR complexed with an electron transporter is a structure of *Ax*NiR complexed with cytochrome c_{551} (PDB: 2ZON) (Figure 5.17)[69]. The structures were aligned by superposition of the secondary structure elements and protein backbone C_α atoms using the SSM algorithm, revealed that complex interface directly involved this surface loop[204]. At pH 6.5, both conformations of Trp144 are present. The electron density of the surface loop is distinct suggesting it has repositioned due to the change in pH. Only a single 'side-on' conformation of NO_2^- is now bound to the T2Cu as well as a partial water positioned as in the SF-ROX structure (Figure 5.18).

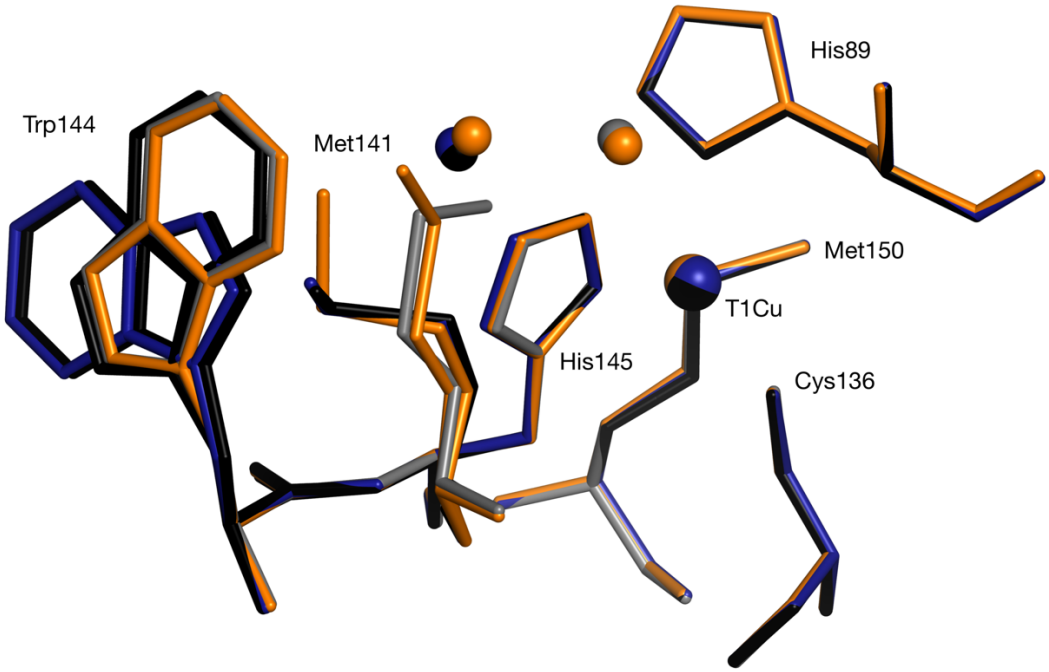

Figure 5.15. The pH dependence of the T1Cu second sphere amino acids. Superposition of the 4 pH range structures. The movement of Met141 and the rotation of Try144 are visible. The partial and then full occupied water takes the place of Met141 after the pH dependent movement. AcNiR at pH 5.0 is shown in grey (PDB: 6GTI), pH 5.5 in orange (PDB: 6GTK), pH 6.0 in blue (PDB: 6GTL) and pH 6.5 in black (PDB: 6GTN).

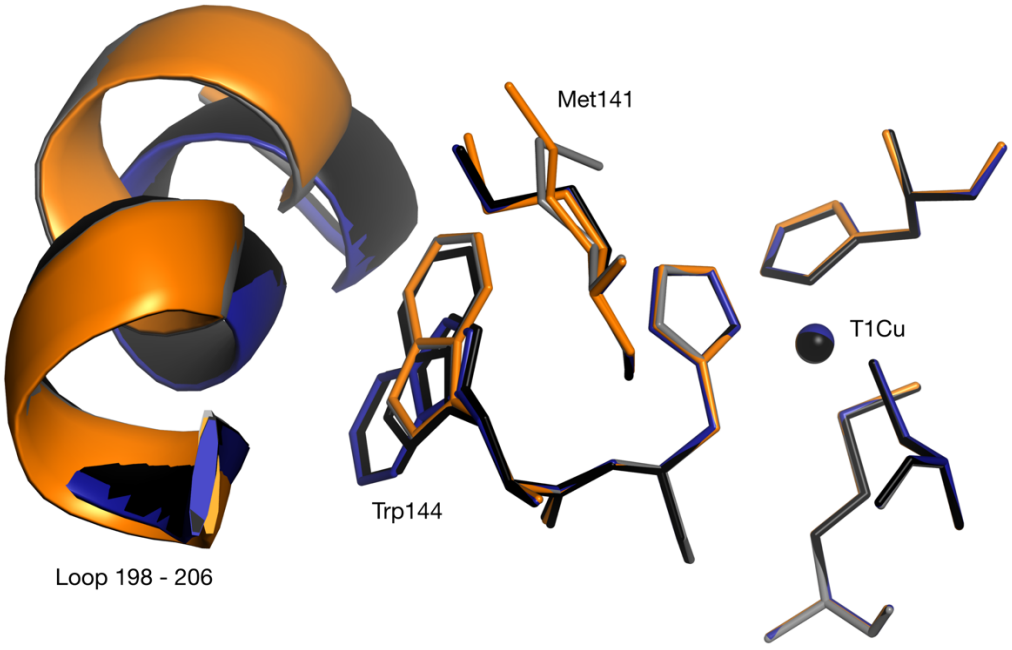

Figure 5.16. The pH dependence in the redox surface loop. Superposition of the four *Ac*NiR structures collected with a pH range. The surface loop rearranges with increasing pH. AcNiR at pH 5.0 is shown in grey (PDB: 6GTI), pH 5.5 in orange (PDB: 6GTK), pH 6.0 in blue (PDB: 6GTL) and pH 6.5 in black (PDB: 6GTN).

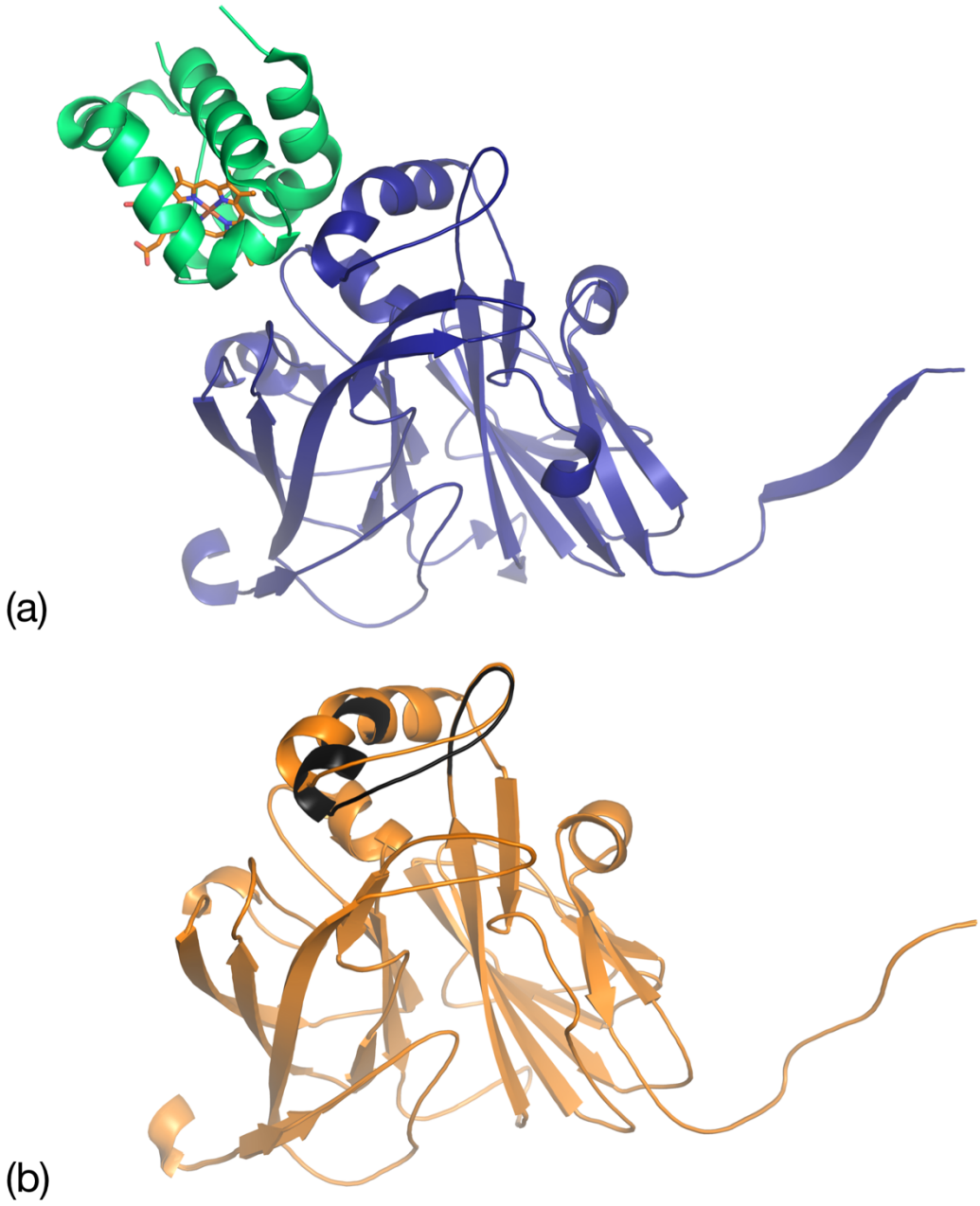

Figure 5.17. The reordering of the redox loop with pH. (a) Crystal structure of *Ax*NiR complexed with cytochrome c_{551} (PDB: 2ZON)[69]. *Ax*NiR is shown in blue, cytochrome c_{551} in green with the haem group shown in orange. (b) A superposition of *Ac*NiR collected using a low dose in-house source at pH 5.5 in (PDB: 6GTK), pH 6.0 (PDB: 6GTL). The shift of the surface loop from pH 5.5 to 6.0 is shown in black. This loop is the part of the docking surface for cytochrome c_{551}.

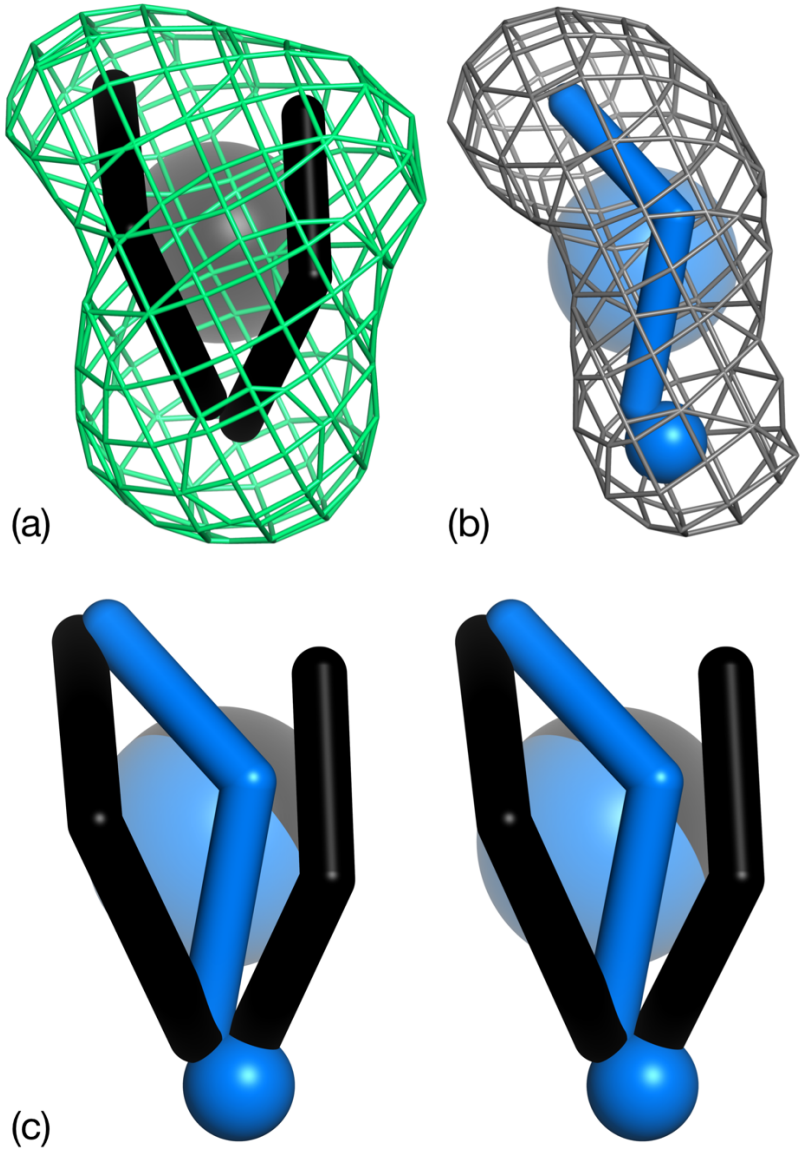

Figure 5.18. The pH dependent binding of NO_2^- to T2Cu. (a) At pH 6.0, NO_2^- binds in both a 'top-hat' and 'side-on' conformation. (b) When the pH is raised to pH 6.5, the 'top-hat' conformation is lost and the 'side-on' conformation remains along with a partial water molecule. (c) A cross-eyed stereo picture of the superposition *Ac*NiR at pH 6.0 and 6.5. *Ac*NiR at pH 6.0 (PDB: 6GTL) is shown in black with Fo-Fc electron density around the NO_2^- contoured at the 4σ level shown as a green mesh. *Ac*NiR at pH 6.5 (PDB: 6GTN) is shown in blue Fo-Fc electron density around the NO_2^- contoured at the 4σ level shown as a grey mesh.

5.4. Neutron crystallography (NX)

5.4.1. Perdeuterated *Ac*NiR crystallisation

The pH effects observed in *Ac*NiR brought into focus an ongoing project to probe *Ac*NiR using NX to visualise the hydrogen positions and determine the mechanism intermediates. Whereas X-rays scatter off atomic electron shells, neutrons scatter off atomic nuclei and so nuclear scattering length density, instead of electron density is observed. Hydrogen atoms have a negative neutron scattering length (-0.374) that means they tend to cancel out the signal from neighbouring carbon (0.665) and nitrogen (0.936) atoms. Deuterium atoms, on the other hand, have a positive neutron scattering length (0.667) and therefore produce a strong signal from neutron scattering experiments. The exchangeable hydrogen positions can be switched to deuterium by buffer exchanging into D_2O based buffers. However, the other positions require the protein to be expressed in D_2O and so all hydrogens are replaced with deuterium. Perdeuterated *Ac*NiR was expressed at the Deuteration Laboratory[180] at the Institut Laue-Langevin, Grenoble, France and crystallised by hanging-drop vapour diffusion in Hampton 24 well crystallisation plates. Crystals were grown from 20 mg/ml perdeuterated *Ac*NiR in 50 mM MES-OH buffer, pH 6.5 set against 1.1 M ammonium sulphate and 100 mM sodium acetate, pH 5.0 solutions made up in D_2O. Over the course of 2 weeks a number of crystals of size 0.9 x 0.4 x 1.0 mm with the volume around 0.36 mm^3 size grew and were mounted in a 2 mm diameter quartz capillary for neutron data collection.

5.4.2. NX data collection

Initial data collection took place at LADI-III[218], Institut Laue-Langevin over the course of 1 week. The first test took place on a single crystal using a neutron wavelength range of 3.05 - 4.00 Å. The crystal was exposed for 18 h at RT but no high-resolution data was observed. The crystal was subsequently tested at three different orientations but no improvement in diffraction was observed. To investigate if the crystals were fundamentally flawed, a single image was collected from the crystal using an X-ray copper rotating anode source. The crystal diffracted to 1.8 Å, the geometric limit of the Mar345 image-plate detector setup (Figure 5.19). The reason for this disparity is unknown. Subsequently, over the course of four years, a full dataset was collected by Dr Matthew P. Blakeley, LADI-III, Large Scale Structures. This dataset was based on crystals grown from the same perdeuterated *Ac*NiR purification as described in Chapter 3 and crystallised as above and has been previously been described here[55] although has not yet been reported on in full. 20 images, each of 18 h exposure time, were collected from four crystal orientations and diffraction spots were recorded at 1.8 Å (Figure 5.20). The images were indexed and integrated using *LAUEGEN*[219], wavelength-normalized using *LSCALE*[220] and scaled and merged using *SCALA*[193].

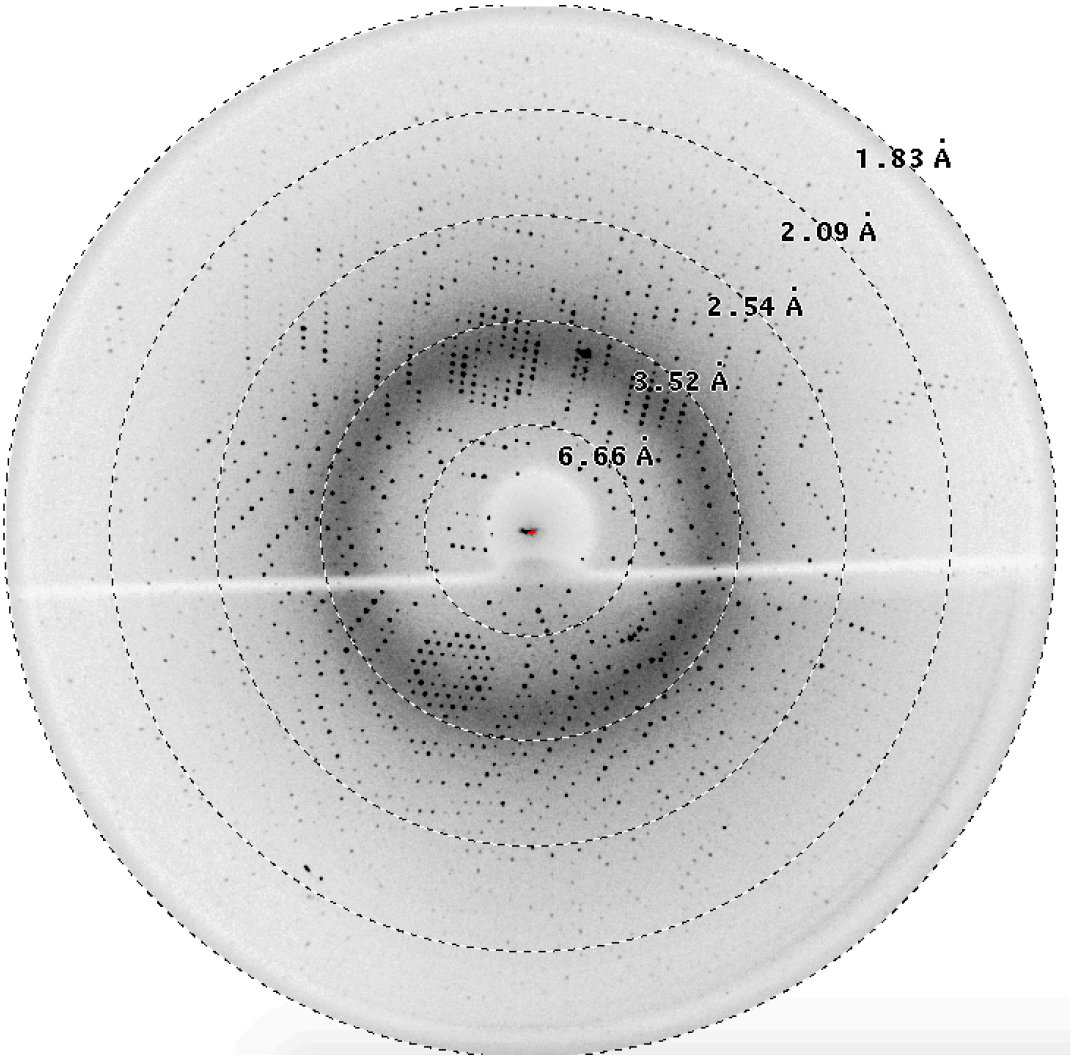

Figure 5.19. An X-ray diffraction pattern collected from a perdeuterated *Ac*NiR crystal. The crystal diffracted to 1.8 Å, the geometric limit of the Mar345 image-plate detector setup.

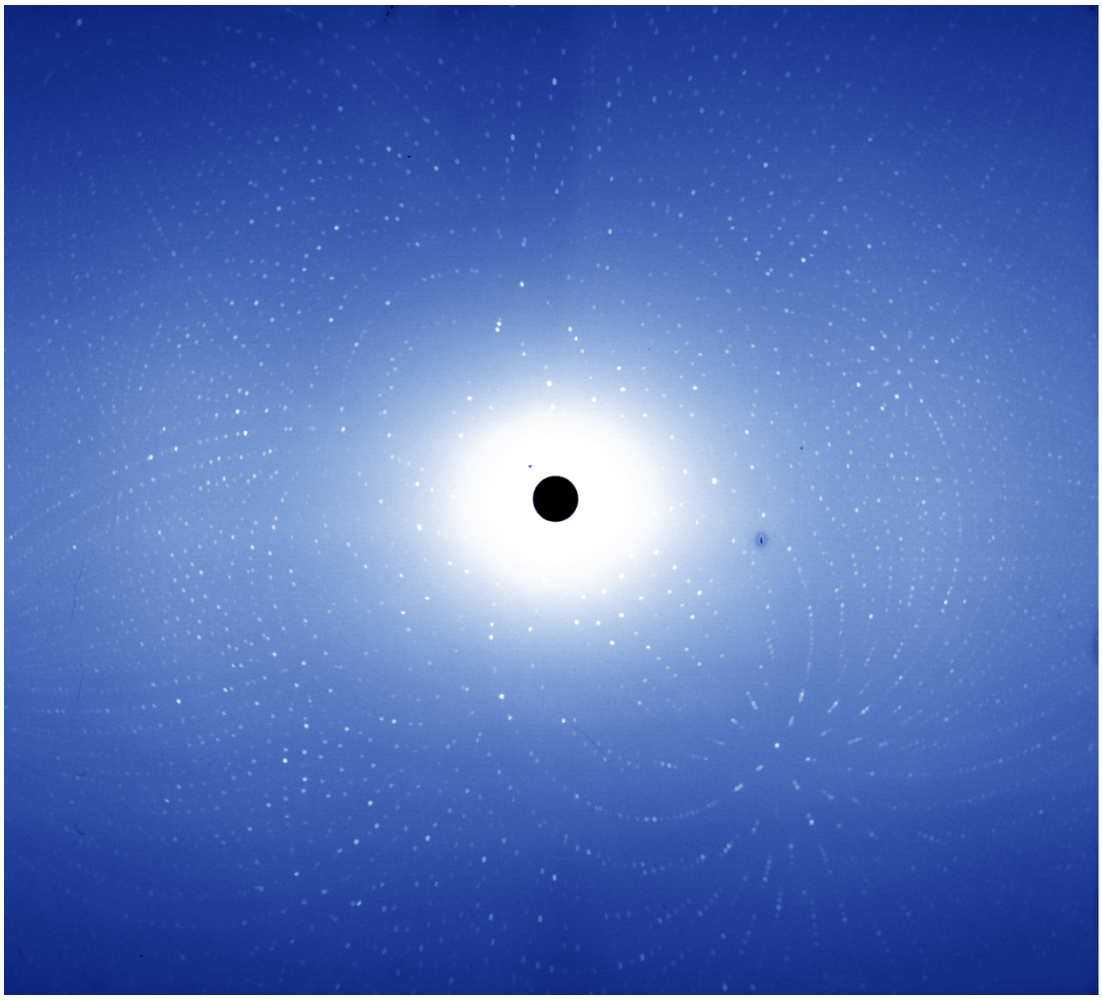

Figure 5.20. A neutron quasi-Laue diffraction pattern collected from a perdeuterated *Ac*NiR crystal. A single image after 18 h exposure revealed diffraction spots to 1.8 Å.

5.4.3. Oxidised structure of perdeuterated AcNiR determined by NX

The RT oxidised neutron data was refined to 1.8 Å using *phenix.refine* with deuteriums added to all hydrogen positions[197,221]. Both the T1 and T2Cu sites were full occupied based on their B-factors relative to the protein backbone. At RT, Met141 is shown in the closed position, covering His145 compared to the oxidized SF-ROX structure were two conformations of Met141 are observed (Figure 5.21). The surface loop (residues 187 - 206) which is disordered in the oxidized SF-ROX structure is ordered in the neutron structure as it is in the reduced SF-ROX structure and the high-pH low dose structures (Figure 5.22). The T2Cu site is coordinated by two water molecules (W1 and W3), with W1 adopting the distorted tetrahedral position observed in the oxidized SF-ROX structure and the SRX structure (Figure 5.23). W3 is also present in the SRX structure again with the same low density observed here. Asp98 is present in a single conformation albeit with a low level of nuclear scattering length density compared to the other active site residue side-chains.

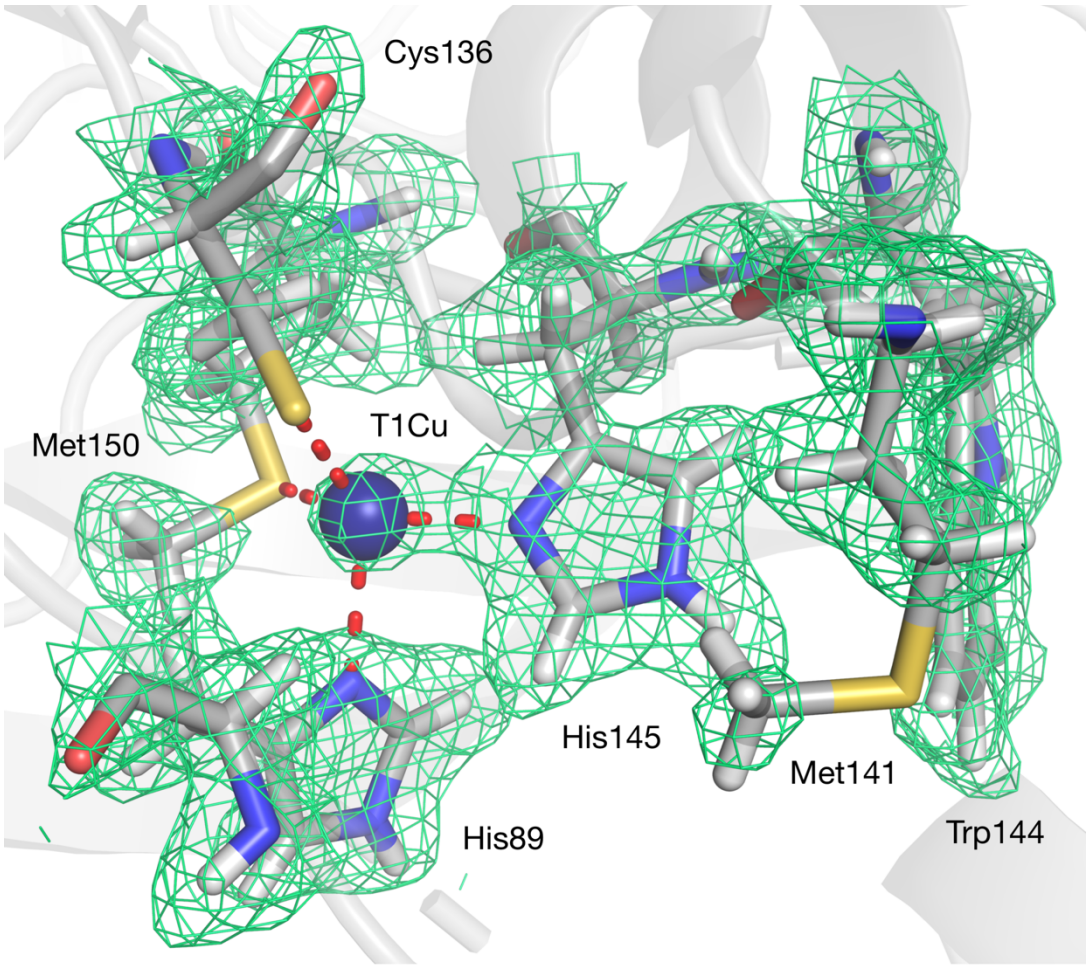

Figure 5.21. The NX structure of oxidised perdeuterated *Ac*NiR T1Cu. The T1Cu site visualised using NX at 1.8 Å at RT. The copper ligands are visible with exchangeable hydrogen positions protonated. Met141 is visible in a single conformation covering His145. 2Fo-Fc nuclear scattering length density map is contoured at the 1σ level and shown as green mesh. Atoms are coloured by element, with a different colour scheme used for the different chains. The T2Cu is shown as a blue sphere, Metal-coordinating bonds are shown as red and green dotted lines (PDB: 6GTJ).

Figure 5.22. Structural alignment of oxidised SF-ROX, reduced SF-ROX and oxidised neutron structures. The oxidised SF-ROX loop is disordered with limited electron density, while the loop in the reduced SF-ROX and oxidised neutron structures is ordered and moved towards the structure. The oxidised SF-ROX (PDB: 6GSQ) is shown in purple, the reduced SF-ROX (PDB: 6GT2) in blue and the oxidised NX (PDB: 6GTJ) in green.

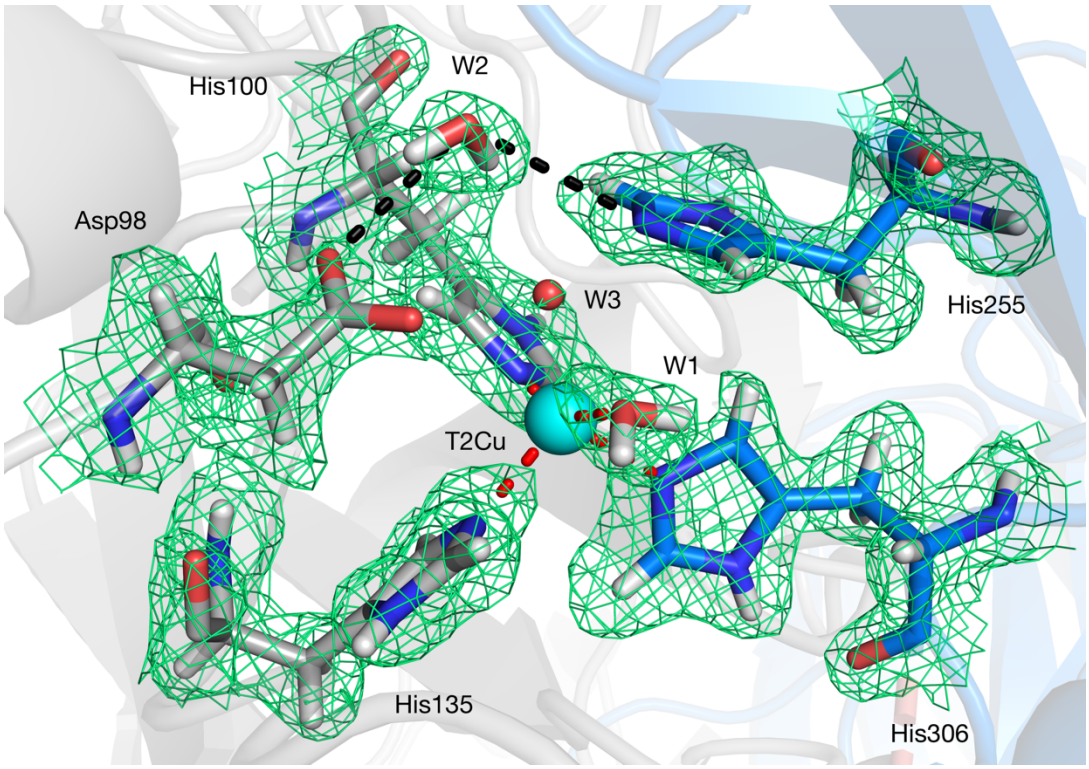

Figure 5.23. The NX structure of oxidised perdeuterated *Ac*NiR T2Cu. The T2Cu is ligated by two water molecules (W1 and W3). W1 is ligated in a distorted tetrahedral geometry consistent with the SF-ROX^{OX} structure and modelled as a protonated water. W3 has low level electron density and is no protonated. The linking water (W2) is hydrogen bonded between Asp98 and His255. Both Asp98 and His255 are unprotonated in the structure crystallised at pH 5.0. 2Fo-Fc nuclear scattering length density map is contoured at the 1σ level and shown as green mesh. Atoms are coloured by element, with a different colour scheme used for the different chains. The T2Cu is shown as a cyan sphere, D_2O water molecules shown as red and white sticks and water molecules as small red spheres. Metal-coordinating bonds are shown as red dotted lines. Selected hydrogen bonds are shown as black dotted lines (PDB: 6GTJ).

5.4.4. Protonation states of the active site residues

The two protons required for catalysis are through to be provided by the active site residues Asp98 and His255[211]. At pH 5.0, it would therefore be expected that both these residues would be protonated, ready for NO_2^- binding and proton donation. It is clear in the oxidised neutron structure that Asp98 and His255 are unprotonated at the expected donation positions. His255 is protonated at the other exchangeable position along with all the T1 and T2Cu ligation residues. The linking water (W2) is fully protonated, hydrogen bonded between Asp98 and His255 with hydrogen positions directed at Asp98 and His255. The structure is also consistent with the two proton uptake mechanism of CuNiR at pH 5.0 when T2Cu is water ligated[222]. The low level of nuclear scattering length density in the oxidized neutron Asp98 may be related to the dual conformation of Asp98 visible in the oxidized SF-ROX structure. At pH 5.0, Asp98 may be in a dynamic equilibrium between the protonated and unprotonated states based on a pKa of 3.9. If W1 is orientated in the same manner in both the oxidized SF-ROX structures as in the oxidized neutron structure with the hydrogen positioned directed away from the T2Cu, then the proximal position represents the unprotonated Asp98 while the distorted proximal position represents the protonated Asp98. The disparity in the unprotonated oxidized neutron Asp98 and equilibrium observed in the oxidized SF-ROX Asp98 is important in the context of pH change induced by radiation damage. Active site residues, especially acidic resides are known to be vulnerable to radiation damage and SRX data collection may explain why the distorted proximal position has not been

previously observed[223]. The ordering of the surface loop displays a similar pattern to Asp98 where its loop is disordered in the cryo oxidized SF-ROX structure but ordered in the RT oxidized neutron structure. The ordering of the loop in the reduced SF-ROX structure is due to a pH induced changed caused by the ascorbate soaking. Synchrotron radiation induced pH changes may result in the loss of intermediates that may be visualized using femtosecond crystallography.

Chapter 6 - General discussion and findings

6.1. Data collection using the SF-ROX method

The SF-ROX method has been used here to characterise the time-frozen structures of CuNiR from *A. xylosoxidans* and *A. cycloclastes*. In the case of *Ax*NiR, the oxidised structure was collected revealing an unprecedented dioxygen species binding to the T2Cu site. Three structures of *Ac*NiR were collected representing the oxidised, reduced and NO_2^--bound states (unpublished). The development of the SF-ROX methodology using cytochrome *c* oxidase allowed the collection of cryo temperature datasets, unlike the SFX method and allowed for the possibility of higher resolution data collection because of the greater volume crystalline material interacting with the XFEL beam[126]. The approach in the work covered in this thesis was collect these structures using femtosecond crystallography and both *Ax* and *Ac*NiR proved high amenable to the SF-ROX method. A number of considerations must be considered however when deciding on the type of XFEL experiment to perform. In the case of SF-ROX, the crystal morphology and underlying symmetry had a large effect on the efficiency of data collection, important given the limited XFEL beamtime available.

When the data collection parameters of the oxidised *Ax* and *Ac*NiR SF-

ROX are compared, the crystal size, morphology and symmetry, have a significant effect on the data collection time and multiplicity of the data (Table 6.1). The *Ac*NiR dataset, which was crystallised in a cubic space group ($P2_13$), had a multiplicity of 246 from 1377 images collected in 8 hours. The *Ax*NiR dataset, containing ~2.5x more images, has ~2.3x lower multiplicity. *Ax*NiR was crystallised in a trigonal space group (H3) with one full dataset taking 12 hours to collect. As the crystal is rotated between snapshots, the number of images that can be collected per crystal is reduced in crystals with 2D morphology. However, with the flat plane of the crystal perpendicular to the beam, a large number of images can be collected from a single crystal. The optimal requirement for SF-ROX crystallisation are therefore the same as standard MX data collection; a large, highly diffracting, high symmetry crystal although the lack of these attributes, which can be overcome in MX, can lead to lengthy SF-ROX data collections. In MX, a low symmetry crystal can be rotated through 360° to fully record the reciprocal space. With femtosecond crystallography, all the recorded reflections are partial, and each Bragg reflection curve must be sampled sufficiently to complete the dataset.

Table 6.1. Comparison of oxidised CuNiR SF-ROX data collection.

Dataset	*Ax*NiR^{OX}	*Ac*NiR^{OX}
Beamline	BL3	BL2
Space group	H3	$P2_13$
No. of crystals	64	75
Indexed images	3656	1377
Average images per crystal	57	18
Degree step (°)	365.6	137.7
Resolution (Å)	1.6	1.6
Multiplicity	106	246
Collection time (h)	12	8
Crystal morphology	2D plate	3D pyramid
Crystal size (W x H x D mm)	1 x 0.8 x 0.05	0.7 x 0.7 x 0.7

6.2. Structural basis for the oxidase activity of *Ax*NiR

Using SF-ROX, the 'time-frozen' oxidised structure of *Ax*NiR has been determined. While the global structure of the enzyme, compared to the SRX structure, was near identical, the T2Cu ligand was altered with T2Cu-H_2O ligation observed in the SRX structure and T2Cu-O_2^- observed in the SF-ROX structure. While other diatoms have been shown binding to the T2Cu site in CuNiRs, notably NO and O_2, this is the first time an end-on bound species has been observed with full occupancy[54,76]. The refined oxygen species had an O-O bond length of 1.24 Å, consistent with O_2 or O_2^- (1.2 – 1.3 Å) and not with a peroxide species (1.4 -1.5 Å)[224]. The observation of this dioxygen ligand provides a structural basis for the oxidase activity of this enzyme although the reason for the appearance of the species is unknown. NO_2^- and NO have been suggested to bind endogenously to T2Cu during purification or crystallisation. Fukuda and colleagues argue that the NO species modelled in this structure (PDB: 2BW5) has a refined N-O bond length of 1.41 Å which is much closer to a dioxygen species than a NO species (1.15 Å)[225]. However, the species refined in the endogenous *Ac*NiR structure is NH_2OH which, in its N-protonated form, has an N-O bond length of 1.41 Å. O_2 binding in *Gt*NiR was conformed based on the functions of CuNiR as an oxygen reductase along with an absorption band at 325 nm relating to a copper(II)-superoxo species[76].

The presence of reduced T2Cu in *Ax*NiR purification could bind O_2, trapping the oxidised T2Cu bound to the reduced O_2 waiting for electron turnover to produce H_2O_2 or a source of O_2^- could simply bind to the oxidised

T2Cu and again stabilise awaiting electron turnover[226]. A source of O_2^- in this case may be the crystallisation media where PEG 550 MME was used as the precipitant which may have decomposed. The presence of the H_2O ligand in SRX structure of CuNiR can be explained by the production of photoelectron *in crystallo* which lead to the reduction of O_2^- to H_2O_2 which is then replaced by H_2O.

6.3. The pH dependence of AcNiR

The visualisation for *Ax*NiR T2Cu bound O_2^- provided a structural basis for the oxidase activity of that particular CuNiR but did not address the question of the true CuNiR resting state with respect to the reaction order. SF-ROX was able to reveal the 'time-frozen' structures of oxidised, reduced and substrate bound *Ac*NiR showing that *Ac*NiR T2Cu is ligated by a water molecule in the resting state that is lost upon the reduction of the copper. This observation was confirmed by the oxidised neutron structure that was collected showing a water molecule bound in the same position as in the oxidised SF-ROX dataset. NO_2^- binding and conversion to NO has been observed in *Ac*NiR using the MSOX method which revealed a switch in the conformation of NO_2^- from 'top-hat' to 'side-on' with increasing X-ray dose[132,156]. The initial interpretation of that observation was that the switch is the result of an initial electron transfer from the T1Cu to the T2Cu and that the 'side-on' bound NO_2^- represents the initial reaction state. However, in the SF-ROX structure both 'top-hat' and 'side-on' conformations of NO_2^- are observed simultaneously, before the onset of any photochemistry. To understand what the cause of the switch from 'top-hat' to 'side-on' NO_2^- was, the pH effect on the crystal was probed revealing the switch from 'top-hat' to 'side-on' occurred between pH 6.0 and 6.5. The effect of SRX data collection was to cause solvent radiolysis in the crystal and increase the pH, thereby causing the conformation of NO_2^- to shift with increasing dose.

The effect of pH was also evident around the T1Cu site. A surface loop, known to form part of the interaction surface for redox partner proteins is

highly disordered at pH 5.5 but becomes ordered at pH 6.0[69]. There is also and accompanying movement in the T1Cu second sphere amino acids, Met141 and Try144 which shift as the loop becomes ordered, uncovering the T1Cu His145 residue and allowing the formation of a water network to connect the protein surface adjacent to the loop to the T1Cu. The suggests a mechanism for intermolecular electron transfer where the redox partner protein interacts with the loop and induces it to take on the ordered conformation. This then causes the rearrangement of the T1Cu second sphere amino acids, establishes the water network and increases the reduction potential of T1Cu, priming it to receive an electron from the redox protein. The results from the *Ac*NiR data collection point to an ordered mechanism of NO_2^- reduction[62,63,222]. The T2Cu is ligated by water in the resting which is replaced by NO_2^- before T1Cu to T2Cu electron transfer.

6.4. Future work and concluding remarks

The SF-ROX data collection carried out here suggests that the interpretation of SRX structures must be tempered based on the actions of X-ray induced photochemistry in CuNiRs. In *Ax*NiR, a change in T2Cu ligand from dioxygen to water is observed necessitating a review into aerobically purified enzyme structure and the corresponding spectroscopic data. In *Ac*NiR, photolysis of solvent induced a pH change causing a geometric rearrangement in ligand binding. The SF-ROX structural visualisation of NO-bound T2Cu would be of great interest to complete the trio of datasets collected here for *Ac*NiR. The binding mode of NO has been observed to be end-on in spectroscopic experiments and predicted by computer simulation[227,228]. This is in opposition to the side-on NO binding observed in crystal structures[54,207]. The diffraction before destruction approach taken here has been important, not only to outrun radiation damage, but to produce 'time-frozen' structure, free of molecular vibration and rotation from as-isolated enzymes that reveal the effects of radiation damage when compared to their synchrotron counterparts.

References

1. Wallace, J. M. & Hobbs, P. V. Introduction and Overview. in *Atmospheric Science* 1–23 (Elsevier, 2006). doi:10.1016/B978-0-12-732951-2.50006-5
2. Vitousek, P. M., Aber, J. D., Howarth, R. H., Likens, G. E., Matson, P. A., Schindler, D. W., Schlesinger, W. H. & Tilman, D. G. Human alteration of the global nitrogen cycle: Source and consequences. *Ecol. Appl.* **7,** 737–750 (1997).
3. Rascio, N. & La Rocca, N. Biological Nitrogen Fixation. in *Reference Module in Earth Systems and Environmental Sciences* 1–16 (Elsevier, 2013). doi:10.1016/B978-0-12-409548-9.00685-0
4. Schindelin, H., Kisker, C., Schlessman, J. L., Howard, J. B. & Rees, D. Structure of ADP·AIF4 –-stabilized nitrogenase complex and its implications for signal transduction. *Nature* **387,** 370–376 (1997).
5. Hoffman, B. M., Lukoyanov, D., Yang, Z.-Y., Dean, D. R. & Seefeldt, L. C. Mechanism of Nitrogen Fixation by Nitrogenase: The Next Stage. *Chem. Rev.* **114,** 4041–4062 (2014).
6. Kim, J. & Rees, D. Structural models for the metal centers in the nitrogenase molybdenum-iron protein. *Science* **257,** 1677–1682 (1992).
7. Eady, R. R. Structure-function relationships of alternative nitrogenases. *Chem. Rev.* **96,** 3013–3030 (1996).
8. Kowalchuk, G. A. & Stephen, J. R. Ammonia-Oxidizing Bacteria: A Model for Molecular Microbial Ecology. *Annu. Rev. Microbiol.* **55,** 485–529 (2001).
9. Leininger, S., Urich, T., Schloter, M., Schwark, L., Qi, J., Nicol, G. W., Prosser, J. I., Schuster, S. C. & Schleper, C. Archaea predominate among ammonia-oxidizing prokaryotes in soils. *Nature* **442,** 806–809 (2006).
10. Caranto, J. D. & Lancaster, K. M. Nitric oxide is an obligate bacterial nitrification intermediate produced by hydroxylamine oxidoreductase. *Proc. Natl. Acad. Sci.* **114,** 8217–8222 (2017).
11. Socolow, R. H. Nitrogen management and the future of food: lessons from the management of energy and carbon. *Proc. Natl. Acad. Sci. U. S. A.* **96,** 6001–6008 (1999).
12. Erisman, J. W., Sutton, M. A., Galloway, J., Klimont, Z. & Winiwarter, W. How a century of ammonia synthesis changed the world. *Nat. Geosci.* **1,** 636–639 (2008).
13. Stewart, W. M., Dibb, D. W., Johnston, A. E. & Smyth, T. J. The contribution of commercial fertilizer nutrients to food production. *Agronomy Journal* **97,** 1–6 (2005).
14. Khalil, M. A. K., Rasmussen, R. A. & Shearer, M. J. Atmospheric nitrous oxide: patterns of global change during recent decades and centuries. *Chemosphere* **47,** 807–821 (2002).
15. Johnson, P. T. J., Townsend, A. R., Cleveland, C. C., Glibert, P. M.,

Howarth, W., Mckenzie, V. J., Rejmankova, E. & Ward, M. H. Linking environmental nutrient enrichment and disease emergence in humans and wildlife. *Ecol. Appl.* **20,** 16–29 (2010).
16. Howarth, R. W. Coastal nitrogen pollution: A review of sources and trends globally and regionally. *Harmful Algae* **8,** 14–20 (2008).
17. Duce, R. A., LaRoche, J., Altieri, K., Arrigo, K. R., Baker, A. R., Capone, D. G., Cornell, S., Dentener, F., Galloway, J. N., Ganeshram, R. S., Geider, R. J., Jickells, T., Kuypers, M. M., Langlois, R., Liss, P. S., Liu, S. M., Middelburg, J. J., Moore, C. M., Nickovic, S., Oschlies, A., Pedersen, T., Prospero, J., Schlitzer, R., Seitzinger, S. P., Sorensen, L. L., Uematsu, M., Ulloa, O., Voss, M., Ward, B. & Zamora, L. Impacts of Atmospheric Anthropogenic Nitrogen on the Open Ocean. *Science* **320,** 893–897 (2008).
18. Gruber, N. & Galloway, J. N. An Earth-system perspective of the global nitrogen cycle. *Nature* **451,** 293–296 (2008).
19. Zumft, W. G. Cell Biology and Molecular Basis of Denitrification. *Microbiol. Mol. Biol. Rev.* **61,** 533–616 (1997).
20. Moreno-vivián, C., Cabello, P., Blasco, R., Castillo, F., Cabello, N., Marti, M. & Moreno-vivia, C. Prokaryotic Nitrate Reduction: Molecular Properties and Functional Distinction among Bacterial Nitrate Reductases. *J. Bacteriol.* **181,** 6573–6584 (1999).
21. Swenson, C. E. & Sadikot, R. T. Achromobacter respiratory infections. *Ann. Am. Thorac. Soc.* **12,** 252–258 (2015).
22. Yabuuchi, E. & Ohyama, A. Achromobacter xylosoxidans n. sp. from Human Ear Discharge. *Jpn. J. Microbiol.* **15,** 477–481 (1971).
23. Yabuuchi, E. [Twenty-seven years with the nomenclature of Achromobacter xylosoxidans]. *JARMAM* **10,** 1–12 (1999).
24. Duggan, J. M., Goldstein, S. J., Chenoweth, C. E., Kauffman, C. A. & Bradley, S. F. Achromobacter xylosoxidans Bacteremia: Report of Four Cases and Review of the Literature. *Clin. Infect. Dis.* **23,** 569–576 (1996).
25. Ridderberg, W., Wang, M. & Nørskov-Lauritsen, N. Multilocus sequence analysis of isolates of Achromobacter from patients with cystic fibrosis reveals infecting species other than Achromobacter xylosoxidans. *J. Clin. Microbiol.* **50,** 2688–2694 (2012).
26. Jakobsen, T. H., Hansen, M. A. M., Jensen, P. Ø., Hansen, L., Riber, L., Cockburn, A., Kolpen, M., Rønne Hansen, C., Ridderberg, W., Eickhardt, S., Hansen, M. A. M., Kerpedjiev, P., Alhede, M., Qvortrup, K., Burmølle, M., Moser, C., Kühl, M., Ciofu, O., Givskov, M., Sørensen, S. J., Høiby, N. & Bjarnsholt, T. Complete Genome Sequence of the Cystic Fibrosis Pathogen Achromobacter xylosoxidans NH44784-1996 Complies with Important Pathogenic Phenotypes. *PLoS One* **8,** e68484 (2013).
27. Green, S. J., Scheller, L. F., Marletta, M. A., Seguin, M. C., Klotz, F. W., Slayter, M., Nelson, B. J. & Nacy, C. A. Nitric oxide: Cytokine-regulation of nitric oxide in host resistance to intracellular pathogens. *Immunol. Lett.* **43,** 87–94 (1994).

28. Li, X., Hu, Y., Gong, J., Zhang, L. & Wang, G. Comparative genome characterization of Achromobacter members reveals potential genetic determinants facilitating the adaptation to a pathogenic lifestyle. *Appl. Microbiol. Biotechnol.* **97,** 6413–6425 (2013).
29. Glance, L. G., Stone, P. W., Mukamel, D. B. & Dick, A. W. Increases in Mortality, Length of Stay, and Cost Associated With Hospital-Acquired Infections in Trauma Patients. *Arch. Surg.* **146,** 794 (2011).
30. González, P. J., Correia, C., Moura, I., Brondino, C. D. & Moura, J. J. G. Bacterial nitrate reductases: Molecular and biological aspects of nitrate reduction. *J. Inorg. Biochem.* **100,** 1015–1023 (2006).
31. Bertero, M. G., Rothery, R. A., Palak, M., Hou, C., Lim, D., Blasco, F., Weiner, J. H. & Strynadka, N. C. J. Insights into the respiratory electron transfer pathway from the structure of nitrate reductase A. *Nat. Struct. Biol.* **10,** 681–687 (2003).
32. Chaudhry, G. R., Chaiken, I. M. & MacGregor, C. H. An activity from Escherichia coli membranes responsible for the modification of nitrate reductase to its precursor form. *J. Biol. Chem.* **258,** 5828–33 (1983).
33. Bell, L. C., Richardson, D. J. & Ferguson, S. J. Periplasmic and membrane-bound respiratory nitrate reductases in Thiosphaera pantotropha. *FEBS Lett.* **265,** 85–87 (1990).
34. Campbell, W. H. Structure and function of eukaryotic NAD(P)H:nitrate reductase. *Cell. Mol. Life Sci.* **58,** 194–204 (2001).
35. Fülöp, V., Moir, J. W. B., Ferguson, S. J. & Hajdu, J. The anatomy of a bifunctional enzyme: Structural basis for reduction of oxygen to water and synthesis of nitric oxide by cytochrome cd1. *Cell* **81,** 369–377 (1995).
36. Einsle, O., Messerschmidt, A., Stach, P., Bourenkov, G. P., Bartunik, H. D., Huber, R. & Kroneck, P. M. H. Structure of cytochrome c nitrite reductase. *Nature* **400,** 476–480 (1999).
37. Grossmann, J. G., Abraham, Z. H. L., Adman, E. T., Neu, M., Eady, R. R., Smith, B. E. & Hasnain, S. S. X-ray scattering using synchrotron radiation shows nitrite reductase from Achromobacter xylosoxidans to be a trimer in solution. *Biochemistry* **32,** 7360–7366 (1993).
38. Abraham, Z. H. L., Lowe, D. J. & Smith, B. E. Purification and characterization of the dissimilatory nitrite reductase from Alcaligenes xylosoxidans subsp. xylosoxidans (N.C.I.M.B. 11015): evidence for the presence of both type 1 and type 2 copper centres. *Biochem. J.* **295 (Pt 2,** 587–593 (1993).
39. Stevanin, T. M., Laver, J. R., Poole, R. K., Moir, J. W. B. & Read, R. C. Metabolism of nitric oxide by Neisseria meningitidis modifies release of NO-regulated cytokines and chemokines by human macrophages. *Microbes Infect.* **9,** 981–987 (2007).
40. Ravishankara, A. R., Daniel, J. S. & Portmann, R. W. Nitrous Oxide (N2O): The Dominant Ozone-Depleting Substance Emitted in the 21st Century. *Science* **326,** 123–125 (2009).
41. Canfield, D. E., Glazer, A. N. & Falkowski, P. G. The Evolution and Future of Earth's Nitrogen Cycle. *Science* **330,** 192–196 (2010).

42. Shiro, Y., Sugimoto, H., Tosha, T., Nagano, S. & Hino, T. Structural basis for nitrous oxide generation by bacterial nitric oxide reductases. *Philos. Trans. R. Soc. B* **367,** 1195–1203 (2012).
43. Hino, T., Matsumoto, Y., Nagano, S., Sugimoto, H., Fukumori, Y., Murata, T., Iwata, S. & Shiro, Y. Structural Basis of Biological N_2O Generation by Bacterial Nitric Oxide Reductase. *Science* **330,** 1666–1670 (2010).
44. Pauleta, S. R., Dell'Acqua, S. & Moura, I. Nitrous oxide reductase. *Coordination Chemistry Reviews* **257,** 332–349 (2013).
45. Pomowski, A., Zumft, W. G., Kroneck, P. M. H. & Einsle, O. N 2O binding at a [4Cu:2S] copper-sulphur cluster in nitrous oxide reductase. *Nature* **477,** 234–237 (2011).
46. Ye, R. W., Fries, M. R., Bezborodnikov, S. G., Averill, B. A. & Tiedje, J. M. Characterization of the Structural Gene Encoding a Copper-Containing Nitrite Reductase and Homology of This Gene to DNA of Other Denitrifiers. *Appl. Environ. Microbiol.* **59,** 250–254 (1993).
47. Nishiyama, M., Suzuki, J., Kukimoto, M., Ohnuki, T., Horinouchi, S. & Beppu, T. Cloning and Characterization of a Nitrite Reductase Gene From Alcaligenes-Faecalis and Its Expression in Escherichia-Coli. *J. Gen. Microbiol.* **139,** 725–733 (1993).
48. Holm, R. H., Kennepohl, P. & Solomon, E. I. Structural and Functional Aspects of Metal Sites in Biology. *Chem. Rev.* **96,** 2239–2314 (1996).
49. Basumallick, L., Szilagyi, R. K., Zhao, Y., Shapleigh, J. P., Scholes, C. P. & Solomon, E. I. Spectroscopic Studies of the Met182Thr Mutant of Nitrite Reductase: Role of the Axial Ligand in the Geometric and Electronic Structure of Blue and Green Copper Sites. *J. Am. Chem. Soc.* **125,** 14784–14792 (2003).
50. Murphy, L. M., Dodd, F. E., Yousafzai, F. K., Eady, R. R. & Hasnain, S. S. Electron donation between copper containing nitrite reductases and cupredoxins: the nature of protein-protein interaction in complex formation. *J. Mol. Biol.* **315,** 859–71 (2002).
51. Ellis, M. J., Dodd, F. E., Sawers, G., Eady, R. R. & Hasnain, S. S. Atomic resolution structures of native copper nitrite reductase from Alcaligenes xylosoxidans and the active site mutant Asp92Glu. *J. Mol. Biol.* **328,** 429–438 (2003).
52. Strange, R. W., Murphy, L. M., Dodd, F. E., Abraham, Z. H. L., Eady, R. R., Smith, B. E. & Hasnain, S. S. Structural and kinetic evidence for an ordered mechanism of copper nitrite reductase. *J. Mol. Biol.* **287,** 1001–1009 (1999).
53. Kataoka, K., Furusawa, H., Takagi, K., Yamaguchi, K. & Suzuki, S. Functional Analysis of Conserved Aspartate and Histidine Residues Located Around the Type 2 Copper Site of Copper-Containing Nitri Reductase. *J. Biochem.* **127,** 345–350 (2000).
54. Antonyuk, S. V., Strange, R. W., Sawers, G., Eady, R. R. & Hasnain, S. S. Atomic resolution structures of resting-state, substrate- and product-complexed Cu-nitrite reductase provide insight into catalytic mechanism. *Proc. Natl. Acad. Sci.* **102,** 12041–12046 (2005).

55. Blakeley, M. P., Hasnain, S. S. & Antonyuk, S. V. Sub-atomic resolution X-ray crystallography and neutron crystallography: Promise, challenges and potential. *IUCrJ* **2,** 464–474 (2015).
56. Boulanger, M. J. & Murphy, M. E. P. Directing the mode of nitrite binding to a copper-containing nitrite reductase from Alcaligenes faecalis S-6: characterization of an active site isoleucine. *Protein Sci.* **12,** 248–256 (2003).
57. Fukuda, Y., Tse, K. M., Lintuluoto, M., Fukunishi, Y., Mizohata, E., Matsumura, H., Takami, H., Nojiri, M. & Inoue, T. Structural insights into the function of a thermostable copper-containing nitrite reductase. *J. Biochem.* **155,** 123–135 (2014).
58. Leferink, N. G. H., Antonyuk, S. V., Houwman, J. A., Scrutton, N. S., Eady, R. R. & Hasnain, S. S. Impact of residues remote from the catalytic centre on enzyme catalysis of copper nitrite reductase. *Nat. Commun.* **5,** 4395 (2014).
59. Sen, K., Horrell, S., Kekilli, D., Yong, C. W., Keal, T. W., Atakisi, H., Moreau, D. W., Thorne, R. E., Hough, M. A. & Strange, R. W. Active-site protein dynamics and solvent accessibility in native *Achromobacter cycloclastes* copper nitrite reductase. *IUCrJ* **4,** 1–11 (2017).
60. Sievers, F., Wilm, A., Dineen, D., Gibson, T. J., Karplus, K., Li, W., Lopez, R., McWilliam, H., Remmert, M., Söding, J., Thompson, J. D. & Higgins, D. G. Fast, scalable generation of high-quality protein multiple sequence alignments using Clustal Omega. *Mol. Syst. Biol.* **7,** (2011).
61. Wijma, H. J., Jeuken, L. J. C., Verbeet, M. P., Armstrong, F. A. & Canters, G. W. A Random-sequential Mechanism for Nitrite Binding and Active Site Reduction in Copper-containing Nitrite Reductase. *J. Biol. Chem.* **281,** 16340–16346 (2006).
62. Leferink, N. G. H., Han, C., Antonyuk, S. V., Heyes, D. J., Rigby, S. E. J., Hough, M. A., Eady, R. R., Scrutton, N. S. & Hasnain, S. S. Proton-coupled electron transfer in the catalytic cycle of Alcaligenes xylosoxidans copper-dependent nitrite reductase. *Biochemistry* **50,** 4121–4131 (2011).
63. Leferink, N. G. H., Eady, R. R., Hasnain, S. S. & Scrutton, N. S. Laser-flash photolysis indicates that internal electron transfer is triggered by proton uptake by Alcaligenes xylosoxidans copper-dependent nitrite reductase. *FEBS J.* **279,** 2174–2181 (2012).
64. Krzemiński, Ł., Ndamba, L., Canters, G. W., Aartsma, T. J., Evans, S. D. & Jeuken, L. J. C. Spectroelectrochemical investigation of intramolecular and interfacial electron-transfer rates reveals differences between nitrite reductase at rest and during turnover. *J. Am. Chem. Soc.* **133,** 15085–15093 (2011).
65. Hough, M. A., Eady, R. R. & Hasnain, S. S. Identification of the proton channel to the active site type 2 Cu center of nitrite reductase: Structural and enzymatic properties of the His254Phe and Asn90Ser mutants. *Biochemistry* **47,** 13547–13553 (2008).
66. Hough, M. A., Ellis, M. J., Antonyuk, S. V., Strange, R. W., Sawers, G., Eady, R. R. & Hasnain, S. S. High resolution structural studies of

mutants provide insights into catalysis and electron transfer processes in copper nitrite reductase. *J. Mol. Biol.* **350,** 300–309 (2005).
67. Barrett, M. L., Harris, R. L., Antonyuk, S. V., Hough, M. A., Ellis, M. J., Sawers, G., Eady, R. R. & Hasnain, S. S. Insights into redox partner interactions and substrate binding in nitrite reductase from Alcaligenes xylosoxidans: Crystal structures of the Trp138His and His313Gln mutants. *Biochemistry* **43,** 16311–16319 (2004).
68. Paraskevopoulos, K., Hough, M. A., Sawers, R. G., Eady, R. R. & Hasnain, S. S. The structure of the Met144Leu mutant of copper nitrite reductase from Alcaligenes xylosoxidans provides the first glimpse of a protein–protein complex with azurin II. *JBIC J. Biol. Inorg. Chem.* **12,** 789–796 (2007).
69. Nojiri, M., Koteishi, H., Nakagami, T., Kobayashi, K., Inoue, T., Yamaguchi, K. & Suzuki, S. Structural basis of inter-protein electron transfer for nitrite reduction in denitrification. *Nature* **462,** 117–120 (2009).
70. Ellis, M. J., Grossmann, J. G., Eady, R. R. & Hasnain, S. S. Genomic analysis reveals widespread occurrence of new classes of copper nitrite reductases. *J. Biol. Inorg. Chem.* **12,** 1119–1127 (2007).
71. Eady, R. R., Antonyuk, S. V. & Hasnain, S. S. Fresh insight to functioning of selected enzymes of the nitrogen cycle. *Curr. Opin. Chem. Biol.* **31,** 103–112 (2016).
72. Yamaguchi, K., Kataoka, K., Kobayashi, M., Itoh, K., Fukui, A. & Suzuki, S. Characterization of two type 1 Cu sites of Hyphomicrobium denitrificans nitrite reductase: A new class of copper-containing nitrite reductases. *Biochemistry* **43,** 14180–14188 (2004).
73. Nojiri, M., Xie, Y., Inoue, T., Yamamoto, T., Matsumura, H., Kataoka, K., Deligeer, Yamaguchi, K., Kai, Y. & Suzuki, S. Structure and function of a hexameric copper-containing nitrite reductase. *Proc. Natl. Acad. Sci.* **104,** 4315–4320 (2007).
74. Antonyuk, S. V., Han, C., Eady, R. R. & Hasnain, S. S. Structures of protein–protein complexes involved in electron transfer. *Nature* **496,** 123–126 (2013).
75. Wojciech, P. & Nicholas, M. D. J. D. Molecular characterization of a copper-containing nitrite reductase from Rhodopseudomonas sphaeroides forma sp. denitrificans. *Biochim. Biophys. Acta* **828,** 130–137 (1985).
76. Fukuda, Y., Tse, K. M., Kado, Y., Mizohata, E., Matsumura, H. & Inoue, T. Insights into unknown foreign ligand in copper nitrite reductase. *Biochem. Biophys. Res. Commun.* **464,** 622–628 (2015).
77. Strnad, H., Ridl, J., Paces, J., Kolar, M., Vlcek, C. & Paces, V. Complete genome sequence of the haloaromatic acid-degrading bacterium achromobacter xylosoxidans A8. *J. Bacteriol.* **193,** 791–792 (2011).
78. Venkatramanan, R., Prakash, O., Woyke, T., Chain, P., Goodwin, L. A., Watson, D., Brooks, S., Kostka, J. E. & Green, S. J. Genome Sequences for Three Denitrifying Bacterial Strains Isolated from a Uranium- and Nitrate-Contaminated Subsurface Environment. *Genome Announc.* **1,**

e00449-13-e00449-13 (2013).
79. Hernandez-Mendoza, A., Lozano-Aguirre Beltran, L. F., Martinez-Ocampo, F., Quiroz-Castaneda, R. E. & Dantan-Gonzalez, E. A Newly Sequenced Alcaligenes faecalis Strain: Implications for Novel Temporal Symbiotic Relationships. *Genome Announc.* **2,** e01246-14-e01246-14 (2014).
80. Zink, F. E. X-ray tubes. *RadioGraphics* **17,** 1259–1268 (1997).
81. Drenck, K. & Pepinsky, R. New X-Ray Diffraction Tubes of High Brilliance. *Rev. Sci. Instrum.* **22,** 539–540 (1951).
82. Grider, D. E., Wright, A. & Ausburn, P. K. Electron beam melting in microfocus X-ray tubes. *J. Phys. D. Appl. Phys.* **19,** 2281–2292 (1986).
83. Elder, F. R., Langmuir, R. V. & Pollock, H. C. Radiation from Electrons Accelerated in a Synchrotron. *Phys. Rev.* **74,** 52–56 (1948).
84. Wille, K. Synchrotron radiation sources. *Reports Prog. Phys.* **54,** 1005–1067 (1991).
85. Lundstrom, K. Structural genomics for membrane proteins. *Cell. Mol. Life Sci.* **63,** 2597–2607 (2006).
86. Joachimiak, A. High-throughput crystallography for structural genomics. *Curr. Opin. Struct. Biol.* **19,** 573–584 (2009).
87. Smart, O. S., Horský, V., Gore, S., Svobodová Vařeková, R., Bendová, V., Kleywegt, G. J. & Velankar, S. Worldwide Protein Data Bank validation information: usage and trends. *Acta Crystallogr. Sect. D Struct. Biol.* **74,** 1–8 (2018).
88. Kamitsubo, H. The JAERI-RIKEN SPring-8 Project. *Rev. Sci. Instrum.* **63,** 1586–1587 (1992).
89. Ueno, G., Kanda, H., Hirose, R., Ida, K., Kumasaka, T. & Yamamoto, M. RIKEN structural genomics beamlines at the SPring-8; high throughput protein crystallography with automated beamline operation. *J. Struct. Funct. Genomics* **7,** 15–22 (2006).
90. Kawano, Y., Shimizu, N., Baba, S., Hasegawa, K., Makino, M., Mizuno, N., Hoshino, T., Ito, R., Wada, I., Hirata, K., Ueno, G., Hikima, T., Murakami, H., Maeda, D., Nisawa, A., Kumasaka, T. & Yamamoto, M. Present status of SPring-8 macromolecular crystallography beamlines. in *AIP Conference Proceedings* **1234,** 359–362 (2010).
91. Hirata, K., Kawano, Y., Ueno, G., Hashimoto, K., Murakami, H., Hasegawa, K., Hikima, T., Kumasaka, T. & Yamamoto, M. Achievement of protein micro-crystallography at SPring-8 beamline BL32XU. *J. Phys. Conf. Ser.* **425,** 012002 (2013).
92. Hasegawa, K., Shimizu, N., Okumura, H., Mizuno, N., Baba, S., Hirata, K., Takeuchi, T., Yamazaki, H., Senba, Y., Ohashi, H., Yamamoto, M. & Kumasaka, T. SPring-8 BL41XU, a high-flux macromolecular crystallography beamline. *J. Synchrotron Radiat.* **20,** 910–913 (2013).
93. Higashiura, A., Yamashita, E., Yoshimura, M., Hasegawa, K., Furukawa, Y., Kumasaka, T., Ueno, G., Yamamoto, M., Tsukihara, T. & Nakagawa, A. SPring-8 BL44XU, beamline designed for structure analysis of large biological macromolecular assemblies. *AIP Conf. Proc.* **1741,** (2016).
94. Nishimasu, H., Ran, F. A., Hsu, P. D., Konermann, S., Shehata, S. I.,

Dohmae, N., Ishitani, R., Zhang, F. & Nureki, O. Crystal structure of Cas9 in complex with guide RNA and target DNA. *Cell* **156,** 935–949 (2014).
95. Huang, Z. & Kim, K. J. Review of x-ray free-electron laser theory. *Physical Review Special Topics - Accelerators and Beams* **10,** 1–26 (2007).
96. Milton, S. V. Exponential Gain and Saturation of a Self-Amplified Spontaneous Emission Free-Electron Laser. *Science* **292,** 2037–2041 (2001).
97. Geloni, G., Kocharyan, V. & Saldin, E. A novel self-seeding scheme for hard X-ray FELs. *J. Mod. Opt.* **58,** 1391–1403 (2011).
98. Amann, J., Berg, W., Blank, V., Decker, F. J., Ding, Y., Emma, P., Feng, Y., Frisch, J., Fritz, D., Hastings, J., Huang, Z., Krzywinski, J., Lindberg, R., Loos, H., Lutman, A., Nuhn, H. D., Ratner, D., Rzepiela, J., Shu, D., Shvyd'Ko, Y., Spampinati, S., Stoupin, S., Terentyev, S., Trakhtenberg, E., Walz, D., Welch, J., Wu, J., Zholents, A. & Zhu, D. Demonstration of self-seeding in a hard-X-ray free-electron laser. *Nat. Photonics* **6,** 693–698 (2012).
99. Emma, P., Akre, R., Arthur, J., Bionta, R., Bostedt, C., Bozek, J. D., Brachmann, A., Bucksbaum, P., Coffee, R., Decker, F.-J., Ding, Y., Dowell, D., Edstrom, S., Fisher, A., Frisch, J., Gilevich, S., Hastings, J., Hays, G., Hering, P., Huang, Z., Iverson, R., Loos, H., Messerschmidt, M., Miahnahri, A., Moeller, S., Nuhn, H.-D., Pile, G., Ratner, D., Rzepiela, J., Schultz, D., Smith, T., Stefan, P., Tompkins, H., Turner, J., Welch, J., White, W. E., Wu, J., Yocky, G. & Galayda, J. First lasing and operation of an ångstrom-wavelength free-electron laser. *Nat. Photonics* **4,** 641–647 (2010).
100. Ishikawa, T., Aoyagi, H., Asaka, T., Asano, Y., Azumi, N., Bizen, T., Ego, H., Fukami, K., Fukui, T., Furukawa, Y., Goto, S., Hanaki, H., Hara, T., Hasegawa, T., Hatsui, T., Higashiya, A., Hirono, T., Hosoda, N., Ishii, M., Inagaki, T., Inubushi, Y., Itoga, T., Joti, Y., Kago, M., Kameshima, T., Kimura, H., Kirihara, Y., Kiyomichi, A., Kobayashi, T., Kondo, C., Kudo, T., Maesaka, H., Maréchal, X. M., Masuda, T., Matsubara, S., Matsumoto, T., Matsushita, T., Matsui, S., Nagasono, M., Nariyama, N., Ohashi, H., Ohata, T., Ohshima, T., Ono, S., Otake, Y., Saji, C., Sakurai, T., Sato, T., Sawada, K., Seike, T., Shirasawa, K., Sugimoto, T., Suzuki, S., Takahashi, S., Takebe, H., Takeshita, K., Tamasaku, K., Tanaka, H., Tanaka, R., Tanaka, T., Togashi, T., Togawa, K., Tokuhisa, A., Tomizawa, H., Tono, K., Wu, S., Yabashi, M., Yamaga, M., Yamashita, A., Yanagida, K., Zhang, C., Shintake, T., Kitamura, H. & Kumagai, N. A compact X-ray free-electron laser emitting in the sub-ångström region. *Nat. Photonics* **6,** 540–544 (2012).
101. Altarelli, M. The European X-ray free-electron laser facility in Hamburg. *Nucl. Instruments Methods Phys. Res. Sect. B Beam Interact. with Mater. Atoms* **269,** 2845–2849 (2011).
102. Ko, I., Kang, H.-S., Heo, H., Kim, C., Kim, G., Min, C.-K., Yang, H., Baek, S., Choi, H.-J., Mun, G., Park, B., Suh, Y., Shin, D., Hu, J., Hong, J., Jung, S., Kim, S.-H. S. S. S.-H. S. S., Kim, K. K. K.-W., Na, D., Park, S.

S.-Y., Park, Y., Jung, Y., Jeong, S., Lee, H. H.-S. H.-S., Lee, S. S., Lee, S. S., Oh, B., Suh, H., Han, J.-H., Kim, M., Jung, N.-S., Kim, Y.-C. Y., Lee, M.-S., Lee, B.-H., Sung, C.-W., Mok, I.-S., Yang, J.-M., Parc, Y., Lee, W.-W., Lee, C.-S., Shin, H., Kim, J. J., Kim, Y.-C. Y., Lee, J., Park, S. S.-Y., Kim, J. J., Park, J. J. J., Eom, I., Rah, S., Kim, S.-H. S. S. S.-H. S. S., Nam, K. H., Park, J. J. J., Park, J. J. J., Kim, S.-H. S. S. S.-H. S. S., Kwon, S., An, R., Park, S. S.-Y., Kim, K. K. K.-W., Hyun, H., Kim, S.-H. S. S. S.-H. S. S., Kim, S.-H. S. S. S.-H. S. S., Yu, C.-J., Kim, B.-S., Kang, T.-H., Kim, K. K. K.-W., Kim, S.-H. S. S. S.-H. S. S., Lee, H. H.-S. H.-S., Lee, H. H.-S. H.-S., Park, K.-H., Koo, T.-Y., Kim, D.-E. & Lee, K. Construction and Commissioning of PAL-XFEL Facility. *Appl. Sci.* **7,** 479 (2017).

103. Milne, C., Schietinger, T., Aiba, M., Alarcon, A., Alex, J., Anghel, A., Arsov, V., Beard, C., Beaud, P., Bettoni, S., Bopp, M., Brands, H., Brönnimann, M., Brunnenkant, I., Calvi, M., Citterio, A., Craievich, P., Csatari Divall, M., Dällenbach, M., D'Amico, M., Dax, A., Deng, Y., Dietrich, A., Dinapoli, R., Divall, E., Dordevic, S., Ebner, S., Erny, C., Fitze, H., Flechsig, U., Follath, R., Frei, F., Gärtner, F., Ganter, R., Garvey, T., Geng, Z., Gorgisyan, I., Gough, C., Hauff, A., Hauri, C., Hiller, N., Humar, T., Hunziker, S., Ingold, G., Ischebeck, R., Janousch, M., Juranić, P., Jurcevic, M., Kaiser, M., Kalantari, B., Kalt, R., Keil, B., Kittel, C., Knopp, G., Koprek, W., Lemke, H., Lippuner, T., Llorente Sancho, D., Löhl, F., Lopez-Cuenca, C., Märki, F., Marcellini, F., Marinkovic, G., Martiel, I., Menzel, R., Mozzanica, A., Nass, K., Orlandi, G., Ozkan Loch, C., Panepucci, E., Paraliev, M., Patterson, B., Pedrini, B., Pedrozzi, M., Pollet, P., Pradervand, C., Prat, E., Radi, P., Raguin, J.-Y., Redford, S., Rehanek, J., Réhault, J., Reiche, S., Ringele, M., Rittmann, J., Rivkin, L., Romann, A., Ruat, M., Ruder, C., Sala, L., Schebacher, L., Schilcher, T., Schlott, V., Schmidt, T., Schmitt, B., Shi, X., Stadler, M., Stingelin, L., Sturzenegger, W., Szlachetko, J., Thattil, D., Treyer, D., Trisorio, A., Tron, W., Vetter, S., Vicario, C., Voulot, D., Wang, M., Zamofing, T., Zellweger, C., Zennaro, R., Zimoch, E., Abela, R., Patthey, L. & Braun, H.-H. SwissFEL: The Swiss X-ray Free Electron Laser. *Appl. Sci.* **7,** 720 (2017).
104. Henderson, R. Cryo-Protection of Protein Crystals against Radiation Damage in Electron and X-Ray Diffraction. *Proc. R. Soc. B* **241,** 6–8 (1990).
105. Schlichting, I. Serial femtosecond crystallography: the first five years. *IUCrJ* **2,** 246–255 (2015).
106. Garman, E. F. Cool data: Quantity AND quality. *Acta Crystallogr. Sect. D Struct. Biol.* **55,** 1641–1653 (1999).
107. Nave, C. & Garman, E. F. Towards an understanding of radiation damage in cryocooled macromolecular crystals. *J. Synchrotron Radiat.* **12,** 257–260 (2005).
108. Teng, T. & Moffat, K. Radiation damage of protein crystals at cryogenic temperatures between 40 K and 150 K. *J. Synchrotron Radiat.* **9,** 198–201 (2002).
109. Thomson, S. J. J. & Thomson, G. P. Conduction of Electricity through

Gases. *J. Phys. Chem.* **38,** 987–987 (1933).
110. Compton, A. H. A Quantum Theory of the Scattering of X-rays by Light Elements. *Phys. Rev.* **21,** 483–502 (1923).
111. Hertz, H. Ueber einen Einfluss des ultravioletten Lichtes auf die electrische Entladung. *Ann. der Phys. und Chemie* **267,** 983–1000 (1887).
112. O'Neill, P., Stevens, D. L. & Garman, E. F. Physical and chemical considerations of damage induced in protein crystals by synchrotron radiation: A radiation chemical perspective. *J. Synchrotron Radiat.* **9,** 329–332 (2002).
113. Sanishvili, R., Yoder, D. W., Pothineni, S. B., Rosenbaum, G., Xu, S., Vogt, S., Stepanov, S., Makarov, O. A., Corcoran, S., Benn, R., Nagarajan, V., Smith, J. L. & Fischetti, R. F. Radiation damage in protein crystals is reduced with a micron-sized X-ray beam. *Proc. Natl. Acad. Sci.* **108,** 6127–6132 (2011).
114. Gonzalez, A. & Nave, C. Radiation damage in protein crystals at low temperature. *Acta Crystallogr. Sect. D Struct. Biol.* **50,** 874–877 (1994).
115. Teng, T. Y. & Moffat, K. Primary radiation damage of protein crystals by an intense synchrotron X-ray beam. *J. Synchrotron Radiat.* **7,** 313–317 (2000).
116. Burmeister, W. P. Structural changes in a cryo-cooled protein crystal owing to radiation damage. *Acta Crystallogr. Sect. D Struct. Biol.* **56,** 328–341 (2000).
117. Ravelli, R. B. G. & McSweeney, S. M. The 'fingerprint' that X-rays can leave on structures. *Structure* **8,** 315–328 (2000).
118. Chinte, U., Shah, B., Chen, Y.-S., Pinkerton, A. A., Schall, C. A. & Hanson, B. L. Cryogenic (<20 K) helium cooling mitigates radiation damage to protein crystals. *Acta Crystallogr. Sect. D Struct. Biol.* **63,** 486–492 (2007).
119. Meents, A., Gutmann, S., Wagner, A. & Schulze-Briese, C. Origin and temperature dependence of radiation damage in biological samples at cryogenic temperatures. *Proc. Natl. Acad. Sci.* **107,** 1094–1099 (2010).
120. Mao, W. L. Hydrogen Clusters in Clathrate Hydrate. *Science* **297,** 2247–2249 (2002).
121. Helliwell, J. R. Protein crystal perfection and the nature of radiation damage. *J. Cryst. Growth* **90,** 259–272 (1988).
122. Weik, M., Ravelli, R. B. G., Kryger, G., McSweeney, S., Raves, M. L., Harel, M., Gros, P., Silman, I., Kroon, J. & Sussman, J. L. Specific chemical and structural damage to proteins produced by synchrotron radiation. *Proc. Natl. Acad. Sci.* **97,** 623–628 (2000).
123. Stumpf, V., Gokhberg, K. & Cederbaum, L. S. The role of metal ions in X-ray-induced photochemistry. *Nat. Chem.* **8,** 237–241 (2016).
124. Dubnovitsky, A. P., Ravelli, R. B. G., Popov, A. N. & Papageorgiou, A. C. Strain relief at the active site of phosphoserine aminotransferase induced by radiation damage. *Protein Sci.* **14,** 1498–1507 (2009).
125. Ravelli, R. B. G., Leiros, H. K. S., Pan, B., Caffrey, M. & McSweeney, S. Specific radiation damage can be used to solve macromolecular crystal

structures. *Structure* **11,** 217–224 (2003).
126. Hirata, K., Shinzawa-Itoh, K., Yano, N., Takemura, S., Kato, K., Hatanaka, M., Muramoto, K., Kawahara, T., Tsukihara, T., Yamashita, E., Tono, K., Ueno, G., Hikima, T., Murakami, H., Inubushi, Y., Yabashi, M., Ishikawa, T., Yamamoto, M., Ogura, T., Sugimoto, H., Shen, J.-R., Yoshikawa, S. & Ago, H. Determination of damage-free crystal structure of an X-ray–sensitive protein using an XFEL. *Nat. Methods* **11,** 734–736 (2014).
127. Antonyuk, S. V. & Hough, M. A. Monitoring and validating active site redox states in protein crystals. *Biochim. Biophys. Acta* **1814,** 778–784 (2011).
128. Yano, J., Kern, J., Irrgang, K.-D., Latimer, M. J., Bergmann, U., Glatzel, P., Pushkar, Y., Biesiadka, J., Loll, B., Sauer, K., Messinger, J., Zouni, A. & Yachandra, V. K. X-ray damage to the Mn4Ca complex in single crystals of photosystem II: A case study for metalloprotein crystallography. *Proc. Natl. Acad. Sci.* **102,** 12047–12052 (2005).
129. Jones, G. D. D., Lea, J. S., Symons, M. C. R. & Taiwo, F. A. Structure and mobility of electron gain and loss centres in proteins. *Nature* **330,** 772–773 (1987).
130. Tavares, P. F., Leemann, S. C., Sjostrom, M. & Andersson, A. The MAX IV storage ring project. *J. Synchrotron Radiat.* **21,** 862–877 (2014).
131. Bourenkov, G. P. & Popov, A. N. Optimization of data collection taking radiation damage into account. *Acta Crystallogr. Sect. D Struct. Biol.* **66,** 409–419 (2010).
132. Horrell, S., Antonyuk, S. V., Eady, R. R., Hasnain, S. S., Hough, M. A. & Strange, R. W. Serial crystallography captures enzyme catalysis in copper nitrite reductase at atomic resolution from one crystal. *IUCrJ* **3,** 271–281 (2016).
133. Garman, E. F. Radiation damage in macromolecular crystallography: What is it and why do we care? *Acta Crystallogr. Sect. D Struct. Biol.* **66,** 69–77 (2013).
134. Neutze, R., Wouts, R., van der Spoel, D., Weckert, E. & Hajdu, J. Potential for biomolecular imaging with femtosecond X-ray pulses. *Nature* **406,** 752–757 (2000).
135. Dantus, M., Bowman, R. M. & Zewail, A. H. Femtosecond laser observations of molecular vibration and rotation. *Nature* **343,** 737–739 (1990).
136. Chapman, H. N., Fromme, P., Barty, A., White, T. A., Kirian, R. A., Aquila, A., Hunter, M. S., Schulz, J., DePonte, D. P., Weierstall, U., Doak, R. B., Maia, F. R. N. C., Martin, A. V., Schlichting, I., Lomb, L., Coppola, N., Shoeman, R. L., Epp, S. W., Hartmann, R., Rolles, D., Rudenko, A., Foucar, L., Kimmel, N., Weidenspointner, G., Holl, P., Liang, M., Barthelmess, M., Caleman, C., Boutet, S., Bogan, M. J., Krzywinski, J., Bostedt, C., Bajt, S., Gumprecht, L., Rudek, B., Erk, B., Schmidt, C., Hömke, A., Reich, C., Pietschner, D., Strüder, L., Hauser, G., Gorke, H., Ullrich, J., Herrmann, S., Schaller, G., Schopper, F., Soltau, H., Kühnel, K.-U., Messerschmidt, M., Bozek, J. D., Hau-Riege,

S. P., Frank, M., Hampton, C. Y., Sierra, R. G., Starodub, D., Williams, G. J., Hajdu, J., Timneanu, N., Seibert, M. M., Andreasson, J., Rocker, A., Jönsson, O., Svenda, M., Stern, S., Nass, K., Andritschke, R., Schröter, C.-D., Krasniqi, F., Bott, M., Schmidt, K., Wang, X., Grotjohann, I., Holton, J. M., Barends, T. R. M., Neutze, R., Marchesini, S., Fromme, R., Schorb, S., Rupp, D., Adolph, M., Gorkhover, T., Andersson, I., Hirsemann, H., Potdevin, G., Graafsma, H., Nilsson, B. & Spence, J. C. H. Femtosecond X-ray protein nanocrystallography. *Nature* **470,** 73–77 (2011).

137. Kupitz, C., Grotjohann, I., Conrad, C. E., Roy-Chowdhury, S., Fromme, R. & Fromme, P. Microcrystallization techniques for serial femtosecond crystallography using photosystem II from Thermosynechococcus elongatus as a model system. *Philos. Trans. R. Soc. B* **369,** 20130316–20130316 (2014).
138. DePonte, D. P., Weierstall, U., Schmidt, K., Warner, J., Starodub, D., Spence, J. C. H. & Doak, R. B. Gas dynamic virtual nozzle for generation of microscopic droplet streams. *J. Phys. D. Appl. Phys.* **41,** 195505 (2008).
139. Botha, S., Nass, K., Barends, T. R. M., Kabsch, W., Latz, B., Dworkowski, F., Foucar, L., Panepucci, E., Wang, M., Shoeman, R. L., Schlichting, I. & Doak, R. B. Room-temperature serial crystallography at synchrotron X-ray sources using slowly flowing free-standing high-viscosity microstreams. *Acta Crystallogr. Sect. D Struct. Biol.* **71,** 387–397 (2015).
140. Sugahara, M., Mizohata, E., Nango, E., Suzuki, M., Tanaka, T., Masuda, T., Tanaka, R., Shimamura, T., Tanaka, Y., Suno, C., Ihara, K., Pan, D., Kakinouchi, K., Sugiyama, S., Murata, M., Inoue, T., Tono, K., Song, C., Park, J., Kameshima, T., Hatsui, T., Joti, Y., Yabashi, M. & Iwata, S. Grease matrix as a versatile carrier of proteins for serial crystallography. *Nat. Methods* **12,** 61–63 (2015).
141. Sugahara, M., Nakane, T., Masuda, T., Suzuki, M., Inoue, S., Song, C., Tanaka, R., Nakatsu, T., Mizohata, E., Yumoto, F., Tono, K., Joti, Y., Kameshima, T., Hatsui, T., Yabashi, M., Nureki, O., Numata, K., Nango, E. & Iwata, S. Hydroxyethyl cellulose matrix applied to serial crystallography. *Sci. Rep.* **7,** 1–9 (2017).
142. Landau, E. M. & Rosenbusch, J. P. Lipidic cubic phases: A novel concept for the crystallization of membrane proteins. *Proc. Natl. Acad. Sci.* **93,** 14532–14535 (1996).
143. Weierstall, U., James, D., Wang, C., White, T. A., Wang, D., Liu, W., Spence, J. C. H., Bruce Doak, R., Nelson, G., Fromme, P., Fromme, R., Grotjohann, I., Kupitz, C., Zatsepin, N. A., Liu, H., Basu, S., Wacker, D., Won Han, G., Katritch, V., Boutet, S., Messerschmidt, M., Williams, G. J., Koglin, J. E., Marvin Seibert, M., Klinker, M., Gati, C., Shoeman, R. L., Barty, A., Chapman, H. N., Kirian, R. A., Beyerlein, K. R., Stevens, R. C., Li, D., Shah, S. T. A., Howe, N., Caffrey, M. & Cherezov, V. Lipidic cubic phase injector facilitates membrane protein serial femtosecond crystallography. *Nat. Commun.* **5,** (2014).
144. Holton, J. M. & Frankel, K. A. The minimum crystal size needed for a

complete diffraction data set. *Acta Crystallogr. Sect. D Struct. Biol.* **66,** 393–408 (2010).
145. Baba, S., Hoshino, T., Ito, L. & Kumasaka, T. Humidity control and hydrophilic glue coating applied to mounted protein crystals improves X-ray diffraction experiments. *Acta Crystallogr. Sect. D Struct. Biol.* **69,** 1839–1849 (2013).
146. Yamamoto, M., Hirata, K., Yamashita, K., Hasegawa, K., Ueno, G., Ago, H. & Kumasaka, T. Protein microcrystallography using synchrotron radiation. *IUCrJ* **4,** 529–539 (2017).
147. Nogly, P., James, D., Wang, D., White, T. A., Zatsepin, N., Shilova, A., Nelson, G., Liu, H., Johansson, L., Heymann, M., Jaeger, K., Metz, M., Wickstrand, C., Wu, W., Båth, P., Berntsen, P., Oberthuer, D., Panneels, V., Cherezov, V., Chapman, H., Schertler, G., Neutze, R., Spence, J., Moraes, I., Burghammer, M., Standfuss, J. & Weierstall, U. Lipidic cubic phase serial millisecond crystallography using synchrotron radiation. *IUCrJ* **2,** 168–176 (2015).
148. Warkentin, M., Hopkins, J. B., Badeau, R., Mulichak, A. M., Keefe, L. J. & Thorne, R. E. Global radiation damage: Temperature dependence, time dependence and how to outrun it. *J. Synchrotron Radiat.* **20,** 7–13 (2013).
149. Hunter, M. S., Segelke, B., Messerschmidt, M., Williams, G. J., Zatsepin, N. A., Barty, A., Henry Benner, W., Carlson, D. B., Coleman, M., Graf, A., Hau-Riege, S. P., Pardini, T., Marvin Seibert, M., Evans, J., Boutet, S. & Frank, M. Fixed-target protein serial microcrystallography with an X-ray free electron laser. *Sci. Rep.* **4,** 1–5 (2014).
150. Cohen, A. E., Soltis, S. M., González, A., Aguila, L., Alonso-Mori, R., Barnes, C. O., Baxter, E. L., Brehmer, W., Brewster, A. S., Brunger, A. T., Calero, G., Chang, J. F., Chollet, M., Ehrensberger, P., Eriksson, T. L., Feng, Y., Hattne, J., Hedman, B., Hollenbeck, M., Holton, J. M., Keable, S., Kobilka, B. K., Kovaleva, E. G., Kruse, A. C., Lemke, H. T., Lin, G., Lyubimov, A. Y., Manglik, A., Mathews, I. I., McPhillips, S. E., Nelson, S., Peters, J. W., Sauter, N. K., Smith, C. A., Song, J., Stevenson, H. P., Tsai, Y., Uervirojnangkoorn, M., Vinetsky, V., Wakatsuki, S., Weis, W. I., Zadvornyy, O. A., Zeldin, O. B., Zhu, D. & Hodgson, K. O. Goniometer-based femtosecond crystallography with X-ray free electron lasers. *Proc. Natl. Acad. Sci.* **111,** 17122–17127 (2014).
151. Beyerlein, K. R., Dierksmeyer, D., Mariani, V., Kuhn, M., Sarrou, I., Ottaviano, A., Awel, S., Knoska, J., Fuglerud, S., Jönsson, O., Stern, S., Wiedorn, M. O., Yefanov, O., Adriano, L., Bean, R., Burkhardt, A., Fischer, P., Heymann, M., Horke, D. A., Jungnickel, K. E. J., Kovaleva, E., Lorbeer, O., Metz, M., Meyer, J., Morgan, A., Pande, K., Panneerselvam, S., Seuring, C., Tolstikova, A., Lieske, J., Aplin, S., Roessle, M., White, T. A., Chapman, H. N., Meents, A. & Oberthuer, D. Mix-and-diffuse serial synchrotron crystallography. *IUCrJ* **4,** 769–777 (2017).
152. Hough, M. A., Antonyuk, S. V., Strange, R. W., Eady, R. R. & Hasnain, S. S. Crystallography with Online Optical and X-ray Absorption

Spectroscopies Demonstrates an Ordered Mechanism in Copper Nitrite Reductase. *J. Mol. Biol.* **378,** 353–361 (2008).
153. Schlichting, I., Berendzen, J., Chu, K., Stock, A. M., Maves, S. A., Benson, D. E., Sweet, R. M., Ringe, D., Petsko, G. A. & Sligar, S. G. The Catalytic Pathway of Cytochrome P450cam at Atomic Resolution. *Science* **287,** 1615–1622 (2000).
154. Kraft, P., Bergamaschi, A., Broennimann, C., Dinapoli, R., Eikenberry, E. F., Henrich, B., Johnson, I., Mozzanica, A., Schlepütz, C. M., Willmott, P. R. & Schmitt, B. Performance of single-photon-counting PILATUS detector modules. *J. Synchrotron Radiat.* **16,** 368–375 (2009).
155. Rajendran, C., Dworkowski, F. S. N., Wang, M. & Schulze-Briese, C. Radiation damage in room-temperature data acquisition with the PILATUS 6M pixel detector. *J. Synchrotron Radiat.* **18,** 318–328 (2011).
156. Horrell, S., Kekilli, D., Sen, K., Owen, R. L., Dworkowski, F. S. N., Antonyuk, S. V., Keal, T. W., Yong, C. W., Eady, R. R., Hasnain, S. S., Strange, R. W. & Hough, M. A. Enzyme catalysis captured using multiple structures from one crystal at varying temperatures. *IUCrJ* **5,** 1–10 (2018).
157. Sauter, N. K. XFEL diffraction: Developing processing methods to optimize data quality. *J. Synchrotron Radiat.* **22,** 239–248 (2015).
158. Shanks, K. S., Philipp, H. T., Weiss, J. T., Becker, J., Tate, M. W. & Gruner, S. M. The high dynamic range pixel array detector (HDR-PAD): Concept and design. *AIP Conf. Proc.* **1741,** (2016).
159. White, T. A. Post-refinement method for snapshot serial crystallography. *Philos. Trans. R. Soc. B* **369,** 20130330 (2014).
160. Joti, Y., Kameshima, T., Yamaga, M., Sugimoto, T., Okada, K., Abe, T., Furukawa, Y., Ohata, T., Tanaka, R., Hatsui, T. & Yabashi, M. Data acquisition system for X-ray free-electron laser experiments at SACLA. *J. Synchrotron Radiat.* **22,** 571–576 (2015).
161. White, T. A., Kirian, R. A., Martin, A. V., Aquila, A., Nass, K., Barty, A. & Chapman, H. N. CrystFEL: A software suite for snapshot serial crystallography. *J. Appl. Crystallogr.* **45,** 335–341 (2012).
162. Hattne, J., Echols, N., Tran, R., Kern, J., Gildea, R. J., Brewster, A. S., Alonso-Mori, R., Glöckner, C., Hellmich, J., Laksmono, H., Sierra, R. G., Lassalle-Kaiser, B., Lampe, A., Han, G., Gul, S., DiFiore, D., Milathianaki, D., Fry, A. R., Miahnahri, A., White, W. E., Schafer, D. W., Seibert, M. M., Koglin, J. E., Sokaras, D., Weng, T.-C., Sellberg, J., Latimer, M. J., Glatzel, P., Zwart, P. H., Grosse-Kunstleve, R. W., Bogan, M. J., Messerschmidt, M., Williams, G. J., Boutet, S., Messinger, J., Zouni, A., Yano, J., Bergmann, U., Yachandra, V. K., Adams, P. D. & Sauter, N. K. Accurate macromolecular structures using minimal measurements from X-ray free-electron lasers. *Nat. Methods* **11,** 545–548 (2014).
163. Kabsch, W. Processing of X-ray snapshots from crystals in random orientations. *Acta Crystallogr. Sect. D Struct. Biol.* **70,** 2204–2216 (2014).
164. Barty, A., Kirian, R. A., Maia, F. R. N. C., Hantke, M., Yoon, C. H.,

White, T. A. & Chapman, H. N. Cheetah: Software for high-throughput reduction and analysis of serial femtosecond X-ray diffraction data. *J. Appl. Crystallogr.* **47,** 1118–1131 (2014).
165. Nakane, T., Joti, Y., Tono, K., Yabashi, M., Nango, E., Iwata, S., Ishitani, R. & Nureki, O. Data processing pipeline for serial femtosecond crystallography at SACLA. *J. Appl. Crystallogr.* **49,** 1035–1041 (2016).
166. Leslie, A. G. W. The integration of macromolecular diffraction data. in *Acta Crystallographica Section D Structural Biology* **62,** 48–57 (2006).
167. Duisenberg, A. J. M. Indexing in single-crystal diffractometry with an obstinate list of reflections. *J. Appl. Crystallogr.* **25,** 92–96 (1992).
168. Kabsch, W. XDS. *Acta Crystallogr. Sect. D Struct. Biol.* **66,** 125–132 (2010).
169. Brehm, W. & Diederichs, K. Breaking the indexing ambiguity in serial crystallography. *Acta Crystallogr. Sect. D Struct. Biol.* **70,** 101–109 (2014).
170. White, T. A., Mariani, V., Brehm, W., Yefanov, O., Barty, A., Beyerlein, K. R., Chervinskii, F., Galli, L., Gati, C., Nakane, T., Tolstikova, A., Yamashita, K., Yoon, C. H., Diederichs, K. & Chapman, H. N. Recent developments in CrystFEL. *J. Appl. Crystallogr.* **49,** 680–689 (2016).
171. Herrmann, S., Boutet, S., Duda, B., Fritz, D., Haller, G., Hart, P., Herbst, R., Kenney, C., Lemke, H., Messerschmidt, M., Pines, J., Robert, A., Sikorski, M. & Williams, G. CSPAD-140k: A versatile detector for LCLS experiments. *Nucl. Instruments Methods Phys. Res. Sect. A Accel. Spectrometers, Detect. Assoc. Equip.* (2013). doi:10.1016/j.nima.2013.01.057
172. Kameshima, T., Ono, S., Kudo, T., Ozaki, K., Kirihara, Y., Kobayashi, K., Inubushi, Y., Yabashi, M., Horigome, T., Holland, A., Holland, K., Burt, D., Murao, H. & Hatsui, T. Development of an X-ray pixel detector with multi-port charge-coupled device for X-ray free-electron laser experiments. *Rev. Sci. Instrum.* **85,** 0–15 (2014).
173. Kirian, R. A., Wang, X., Weierstall, U., Schmidt, K., Spence, J. C. H., Hunter, M., Fromme, P., White, T. A., Chapman, H. N. & Holton, J. Femtosecond protein nanocrystallography—data analysis methods. *Opt. Express* **18,** 5713–5723 (2010).
174. Kirian, R. A., White, T. A., Holton, J. M., Chapman, H. N., Fromme, P., Barty, A., Lomb, L., Aquila, A., Maia, F. R. N. C., Martin, A. V, Fromme, R., Wang, X., Hunter, M. S., Schmidt, K. & Spence, J. C. H. Structure-factor analysis of femtosecond microdiffraction patterns from protein nanocrystals. *Acta Crystallogr. Sect. A Found. Crystallogr.* **67,** 131–140 (2011).
175. Uervirojnangkoorn, M., Zeldin, O. B., Lyubimov, A. Y., Hattne, J., Brewster, A. S., Sauter, N. K., Brunger, A. T. & Weis, W. I. Enabling X-ray free electron laser crystallography for challenging biological systems from a limited number of crystals. *Elife* **4,** (2015).
176. Karplus, P. A. & Diederichs, K. Linking Crystallographic Model and Data Quality. *Science* **336,** 1030–1033 (2012).
177. Diederichs, K. & Karplus, P. A. Better models by discarding data? *Acta*

Crystallogr. Sect. D Struct. Biol. **69,** 1215–1222 (2013).
178. Lintuluoto, M. & Lintuluoto, J. M. DFT Study on Nitrite Reduction Mechanism in Copper-Containing Nitrite Reductase. *Biochemistry* **55,** 210–223 (2016).
179. Fukuda, Y., Tse, K. M., Nakane, T., Nakatsu, T., Suzuki, M., Sugahara, M., Inoue, S., Masuda, T., Yumoto, F., Matsugaki, N., Nango, E., Tono, K., Joti, Y., Kameshima, T., Song, C., Hatsui, T., Yabashi, M., Nureki, O., Murphy, M. E. P., Inoue, T., Iwata, S. & Mizohata, E. Redox-coupled proton transfer mechanism in nitrite reductase revealed by femtosecond crystallography. *Proc. Natl. Acad. Sci.* **113,** 2928–2933 (2016).
180. Haertlein, M., Moulin, M., Devos, J. M., Laux, V., Dunne, O. & Trevor Forsyth, V. Chapter Five - Biomolecular Deuteration for Neutron Structural Biology and Dynamics. in *Isotope Labeling of Biomolecules - Applications* (ed. Kelman, Z. B. T.-M. in E.) **566,** 113–157 (Academic Press, 2016).
181. Drenth, J. & Mesters, J. *Principles of protein X-ray crystallography: Third edition*. *Principles of Protein X-Ray Crystallography: Third Edition* (2007). doi:10.1007/0-387-33746-6
182. Taylor, G. The phase problem. in *Acta Crystallographica - Section D Biological Crystallography* (2003). doi:10.1107/S0907444903017815
183. Bragg, W. L. The diffraction of short electromagnetic waves by a crystal. *Proc. Camb. Philol. Soc.* (1913). doi:10.1107/S0567739472000609
184. Ewald, P. P. Introduction to the dynamical theory of X-ray diffraction. *Acta Crystallogr. Sect. A* (1969). doi:10.1107/S0567739469000155
185. Dauter, Z. & Jaskolski, M. How to read (and understand) Volume A of International Tables for Crystallography: An introduction for nonspecialists. *J. Appl. Crystallogr.* (2010). doi:10.1107/S0021889810026956
186. Evans, P. R. An introduction to data reduction: Space-group determination, scaling and intensity statistics. *Acta Crystallogr. Sect. D Biol. Crystallogr.* (2011). doi:10.1107/S090744491003982X
187. Yeates, T. O. & Fam, B. C. Protein crystals and their evil twins. *Structure* **7,** R25–R29 (1999).
188. Padilla, J. E. & Yeates, T. O. A statistic for local intensity differences: Robustness to anisotropy and pseudo-centering and utility for detecting twinning. *Acta Crystallogr. Sect. D Struct. Biol.* **59,** 1124–1130 (2003).
189. Lebedev, A. A., Vagin, A. A. & Murshudov, G. N. Intensity statistics in twinned crystals with examples from the PDB. *Acta Crystallogr. Sect. D Struct. Biol.* **62,** 83–95 (2006).
190. Tono, K., Nango, E., Sugahara, M., Song, C., Park, J., Tanaka, T., Tanaka, R., Joti, Y., Kameshima, T., Ono, S., Hatsui, T., Mizohata, E., Suzuki, M., Shimamura, T., Tanaka, Y., Iwata, S. & Yabashi, M. Diverse application platform for hard X-ray diffraction in SACLA (DAPHNIS): Application to serial protein crystallography using an X-ray free-electron laser. *J. Synchrotron Radiat.* **22,** 532–537 (2015).
191. Tono, K., Togashi, T., Inubushi, Y., Sato, T., Katayama, T., Ogawa, K., Ohashi, H., Kimura, H., Takahashi, S., Takeshita, K., Tomizawa, H.,

Goto, S., Ishikawa, T. & Yabashi, M. Beamline, experimental stations and photon beam diagnostics for the hard x-ray free electron laser of SACLA. *New J. Phys.* **15,** 83035 (2013).
192. Yumoto, H., Mimura, H., Koyama, T., Matsuyama, S., Tono, K., Togashi, T., Inubushi, Y., Sato, T., Tanaka, T., Kimura, T., Yokoyama, H., Kim, J., Sano, Y., Hachisu, Y., Yabashi, M., Ohashi, H., Ohmori, H., Ishikawa, T. & Yamauchi, K. Focusing of X-ray free-electron laser pulses with reflective optics. *Nat. Photonics* **7,** 43–47 (2012).
193. Winn, M. D., Ballard, C. C., Cowtan, K. D., Dodson, E. J., Emsley, P., Evans, P. R., Keegan, R. M., Krissinel, E. B., Leslie, A. G. W., McCoy, A. J., McNicholas, S. J., Murshudov, G. N., Pannu, N. S., Potterton, E. A., Powell, H. R., Read, R. J., Vagin, A. A. & Wilson, K. S. Overview of the CCP4 suite and current developments. *Acta Crystallogr. Sect. D Struct. Biol.* **67,** 235–242 (2011).
194. Vagin, A. A. & Teplyakov, A. Molecular replacement with MOLREP. *Acta Crystallogr. Sect. D Struct. Biol.* **66,** 22–25 (2010).
195. Murshudov, G. N., Skubák, P., Lebedev, A. A., Pannu, N. S., Steiner, R. A., Nicholls, R. A., Winn, M. D., Long, F. & Vagin, A. A. REFMAC5 for the refinement of macromolecular crystal structures. *Acta Crystallogr. Sect. D Struct. Biol.* **67,** 355–367 (2011).
196. Emsley, P. & Cowtan, K. Coot: Model-building tools for molecular graphics. *Acta Crystallogr. Sect. D Struct. Biol.* **60,** 2126–2132 (2004).
197. Adams, P. D., Afonine, P. V., Bunkoczi, G., Chen, V. B., Davis, I. W., Echols, N., Headd, J. J., Hung, L. W., Kapral, G. J., Grosse-Kunstleve, R. W., McCoy, A. J., Moriarty, N. W., Oeffner, R., Read, R. J., Richardson, D. C., Richardson, J. S., Terwilliger, T. C. & Zwart, P. H. PHENIX: A comprehensive Python-based system for macromolecular structure solution. *Acta Crystallogr. Sect. D Struct. Biol.* **66,** 213–221 (2010).
198. Mahalanobis, P. C. On the generalised distance in statistics. in *Proceedings National Institute of Science, India* **2,** 49–55 (1936).
199. Suga, M., Akita, F., Hirata, K., Ueno, G., Murakami, H., Nakajima, Y., Shimizu, T., Yamashita, K., Yamamoto, M., Ago, H. & Shen, J.-R. Native structure of photosystem II at 1.95 Å resolution viewed by femtosecond X-ray pulses. *Nature* **517,** 99–103 (2014).
200. Evans, P. R. & Murshudov, G. N. How good are my data and what is the resolution? *Acta Crystallogr. Sect. D Struct. Biol.* **69,** 1204–1214 (2013).
201. Davis, I. W., Murray, L. W., Richardson, J. S. & Richardson, D. C. MolProbity: Structure validation and all-atom contact analysis for nucleic acids and their complexes. *Nucleic Acids Res.* **32,** W615--W619 (2004).
202. Murakami, H., Ueno, G., Shimizu, N., Kumasaka, T. & Yamamoto, M. Upgrade of automated sample exchanger SPACE. *J. Appl. Crystallogr.* **45,** 234–238 (2012).
203. Zhang, Z., Sauter, N. K., Van Den Bedem, H., Snell, G. & Deacon, A. M. Automated diffraction image analysis and spot searching for high-throughput crystal screening. *J. Appl. Crystallogr.* **39,** 112–119 (2006).
204. Krissinel, E. & Henrick, K. Secondary-structure matching (SSM), a new

tool for fast protein structure alignment in three dimensions. *Acta Crystallogr. Sect. D Struct. Biol.* **60,** 2256–2268 (2004).
205. Godden, J. W., Turley, S., Teller, D. C., Adman, E. T., Liu, M. Y., Payne, W. J. & LeGall, J. The 2.3 angstrom X-ray structure of nitrite reductase from Achromobacter cycloclastes. *Science* **253,** 438–442 (1991).
206. Ellis, M. J., Dodd, F. E., Strange, R. W., Prudêncio, M., Sawers, G., Eady, R. R. & Hasnain, S. S. X-ray structure of a blue copper nitrite reductase at high pH and in copper-free form at 1.9 Å resolution. *Acta Crystallogr. Sect. D Struct. Biol.* **57,** 1110–1118 (2001).
207. Tocheva, E. I. Side-On Copper-Nitrosyl Coordination by Nitrite Reductase. *Science* **304,** 867–870 (2004).
208. Prigge, S. T., Eipper, B. A., Mains, R. E. & Amzel, L. M. Dioxygen Binds End-On to Mononuclear Copper in a Precatalytic Enzyme Complex. *Science* **304,** 864–867 (2004).
209. Fujisawa, K., Tanaka, M., Moro-oka, Y. & Kitajima, N. A Monomeric Side-On Superoxocopper(II) Complex: Cu(O2)(HB(3-tBu-5-iPrpz)3). *J. Am. Chem. Soc.* **116,** 12079–12080 (1994).
210. Itoh, S. Mononuclear copper active-oxygen complexes. *Curr. Opin. Chem. Biol.* **10,** 115–122 (2006).
211. Ghosh, S., Dey, A., Sun, Y., Scholes, C. P. & Solomon, E. I. Spectroscopic and computational studies of nitrite reductase: Proton induced electron transfer and backbonding contributions to reactivity. *J. Am. Chem. Soc.* **131,** 277–288 (2009).
212. Winter, G. Xia2: An expert system for macromolecular crystallography data reduction. *J. Appl. Crystallogr.* **43,** 186–190 (2010).
213. Winter, G., Waterman, D. G., Parkhurst, J. M., Brewster, A. S., Gildea, R. J., Gerstel, M., Fuentes-Montero, L., Vollmar, M., Michels-Clark, T., Young, I. D., Sauter, N. K. & Evans, G. DIALS : implementation and evaluation of a new integration package. *Acta Crystallogr. Sect. D Struct. Biol.* **74,** 85–97 (2018).
214. Hara, T., Fukami, K., Inagaki, T., Kawaguchi, H., Kinjo, R., Kondo, C., Otake, Y., Tajiri, Y., Takebe, H., Togawa, K., Yoshino, T., Tanaka, H. & Ishikawa, T. Pulse-by-pulse multi-beam-line operation for x-ray free-electron lasers. *Phys. Rev. Accel. Beams* **19,** (2016).
215. Zhao, Y., Lukoyanov, D. A., Toropov, Y. V., Wu, K., Shapleigh, J. P. & Scholes, C. P. Catalytic function and local proton structure at the Type 2 copper of nitrite reductase: The correlation of enzymatic pH dependence, conserved residues, and proton hyperfine structure. *Biochemistry* **41,** 7464–7474 (2002).
216. Abraham, Z. H. L., Smith, B. E., Howes, B. D., Lowe, D. J. & Eady, R. R. pH-dependence for binding a single nitrite ion to each type-2 copper centre in the copper-containing nitrite reductase of Alcaligenes xylosoxidans. *Biochem. J.* **324,** 511–516 (1997).
217. Jacobson, F., Pistorius, A., Farkas, D., De Grip, W., Hansson, Ö., Sjölin, L. & Neutze, R. pH Dependence of Copper Geometry, Reduction Potential, and Nitrite Affinity in Nitrite Reductase. *J. Biol. Chem.* **282,** 6347–6355 (2007).

218. Blakeley, M. P., Teixeira, S. C. M., Petit-Haertlein, I., Hazemann, I., Mitschler, A., Haertlein, M., Howard, E. & Podjarny, A. Neutron macromolecular crystallography with LADI-III. *Acta Crystallogr. Sect. D Struct. Biol.* **66,** 1198–1205 (2010).
219. Campbell, J. W., Hao, Q., Harding, M. M., Nguti, N. D. & Wilkinson, C. LAUEGEN version 6.0 and INTLDM. *J. Appl. Crystallogr.* **31,** 496–502 (1998).
220. Arzt, S., Campbell, J. W., Harding, M. M., Hao, Q. & Helliwell, J. R. LSCALE - The new normalization, scaling and absorption correction program in the Daresbury Laue software suite. *J. Appl. Crystallogr.* **32,** 554–562 (1999).
221. Afonine, P. V., Mustyakimov, M., Grosse-Kunstleve, R. W., Moriarty, N. W., Langan, P. & Adams, P. D. Joint X-ray and neutron refinement with phenix.refine. *Acta Crystallogr. Sect. D Struct. Biol.* **66,** 1153–1163 (2010).
222. Brenner, S., Heyes, D. J., Hay, S., Hough, M. A., Eady, R. R., Hasnain, S. S. & Scrutton, N. S. Demonstration of proton-coupled electron transfer in the copper-containing nitrite reductases. *J. Biol. Chem.* **284,** 25973–25983 (2009).
223. Fioravanti, E., Vellieux, F. M. D., Amara, P., Madern, D. & Weik, M. Specific radiation damage to acidic residues and its relation to their chemical and structural environment. *J. Synchrotron Radiat.* **14,** 84–91 (2007).
224. Cramer, C. J. & Tolman, W. B. Mononuclear Cu—O2 Complexes: Geometries, Spectroscopic Properties, Electronic Structures, and Reactivity. *ChemInform* **38,** (2007).
225. McCleverty, J. A. Chemistry of Nitric Oxide Relevant to Biology. *Chem. Rev.* **104,** 403–418 (2004).
226. Hayyan, M., Hashim, M. A. & Alnashef, I. M. Superoxide Ion: Generation and Chemical Implications. *Chem. Rev.* **116,** 3029–3085 (2016).
227. Fujisawa, K., Tateda, A., Miyashita, Y., Okamoto, K., Paulat, F., Praneeth, V. K. K., Merkle, A. & Lehnert, N. Structural and Spectroscopic Characterization of Mononuclear Copper(I) Nitrosyl Complexes: End-on versus Side-on Coordination of NO to Copper(I). *J. Am. Chem. Soc.* **130,** 1205–1213 (2008).
228. Merkle, A. C. & Lehnert, N. The side-on copper(I) nitrosyl geometry in copper nitrite reductase is due to steric interactions with isoleucine-257. *Inorg. Chem.* **48,** 11504–11506 (2009).